

The onset of cardiovascular disease in mice: an image-based, computational-experimental approach.

Thèse N° 9676

Présentée le 22 novembre 2019

à la Faculté des sciences et techniques de l'ingénieur
Laboratoire d'hémodynamique et de technologie cardiovasculaire
Programme doctoral en biotechnologie et génie biologique

pour l'obtention du grade de Docteur ès Sciences

par

Lydia ASLANIDOU

Acceptée sur proposition du jury

Prof. P. De Los Rios, président du jury
Prof. N. Stergiopulos, directeur de thèse
Prof. C. Goergen, rapporteur
Prof. U. Raaz, rapporteur
Prof. D. Pioletti, rapporteur

2019

Parler, penser, travailler, lutter, aimer, mourir - adonnez-vous à tout cela, sans fanatisme aveugle, sans tiède cécité -, en jouant. Ainsi parle un commandement central de l'éthique problématique. En recommandant également de ne pas oublier que nous sommes aussi joués par toutes ces forces élémentaires.

Kostas Axelos, *Pour une éthique problématique* (1972)

The aim of science is not to open the door to infinite wisdom,
but to set a limit to infinite error.

Bertolt Brecht, *Life of Galileo* (1939)

Το να δοθεί μορφή στο χάος - νομίζω ότι αυτός είναι ο καλύτερος ορισμός της παιδείας.
Κορνήλιος Καστοριάδης, *Ανθρωπολογία, Πολιτική, Φιλοσοφία* (1993)

To Spyros, Stella and Ioanna

Acknowledgments

Firstly, I would like to express my immense gratitude to Professor Nikos Stergiopulos, for the introduction to biomedical engineering and for the opportunity to carry out my PhD in his lab. Thank you for your trust over the years, and for believing in me. To the outstanding academic Dr Bram Trachet, who has been my supervisor from my master thesis project to the very end of my PhD, I owe my deepest thanks. Beyond his endless scientific (and encyclopedic) knowledge, moral integrity and many inspiring talents, I wish to acknowledge his unwavering support, generosity, patience and advice. I probably also owe Bram an increased life expectancy by several decades, thanks to the laughs from his astute sense of humor.

I am also very fortunate to have met Professor Annarita Di Lorenzo, an inspiring lady of science who has a passion for research I was to discover 4 years into my PhD and an ocean further than the EPFL campus. Transitioning from the dry to the wet lab was undoubtedly one of the most educational experiences of my PhD, and I am particularly grateful it was under her guidance. In the lab, ‘Good morning’ would unfailingly be followed by an inquisitive ‘Novità?’ for any new findings she might have missed during the brief hours of the night. Thank you for reminding me how important it is to have the fire in the belly in science, and in every aspect of life.

To Professor Patrick Segers, Professor Jay Humphrey and Dr Matthew Bersi, thank you for your feedback and for your meticulous manuscript revisions; reading your comments in itself has many times been more educational than an academic course. I owe a special thanks to my committee members, Professor Craig Goergen, Professor Uwe Raaz, and Professor Dominique Pioletti, for taking the time to read and discuss this dissertation.

I must also express my gratitude to the people behind the histology, microscopy and imaging core facilities of EPFL. Thank you Alessandra, Jessica, Agnès, Gianni, Roy, Céline and Giacomo for the smooth collaboration over the years.

To my dear labmates, thank you for creating such a pleasant and positive atmosphere in the lab, and for all the laughs and interesting discussions shared over lunch, office breaks or post-work beers. To Adan for his advice (and for being the garant for more than half of our lab, including myself), to Rodrigo for his impeccable microsurgery skills and innumerable funny stories, to Fabiana for her sweetness, her help with experiments and for teaching me the very basics of a dissection just before I left for my exchange, to Mike for his all-weather positivity and kindness, to Stéphane (l’oiseau du labo) for his smile and the best parapente flight I ever had (well, it’s only been one so far), to Sylvia for her constant support in administrative troubleshooting, to Maiia (Ой бcé!) for her radiant and positive personality, to Seb for enriching my fribourgeois

Acknowledgments

vocabulary with improbable words and for being the funniest dancing partner, to Augusto for always being supportive and last, but certainly not least, to the beautiful Greek corner of our lab: Constantinos, Vicky, Matina, George: a warm-hearted thanks for making the office such a fun place every day. Certain people may have left the lab but I still carry them with me: Dr Mauro Ferraro, our finite element (and sangria) expert, thank you for everything you've taught me as well as for the valuable professional and personal advice. Thank you also for holding the most epic wedding with obscene amounts of Sardinian food! To Stefanie, Natália, Elira, Carla, Valeria: you've each spent a brief amount of time in the lab, but you are all inspiring ladies that I look forward to meeting again in the future. I'd also like to thank all the lab immersion, semester and master project students who have contributed with their earnest work to this PhD.

Un po' più lontano, I wish to express my gratitude to the multitasker Luisa Rubinelli for her patience and support in teaching me the wire myography technique. To her, to my beloved Doctors Linda and Alice, and to my dear Ilaria, thank you for the late-hour laughs in the lab, for teaching me what happens when we boil BSA and for making Manhattan feel like (an Italian) home. Ci rivediamo presto!

To all the friends I've met over the years from (literally) all around the world, and to my friends from Greece, thank you for making me a better person, and for all the memorable moments we've shared that have made me genuinely happy during these years. An honorable mention to Εύη, Εύα and Αλίκη for making Lausanne feel like home, and to Ίριδα and Μαρία : the moments in your company cannot be topped (except during topless sunbathing on Greek islands). Merci aussi à Babou, qui comprend vite - suffit de lui expliquer longtemps. Thank you for taking care of me across two continents, and for our carefree breaks when you were worried I was working too much.

A Vincenzo, mi dispiace che non leggerai questa tesi, ma so che saresti felice per me. To Michalis and Pelina, thank you for the continuous love and encouragement; to Celia and Lydia (junior), thank you for being a continual source of inspiration and for making me so incredibly proud.

To my parents Spyros and Stella, and to my sister Ioanna, σας ευχαριστώ... για όλα!

Τέλος, στον Θανάση ένα μεγάλο ευχαριστώ για την άνευ όρων αγάπη και υποστήριξή του μες στα χρόνια.

Lydia Aslanidou
Lausanne, September 2019

Abstract

In a number of cardiovascular diseases, the paucity of longitudinal human data hinders our understanding of disease evolution and forestalls the discovery of new therapeutic strategies. We therefore heavily rely on animal models to elucidate the pathophysiological mechanisms that govern disease development. Mice in particular dominate the preclinical field due to their fast disease cycles and ease of genetic manipulation. Nonetheless, the reference mouse arterial physiology and hemodynamics of its systemic circulation have yet to be described. But preclinical research is not limited to healthy mice; it helps decode the elusive etiology of deadly pathologies. Among these are aortic aneurysms and dissections, two vascular injuries that portend the potentially fatal consequence of aortic rupture. A key question is: Why are these pathologies so location-specific? In humans, abdominal aortic aneurysms affect the infrarenal aorta (below the kidneys) and aortic dissections form in the thoracic aorta. Inversely, in the most commonly used mouse model of this field, aortic dissections preferentially form in the suprarenal abdominal aorta (above the kidneys) but reasons for such localization remain unknown in humans and mice.

The first step of this work aimed to fill the knowledge gap of mouse hemodynamics, by translating an existing 1D model of the human arterial circulation to the healthy mouse. Our next steps aimed to unravel the origins of site-specific aortic dissections in the mouse model of Angiotensin II infusion. Initially, we imaged the inceptive stage of disease to understand *what* happens in the suprarenal mouse aorta. Then, we explored *why* both from a biomechanical and a mechanobiological standpoint.

Firstly, we present a validated *in silico* model of an average anesthetized healthy mouse. Our 1D model combines a broad range of literature data with a detailed description of the murine vasculature. Model predictions of pressure and flow were validated against pressure, velocity and diameter measurements from a large independent dataset of mice. This versatile tool can be used to simulate pathology and facilitate the implementation of the 3R's principle in research practice.

Thereafter, we use high-resolution synchrotron imaging to characterize the early morphology of the suprarenal aorta in mice infused with Angiotensin II, prior to overt dissecting events. Taking a hint from previous findings on the importance of aortic side branches in fully developed dissections, we observed that the primary damage of the wall's microstructure preferentially occurs around two major side branches of the aorta. Following this evidence of direct involvement of side branches in disease onset, we investigated the underlying reasons from two distinct perspectives.

Acknowledgments

In a synchrotron-based computational study, we hypothesized that biomechanical forces may expose branching sites to early vascular injury. We used an in-house framework which enables a. computational structural mechanics of the aortic wall using mouse-specific geometries, and b. mouse-specific validation to indicate whether high mechanical strain spatially coincides with microstructural defects. Branching sites of the aorta concentrated the highest levels of mechanical strain, while non-branching sites were generally spared. Branch-related hotspots of strain co-localized with early damaged microstructure, thus pointing towards a mechanically-driven mechanism of disease that nucleates around the aortic branches.

We lastly explored from a mechanobiological perspective whether the suprarenal aorta's vascular function changes prior to dissection. We found a regional variation: both the contractile and the endothelial function were severely compromised in the suprarenal aorta's dissection-prone segment, but only mildly so in its dissection-protected segments. Surprisingly, vascular function was largely preserved in the adjacent side branches, creating a local discontinuity in the profile of contractile capacity between the (diseased) aorta and the (non-diseased) branches.

Key words: 1D model, aortic dissection, aortic aneurysm, Angiotensin II, ApoE-deficient, mouse, Synchrotron, finite element simulations, computational structural mechanics, wire myography, isometric testing

Résumé

Dans de nombreux cas de maladies cardiovasculaires, la pénurie d'informations longitudinales sur l'humain freine notre compréhension de la maladie, empêchant la découverte de nouvelles stratégies thérapeutiques. C'est pourquoi nous nous appuyons fortement sur des modèles animaliers afin d'élucider les mécanismes pathologiques régissant le développement de la maladie. Du fait de leur courte durée de vie, de leurs cycles rapides de maladie et de la facilité à les manipuler génétiquement, les souris dominent distinctement le domaine préclinique. Ceci étant, la physiologie artérielle et les modèles hémodynamiques de leur circulation systémique restent encore à élucider. Les anévrismes et les dissections aortiques sont des blessures vasculaires qui présagent d'une potentielle conséquence fatale de rupture aortique. Ces aorthopathies ont recueilli une attention croissante en recherche fondamentale dans le but de décoder leur étiologie évasive. La question clé est : pourquoi ces pathologies sont-elles si précisément localisées dans l'aorte ? Dans le modèle de souris le plus couramment utilisé dans ce domaine, les dissections aortiques se forment préférentiellement dans l'aorte suprarénale abdominale, mais les raisons d'une telle localisation restent inconnues à ce jour. La première étape du présent travail vise à combler les lacunes dans nos connaissances de l'hémodynamique des souris, en transposant un modèle 1D de la circulation artérielle humaine à la souris. Les étapes suivantes de cette recherche ont pour objectif de mettre à jour les facteurs décisifs biomécaniques et mécano-biologiques qui suscitent de façon synergétique des dissections aortiques à des endroits précis dans le modèle d'infusion Angiotensin II de la souris.

Premièrement, nous présentons un modèle validé *in silico* d'une souris typique sous anesthésie. Notre modèle 1D associe un vaste panel de données issues de la littérature à une description détaillée d'un système vasculaire artériel murine. En partant d'un large panel de données indépendantes sur les souris, les modèles de prévision de la pression et du flux ont été validés à travers des mesures de pressions invasives ainsi que des mesures de diamètre et de vitesse non-invasives. Cet outil versatile peut être utilisé afin de simuler des pathologies et faciliter l'implémentation du principe 3R dans les pratiques de recherche.

Ensuite, grâce à un indice trouvé lors de nos précédentes découvertes sur l'importance des branches aortiques latérales dans les dissections aortiques complètement développées, nous avons utilisé les images synchrotron à haute résolution pour caractériser la morphologie précoce de l'aorte, avant la manifestation des événements de la dissection. Nous avons découvert des dommages internes microstructuraux très localisés autour de branches latérales de l'aorte abdominale. En suivant ces preuves de l'implication directe des branches latérales dans la

manifestation de la maladie, nous avons investigué ici les raisons sous-jacentes depuis deux perspectives distinctes.

Dans une étude computationnelle basée sur le synchrotron, nous avons supposé que les forces biomécaniques exposent les sites latéraux à des blessures vasculaires précoces. Nous avons utilisé une structure computationnelle maison nous permettant d'établir a. des géométries spécifiques aux souris pour des mécaniques computationnelles structurelles du mur aortique abdominal, ainsi que b. la validation propre aux souris indiquant si les localisations de hautes contraintes mécaniques coïncident spatialement avec les dégâts micro-structurels précoces du mur. Les sites de l'aorte adjacents à des ramifications ont concentré le niveau le plus élevé de contraintes mécaniques, tandis que les segments non-ramifiés ont été généralement épargnés. Les zones à risques de contraintes se retrouvent donc co-localisées avec les défauts micro-structurels du mur, pointant ainsi vers un mécanisme d'amorçage entraîné mécaniquement pour les maladies se développant autour des branches aortiques.

L'identification d'un mécanisme pathogène n'exclue cependant pas la synergie avec d'autres; nous avons par la suite exploré d'un point de vue mécano-biologique les altérations précoces dans la vasoréactivité de l'aorte supra-rénale vulnérable (mais pas encore en état de dissection). Nous avons découvert une réponse qui varie en fonction de la région : la fonction vasculaire (contractile et endothéliale) a été sévèrement compromise dans les sections de l'aorte les plus propices à la dissection, mais seulement de façon légère dans les segments protégés. Qui plus est, la fonction vasculaire a été majoritairement préservée dans les branches latérales adjacentes, créant ainsi une discontinuité locale au sein du profil de la capacité contractile entre l'aorte (affectée) et les branches (saines).

Mots clés : modèle 1D, dissection aortique, anévrisme aortique, Angiotensin II, déficience ApoE, souris, synchrotron, simulations en éléments finis, mécaniques structurelles computationnelles, myographie filaire, essais isométriques.

Contents

Acknowledgments	i
Abstract (English/Français)	iii
Introduction	1
1 Motivation	1
2 Arterial structure and functional layers	1
2.1 Physiology	1
2.2 Arterial function	3
3 Aortopathies: aneurysms and dissections	9
3.1 Abdominal aortic aneurysms (AAAs)	10
3.2 Thoracic aortic aneurysms (TAAs)	14
3.3 Aortic dissection	16
4 Preclinical research: powerful tools from imaging to myography	19
4.1 Small animal imaging techniques	19
4.2 Numerical models of the cardiovascular system	30
4.3 Vascular reactivity assessment	33
5 The Angiotensin II infusion mouse model	35
5.1 Mouse models of aortic aneurysm and dissection	35
5.2 The Angiotensin II infusion model of aneurysm and dissection	37
5.3 Insights from high-resolution 3D synchrotron imaging	54
6 Aims of the thesis	70
7 Summary of chapters	70
Bibliography	73
1 Chapter 1	
A 1D model of the arterial circulation in mice	95
1 Introduction	95
2 Methods	96
3 Results	106
4 Discussion	111
Bibliography	117

2 Chapter 2

Early characterization of Angiotensin II-induced dissections: do side branches hold the key? 125

1	Introduction	125
2	Methods	127
3	Results	129
4	Discussion	130
	Bibliography	134

3 Chapter 3

Co-Localization of Microstructural Damage and Excessive Mechanical Strain at Aortic Branches in Angiotensin-II Infused Mice 137

1	Introduction	137
2	Methods	139
3	Results	144
4	Discussion	150
5	Appendix	156
	Bibliography	157

4 Chapter 4

Early alterations in vascular function of the suprarenal aorta in AngII-infused ApoE-deficient mice 163

1	Introduction	163
2	Methods	165
3	Results	169
4	Discussion	173
5	Limitations and future work	177
6	Conclusions	178
	Bibliography	183

5 Conclusions 189

1	Modelling the arterial circulation of the mouse	189
2	Disease pathogenesis in a mouse model of aortic aneurysm and dissection . . .	190
	2.1 The initiation of aortic dissection: a biomechanical perspective	192
	2.2 The initiation of aortic dissection: a mechanobiological perspective . . .	193
	2.3 A unified approach to explain a branch-related disease onset	193
3	Limitations and future perspectives	194
	3.1 1D modelling of the arterial tree	195
	3.2 Mouse models: what is their translational value?	195
	3.3 Blood pressure measurements	196
	3.4 Computational structural mechanics	197
	3.5 Vascular reactivity assessment	198
4	What's next?	199

Bibliography	200
Curriculum Vitae	203
List of Publications	205

Introduction

1 Motivation

Cardiovascular diseases represent the leading cause of morbidity and mortality in the western world. Aortopathies in particular, including dissections and aneurysms, represent an important healthcare burden due to excess early mortality, increasing incidence, and underdiagnosis^{1,2}. Aortic dissections and aneurysms are multifactorial diseases associated with numerous cardiovascular risk factors such as aging and hypertension. The regular occurrence of dissections and aneurysms in consistent locations such as the ascending and infrarenal abdominal aorta, suggests that arterial wall mechanics, hemodynamics and geometry may play significant roles in disease formation. Aortic aneurysms are typically indolent, while aortic dissections are acute; in both cases, patients are not forewarned with symptoms, hampering the design of prospective human cohort studies. Where lack of longitudinal human data, particularly at the early stage, limits our understanding of disease pathogenesis, animal models offer an excellent alternative to investigate the etiology of the disease. The purpose of this thesis is to establish a numerical model of the mouse arterial system and investigate the biomechanics and early functional changes linked to disease initiation in the most common experimental mouse model of aortic aneurysm and dissection.

2 Arterial structure and functional layers

2.1 Physiology

Typically, the arterial wall consists of three concentric layers: the intima, the media and the adventitia (Figure 1). These layers respectively occupy about 5%, 80% and 15% of the arterial wall³. The innermost layer, termed *tunica intima*, consists of a monolayer of endothelial cells that adheres to an internal basal membrane made of fibronectin, laminin and type IV collagen. The endothelium is not only a non-thrombogenic surface separating the vascular wall from free-flowing blood, but it is also biologically active⁴. As we will see in subsection 2.2, the endothelium is a regulator of vascular tone through the synthesis and release of vasoactive mediators.

The medial layer (*tunica media*) mainly consists of alternating elastic lamellae and embedded

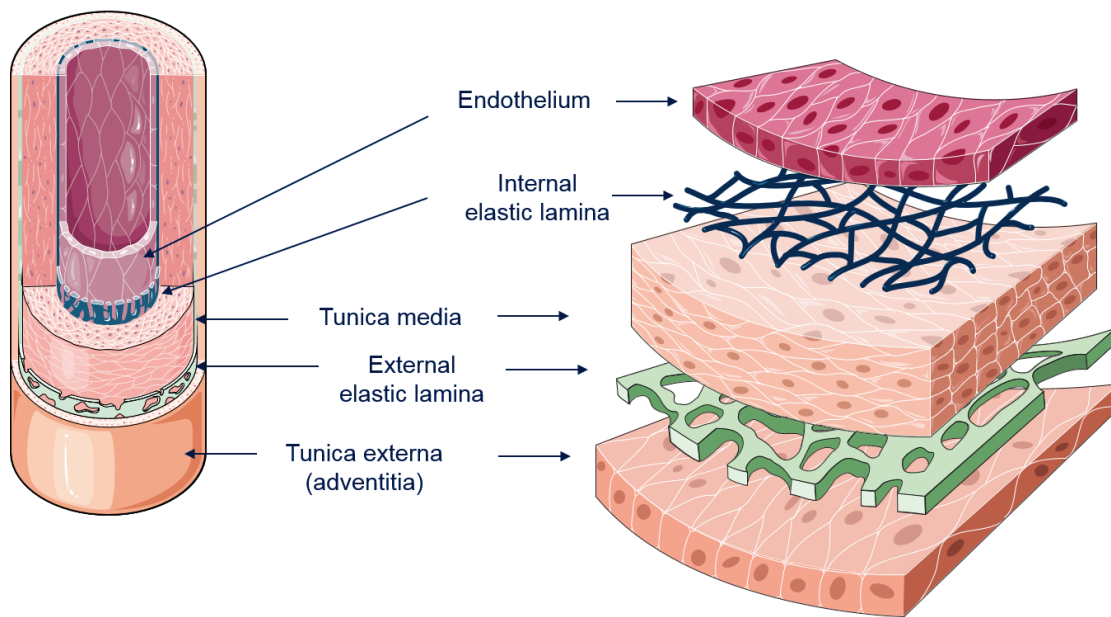


Figure 1: Schematic depiction of layers in a healthy arterial wall. Adapted from Servier Medical.

smooth muscle cells along with various types of collagen (I, III, V, etc.), and proteoglycans. The more proximal the vessels are to the heart the more elastin they have (elastic arteries), and the further away the more smooth muscle they have (muscular arteries). It has been suggested that large arteries tend to maintain their mean circumferential wall stress around a homeostatic value of 100kPa⁵. Smooth muscle cells regulate the vascular tone through vessel contraction and dilation.

The outermost adventitial layer (*tunica adventitia*) consists primarily of collagen (axially oriented, type I⁶), fibroblasts and elastic fibers. A network of microvasculature arises here, the vasa vasorum, whose mission is to supply oxygen and nutrients to the outer layers of the arterial wall. The adventitia can act as a protective layer that prevents the media from overdistending under conditions of acute, extreme loading of the wall. Fibroblasts are responsible for regulating the extracellular matrix, which we will describe below.

Extracellular matrix

The major constituent of the vessel wall is the extracellular matrix (ECM). In arteries or veins, the ECM represents more than half of the wall mass⁷ and is constructed from multiple matrix proteins (mainly collagens and elastin), which provide the necessary support to cells and tissues. Depending on their function, the proteins constituting the ECM can be classified as either structural or non-structural. Examples of structural proteins include collagens and elastin, while instances of non-structural proteins include fibronectin, laminin and tenascin. Other important components of the ECM are integrins, growth factors and a group of matrix metalloproteinases.

Elastin is the structural protein of the ECM which provides tissue with the ability to stretch and recoil, alongside glycoproteins such as fibrillin and fibulin. Elastin is composed of single tropoelastin subunits cross-linked with fibrillin microfibrils, to form an elastic fiber. Elastin is composed during development and its half-life is approximately 40 years in humans⁸. However, arterial elastin undergoes extensive fragmentation and degradation in the setting of cardiovascular diseases such as hypertension or aneurysms⁷. Reparative elastogenesis in those cases proves mostly ineffective⁹.

Collagen provides the necessary structural integrity for tissues. It is arranged into fibrils¹⁰, an organization that endows the normal aortic wall with stiffness and tensile strength. Such properties are required to sustain the different mechanical stresses acting on the wall, which we will see in the following section. Apart from fibroblasts, collagen is synthesized by endothelial and epithelial cells⁴. Fibrillar collagen plays important roles in many disease processes. As we will see below, in the case of aneurysms, where extensive elastin fragmentation and loss of smooth muscle cell functionality takes place, collagen plays an instrumental role in controlling the expansion of these lesions through wall remodelling.

2.2 Arterial function

Endothelial cell function

The endothelial cells form a monolayer that serves as a selective barrier between the blood and the vessel wall, but they are also modulators of several biological processes. Endothelial cells secrete growth factors to control vessel remodelling or thrombotic factors to control thrombosis. They also regulate inflammatory responses, through adhesion of leukocytes, as well as the contractile state of their adjacent smooth muscle cells, through secretion of vasoactive substances.

One such vasoactive substance is nitric oxide (NO), an important mediator of the control of blood vessel tone. The discovery of nitric oxide as a signaling molecule in the cardiovascular system earned the 1998 Nobel Prize in Medicine or Physiology to Furchgott, Ignarro and Murad. It has been shown that the endothelium responds to frictional forces (shear stress) arising from circulating blood by releasing a neurotransmitter called acetylcholine¹¹. Acetylcholine in turn induces the release of nitric oxide in the endothelium, which through diffusion within the wall leads to the vasorelaxation of smooth muscle cells¹². In a state of endothelial dysfunction, acetylcholine does not induce the release of NO and instead acts on the smooth muscle cells directly, thereby causing vasoconstriction¹³.

Vascular smooth muscle cell function

The aorta has varying structural and biochemical influences above and below the diaphragm¹⁵. This spatial heterogeneity starts at embryonic development and affects the medial smooth muscle cells' synthetic and contractile behavior¹⁶. The majority of smooth muscle cells

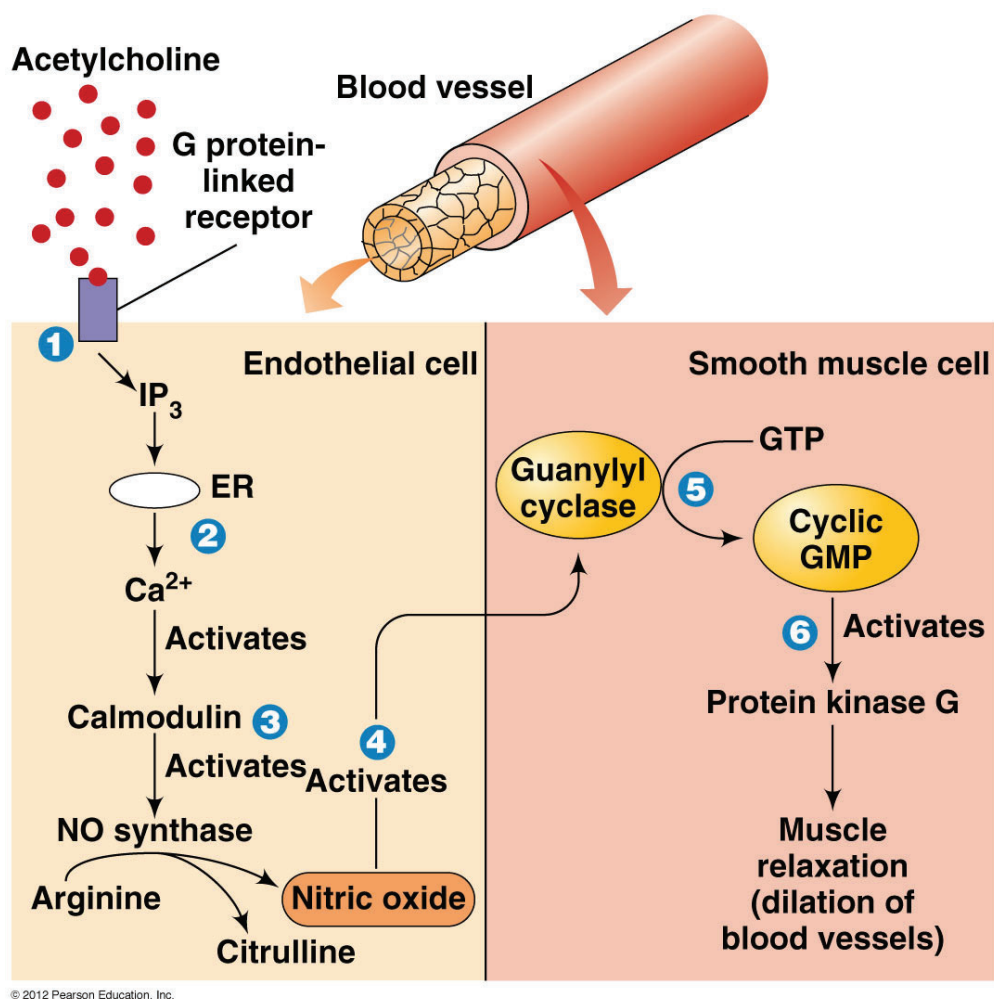


Figure 2: Nitric oxide mediates acetylcholine-induced relaxation. The neurotransmitter acetylcholine stimulates blood vessel dilation by activating a G protein-coupled receptor -the muscarinic acetylcholine receptor- on the surface of endothelial cells. This receptor activates a G protein, Gq, thereby stimulating IP₃ synthesis and Ca²⁺ release. Ca²⁺ activates nitric oxide synthase, causing the endothelial cells to produce NO from arginine. The NO diffuses through the wall to reach the adjacent smooth muscle cells, where it activates guanylyl cyclase to produce cyclic GMP. In turn, the cyclic GMP triggers a response that causes the smooth muscle cells to relax, increasing blood flow through the vessel.

IP₃: Inositol 1,4,5-triphosphate, Gq: G protein, GMP: guanosine monophosphate. Reproduced from¹⁴.

are circumferentially oriented. Several aspects of smooth muscle cell modulations, such as hypertrophy (meaning increase in size), hyperplasia (meaning increase in number), apoptosis (programmed cell death), and migration play central roles in diseases such as aneurysms. A fascinating aspect of vascular smooth muscle cell behavior is their ability to undergo a profound phenotypic transition (termed phenotypic switch) from quiescent contractile cells to proliferating cells, with the accompanying loss of contractile protein expression (for example

α -actin, calponin, β -myosin heavy chain) but with increased synthesis of ECM-degrading proteases. This plasticity in the phenotypic differentiation of smooth muscle cells helps repair the vascular wall after injury. Smooth muscle cells that have switched to the synthetic phenotype secrete proteinases to degrade the ECM and manage to migrate towards the injured area of the wall. They can also proliferate and synthesize ECM in order to repair the injured site. Once the wall is restored, they can switch again toward a contractile phenotype¹⁷.

Both endothelial and vascular smooth muscle cells sense and respond to changes in their mechanical environment^{18,19}. It is therefore important to understand the mechanics within the vasculature at multiple scales: at the macro-level of the aorta as a load-bearing vessel, but also at the cellular level in terms of mechanical stimuli that trigger local cellular responses.

Properties of the aorta

At every heartbeat, the aorta expands to accommodate the blood ejected from the left ventricle during systole and then releases this stored energy by dynamic elastic recoil during diastole²⁰. This function of the aorta as an elastic reservoir converts the pulsatile flow to a nearly continuous supply of blood in the peripheral beds. This is called the windkessel effect (Figure 3), based on the hydraulic analog of the arterial system with a fire engine that uses a Windkessel.

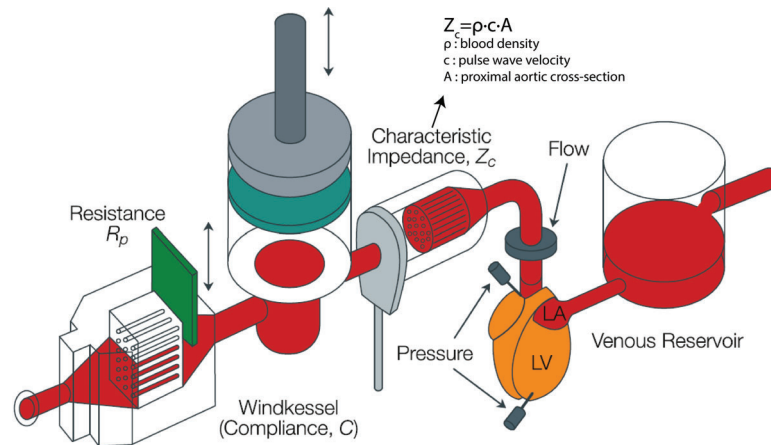


Figure 3: Schematic of the Windkessel layout. This approach can be used for lumped models of the arterial network, which mimic the load on the heart (e.g. three-element Windkessel models, as shown here). R_p is peripheral resistance (summed resistance of peripheral beds). Total arterial compliance is the sum of compliances of all arteries; the compliance is significant in the large conduit arteries, with the greatest part in the (proximal) aorta. Reproduced from²¹.

The systolic contraction of the heart generates pressure waves, which propagate along the arterial tree with a speed defined as the pulse wave velocity. As the distance from the heart increases, the amplitude between the systolic and diastolic blood pressure (the pulse pressure) increases, while the mean arterial pressure drops (~ 4 mmHg along the length of the aorta)²². The amplification of pulse pressure increases until the periphery, where it rapidly decreases,

Introduction

along with the mean arterial pressure, to the microcirculation levels.

Waves are reflected as they encounter reflection sites in the circulation (for example bifurcations). At any point in the arterial tree, pressure and flow waves are the sum of forward waves travelling from the heart to the periphery, and backward waves travelling from the periphery to the heart (Figure 4).

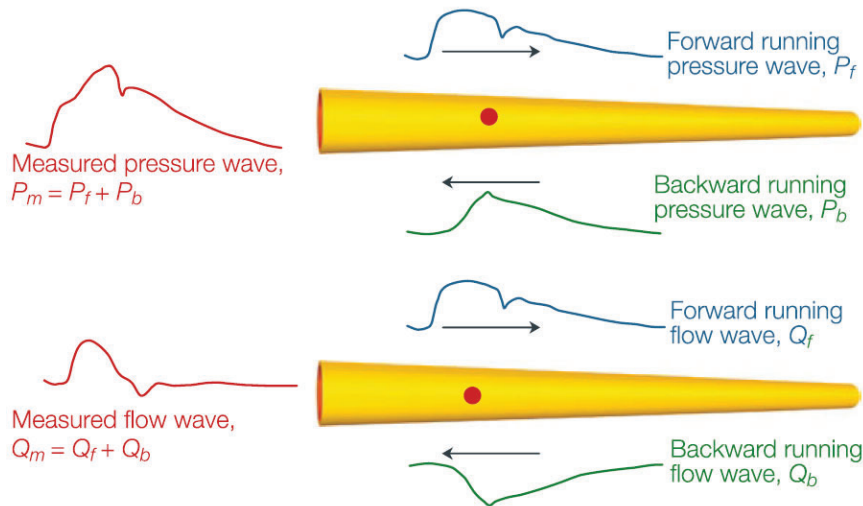


Figure 4: Separation of forward and backward components in running pressure and flow waves. Taken from²¹.

To characterize the aorta's elasticity, the quantity of compliance is used. Volume compliance is defined as the ratio of changes in volume to changes in pressure, $\frac{\Delta V}{\Delta P}$, but can also be defined based on area changes, $\frac{\Delta A}{\Delta P}$. To facilitate comparison of properties across vessels, compliance can be normalized to the volume of the organ it describes to yield its distensibility $\frac{(\Delta V/V)}{\Delta P}$.

At this point we make a distinction between the aortic active and passive mechanical properties, both of which play a central role in maintaining vascular homeostasis. The active tension component within the aortic wall is provided by aortic contractility, meaning the contractile force generated primarily by the vascular smooth muscle cells²³. Compliance of the aorta is generally associated with the composition of the extracellular matrix²⁰. Collagen and elastin endow the aortic wall with tensile strength and elastic recoil and contribute to maintaining the compliant properties of the aorta²⁴. The elastic fibers, which are distensible with a low tensile strength, form an interconnected lamellar network in the medial layer of the aorta and dominate behavior at low distending pressures²⁰. At high pressures, the circumferentially aligned collagen fibers, originally in a corrugated state, straighten out and bear most of the load²⁰. When altered, the extracellular and cellular components that regulate the aorta's mechanical properties could contribute to its pathophysiology.

Mechanical forces on the arterial wall

The most important components of aortic stress for a straight arterial segment are shown in Figure 5 and listed below. Nonlinear differential equations need to be solved to quantify stresses as a function of position and time, but their mean values can be estimated in straight segments²⁵.

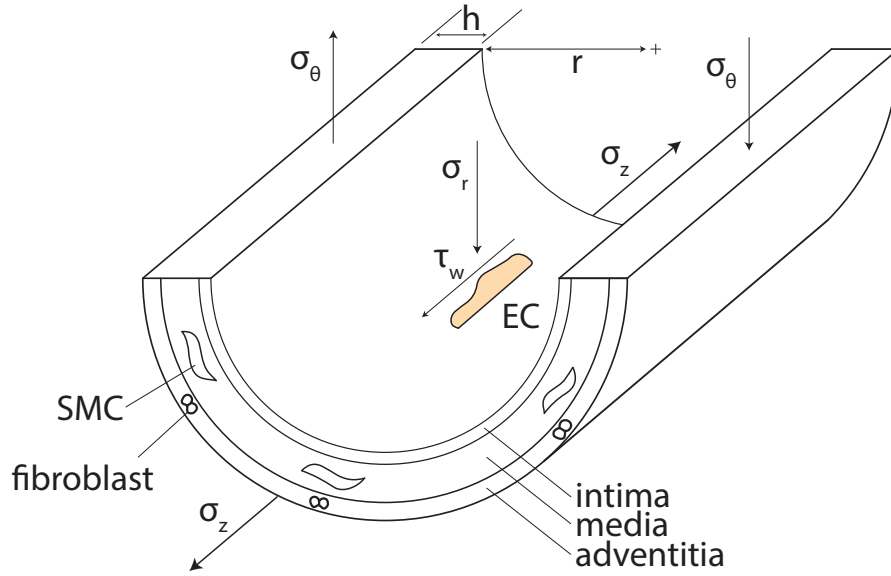


Figure 5: Mechanical stresses on the vascular wall that result from hemodynamic loading. Of the 4 stresses depicted, σ_θ and σ_z are the largest in the aorta. Modified from Humphrey et al.²⁶.

1. The **circumferential stress** σ_θ (caused by the distending blood pressure changing the circumference cyclically). From Laplace's law:

$$\sigma_\theta = \frac{P \cdot r}{h} \approx 150 \text{ kPa}$$

where P : transmural pressure, r : the inner radius of the lumen, h : the wall thickness, with r/h equal to 7-10 in large normal arteries in humans²⁷. In response to changes in transmural pressure, there is a tendency to maintain a homeostatic value of the mean circumferential stress; this implies that changes in vascular wall thickness may occur accordingly²⁷. Even if wall thickness changes slightly during the vasoactive responses of contraction or relaxation, marked changes in thickness arise from changes in the mass of extracellular matrix (through synthesis/degradation) and changes in smooth muscle (hyperplasia/hypertrophy). In order to explain the mechano-control of the aorta in disease, Wolinsky and Glagov²⁸ applied Laplace's law in a range of animals including mice, rabbits, dogs, pigs and humans. They found that in mammals the number of elastic laminae in the aorta increases proportionally with the diameter. They concluded that "the average tension per lamellar unit of aortic media was remarkably independent of species and very nearly constant" ($\sim 2 \text{ N/m}$).

Introduction

2. The **axial stress** σ_z (caused by forces in the axial direction):

$$\sigma_z = \frac{f}{\pi h(2r + h)} \approx 125kPa$$

where f : the axial force, r : the inner radius of the lumen, h : the wall thickness.

3. The **radial stress** σ_r (due directly to blood pressure and perivascular constraints)

$$\sigma_r = \frac{-P}{2} \approx 50kPa$$

where P : transmural pressure.

4. The **wall shear stress** τ_w (caused by frictional interactions between the endothelium and flowing blood), here given by the solution of a steady, fully developed, laminar, one-dimensional, incompressible flow of a Newtonian fluid within a rigid circular tube (a rough approximation for an artery):

$$\tau_w = \frac{4\mu Q}{\pi r^3} \approx 1.5Pa$$

where P : transmural pressure, r : the inner radius of the lumen, h : the wall thickness, f : the axial force, Q : the mean volumetric blood flow, and μ : the viscosity of the blood.

To understand the mechanics of the wall subjected to these stresses, mathematical constitutive modelling has been informative in defining the relative contribution of elastin and collagen (passive mechanical properties of the aorta, cf section 2.2). Early constitutive models considered the arterial wall as a homogeneous material (detailed review by Vito and Dixon²⁹). Later efforts focused on incorporating the arterial wall's microstructure (detailed review by Holzapfel and Ogden³⁰). As an example, Holzapfel, Gasser and Ogden proposed a constitutive model using two families of collagen fibers oriented symmetrically with respect to the circumferential axis and embedded in an isotropic elastin matrix³¹. This model was extended with two additional families of collagen fibers in the circumferential and axial direction³². Versions of the four-fiber-family model have been used to fit mechanical data of arteries from wildtype³³ or genetically manipulated mice that present alterations in the extracellular matrix^{34,35,36}.

3 Aortopathies: aneurysms and dissections

Aortic aneurysms

An aortic aneurysm is a degenerative cardiovascular disease defined as a permanent and localized dilation of the aorta to a diameter at least 1.5-times greater than normal. In comparison, the term aortic ectasia is used for aortic enlargement <1.5 -times normal diameter³⁷. Catastrophic rupture of an aneurysm with egress of blood into the peritoneal cavity causes hemorrhagic and hypovolemic shock (i.e. decreased peripheral perfusion and hypotension)³⁸. Aortic aneurysms represent the 18th most common cause of death, responsible for 1% to 2% of all deaths in the industrialized world³⁹. Most patients with aortic aneurysms are asymptomatic, and their aneurysms are discovered upon rupture or incidentally during physical examination or unrelated imaging.

Based on their aortic location, aneurysms appearing in the ascending or descending aorta are termed **thoracic aortic aneurysms** (occurring above the diaphragm) while aneurysms appearing in the abdominal aorta are termed **abdominal aortic aneurysms**. This dichotomy not only distinguishes the topography of the aneurysms but also reflects fundamental mechanistic distinctions in the risk factors, etiology and pathophysiology of these conditions. The disparate features of the two conditions are described in the following sections. Both pathologies, however, culminate to matrix degeneration and the potential biomechanical failure of rupture, which occurs when wall stresses locally exceed the wall strength.

Based on their shape, aortic aneurysms can be broadly described as saccular or fusiform (cf. Figure 6B and C). A saccular aneurysm bulges in a unilateral manner and forms a distinct pouch of dilated vascular wall. On the contrary, fusiform aneurysms expand circumferentially and are therefore somewhat symmetrical. Saccular aortic aneurysms are less frequent but their risk of rupture is considered to be higher^{40,41}.

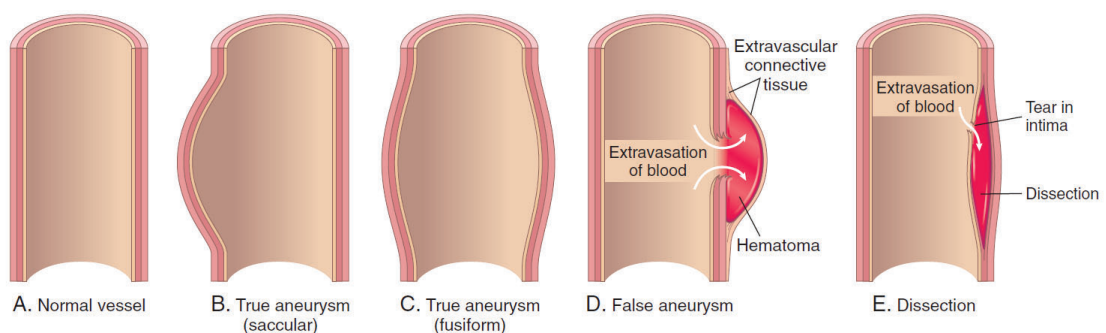


Figure 6: Aneurysm morphologies. A, Normal morphology. B, True (saccular) aneurysm. The wall focally expands outward and all wall layers are present. C, True (fusiform) aneurysm. There is symmetric circumferential dilatation and all wall layers are present. D, False aneurysm. The wall is ruptured, and there is a hematoma that is externally bound. E, Dissection. Blood has entered the wall of the vessel through a tear in the lumen (intimal tear) and separated the layers. Reproduced from³⁸.

3.1 Abdominal aortic aneurysms (AAAs)

Ruptured AAA is the 13th-leading cause of death in the United States and is estimated to cause $\approx 15,000$ deaths per year. The frequency of rupture is 4.4 per 100,000 patients. Despite increased survival following diagnosis, both incidence and crude mortality seem to be increasing⁴². Globally, the frequency rate of asymptomatic AAA ranges from 4% to 8% while the frequency of AAA rupture ranges from 4 to 13 cases per 100,000 persons⁴³. The surgical procedures used to treat AAA are standard open surgery or endovascular aortic repair, which are generally performed when the AAA diameter surpasses a critical level of 5.5 cm⁴⁴. However, small AAAs may rupture whereas large ones may not, underscoring the fact that dynamic wall degradation and remodelling govern the aneurysm rupture risk⁴⁵. There is thus a need for a more elaborate rupture potential index than the mere value of the aortic diameter.

Aging and male gender are two strong risk factors of AAA⁴⁶. Caucasian men have the highest incidence of AAA (≈ 3.5 times that in African American men)⁴⁶. In women who do get the disease, the mortality is higher than in men⁴⁷. Other risk factors include smoking, hypertension, and atherosclerosis in the coronary or peripheral arteries⁴⁶. Most AAAs occur in individuals with advanced atherosclerosis. Indeed, most AAAs begin below the renal arteries and terminate above the iliac arteries, and this location is also a site for atherosclerotic non-aneurysmal occlusive disease. Atherosclerosis could induce AAAs through the mechanical weakening of the aorta with loss of elastic recoil. However, it is unclear whether atherosclerosis is causing AAA or conspiring with other pro-AAA factors⁴⁸. It is interesting to note that the patients at greatest risk for AAA are men who are older than 65 years and have peripheral atherosclerotic disease⁴⁶.

Pathophysiology of AAAs

Most abdominal aortic aneurysms develop infrarenally (below the renal arteries) and end above the bifurcation of the iliac arteries, typically with a fusiform morphology of symmetrical dilatation involving all layers of the aortic wall. Less frequently, AAAs have a saccular morphology, where wall degeneration affects only part of the aortic circumference. Over 75% of AAAs harbor an intraluminal thrombus, which is believed to contribute to the natural history of these potentially lethal lesions⁴⁹. During aneurysm evolution, the extracellular matrix undergoes extensive turnover with continuous degradation and deposition of matrix proteins.

The main pathological hallmarks of AAAs are^{50,51}: **(i) proteolysis, (ii) inflammation, (iii) apoptosis of vascular smooth muscle cells** and **(iv) oxidative stress**.

(i) Proteolytic damage

Proteolysis is protein degradation by proteolytic enzymes called proteases; in the context of AAA, proteolytic damage degrades the extracellular matrix proteins. If unabated, this process can severely weaken the aortic wall and result in the loss of its structural integrity^{52,53}. The two classes of proteases commonly considered responsible for the ECM degradation in abdominal

aortic aneurysms are **matrix metalloproteinases (MMPs)** and cathepsins. Cathepsins are a group of enzymes with elastolytic and collagenolytic activity (meaning they are able to degrade elastin and collagen)⁵⁴.

The most studied class of proteases is MMPs, a family of zinc-dependent enzymes with collagenolytic activity⁵⁵. In AAAs, the implicated MMPs include MMP-1, MMP-2, MMP-9 and MMP-3⁹. In an aneurysmal aorta, MMPs are significantly upregulated compared to a healthy aorta. Each of these MMPs is produced by different cell types (e.g. macrophages, B-cells or smooth muscle cells), and plays a distinct role in disease progression. The fragments of elastin and extracellular matrix resulting from the proteolytic process recruit inflammatory cells and initiate an immune response that attempts to resolve the damage of the wall⁵⁶, as explained in the next section.

Inflammation

Chronic medial and adventitial inflammatory infiltration is a salient feature of AAAs. One important distinction to be made here is the difference between innate and adaptive immunity. The innate immunity entails the immune responses present from birth whereas the adaptive immunity refers to responses generated after exposure to specific new antigens. The innate immunity is the first line of defense and is made up of the cells and molecules that act as first responders in the face of an insult⁵⁷ (examples are mast cells, macrophages, neutrophils and dendritic cells). The adaptive immunity is associated with immunologic memory (examples are B cells and T cells).

The inflammatory response within the aneurysmal wall entails numerous inflammatory cell types, with macrophages and lymphocytes being the most prominent and mast cells and neutrophils migrating to a lesser extent^{58,59}. Due to the presence of B cells and T cells, a potentially autoimmune process driving AAA formation or progression has been suggested⁵⁶. **Macrophages**, which are major components of the inflammatory process, have been shown to play a key role in AAA progression⁶⁰ (Figure 7). They are recruited by ECM degradation by-products and numerous chemokines⁶¹. While macrophages begin a positive feedback loop aggravating inflammation, their role may not always be harmful (Figure 7). Macrophages have the plasticity to switch between an M1 (pro-inflammatory) or an M2 (anti-inflammatory and reparative) phenotype⁵⁶. In AAAs the imbalance of M1/M2 has been suggested to dictate disease evolution.

Apoptosis of vascular smooth muscle cells

Inflammation, reactive oxygen species production and endoplasmic reticulum stress all contribute to smooth muscle cell apoptosis. TNF- α secreted by macrophages⁶² and chymase, a protease secreted by the mast cells⁶³ can cause vascular smooth muscle cell apoptosis. Loss of smooth muscle cells in AAA tissue has been documented extensively, however it is not clear whether apoptosis is an active pathological event or simply a consequence of tissue deterioration^{64,44}.

Introduction

Oxidative stress

Oxidative stress occurs when the capacity of antioxidant defense is exceeded by the free radical production. This imbalance leads to cell death, resulting from the production of oxidized proteins, peroxides and DNA damage⁶⁵. Oxidative stress activates pro-MMP2 and pro-MMP9 (the inactive forms of MMP-2 and MMP-9, respectively), which degrade the collagen fibers in the arterial wall⁶⁶, and also affects the immune adaptive response⁶⁷.

Pathogenesis of AAAs

The current theories on AAA pathogenesis can be grouped in the following four conceptual categories⁶⁸:

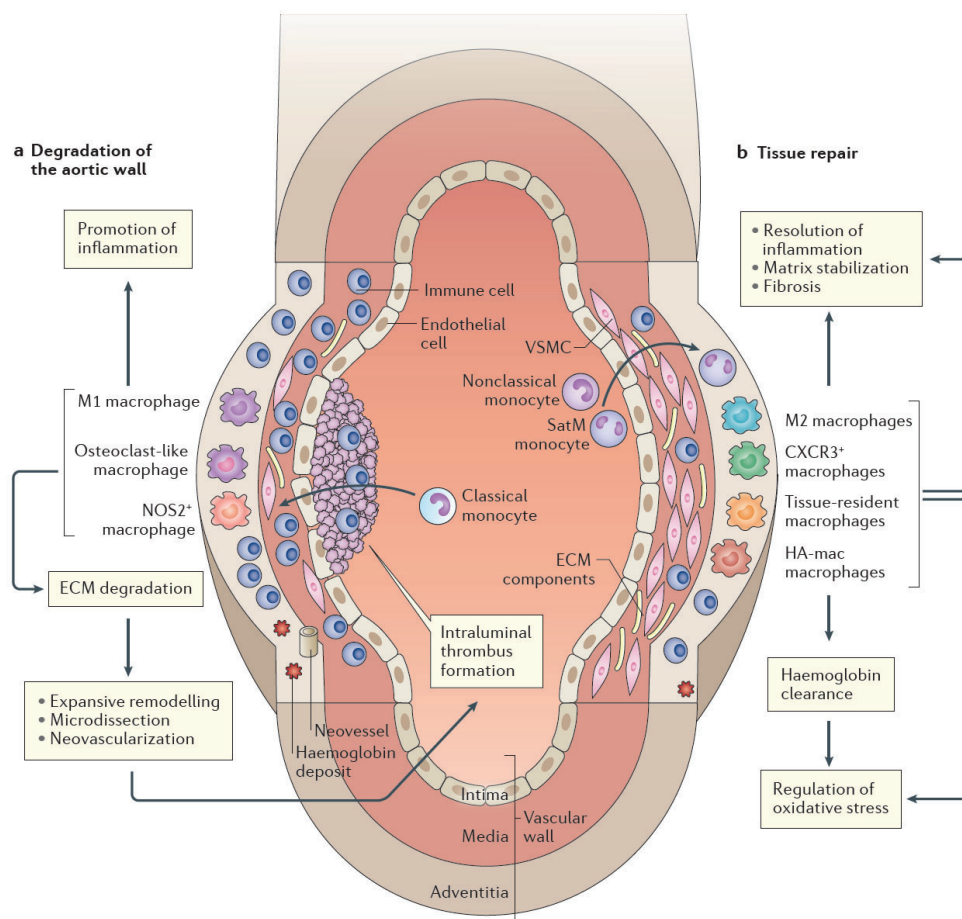


Figure 7: Two opposing mechanisms in AAA inflammation. a. Immune cell infiltration in abdominal aortic aneurysms. Classical monocytes are present in all layers of the vascular wall. Pro-inflammatory macrophage types weaken the aortic wall and promote expansive remodelling. b. As a compensatory mechanism, anti-inflammatory types of macrophages can limit AAA expansion and sustain the wall integrity. Reproduced from⁶⁰.

(a) AAA as an acquired, immune-driven destruction of the aortic wall

According to the inflammation theory of AAA pathogenesis, depicted in Figure 8, a plethora of innate immune cells invade the aortic wall via the adventitial vasa vasorum, a pre-existing atherosclerotic plaque or other sites. Cytokines secreted by these cells then potentiate the inflammatory response. Free radicals and other by-products invoke smooth muscle cell apoptosis and phenotypic switching, leading to a loss of the matrix-regulating capacity of the media. The sum of these effects is a severely weakened aortic wall.

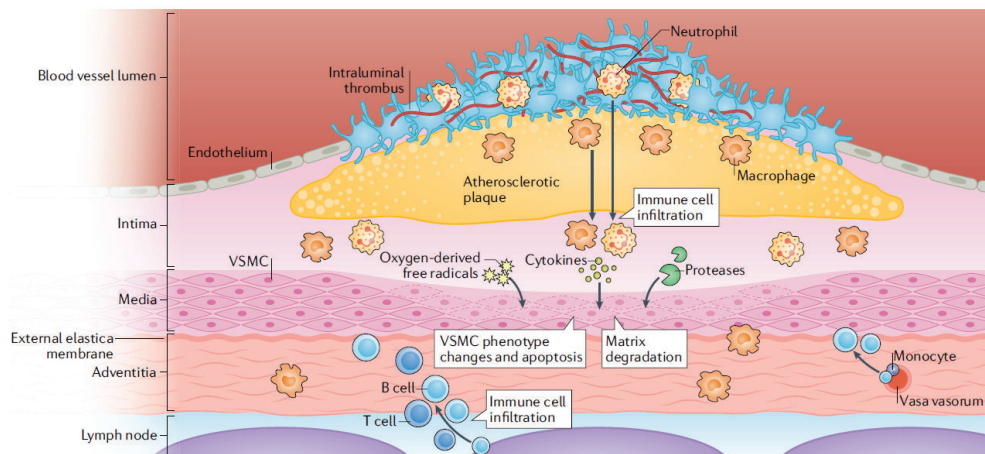


Figure 8: The inflammatory theory of AAA pathogenesis schematically shown. Reproduced from⁶⁸.

(b) AAA as a response to atherosclerosis and thrombosis

A traditional view on AAA, still favored by some researchers, has been that it is one of the end-stages of atherosclerosis. The vessel expands in order to compensate for the atherosclerotic plaque, which is obstructing the free lumen. However, the effectiveness of therapeutic efforts aimed at limiting atherosclerosis or thrombosis in controlling AAA growth is not clear^{69,68}.

(c) AAA as a result of inherited factors

Studies in twins⁷⁰, as well as the increased risk of AAA in people with positive family history⁷¹ point towards certain genetic factors that predispose to AAA.

(d) AAA as a result of biomechanical determinants

The consistent formation of abdominal aortic aneurysms has been associated with the unique mechanical characteristics of the infrarenal aorta. For example, its local high oscillatory shear index could explain this region's propensity for aneurysm formation⁷². Local hemodynamic stresses may determine the infiltration of inflammatory cells as well as the progression of atherosclerosis⁷³. Once inflammatory cells infiltrate the wall and initiate its degeneration, the damage can be further exacerbated by high wall stress.

Inflammation of the aortic wall evaluated with PET imaging is reportedly aggravated in sites of high peak wall stress⁷³.

In the event of a transmural rupture, the local wall strength can no longer withstand wall stress; it is thus an event of mechanical failure. Peak wall stress is higher in patients with ruptured or symptomatic AAA than in those with asymptomatic AAAs⁷⁴. Computed intramural stresses with finite element models that are built on patient-specific geometries may be better indicators of rupture potential than the standard metric of maximum diameter⁷⁵.

3.2 Thoracic aortic aneurysms (TAAs)

Thoracic aortic aneurysms (TAAs) have an incidence of approximately 1 per 10,000 people⁷⁶. They usually occur in the ascending aorta (~60% of cases), between the aortic valve and the brachiocephalic trunk⁷⁷. Thoracic aortic aneurysms are associated with risk factors such as hypertension, smoking and aging. Much more overt than in abdominal aortic aneurysms, thoracic aortic aneurysms have a strong genetic component. Several genetic syndromes that affect the vascular wall integrity have been associated with thoracic aneurysm formation, including the Marfan, Loeys-Dietz and Ehlers-Danlos syndromes⁷⁸. The presence of a bicuspid aortic valve also predisposes the patient for development of thoracic AA and/or dissection⁷⁹. More than half of all patients with BAV may develop a thoracic aortic aneurysm.

Up to 29 genes associated with TAA formation have been identified to date. Most of them encode signaling molecules in the TGF- β pathway, extracellular matrix proteins or proteins of smooth muscle cells in the contractile state⁸⁰. One of the first genes to be associated with TAA was fibrillin-1, a scaffolding matrix protein which also interacts with TGF- β . Mutations in fibrillin-1 can cause Marfan Syndrome, characterized by changes in the skeletal, ocular, and cardiovascular system and associated with increased incidence of TAA. Depending on whether a TAA is associated with a congenital disorder or not, the therapeutic management of TAA may vary⁷⁷.

Pathophysiology of TAAs

The pathological hallmark of TAA is medial degeneration; therefore, smooth muscle cells, a key component of the medial layer, are of great importance in this pathology⁸¹. The medial degeneration is characterized by fragmentation and loss of elastic fibers, as well as accumulation of proteoglycans in the aortic media. In stark contrast with the intraluminal thrombus formation and invasion of inflammatory cells that characterizes AAAs, TAAs primarily arise from non-inflammatory mechanisms that often involve underlying genetic mutations^{82,83,84}. Given the lack of inflammatory cells producing medial degrading proteases in thoracic aneurysms, it has been postulated that resident aortic wall cells are actually the source of the ECM proteases in the ascending aortic wall^{84,85}.

Pathogenesis of TAAs

(a) Poor intrinsic quality of the vascular wall connective tissue

As we saw, in Marfan syndrome the defective synthesis of fibrillin-1 leads to aberrant TGF- β activity and progressive weakening of elastic tissue. As a result, there is progressive aortic enlargement due to remodelling of the inelastic media⁸⁶. In the Loeys-Dietz disorder, mutations in TGF- β receptors lead to abnormalities in elastin and collagen types I and III. TAAs in those individuals can rupture easily, even at small sizes⁸⁷. In the setting of Ehlers-Danlos syndrome, defective synthesis of collagen type III weakens the vascular wall. Nutritional deficiency in vitamin C (ascorbate) is associated with altered collagen cross-linking, showing that TAA formation can also have a nutritional basis³⁸. There is an apparent importance of TGF- β and possibly Angiotensin II signaling in TAAs^{81,88}.

Non-syndromic TAAs, in the absence of a congenital syndrome, also occur. In approximately 20% of those patients there is an affected family member, thus pointing towards familial patterns of inheritance⁸⁹. Familial TAAs present earlier and evolve quicker than sporadic TAAs. There are several mutations associated with familial TAAs, with ACTA2 being the most common site of mutation¹⁶. The ACTA2 gene encodes smooth muscle α actin, and its mutation leads to vascular smooth muscle cell deregulation. The smooth muscle cells in this case have disorganized and aggregated actin filaments and as a result are unable to successfully adapt to changes in local mechanical stress^{90,91}. The precise link between VSMC dysregulation and aortic medial degeneration has yet to be determined.

(b) Dysfunctional mechanosensing

As we saw above, identified mutations affect structural components of the aortic wall (e.g. collagen, fibrillin-containing microfibrils), cellular force generation (e.g. α actin) and transmembrane structures that transduce mechanical stimuli (e.g. polycystins). Essentially, these mutations disrupt the ability of aortic SMCs to properly *sense* but also *respond* to forces⁹². The adaptation of the aortic wall to elevated wall stress includes smooth muscle proliferation, synthesis of collagen and other matrix components and increased cell signaling through angiotensin II receptors. These pathways promote adaptive remodelling to thicken the aortic wall. Conversely, adaptation to reduced wall stress involves smooth muscle cell death, proteolytic activity and thinning of the wall. Defects in force transmission or mechanosensing can lead to the misperception of high stress as low stress with the resulting inappropriate remodelling^{88,93} (Figure 9). Given that the thoracic aorta is subjected to the largest cyclic circumferential stretch from the distending blood pressure, and axial stretch from gross motions of the heart, maladaptive remodelling can have dire consequences on its load-bearing capability.

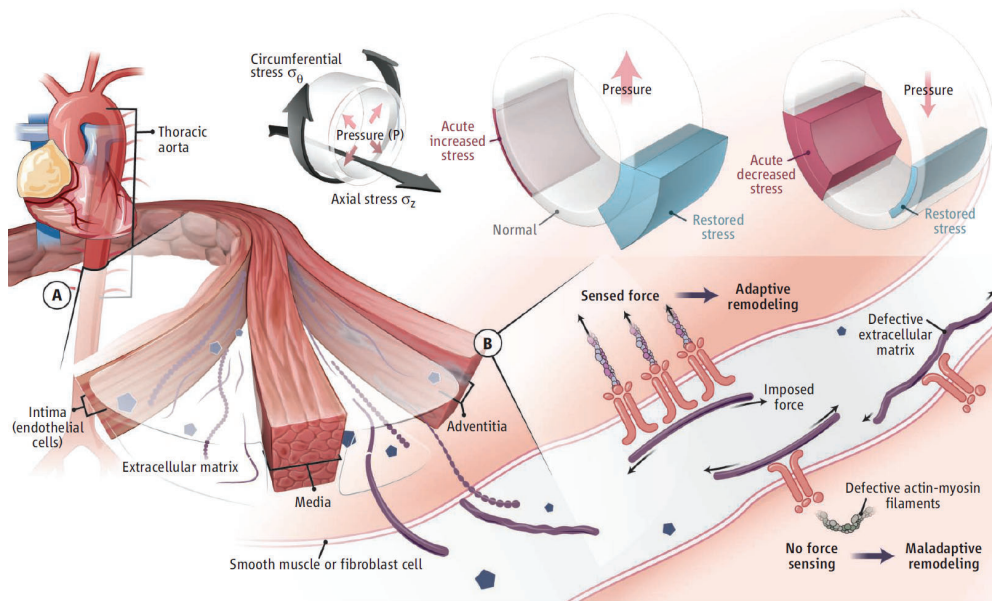


Figure 9: Aortic mechanobiology. A. The endothelial cells sense changes in the wall shear stress, whereas smooth muscle cells and fibroblasts sense changes in intramural circumferential and axial stresses. Increased blood pressure (P) increases wall stress, but adaptive thickening restores stress values back to normal; decreased pressure decreases wall stress, but adaptive thinning restores stress values. B. Smooth muscle cells and fibroblasts sense and regulate the ECM, and sensing low vs high stress results in disparate cell signaling. Misperception of high stress as low can cause maladaptive remodelling. Reproduced from⁹³.

3.3 Aortic dissection

Aortic dissection is the most common catastrophic event of the aorta, with a higher incidence than ruptured abdominal aortic aneurysm in western populations^{94,95}. Timely diagnosis and clinical action is of paramount importance, since the condition has poor outcome. In an aortic dissection, blood splays apart the layers of the media to form a blood-filled channel within the aortic wall (cf. previous Figure 6E). An indicative histological section of a dissected aortic wall is shown in Figure 10. The resulting insufficient blood in the normal pathway of the aorta may cause ischemia, malperfusion (due to decreased blood supply distally) or aortic valve insufficiency.

An acute aortic dissection begins with an intimal flap, caused by blood flowing in the medial layer. This flap separates the true lumen from a false lumen (a newly created route of flow in the medial layer), as shown in Figure 11. In most patients there is an intimal tear that links the two lumens, there are however also cases where bleeding within the wall of the aorta occurs as a primary event, in the absence of an intimal tear (Figure 11B). As blood flows into the aortic wall, the intimal flap can propagate in an antegrade and a retrograde direction from the site of the intimal tear, and may involve aortic side branch as it progresses. Progression of the dissection can lead to re-entry⁸³ of the blood in the true lumen through a second intimal tear

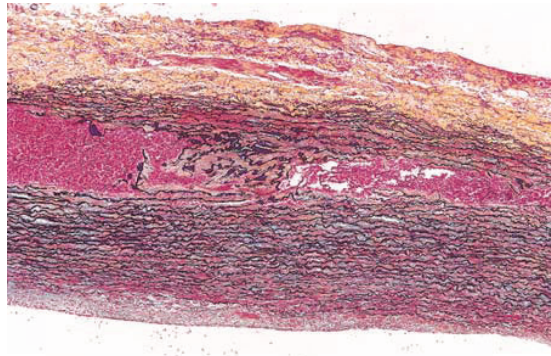


Figure 10: Histological section (Movat's stain) of a dissection³⁸. The intramural space can be seen filled with blood within the medial layer.

(double-barreled aorta), and the false channel may become re-endothelialized.

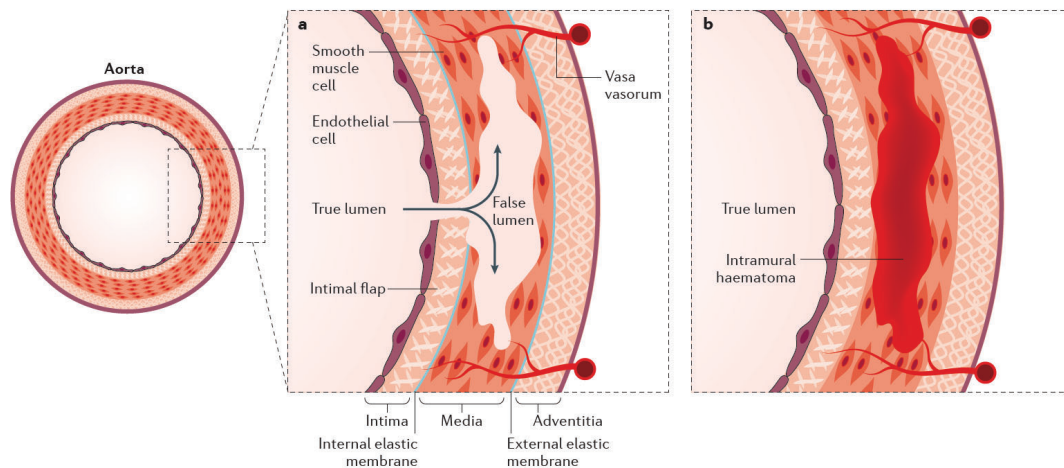


Figure 11: Aortic dissection. a. In most cases, the aortic dissection initiates with an intimal tear. b. In some cases, the initial event is a rupture of the vasa vasorum which results in an intramural hematoma progressing to a dissection. Reproduced from Niebaber et al.⁹⁶.

Aortic dissections are classified according to the origin of the intimal tear (DeBakey classification), or according to whether the dissection involves the ascending aorta, regardless of the intimal tear site (Stanford classification) (Figure 12). An accurate classification is important since it drives the therapeutic management decisions⁹⁷.

Regarding dissection pathogenesis, there is increased risk of aortic dissections in patients with TAAs, at the level of the aneurysmal segment⁹⁹. The association between aneurysm size and dissection is unknown. Genetic studies have established disorders that predispose to aortic dissections, which include the Marfan, Loeys-Dietz and Ehler-Danlos syndrome, as well as non-syndromic mutations (e.g. for ACTA2), similar to what we saw in section 3.2. The confluence of factors leading to TAA and aortic dissections leads to the two entities usually

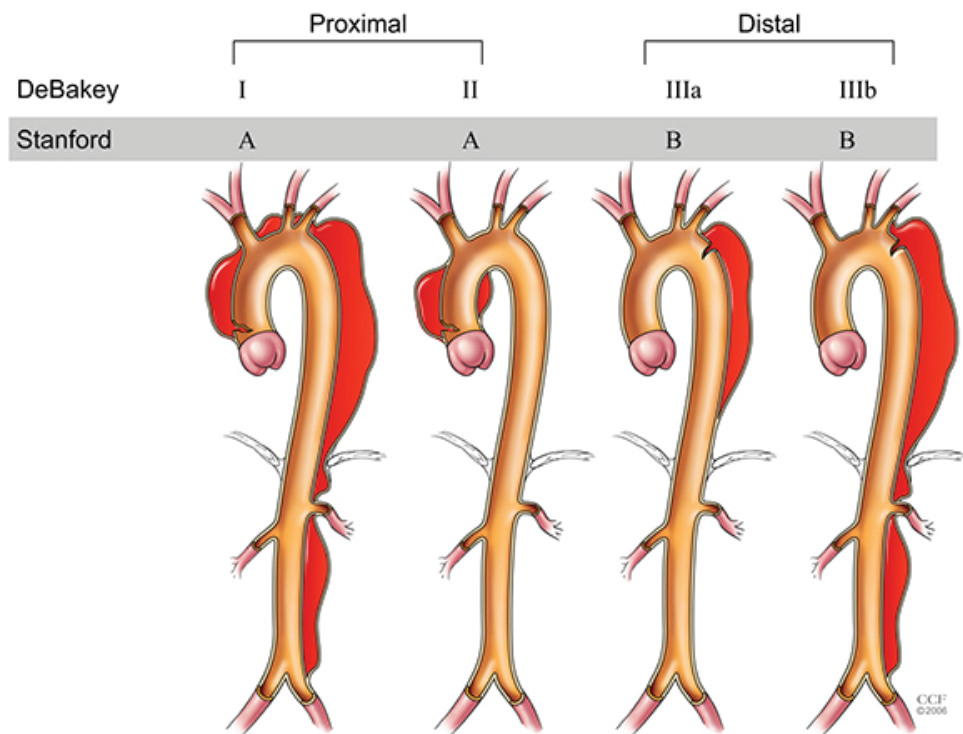


Figure 12: Classification of dissections. DeBakey system: Dissection originates in the ascending aorta and propagates (I) or is confined (II). Dissection originates in the descending aorta and propagates below the diaphragm (IIIb) or is confined (IIIa). Stanford system: Dissections involve the ascending aorta (type A) or not (type B). More than 60% of deaths associated with acute type B aortic dissection result from local aortic rupture, usually of the false lumen. Reproduced from ⁹⁸.

being studied together (as TAADs, thoracic aortic aneurysms and dissections) ^{88,93}, hence their shared pathogenetic mechanisms have been described in the previous section.

Aneurysm, dissection... or pseudoaneurysm?

It is noteworthy to make a distinction between an aneurysm and a dissection (cf. Figure 6). A true aneurysm is a dilatation involving all three layers of the vascular wall ^{100,83}. In a dissection, blood enters the wall through a intimal tear and progressively separates the layers of the wall. A dissection's intramural infiltration of blood is not an aneurysm, within the strict meaning of the term. Note also the distinction between an aneurysm and a false aneurysm (pseudoaneurysm). In a pseudoaneurysm, a substantial part of the vascular structure in the region of dilatation is missing and the hematoma is sustained by amorphous fibrous material (cf. Figure 6D).

4 Preclinical research: powerful tools from high-resolution imaging to evaluation of vascular function

Mice have garnered particular attention in preclinical research owing to their small size and relative cheapness, their fully decrypted genome, their fast disease progression as well as the ability to delete or overexpress specific genes.

Mice and humans have four-chambered hearts comprising of left and right atria, a dominant left ventricle and a thinner-walled right ventricle. While the mouse heart is far smaller than the human heart (a mouse heart weighs 0.12-0.15g while an adult human heart weighs 250-350g), the ratio of heart to body weight is equivalent in both species (around 0.45%)¹⁰¹. The average aortic diameter in humans tapers from 3 cm in the ascending aorta to 1.8 cm in the abdominal aorta, while in mice the corresponding values are considerably smaller - from roughly 1 mm in the ascending aorta to 0.8 mm infrarenally¹⁰². But except for the considerably smaller vessel dimensions in mice, the microscopic anatomy is generally similar in the two species, with the same vessel wall constituents. However mice have far fewer elastin layers, typically less than 10 (with somewhat more lamellae near the aortic root¹⁰¹) than the human aorta, which has ~50 elastin layers. The vasa vasorum is also more prominent in humans than it is in mice¹⁰¹. Discrepancies between humans and mice in physiological parameters such as blood shear rates, red blood cell aggregation and red blood cell geometry are exemplified in contradictory findings of studies that evaluate particulate drug delivery systems in humans and mice¹⁰³. The smaller size of the mouse cardiovascular system also implies inherent allometric differences in hemodynamic conditions within mouse vessels compared to human, while the mouse heart rate is 100-times faster than humans.

The small dimensions of the murine vasculature, combined with their fast heart rate, impose significant challenges in engineering dedicated small animal imaging systems, both in vivo and ex vivo. On the premise that an animal model mimics aspects of the human condition, insight on its genetic, cellular and biomechanical mechanisms through advanced imaging can be of paramount translational value and may even impact potential therapeutic targets.

4.1 Small animal imaging techniques

In order to study the progression of small animal aortopathies (and other diseases), a wide range of imaging techniques have been used in the recent years. These include, but are not limited to, conventional histology, ultrasound, computed tomography (CT), magnetic resonance (MR), positron emission tomography (PET), single-photon emission computed tomography (SPECT), near-infrared fluorescence (NIRF) and bioluminescence. Each technique has its strengths and limitations, and the choice of one over the other depends on the specific application and question a study aims to answer. Here, we will provide the basic background for some of the techniques which are of importance for this dissertation.

Introduction

Histology

Histological analysis is to date, despite huge technological advances, the gold standard for the assessment of anatomical and functional details in small animals. Post mortem histopathology and immunohistochemistry have excellent spatial resolution and molecular sensitivity and specificity¹⁰⁴, and still represent the reference technique most widely used in preclinical research today. In vivo results obtained with small animal imaging systems are usually validated through ex vivo histology. Combining the high-resolution postmortem histological data with the anatomical and geometrical data of in vivo images (which are usually of lower resolution) can greatly help in deciphering pathological events. Studies that correlate in vivo estimated parameters with postmortem findings still visually assess their results by selecting similar 2D slices from both techniques.

The major caveat of histology is the necessary destructive tissue sectioning, that can lead to vast amounts of serial sections and also abolishes any 3D spatial consistency of the sample. Histological preparation can also introduce deformations of the sectioned tissue on each slice, owing to the fixation process (dehydration), the sectioning process (shearing or folding of sections, tearing when mounting on slides, displacements etc.)¹⁰⁴ or contraction of tissues for specific stains.

The low-throughput and invasive nature of histology makes the acquisition of spatially and temporally indexed datasets on healthy and diseased tissues an exceptionally arduous task. Conversely, noninvasive imaging allows longitudinal monitoring of animals over the entire course of the disease from inception to the end-stage. In line with animal welfare regulations, such capabilities also serve to minimize the number of animals required for a single study. In vivo ultrasound was one of the first dedicated small animal imaging techniques to provide unparalleled insight into disease evolution and response to therapy.

High-frequency in vivo ultrasound

Ultrasonography, first used for medical imaging in the late 1940s and early 1950s¹⁰⁵, is a diagnostic imaging technique used to visualize internal body structures. The term ultrasound describes sound of frequencies above 20,000 Hertz (Hz), beyond the range of human hearing. In ultrasound imaging, sound waves are emitted from a transducer into the tissue and are reflected back (echoed) as they encounter boundaries. The time transit between returning sound waves and their strength are then used to construct the ultrasound image. The transducer transmits sound waves by using piezoelectric crystals, and receives the echoes to convert them to electric current.

There is only one manufacturer of dedicated preclinical high-resolution micro-ultrasound systems (VisualSonics, Toronto, Canada)¹⁰⁴. These systems operate at frequencies between 15 and 70 MHz (compared to frequencies of 3–15 MHz for clinical systems). Here, the wavelength is inversely proportional to the frequency and the shorter the wavelength, the higher the

resolution.

In mice, ultrasound can be used for imaging anatomy (BMode imaging), measurement of diameter (MMode imaging), measurement of aortic blood flow (Pulsed Doppler and Color Doppler imaging), as well as measurement of volume (3D ultrasound).

In ultrasound, reverberations, reflections or air bubbles can impair imaging. Moreover, measurements are strongly affected by manual positioning of the imaging plane, which makes the technique operator-dependent and thus prone to subjective interpretation. These drawbacks can be overcome by the use of dedicated automated 3D imaging techniques such as microcomputed tomography (micro-CT). In vivo contrast enhanced micro-CT allows for visualization of the blood-filled aortic lumen, as we will see next.

In vivo micro-CT

The first commercial small animal micro-CT has been on the market since 1999¹⁰⁶. As is the case for clinical CT scanners, the principle of micro-CT is based on X-ray attenuation through the animal being imaged. As an incident X-ray beam passes through tissue, its intensity is attenuated according to the equation

$$I_x = I_0 e^{-\mu x}$$

where I_0 is the intensity of the incident beam, x is the distance from the source, I_x is the intensity of the beam at distance x from the source, and μ is the linear attenuation coefficient¹⁰⁷. The attenuation therefore depends both the sample material and the source energy. After the beam passes through the sample and exits with reduced intensity, it is collected by a detector array.

There are two common geometries for a micro-CT: a rotating gantry and a rotating specimen. Most of the in vivo micro-CT systems use a rotating gantry geometry, where both the X-ray tube and detector are assembled on a single gantry. The gantry rotates while the animal lies on a table, between the tube and the detector (Figure 13). The rotating specimen geometry has primarily been used for ex vivo systems.

For any geometry, a balance must be struck between the system dimensions, the required spatial resolution, the focal spot size of the X-ray source, and the photon flux produced by the X-ray source¹⁰⁸.

Contrast agents

Micro-CT imaging is ideal to image bone and its microstructure^{108,109} thanks to the high attenuation of hard tissues. Such is not the case for blood vessels, whose similar densities with surrounding soft tissues make them impossible to distinguish on a micro-CT image. To enable micro-CT imaging of the vasculature, contrast agents of radiopaque materials have been

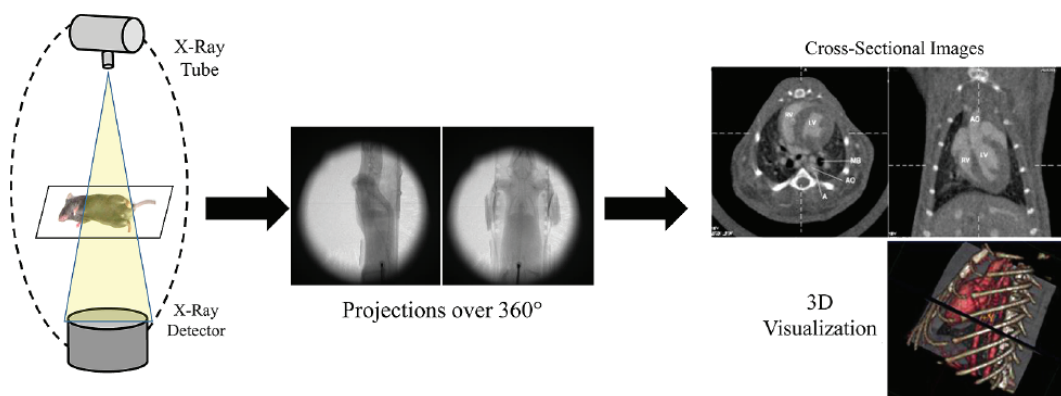


Figure 13: micro-CT setup. A micro-CT typically produces 3D tomographic data proportional to the mean linear attenuation coefficient at microscopic resolution (voxel size $100 \leq \mu\text{m}^3$) by taking a few hundreds of 2D cone beam projections from several angles around the animal. Reproduced from¹⁰⁹.

developed. We can categorize contrast agents based on their formulation into water-soluble agents, typically used in the clinics, and blood-pool agents, used in basic research imaging¹¹⁰.

Water-soluble agents are based on organically bound iodine, which has the highest X-ray attenuation among nonmetal elements, as well as low toxicity¹¹¹. Water-soluble agents are characterized by rapid clearance rates and hence impose short imaging times. While this is achievable in the clinic, in small animal microCT the imaging time is not comparable to the tracers' fast kinetics. This implies that a water-soluble contrast agent in a mouse would need to be administered at a constant infusion rate during the scan. As an alternative, **blood-pool contrast agents** were developed for experimental research. The salient features of these agents are, as their name attests, long residence times in the vasculature, and the ability to maintain a stable concentration in the bloodstream following a single injection.

In order to prevent the swift extravasation of the contrast agent through the capillaries, the molecule size of these agents is larger than the size of capillary fenestrations. Owing to their big size, the molecules of these agents cannot be cleared through the renal system like their water-based equivalents. Instead, they are slowly cleared out through the hepatobiliary system¹¹¹.

The first blood-pool agent for micro-CT was introduced in 1998 and involved an iodinated contrast medium embedded in a lipidic formulation¹¹¹. While it could reside in the bloodstream for over 3 hours, its low iodine content did not yield strong contrast. A new group of contrast agents that uses metal nanoparticles has recently gained popularity. A schematic of a nanoparticle contrast agent designed for CT is depicted in Figure 14. Metal-based agents provide higher attenuation than iodine, meaning that smaller amounts are required and hence smaller injection volumes. Similarly to the iodinated blood-pool agents, the molecules of these tracers are sufficiently large to prevent their extravasation. **Exitron nano 12000** (Mil-

4. Preclinical research: powerful tools from imaging to myography

tenyi Biotec, Berlin, Germany) is an innovative agent that uses alkaline earth metal-based nanoparticles and has been shown to enhance the blood compartment for up to 3 hours¹¹⁰. Another contrast agent based on gold nanoparticles has also shown great potential in imaging the vascular compartment and is commercially available under the name AuroVist 15 nm (Nanoprobe, Yaphank, NY). However, the appearance of a dark staining on the skin of animals infused with Aurovist has been reported, which makes the localization of the caudal vein for subsequent injections extremely difficult. Therefore this tracer is not ideal for longitudinal follow-up imaging on the same animals.

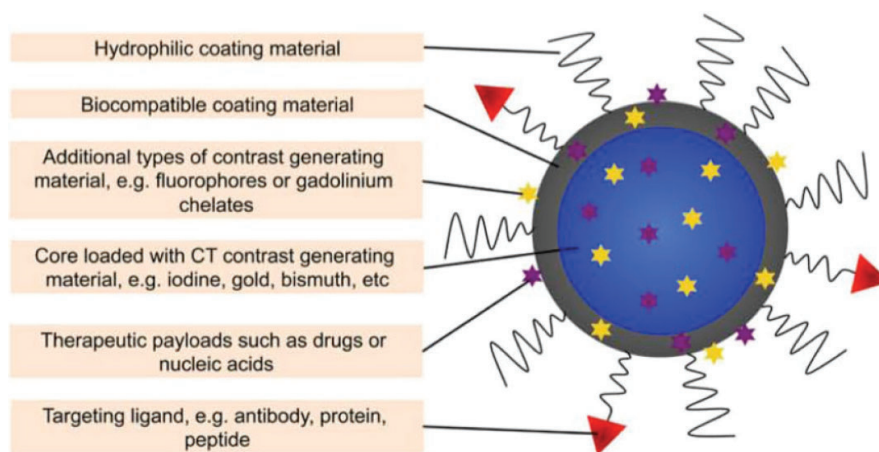


Figure 14: Generalized schematic of a nanoparticle contrast agent. The material used to generate contrast is usually in the core of the particle (most frequently iodine, gold or bismuth). The core is coated with a polymer, lipid, protein, silica or other compounds of high solubility and biocompatibility. Last, the coating or core can also be loaded with drugs or nucleic acid. Reproduced from¹¹².

In CT, the signal-to-noise ratio is inversely proportional to the square root of the number of X-rays passing through each voxel¹⁰⁹. In order to achieve lower voxel sizes while maintaining the signal-to-noise ratio, the number of X-rays increases significantly; meaning that higher radiation doses are necessary to achieve higher resolution. A tradeoff must be made however between the desired image quality and the levels of exposure to radiation for the animal, which can lead to biological damage and long-term health effects¹⁰⁹. The lethal dose for a population, $LD_{50/30}$ is defined as the whole-body radiation dose that would kill 50% of the exposed animals within 30 days¹⁰⁸. In mice, this value is reported to range between 5 and 7.6 Gy (gray units), depending on mouse strain, age and other factors. Typical doses for a 3D micro-CT range from 0.017 to 0.78 Gy, depending on the specific setup¹⁰⁹. Within a few hours, mice can repair sublethal doses of radiation¹¹³ and repeated exposures of ≈ 30 cGy have not compromised the survival of mice in previous studies. The cumulative dose resulting from longitudinal follow-up with micro-CT is unlikely to reach dangerous levels, however the radiation dose should be minimized wherever possible¹⁰⁸.

Future directions of micro-CT: phase contrast imaging

Treating X-rays as electromagnetic waves, their complex index of refraction n is expressed as $n = 1 - \delta + i\beta$, where δ is responsible for the phase shift and β is for the beam attenuation¹¹⁴. The index of refraction relates to the linear absorption coefficient, μ_0 as $\beta = \mu_0(\lambda/4\pi)$ and to the coefficient of phase change, η , as $\delta = \eta(\lambda/2\pi)$ for an X-ray wavelength of λ . For diagnostic X-rays (10-100 keV) and low atomic number elements ($Z \leq 20$), δ is ~ 2 -3 orders of magnitude larger than β and decreases more slowly with increasing X-ray energy ($\sim 1/E^2$ vs. $\sim 1/E^3$). Phase contrast holds great potential in the imaging of soft tissue without the need of contrast agents, and at lower radiation doses¹⁰⁸.

Theoretical findings have been practically validated with the use of monochromatic, synchrotron X-ray sources, with experiments carried out for propagation based, grating interferometer based and analyzer crystal based phase contrast imaging. The challenge in transferring these methods from the synchrotron beamline to the (pre-)clinical application is the low brilliance and low coherence of non-synchrotron X-ray sources, but developments in this area are promising¹⁰⁸.

Visualizing the diseased murine vascular wall

We have so far seen histological assessment, ultrasound and micro-CT methods as potential tools in assessing cardiovascular disease in mice. The scope of our work is to assess the diseased vascular wall and a 3D morphological assessment is imperative to this end, to reveal microstructural changes and their preferential location within certain areas of the wall. Mice have an abdominal diameter of 0.8 mm, a wall thickness of 50-100 μ m and (<10) elastic laminae¹⁰¹, with an elastin thickness of ~ 15 -25 μ m¹¹⁵. Histology, at a 4 μ m slice thickness, allows for 'functional' imaging of wall constituents, it is however essentially 2D (3D projections can be acquired, but are very arduous). Most importantly, the sectioning process disrupts the structure of organs such as large arteries since it introduces artifacts. Through avoiding mechanical sectioning, 3D imaging techniques are capable of imaging a structurally intact sample. X-ray micro-CT, which is ideal for obtaining the in vivo pressurized geometry of the blood-filled lumen, does not have enough soft tissue contrast to discern the wall and thus is an ill-fated imaging choice for this purpose. Another technique offering 3D imaging at high resolution is ultrasound, however the technique is very operator-dependent and is often subject to interpretation, as we saw previously. Other methods have additionally been used that we have not described here: for example, micro-magnetic resonance imaging, with sufficient (but suboptimal) soft tissue contrast but large axial inter-slice distance, which means crucial parts of the microstructural anatomy may be missed. Multiphoton microscopy has also been used to image the mouse arteries (Figure 15), but a crucial limitation is its small field of view, impeding the visualization of the entire vessel circumference. An alternative approach to image the murine wall's microstructure is the use of X-ray synchrotron imaging, as we will see in the next section.

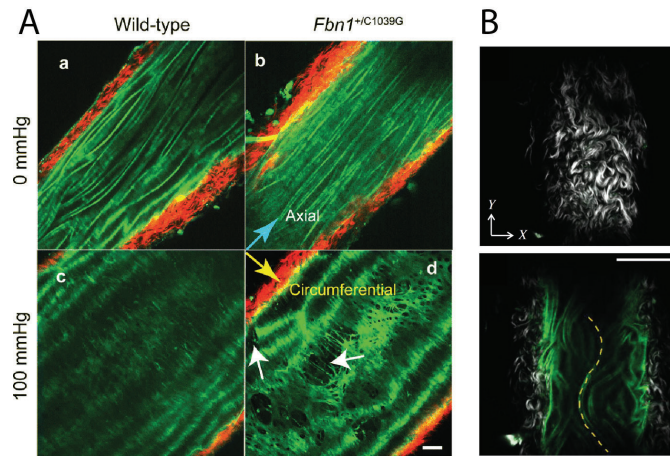


Figure 15: A. Two-photon images of descending aortas of 8-month-old mice, collagen in red, elastin fibers in green. Scale bar is not specified. Taken from¹¹⁶. B. Multiphoton image of mouse carotid artery. Wavy collagen fibers in grey, elastin in green. A longitudinally undulated elastic lamella has been highlighted with a dashed line. Scale bar 100 μm . Taken from¹¹⁷.

Synchrotron imaging

Synchrotron radiation occurs when a charge traveling at a relativistic speed in a synchrotron changes its direction of movement (Figure 16)¹¹⁸. Synchrotron radiation covers a large spectrum of electromagnetic waves, from infrared to hard x-rays (in wavelength, tens of micrometers to less than 0.01 nm). Its characteristic is high brilliance; it is a very intense beam with low divergence. Synchrotron radiation was predicted in theory in the mid-1940s¹¹⁹ and observed for the first time in 1947 by scientists of the General Electric company¹²⁰. The first observed synchrotron radiation was in the visible range of the spectrum, but later the synchrotron energy was increased to produce radiation in the X-ray range.

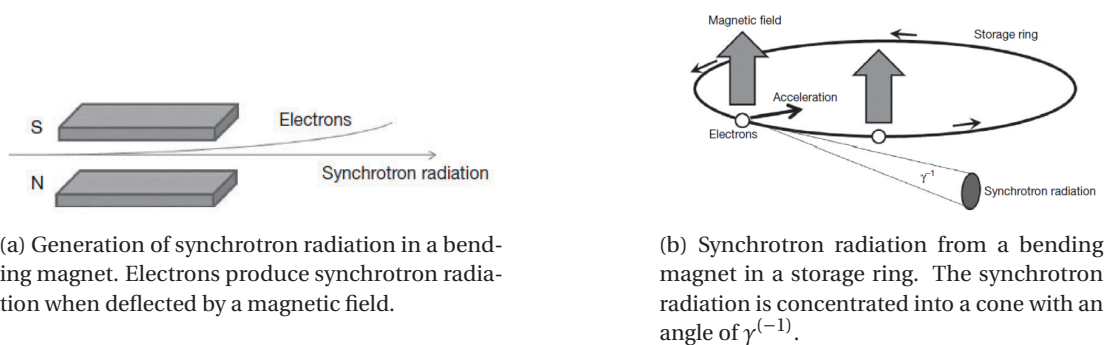


Figure 16: Generation of synchrotron radiation. Reproduced from¹¹⁸.

Three generations of synchrotrons

First generation synchrotron radiation sources were synchrotrons built as particle accelerators for high-energy physics. In these facilities, the energy loss due to production of synchrotron radiation was considered a nuisance and the scientists using this synchrotron radiation were called parasite users. **Second generation** synchrotrons, called storage rings, were dedicated to obtaining synchrotron radiation. The majority of these facilities used bending magnets for the generation of X-rays. Since synchrotron radiation is produced independently at all bending magnets, all ports (beamlines) can be used simultaneously for experiments without interfering with each other. The so-called **third-generation** synchrotron radiation sources make use of insertion devices as X-ray sources, but bending magnets are still being used. Three large third-generation synchrotron radiation facilities with high ring energies were initially built in Grenoble (France), Argonne (Illinois, USA) and Hyogo (Japan). Then smaller third-generation synchrotron facilities were built, such as DIAMOND (Oxford, UK), Advanced Light Source (ALS; Berkeley, CA), SSRL-II (Upton, NY), Elettra (Trieste, Italy), Petra-III (Hamburg, Germany), Canadian Light Source (CLS; Saskatoon, Canada), Australian Synchrotron (Melbourne, Australia), Soleil (Paris, France), and **Swiss Light Source (SLS; Villigen, Switzerland)**. These new storage rings make use of the technologies developed at the larger storage rings and thus, even though they operate at lower electron energies, they are low-emittance rings that produce highly collimated X-rays¹¹⁸.

It should be noted that synchrotron radiation can be produced not only by electrons but also by positrons. Use of positrons is sometimes preferred for the stability of the storage ring, but at the moment electron storage rings are more widely used - mainly because positrons are more challenging to produce¹¹⁸.

In this dissertation, imaging was carried out at the **Swiss Light Source (SLS)** at the Paul Scherrer Institut, a third generation synchrotron as described above. SLS employs a 2.9 T wavelength shifter with a critical energy of 11.1 keV for the phase-contrast microtomography beamline, TOMCAT, at the X02DA port^{121,122} on a 2.4 GeV storage ring (with ring current $I = 400$ mA, top-up mode). The X-ray beam is monochromated with a double-multilayer monochromator. An image of the beamline interior is shown in Figure 17A.

Synchrotron-based X-ray phase-contrast imaging allows for detailed 3D insight into the microstructure of soft tissue and is increasingly used to improve our understanding of mouse models of cardiovascular disease. Two techniques dominate the field: grating interferometry, with superior density contrast at mid to lower microscopic resolutions, and propagation-based phase contrast, facilitating high resolution tissue imaging. A schematic flow chart of each approach is shown in Figure 18. The choice between these techniques depends on which features one is interested in visualizing and is thus highly sample-dependent¹²³

The two different endstations of the experimental setup used for the two techniques are shown in Figure 19. For each imaging technique, the aortic samples to be imaged were prepared in a

4. Preclinical research: powerful tools from imaging to myography

Figure 17: A: The TOMCAT beamline of the SLS. B: Sample preparation. Aortas are stabilized (embedded) in agarose gel during the scan to prevent moving artifacts.

Figure 18: Phase propagation versus grating interferometry. Each technique's flow chart is shown. Reproduced from¹²³.

In the endstation I, schematically shown in Figure 19, **propagation-based phase-contrast mi-**

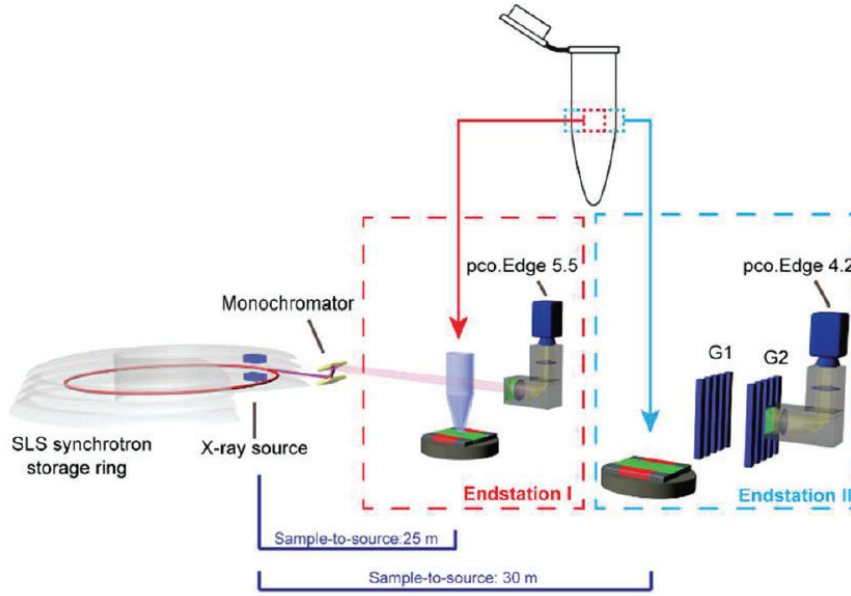


Figure 19: The experimental setup at the TOMCAT beamline with two different endstations. Reproduced from ¹²³.

croto-mography was performed at 25m source-to-sample distance, 25 cm sample-to-detector distance and at 21 keV. A scientific CMOS detector (pco.Edge 5.5) was used in combination with a 4x magnifying (UPLAPO4x) visible-light optics and a 20 μm thick scintillator. The effective pixel size in the setup was $1.625 \times 1.625 \mu\text{m}^2$. Indicative examples of imaging with propagation-based phase-contrast are shown in Figure 20.

In endstation II, schematically shown in Figure 19, **grating-based phase-contrast microtomography** was performed at 30 m source-to-sample and at 25 keV. Phase retrieval was based on single defocused images using a transport-of-intensity approximation as originally proposed by Paganin et al. ^{124,125}. A grating interferometer is mounted right after the sample and consists of a phase grating (G1) with a pitch of 4 μm and an absorption grating (G2) with a 2 μm pitch positioned at a distance corresponding to the third Talbot order. The detector used in the grating interferometry setup is a scientific CMOS detector (pco.Edge 4.2) in combination with 1:1 magnifying visible light optics and a 300 μm thick scintillator, yielding an effective pixel size of $6.5 \times 6.5 \mu\text{m}^2$.

In this dissertation both grating interferometry (Chapters 2, 3) and propagation-based (Chapter 4) phase contrast imaging has been used, with phase retrieval. In both grating interferometry and phase propagation, vertical stacking was necessary in order to image the whole tubular structure of the aorta. The term Phase Contrast X-Ray Tomographic Microscopy (PCXTM), or simply synchrotron, is used throughout the rest of this dissertation to denote this imaging technique. In section 5.3 of this Introduction, we will see how the application of synchrotron imaging has given unique insight into the pathology of an experimental model of aneurysm

and dissection.

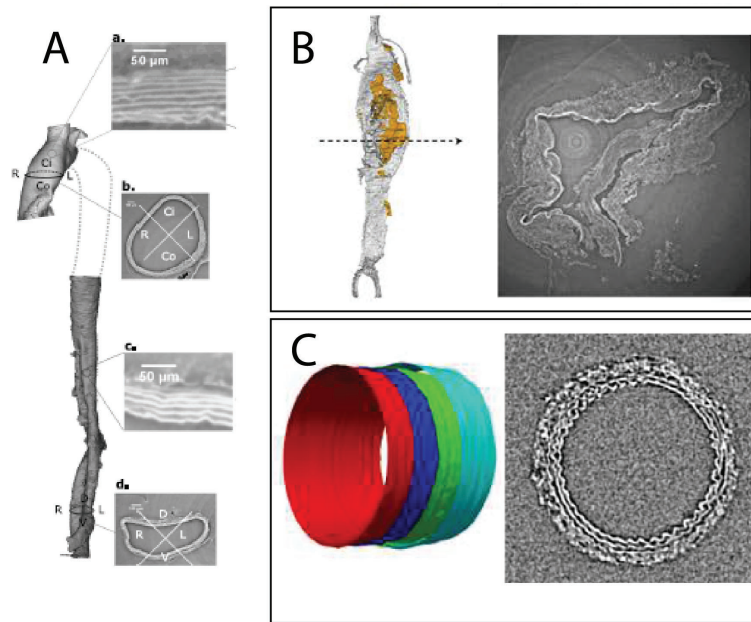


Figure 20: Imaging of diseased and healthy mouse aortas using synchrotron propagation-based phase contrast. The segmented 3D volume is on the left for each study. A, B. Phase-retrieval was performed according to Paganini's method. Phase propagation without phase retrieval would have resulted in a slightly better resolution, but authors opted for phase retrieval since it offers the best compromise between resolution (necessary to visualize medial ruptures) and image contrast (necessary to visualize the presence of hematomas)^{126,127} C. No phase retrieval used, in order to optimally visualize the elastic lamellae of the aortic wall¹²⁸. No scale bars available.

4.2 Numerical models of the cardiovascular system

Advances in 3D medical imaging techniques and numerical methods, together with the increase of computational resources, have given rise to computational studies of the cardiovascular system. **Computational fluid dynamics** (CFD) simulations of blood flow as well as **computational structural mechanics** (CSM) simulations of the vascular wall can be used to assess complex hemodynamics and biomechanical determinants in cardiovascular disease. While most computational research has focused on human data, recent breakthroughs in small animal imaging techniques have allowed the setup of computational studies in animal models of disease; the latter in fact present several advantages in comparison to clinical models, not the least of which is their potential for validation. Within the context of an animal study, we can systematically collect hemodynamic and geometric imaging information prior to disease initiation and in controlled time marks throughout disease evolution - data that are difficult to acquire in a clinical setting as patients are rarely imaged before pathologies such as aortic aneurysms develop. While human tissue is difficult to acquire, animal studies can be tailored for in vivo longitudinal follow-up and tissue collection at different stages of disease progression for ex vivo analyses - which may include mechanical testing, mRNA expression levels or histology¹²⁹. By combining ex vivo analysis with in vivo imaging and subsequently CFD or CSM in animal studies, the role of mechanics and hemodynamics in disease progression can be elucidated. It is worth mentioning that **fluid-structure interaction** simulations (FSI) account for both the fluid mechanics and structural mechanics problem simultaneously, however they are much more computationally demanding than CFD or CSM. Regardless of the application, accurate anatomical and physiological modelling is crucial for these simulations¹³⁰.

The **finite element method** (FEM) is a numerical technique, which was first developed to solve complex structural analysis problems in civil and aeronautical engineering. The FEM assumes the object of analysis can be divided into finite elements, which take the form of lines in one dimensional problems, triangles or rectangles in two-dimensional problems, and tetrahedra, hexahedra or prisms in three-dimensional problems. In general, CFD uses numerical methods (for example FEM) to solve the Navier–Stokes equations. The Navier–Stokes equations represent the conservation of mass and momentum in flows, mathematically given in their incompressible form by 1 and 2, respectively

$$\nabla \cdot \mathbf{u} = 0 \quad (1)$$

$$\frac{\partial \mathbf{u}}{\partial t} + (\mathbf{u} \cdot \nabla) \mathbf{u} = -\frac{\nabla P}{\rho} + \nu \nabla^2 \mathbf{u} \quad (2)$$

where \mathbf{u} is the velocity vector, P is the pressure, ρ is the density, and ν is the kinematic viscosity of the working fluid. In structural simulations, the FEM solves the partial differential equations governing the problem, known as the equilibrium equations, with the stress-strain relations (constitutive equations) and the strain-displacement relations, subject to appropriate boundary conditions.

1D models of the arterial circulation

Three-dimensional CFD, CSM or FSI models may be amenable to describe wave phenomena but they come with high computational demands, and are thus better fitted for the study of detailed local flow fields rather than pressure and flow wave propagation over the entire arterial tree. In short, the choice of dimensionality in a model representation of the vasculature, varying from 0-D to 3-D, is dictated by the aim and the accuracy requirement of the research study.

Lumped parameter (0-D) models entail the assumption of uniform distributions of fundamental variables (pressure, flow, volume) within any compartment of the model (vessel or part of vessel) at any instant in time, while in higher dimensional models these parameters can vary spatially¹³¹. The Windkessel models (briefly mentioned in section 2.2) may give an overall description of the arterial network, but cannot be used to study pressure and flow wave propagation in the arterial tree. This requires tube models or distributed models which take into account the arterial geometry. The principle behind distributed models is that they discretize the arterial vasculature in small segments with known mechanical and anatomical properties. The wave transmission characteristics of each arterial segment can be described using Womersley's oscillatory flow theory.

In distributed models of the arterial tree, the one dimensional form of the blood flow equations describing the conservation of mass and momentum (simplified form of previous equations 1 and 2):

$$\begin{aligned}\frac{\partial Q}{\partial x} + \frac{\partial A}{\partial t} &= 0 \\ \frac{\partial Q}{\partial t} + \frac{\partial(Q^2/A)}{\partial x} &= -\frac{1}{\rho} \cdot A \cdot \frac{\partial P}{\partial x} - 2\pi r_i \cdot \frac{\tau}{\rho}\end{aligned}$$

where A is the vessel cross-sectional area and τ is wall shear stress, usually estimated using Poiseuille's law. The two equations above have three variables: pressure P , flow Q , and area A . Therefore a constitutive law relating cross-sectional area, A , to pressure, P , is needed to form a system of three equations with three unknowns, which can be then easily solved using different numerical techniques (i.e., finite differences, or method of characteristics).

Extensive use of distributed 1D models of the arterial tree has been documented in literature to simulate wave propagation in parts or the entirety of the human arterial tree, under various physiological or pathological conditions^{132,133,134}. These models are fairly accurate and compare well to human measurements of flow and pressure. Moreover, they are able to capture physiological aspects of pressure wave propagation such as the systolic pressure amplification or the smoothing of the pulse.

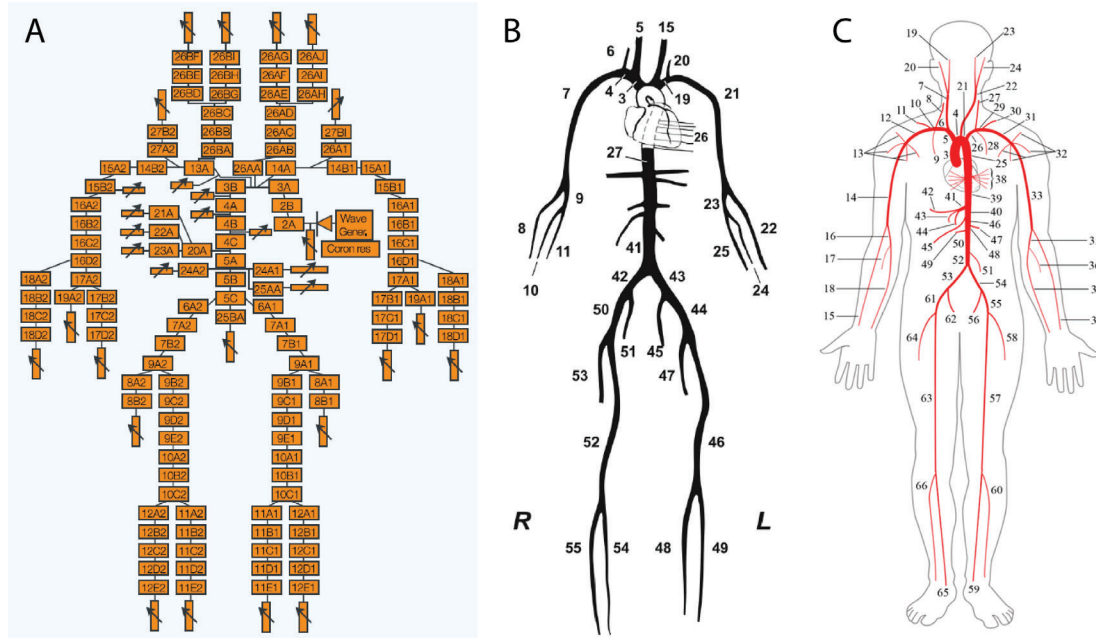


Figure 21: Distributed 1D models of the entire human arterial tree, distributed over a span of 46 years: A. Westerhof's model in 1969¹³⁵, B. Raymond's model in 2009¹³³, C. Mynard's model in 2015¹³⁴.

One dimensional models of the arterial tree are, to date, ideal for the study of pressure and flow wave propagation in the arterial system. The available 1D models in literature have substantial variations in their approaches: examples are the incorporation (or not) of a heart left ventricular (LV) model (important to grasp ventricular-vascular coupling effects), inclusion (or not) of cerebral circulation, formulations for the viscoelasticity of the aortic wall, approximations for wall shear stress and convective acceleration term and boundary conditions at terminal sites (peripheral beds)¹³³. While the mouse is the small animal of choice in experimental research, strikingly a detailed description of the 'reference' murine arterial anatomy and physiology does not exist in literature, and a validated 1D model of the average murine systemic tree and its hemodynamics has not been proposed. We address this knowledge gap in Chapter 1, as we will see later on.

4.3 Vascular reactivity assessment

The previous section focused on computational modelling, which is essential to explore hemodynamic and biomechanical conditions within the vasculature. A different perspective is that of vascular biology and mechanobiological characterization. Blood vessel myography is a valuable in vitro technique for the quantification of constriction and relaxation of blood vessels in response to vasoactive stimuli. It is a powerful tool in the pharmaceutical industry when assessing potential new drugs on the vasculature, as well as in vascular biology research when assessing the (patho-)physiological vascular function of vessels, or molecular pathways that control vascular tone.

As we saw previously, aberrant structural and mechanical changes in the vascular extracellular matrix can lead to life-threatening conditions, including aneurysm, dissection, and aortic rupture. Mounting evidence suggests that altered SMC force generation contributes significantly in thoracic aortic aneurysms and dissections⁹¹, while more recently a role for SMC contractile dysfunction has also been suggested for sporadic AAAs¹³⁶. There is therefore increased motivation to characterize and understand the role of SMC function in the pathophysiology of aortic disease.

Wire myography or pressure myography?

There are two main approaches to myography: conducting an experiment under either isometric (constant length) conditions, typically using a wire myograph, or under isobaric (constant pressure) conditions, typically using a pressure myograph. In an isometric experiment, an arterial ring is held under a constant stretch and contractile or relaxatory responses are measured using a sensitive force transducer (Figure 22). In an isobaric experiment, a cylindrical vessel is cannulated at both ends and remains pressurized and perfused (with physiological solution) while measurements of diameter are made using an optical video dimension analyzer. Wire myography is a high-throughput technique in which the vessels can remain viable for 12 hours or more. On the other hand, pressure myography better mimics in vivo conditions such as blood flow and blood pressure and is therefore ideal to study specific components such as flow-mediated dilatation or pressure-diameter relationships, it is however more challenging and low-throughput.

Murtada et al. developed a multiscale model of the contractile apparatus that vascular smooth muscle cells use to control the vascular tone, which accurately captures both uniaxial (wire myograph) and biaxial (pressure myograph) contraction data for the mouse descending thoracic aorta¹³⁷. After parameter sensitivity studies, the authors submitted that uniaxial contraction tests are not as efficient as biaxial tests for identifying changes in vascular smooth muscle function (see also¹³⁸). Note that in order to develop the active tone of smooth muscle cells, force is generated and transmitted thanks to multiple structural constituents across scales including actin and myosin filaments, the intracellular network of cytoskeletal filaments, focal adhesions at the cell membrane, extracellular elastic fibers, and neighboring cells. The active force thus depends on structural and mechanical properties of these multiple com-

Introduction

ponents in radial, circumferential, and axial directions. Since the applied mechanical strain affects the intracellular organization of the numerous elements comprising the contractile apparatus, it is not surprising that it ultimately influences the magnitude of the developed active force.

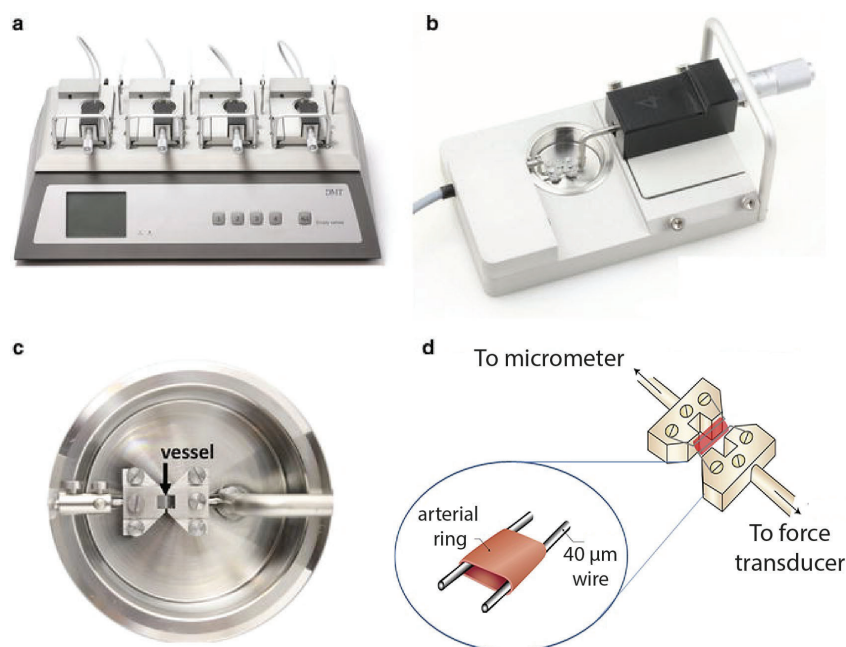


Figure 22: Wire myography setup. a: DMT multi-chamber 620M Wire Myograph. The wire myograph interface holds four myograph units. b: Each myograph unit contains a force transducer (left) and a micrometer (right), which are connected to the two jaws supporting the vessel inside the chamber. c: Detail of the chamber with the jaws and a mounted vessel segment. d: Schematic of the vessel segment mounted on the myograph with two wires through the lumen. Panels a-c adapted from ¹³⁹, panel d adapted from ¹⁴⁰.

For an exploratory study intending to characterize a vessel's global vasoreactivity, as is the case in our study, wire myography has a straightforward implementation and allows the investigation of several pharmacological agents. Moreover, in a wire myograph vessel rings of small axial length (~ 1 mm) can be tested; on the contrary their cannulation in a pressure myograph is challenging. The wire myography method was developed in 1977 by Mulvany and Halpern ¹⁴¹ for rat mesenteric arteries to measure their vasoconstriction or vasodilation to different substances or procedures, assess the vessel's endothelium and evaluate the pathways that regulate the vascular tone. Vessel segments are maintained in an organ bath setting and mounted between two wires that go through the lumen (Figure 22). One wire is connected to a force transducer that records the isometric tension developed by the vessel during its vasomotor response, and the other is connected to a micrometric screw that allows setting up the initial distension. The wire myograph was designed to study vessels from approximately 50 to 600 μ m in diameter. However, bigger arteries (even up to 5-10 mm in diameter) can be studied by adjusting the mounting supports ¹⁴². One of the most studied vessel functions

using wire myography is endothelial function. It is typically determined by performing relaxation–response curves to acetylcholine (mentioned in subsection 2.2) in vessel segments precontracted with a vasoconstrictor (e.g. phenylephrine).

5 The Angiotensin II infusion mouse model

5.1 Mouse models of aortic aneurysm and dissection

Many mouse models have been developed to explore the pathophysiology of aortic aneurysm and dissection, most of which use either genetic manipulation or chemical means to induce the disease¹⁴³. A classification of experimental aneurysm models based on whether they involve intraluminal dilation (nondissecting AAAs) or a contained intramural rupture (dissecting models) has been recently proposed¹⁴⁴. It should be noted that no ideal model exists: animal models are usually not able to capture all aspects of the human pathophysiology and natural history of disease. Instead, experimental models replicate only a part of aneurysmal pathology hallmarks (Figure 23): be it genetic or acquired defects in extracellular matrix, loss of vascular smooth muscle cells, and innate or adaptive immune response. Their value therefore lies in the unique mechanistic insight they can provide where our knowledge on the human condition and fundamental disease mechanisms is scant.

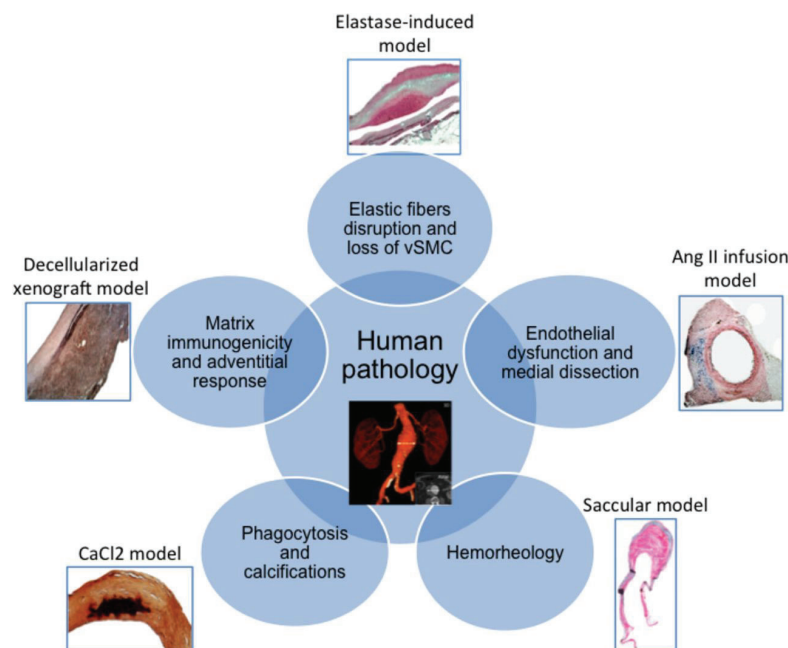


Figure 23: Animal models partially recapitulate aspects of the human disease. Reproduced from¹⁴⁴.

Several detailed reviews of the available experimental models of aortic aneurysm have been published^{145,146,147,148,144}. Most of the mouse models of AAA are evoked either by genetically defined approaches or by chemical means. An overview of aneurysm induction methods is

Introduction

presented in Table 1. The genetic approaches are spontaneous and engineered mutations, which include defects in extracellular matrix constituents, maladaptive cholesterol homeostasis, and increased production of angiotensin peptides. The chemical approaches most commonly include the intraluminal infusion of elastase, periaortic applications of calcium chloride, and subcutaneous infusion of AngII (the latter usually performed on genetically modified animals). A common feature of these models is the reduction of AAA incidence and severity following pharmacological treatment with MMP inhibitors or in the case of mice with genetically engineered deficiencies of specific MMPs¹⁴³.

Table 1: Overview of methods of aneurysm induction.

Method of induction	Features	Location	Year, ref.
Genetically induced			
Blotchy	MD	AAA,TAA	1988 ¹⁴⁹
Lox-deficient	MD	AAA,TAA	1990 ¹⁵⁰
FFN1-/- (MFS)	MD	TAA	1991 ¹⁵¹
ApoE-/-	MD,A	AAA	1992 ^{152,153}
Transgenic renin/angiotensinogen	MD	AAA	1993 ¹⁵⁴
LDL receptor-/-	MD	AAA	1994 ¹⁵⁵
ApoE-/- x eNOS-/-	MD,T,A	AAA	2001 ¹⁵⁶
MMP-3, TIMP-1 deficient	MD	AAA,TAA	2001,2002 ¹⁵⁷
PLOD1-/- (EDS type VIa)	MD	AAA,TAA	2007 ¹⁵⁸
Transgene S100A12	MD	TAA	2010 ¹⁵⁹
Chemically induced			
Elastase	MD,I	AAA	1990 ^{160,161}
Calcium chloride	MD,I	AAA	2001 ^{162,163}
AngII infused:			2000 ¹⁶⁴
ApoE-/-	MD,I,T,A	AAA,TAA	2000 ^{164,165}
LDL receptor-/-	MD,I,T,A	AAA	2003 ¹⁶⁶
C57BL/6	MD,I,T	AAA,low incidence	2003 ¹⁶⁶
C57BL/6 anti-TGF- β	MD,I,T,A	AAA,TAA,high rupture	2010 ¹⁶⁷

AAA: abdominal aortic aneurysm, TAA: thoracic aortic aneurysm, MD: medial degeneration, I: inflammation, T: thrombus, A: atherosclerosis.

The three most commonly^{168,147,148,169} used mouse AAA models are: adventitial exposure to calcium chloride, transient perfusion of elastase into the infrarenal aorta, and chronic subcutaneous infusion of angiotensin II (AngII) and are compared in Table 2.

Calcium chloride-induced AAAs. This method was initially developed in rabbits¹⁶² and it consists in the periaortic application of calcium chloride between the renal arteries and the iliac bifurcation, resulting in significant expansions 14 days after the procedure.

Elastase-induced AAAs. This model was initially developed in rats, and involves the transient perfusion of the isolated abdominal aorta with porcine pancreatic elastase¹⁶¹. The injury results in mild-moderate immediate aortic dilatation, with subsequent luminal expansion

5. The Angiotensin II infusion mouse model

within 14 days. Degradation of medial elastin and aortic wall inflammation are hallmarks of this model.

AngII-induced AAAs. The first description of this model was on female hyperlipidemic ApoE-deficient mice, ~25% of which developed suprarenal saccular dilatation¹⁶⁴ (rather than infrarenal fusiform expansions). The reasons behind the preferential localization to the suprarenal abdominal aorta are unknown. We note here, as will also be clarified in the next section, that although this model is generally suggested for aneurysm research, its abdominal pathology recapitulates salient features of an aortic dissection. For this reason, the term dissecting AAAs has been suggested for the AngII-induced abdominal pathology¹⁷⁰.

Table 2: Comparison of the 3 most common mouse models of abdominal lesions (aneurysms and, for AngII, dissecting aneurysms) with the human aneurysmal pathophysiology. Adapted from¹⁴⁴.

Feature	Human Pathology	Elastase	CaCl ₂	AngII infusion
Rupture	+	-*	-	+
Persistent growth	+	-	-	+
ILT	+	+	-	-
Atherosclerosis	+	-	-	+
Medial generation	+	+	+	+
Leukocyte infiltration	+	+	+	+

* may occur very early. ILT: intraluminal thrombus. Contrary to the original table, persistent growth for AngII infused animals has been noted as present after findings by¹⁷¹.

While in the elastase and calcium chloride induction methods aortic dilatation occurs 100% of the time, in both cases induction requires major surgery with high mortality rates. The AngII model is the one most commonly used¹⁴⁸ due to the ease of lesion creation and its recapitulation of several features of the human pathology, as shown in Table 2. For these reasons, we have opted for this model within this dissertation. One additional reason is that in AngII infusion, the location of the abdominal lesion is not determined by the induction method. This makes it a particularly well-suited model to study the mechanisms defining the location-specific formation of aneurysms and dissections.

5.2 The Angiotensin II infusion model of aneurysm and dissection

The Angiotensin II (AngII) infusion model came about through the combination of an experimental model of hypertension and an experimental model of atherosclerosis. Here we will present a short overview on the history of the model, followed by a detailed description of the aortic lesions it induces on mice.

AngII infusion as a model of hypertension

Angiotensin II is the primary effector hormone of the renin-angiotensin system, which plays crucial roles in cardiovascular (patho)physiology. The octapeptide AngII mediates myriad processes, not the least of which is the regulation of systemic blood pressure. As an example of its many actions, AngII is a powerful vasoconstrictor of peripheral vessels, but also a modulator of vascular smooth muscle cell growth¹⁷² as well as a potent mediator of inflammation¹⁷³. Early studies of AngII infusion in dogs in the '70s aimed to characterize the role of the renin-angiotensin-aldosterone system in hypertension¹⁷⁴. The model was subsequently adapted for long-term subcutaneous infusion in rodents.

The ApoE-deficient mouse model of experimental atherosclerosis

Experimental studies of vascular lesions in rodents began in the mid-50's with the feeding of cholesterol and cholate-rich diets in rats¹⁷⁵. In 1992, the groups of Jan Breslow¹⁵² and Nabuyo Maeda¹⁵³ independently described the Apolipoprotein E (ApoE) deficient mouse (ApoE-/-), which develops atheromatous plaques even when fed standard chow diets. This model has been extensively used for basic research of atherosclerosis¹⁷⁵. Another widely used mouse model is the LDL receptor deficient (LDLR-/-) mouse, which is a mouse model of human familial hypercholesterolemia¹⁷⁶.

ApoE is carried on plasma lipoproteins, mostly chylomicron remnants, VLDL and large HDL. It serves as a ligand for the liver uptake of non-HDL lipoproteins by members of the LDL receptor superfamily. The lipoprotein phenotype of ApoE-/- mice consists of a predominance of remnant lipoproteins that are enriched in cholesteryl ester and apoB48¹⁷⁵. Though atherosclerosis still develops when ApoE-/- mice are fed standard chow, its development is accelerated with a Western-type diet. Lesions develop at the aortic root, the aortic arch, the brachiocephalic trunk, the carotid arteries and other arterial sites depending on the diet and the duration of feeding¹⁷⁷. In this model there is little or no coronary artery lesion¹⁷⁵.

The model of Angiotensin II-infusion in ApoE-deficient mice

Between 1999 and 2001, two separate labs in Lexington, Kentucky and Atlanta, Georgia were examining whether chronic exposure to elevated blood pressure influences the atherogenic process^{178,164,179}. They induced hypertension through the implantation of Alzet osmotic minipumps administering Angiotensin II (Figure 24) over a period of 28 days in mice generally used for the study of experimental atherosclerosis (ApoE-deficient or LDL receptor-deficient, as described above). Indeed, in a hypertensive setting the atheromatous lesions were enlarged and were characterized by lipid-laden macrophages and large numbers of T-lymphocytes. Unexpectedly, Daugherty and colleagues also observed that pronounced abdominal aortic aneurysms were present in ApoE-/- and LDL receptor-/- mice^{178,164}. Following this incidental observation emerged what would prove to be the most commonly used model of preclinical

5. The Angiotensin II infusion mouse model

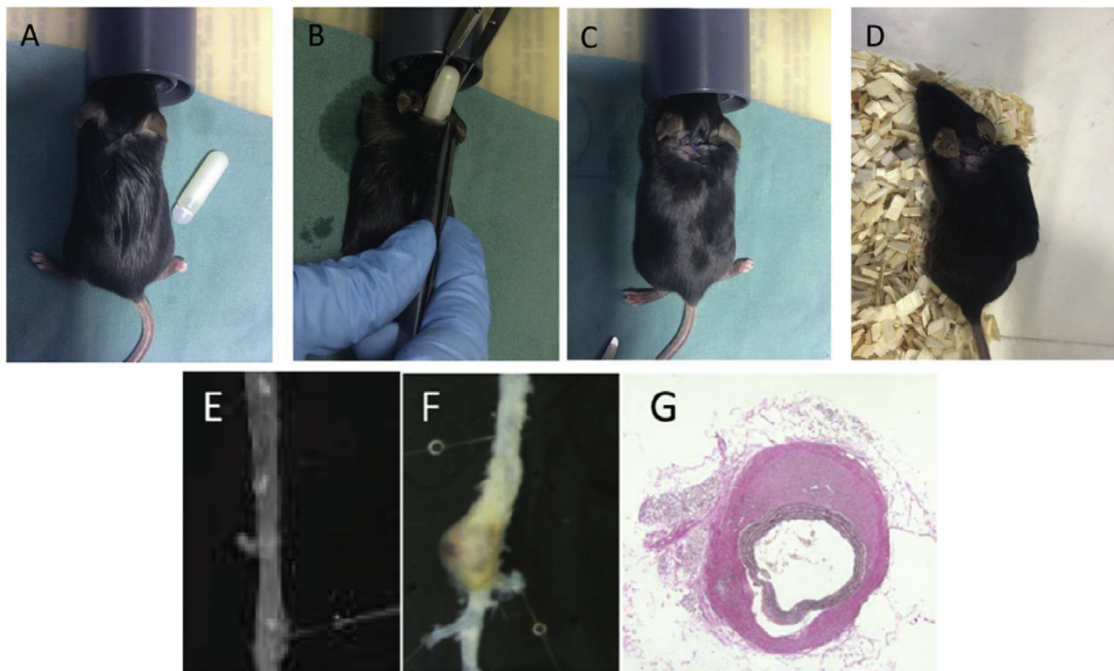


Figure 24: Procedure of pump implantation in AngII infusion model. A-D: The mouse is anesthetized and an Alzet osmotic mini pump filled with AngII is implanted subcutaneously, through an incision above the neck. E: Healthy abdominal aorta. F: Abdominal aorta following 28 days of AngII infusion. G: Section of the diseased abdominal aorta, Miller's elastin stain. Adapted from¹⁴⁸.

aneurysm research; between 1999 and the end of 2014, a total of 10,465 mice had been used in no less than 252 studies that employed the Angiotensin II-infusion model to study its abdominal pathology¹⁸⁰. Further research revealed that AngII infused mice also develop ascending aortic aneurysms¹⁶⁵. A selection (by no means exhaustive, but indicative) of the publications that were instrumental for our understanding of Angiotensin II-induced aortic lesions are presented in the timeline infographic of Figure 25, and an overview is presented below.

To form AngII-induced lesions in mice, constant AngII infusion is performed by subcutaneously implanting osmotic mini-pumps filled with AngII solution¹⁸¹ (Figure 24). The most routinely used AngII infusion rate is 1000 ng/(kg·min) (or 1.44 mg/(kg·d)) for 28 days.

A meta-analysis of 194 publications on the AngII model showed that dissecting AAAs form in approximately 60% of the animals while the mortality rate (presumably due to spontaneous aortic rupture) is 20%¹⁸⁰. Abdominal aortic rupture occurs within the first 5 days of infusion in about 2-10% of the animals. Incidence rates of ascending aortic aneurysms are approximately 54-56%^{182,183}. There is a high variation in doses, age and genetic backgrounds of the animals used in this mouse model which, combined with non-uniform reporting in literature and different criteria used, does not allow for a clear picture of the incidence rates of ascending

Introduction

aortic aneurysms or the incidence of their concomitant presence with abdominal dissections, since the two pathologies are generally studied separately.

By controlling the genetic background, the duration of infusion and diet, this model offers numerous possibilities for pathophysiologic explorations such as the role of lipids^{178,164} and obesity^{184,185} in dissecting AAA development. Given the rapid disease progression, it also allows researchers to focus on a specific disease stage (be it early, intermediate or late). As an example of a final stage study, AngII infusion can be combined with anti-transforming growth factor- β antibody administration in normocholesterolemic C57BL/6 mice¹⁶⁷ to achieve occurrence of fatal AAA rupture as high as 80% while also avoiding the use of costly ApoE-/- mice. With such a relevant rate of AAA rupture, this variation of the AngII model allows for monitoring of the mechanisms at play in the fatal process of rupture. We will see an application of this rupture-prone model in a study presented in section 5.3.

Pathophysiology

After AngII infusion, one or several intimal tears occur in the abdominal aorta¹⁸⁶ leading to penetration of blood into the aortic wall, causing an intramural hematoma and ultimately external dilation. Early medial phagocyte accumulation has been observed, as well as elastic network degradation and T- and B-lymphocyte infiltration¹⁸⁶. The ascending aorta on the other hand presents with concentric, uniform dilatation (without any false channel formation), with an intramural hematoma predominantly in the outer aspect of the aortic wall¹⁸². The heterogeneity of AngII-induced responses within the aorta is striking; an additional observation has been made on the region-specific response of VSMCs. In response to AngII, VSMC hyperplasia occurs in the ascending aorta while VSMC hypertrophy in the rest of the aorta^{187,188}.

AngII-induced abdominal dissecting aneurysms

Studies of the Angiotensin II infusion model primarily focused on abdominal aortic aneurysms, on the premise that several facets of the human disease were replicated in the murine setting. Here we will recapitulate the shared aspects but also the striking discrepancies between the mouse model and the human pathology.

Similarities with human aneurysmal pathology

One of the salient features of human AAAs is the **proteolytic damage induced by matrix metalloproteinases (MMPs)**, as presented in section 3. MMPs are known to degrade the extracellular matrix, including collagen and elastin, thus impairing the structural integrity of the vascular wall and contributing to AAA formation¹⁹⁷. Beginning almost immediately after the appearance of the seminal paper by Daugherty et al.¹⁶⁴, different groups observed

5. The Angiotensin II infusion mouse model

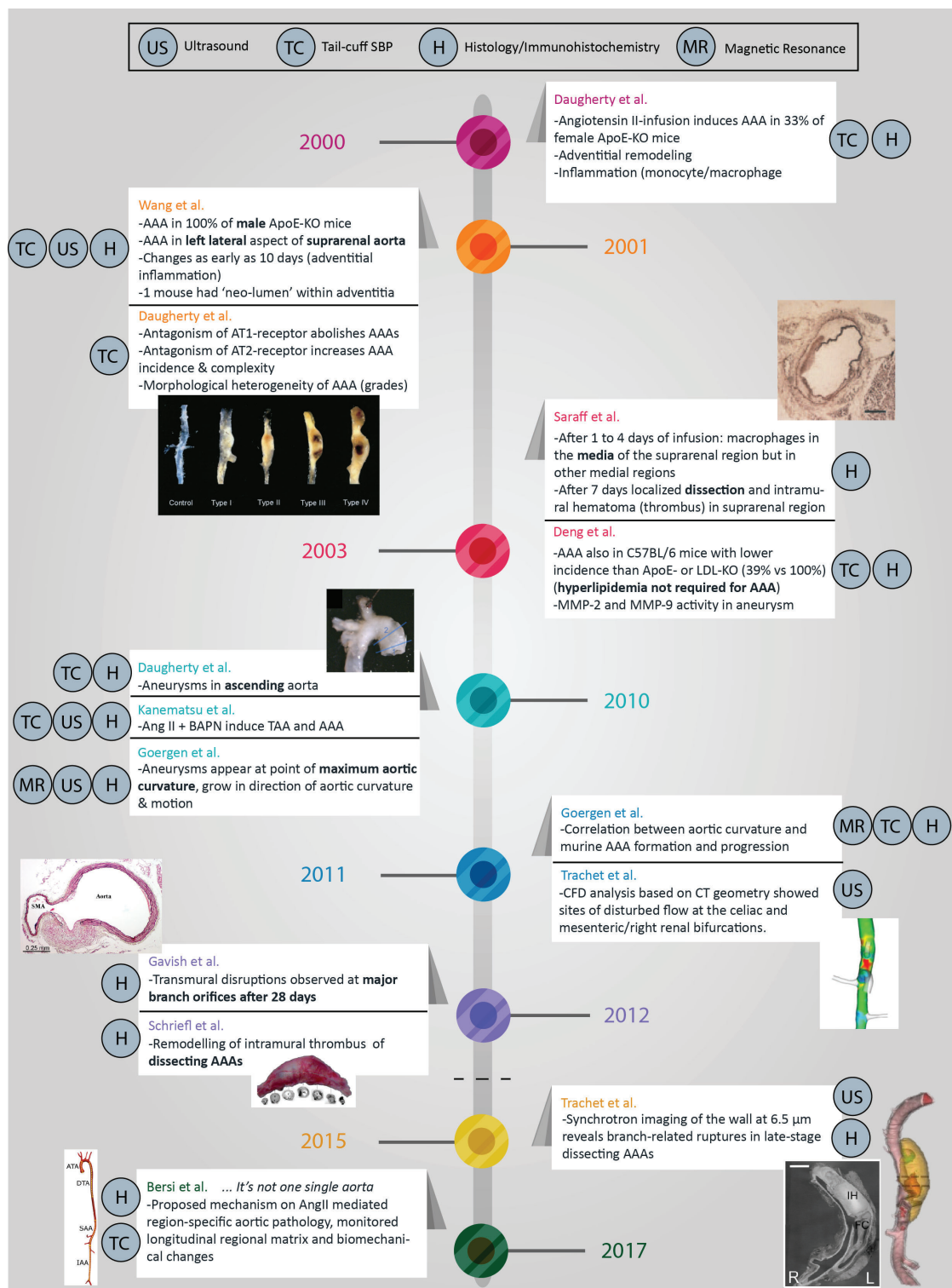


Figure 25: Selected publications on the Angiotensin II infusion model. Indicated for each study are the imaging methods if they entailed ultrasound (US) or magnetic resonance (MR) as well as use of histology (H) and measurement of systolic blood pressure using tail-cuff (TC) method, in either anesthetized or conscious mice. Dashed line marks the start of this dissertation. Studies by ^{164,189,190,166,186,165,102,191,192,193,194,195,170,196,188}.

increased proteolytic activity of MMP-2 and MMP-9^{189,166,198,199,200} and treatment with a broad spectrum MMP inhibitor (the antibiotic doxycycline) was found to significantly reduce experimental AAA formation²⁰¹. In addition, deficiency of cathepsins (the second class of proteases that is responsible for the degradation of ECM in aneurysms) protects from AAA formation²⁰². We note here that *medial elastolysis*, a term frequently encountered in publications of this mouse model, refers to the enzymatic hydrolysis of elastin fibers - which results primarily from increased activity of MMPs. Similar to human AAAs, a paucity of smooth muscle cells in the medial layer (**smooth muscle cell apoptosis**) has been documented in AngII AAAs^{198,202,203}, occurring as early as 3 days after AngII infusion²⁰⁴. The often-used term *medial degeneration* refers to the global compromise of medial layer integrity, due to extracellular matrix degradation and SMC apoptosis.

Macrophage infiltration²⁰⁵ in the medial layer and activation of the **inflammatory response** (which further potentiates the proteolytic cascade) has also been observed in the mouse model, concordant with the human pathology. The migrating pattern of monocyte subsets mobilized from the splenic reservoir has been investigated in AngII infused ApoE deficient mice. After 3 days of AngII infusion, higher levels of circulating LY6C^{high} monocytes, i.e. the murine equivalent of classical pro-inflammatory CD14⁺ human monocytes²⁰⁶, were found in mice that later developed dissecting AAAs after 28 days of infusion, when compared to the mice that later on were not afflicted by an aneurysmal pathology²⁰⁷. Inversely, after 7 days of Ang-infusion, it was the LY6C^{low} monocyte levels, i.e. the murine equivalent of nonclassical CD14^{low}CD16⁺ monocytes promoting tissue repair²⁰⁶, that were found to be higher in the mice eventually developing dissecting AAAs against those not developing them²⁰⁷. A protective role for LY6C^{low} monocytes against lesion development has also been suggested⁶⁰. The contribution of monocytes and macrophages to AAA formation is shown in Figure 26. The term *leukocyte accumulation* denotes that, in addition to macrophages, the mouse AAAs show large numbers of T- and B-lymphocytes (adaptive immune response) in the outer media and adventitia^{186,208}. The term *leukocyte extravasation* refers to the migration of leukocytes from the circulation, across the endothelium and its basement membrane, and into the affected tissue (here, the vascular wall).

The **concomitant presence of atherosclerosis** in the atheroprone ApoE-deficient or the dyslipidemic LDLR receptor-deficient mice is a common denominator with humans, since patients with AAAs frequently have atherosclerosis - it is however unknown whether the association between AAA and atherosclerosis is causal or simply due to common risk factors⁴⁸. While hyperlipidemia (mild or severe, depending on whether mice are fed a regular or high-fat diet) potentiates AAA development, it is not essential: normolipidemic mice also present AAAs, albeit at lower incidence rates^{166,209}. The strong **male gender proclivity** for AAAs is also recapitulated in the AngII-model, with male mice presenting a 3.3-times higher prevalence of AAAs compared to female mice^{210,211}. The two initial studies of this mouse model were performed on hypercholesterolemic ApoE^{-/-} and LDLR^{-/-} female mice^{178,164}. No AAAs developed in normocholesterolemic female mice¹⁶⁴.

5. The Angiotensin II infusion mouse model

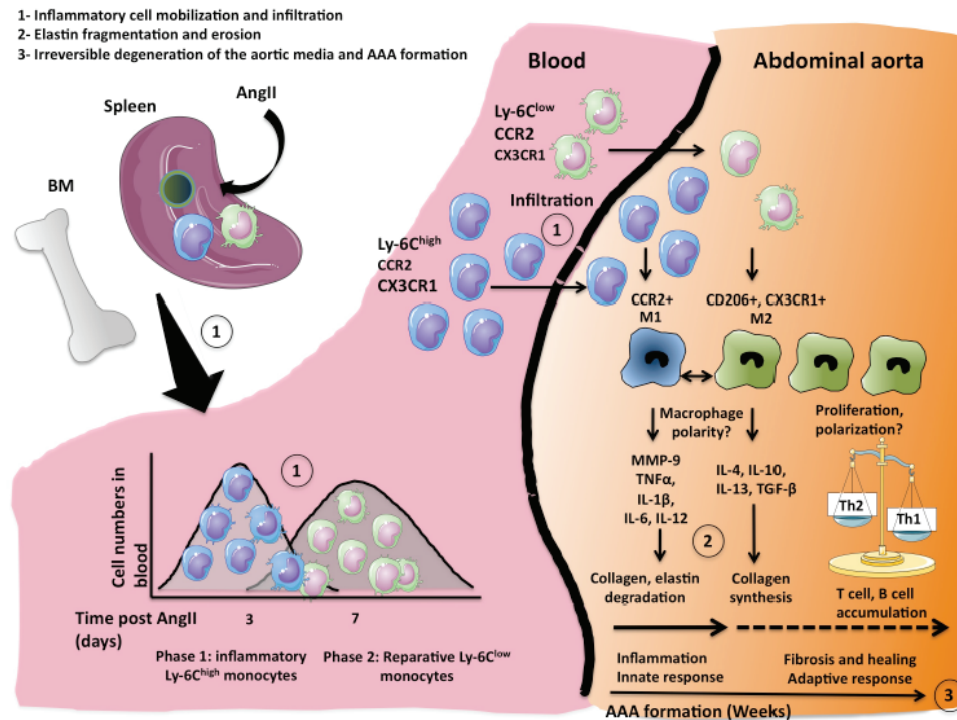


Figure 26: Monocyte and macrophage contribution to aortic abdominal aneurysm formation. In response to AngII, classical (inflammatory) Ly6C^{high} and non classical (resident/reparative) Ly6C^{low} monocytes are rapidly mobilized from the spleen in a B cell-dependent way (1). Ly6C^{high} monocytes increase first in blood (day 3) and are followed by Ly6C^{low} monocytes (day 7). Ly6C^{high} monocyte infiltration predominates during the first days and is associated with collagen and elastin degradation (1,2). After one week, CX3CR1⁺ CD206⁺ M2-type macrophages accumulate in the forming AAA and take the advantage. Possible reasons for M2 accumulation are Ly-6C^{low} sustained monocyte infiltration, conversion from infiltrated Ly-6C^{high} monocytes, local proliferation or Th2-induced polarization (2). Despite probable implementation of a healing phase by M2 macrophages, irreversible medial degeneration and lymphocyte accumulation probably contribute to AAA aggravation (3). Reproduced from ²⁰⁸.

Differences from human aneurysmal pathology - Open questions

The finding of localized aortic enlargement has been misleadingly termed "luminal expansion" in a number of studies, even though an early report showed that AngII-induced abdominal lesions arise following an aortic dissection¹⁸⁶. We refer here to Figure 6 and recall the distinction between a true aneurysm, involving a uniform dilatation of all three aortic layers, and a false aneurysm, which involves an intimal tear and a false channel formation parallel to the true aorta. While the AngII-induced abdominal aortic lesions are typically suggested to model aspects of human AAAs in numerous studies, the presence of an aortic dissection suggests otherwise. For this reason, this model may be more well-suited to model aspects of TAAs which often dissect¹⁷⁰. Regardless of a direct equivalent of human pathology, a detailed

Introduction

study of the pathophysiological and mechanical characteristics of these lesions can increase our general understanding of the initiation and propagation of dissections and aneurysms. To accurately describe these lesions, the term dissecting abdominal aortic aneurysms has been suggested^{212,170} which has led to a paradigm shift. Characterization of the AngII pathology using advanced 3D synchrotron imaging, as we will see in section 5.3, unequivocally showed that the ostensible dilatation is not luminal, but rather due to the presence of a false channel¹⁹⁶. While thrombus formation is considered a common point with the human disease, its localization intramurally rather than intraluminally is also at odds with the human AAA pathology. One of the longstanding issues in this mouse model has been:

Why is there such big variability in abdominal lesion morphology?

Acknowledging the heterogeneity of mouse AAAs in this model early on, the researchers who had first reported the model proposed a classification of the observed lesions. Based on macroscopic observation of excised tissue samples and presence of thrombus and bulbous expansions, they formulated a scale of murine AAAs ranging from Grade I to Grade IV¹⁹⁰ (Figure 27).

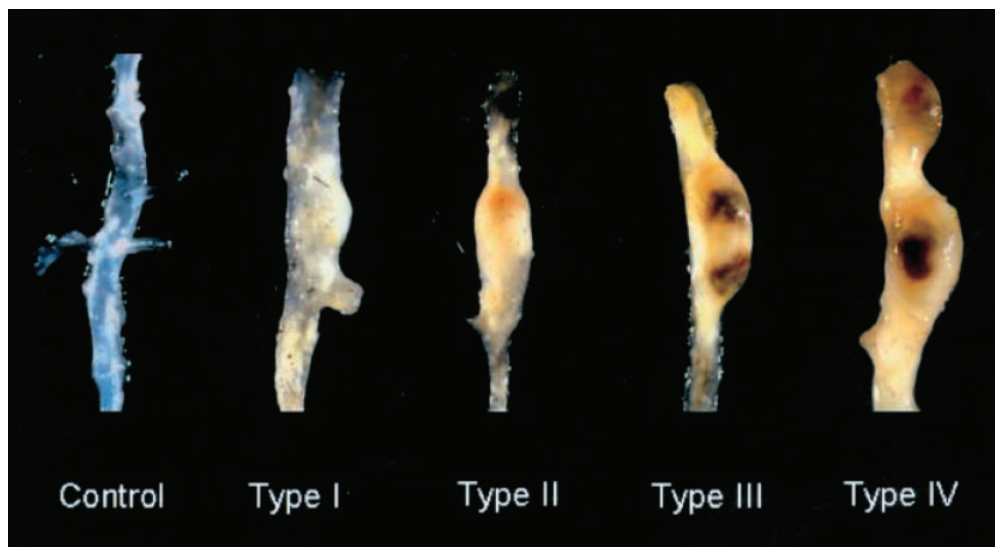


Figure 27: Morphological non-uniformity of AngII-induced AAAs. Reproduced from¹⁹⁰.

The question on lesion variability can be expanded to several pertaining, inter-connected questions which we will see below, along with studies contributing towards their answers.

Why are the growth trends and lesion severity so inconsistent between animals?

Adelsperger et al.²¹³ developed 2 statistical models to predict disease status (diseased or non-diseased) based on noninvasive ultrasound metrics taken on (healthy) animals at baseline, such as suprarenal diameter, peak velocity, Green-Lagrange circumferential strain and 3D volume of AAA/length, in addition to age and initial body mass. They also developed for

the first time a model to predict final AAA size based on ultrasound measurements taken on the day the AAA was first diagnosed. One of the metrics they considered was the number of branching vessels feeding into the aneurysm (celiac artery, celiac and superior mesenteric arteries or none). At this point, since the branching topology of the abdominal aorta is a recurrent theme in this dissertation, it is useful to clarify its local anatomy for reasons of reference, along with some indicative local vessel dimensions (Figure 28).

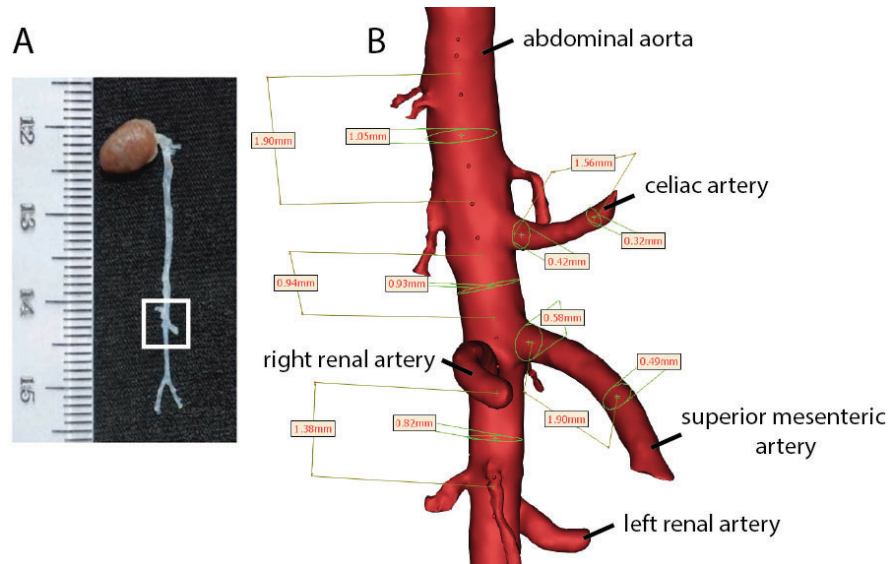


Figure 28: Major branches of the abdominal aorta. A. Aorta of a male ApoE^{-/-} mouse (age unspecified), adapted from²¹⁴. Note that the aorta has been excised and is therefore not under in vivo axial stretch or physiological distension. B. Zoomed abdominal region, taken from a micro-CT scan of a healthy animal at 12 weeks of age. Diameters shown reflect the local inner diameters of the aorta. Both the celiac and the superior mesenteric arteries branch off ventrally. Minor surrounding branches can be seen, secondary to the major branching vessels annotated.

In the study by Adelsperger et al.²¹³, longitudinal followup showed that mice which had only the **celiac artery** feeding into the aneurysmal sac had larger AAA volumes than mice which had both the celiac and the superior mesenteric arteries branching into the aneurysm. The authors hypothesized that major branching vessels could be restricting the expansion along the aorta. An image-based approach with synchrotron imaging to explain marked mouse-to-mouse differences in a cohort of animals was reported by Trachet et al.²¹⁵, as will later be described in section 5.3.

Why do some animals form a dissecting AAA while others don't?

Phillips et al. performed RNA sequencing and gene expression analysis on AngII-infused mice with (n=7) and without (n=5) dissecting AAAs as well as on saline-infused mice (n=5) to evaluate differences in gene expression among the experimental cohorts²¹⁶. In their study, animals were sacrificed on the same day they were diagnosed with dissecting AAA via ultrasound,

Introduction

or (in absence of AAA) at 10 days post-implantation; their findings hence reflect *the onset of grossly perceivable disease* (overt wall changes have already occurred). When comparing the AngII-infused animals that did and did not develop AAAs, the AAA genes that were most upregulated in the AAA cohort were encoding inflammatory factors and receptors as well as matrix metalloproteinases. The authors further identified uniquely enriched gene ontology terms in the group of animals with AAAs, which regarded biological processes such as the regulation of neutrophil migration, innate immune response, blood coagulation (relating to the presence of thrombus), collagen metabolism and cellular extravasation. When compared to the saline-infused controls, the cohort of AngII-infused animals that did not develop a dissecting AAA was uniquely enriched for processes including muscle contraction and wound healing²¹⁶. Whether this finding could imply a role for **smooth muscle cell contractility** in locally protecting the vascular wall from developing a dissection is unknown.

The most perplexing open question of this mouse model is:

Why do mouse dissecting AAAs consistently form suprarenally (above the kidneys), unlike their infrarenal localization in humans?

and its answer would likely provide great insight into the disease process. In other words, are there predisposing factors making the suprarenal abdominal aorta specifically prone to dissection, while sparing the infrarenal aortic portion (cf. Figure 29)?

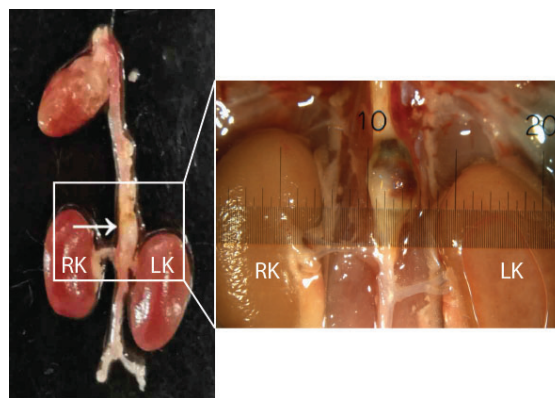


Figure 29: Example of Angiotensin II-induced suprarenal dissecting aneurysm (left), with a zoomed view (right). The celiac and superior mesenteric arteries branch off ventrally at the level of the arrow and thus are difficult to annotate on this image. RK: right kidney, LK: left kidney. Adapted from^{217,218}.

Remarkable research efforts have been directed in identifying inflammatory pathways that may explain such preferential localization, such as the inflammatory activation of the vessel wall through angiotensin receptors with the activation of the NADPH oxidase p47phox²¹⁹ and Rho-kinases¹⁹⁸. Factors that have been investigated include the role of monocytes and macrophages⁶⁰ and their enhanced recruitment through -for example- the CCL2/CCR2 pathway¹⁷⁶ and increased production and activation of several proteases²²⁰. Gene expression

analyses have underlined the upregulation of proinflammatory and remodelling genes in the AngII-infused suprarenal aorta^{221,216}. The role of AngII receptors has also received particular attention. Whole body depletion of the AT1a receptor was shown to ablate dissecting AAAs²²², but the same was not true for cell-specific AT1a receptor depletions in endothelial or smooth muscle cells²²³. Another important difference between the suprarenal and the infrarenal aortic portion may arise, however, from local hemodynamic and biomechanical conditions.

The hemodynamic conditions in the murine suprarenal and infrarenal aorta were compared and the latter were contrasted to human conditions in a study by Amirbekian et al.²²⁴. In the mouse, notwithstanding similar values of mean blood velocities in the suprarenal and infrarenal aortas, the mean and maximum blood volumetric flowrates were much lower (~ 50%) in the infrarenal portion, due to the blood flow being diverted to the kidneys. In the human infrarenal aorta, which is susceptible to AAA formation, flow reversal during early diastole has been associated with oscillatory wall shear stress, in turn linked with AAA development. In mice, neither the infrarenal nor the suprarenal aorta experience flow reversal. Overall, both the suprarenal and the infrarenal aortas have similar axial prestretch and structural stiffness in the mouse, with the suprarenal aorta tending to be only slightly stiffer^{224,192,168} (but in any case significantly less stiff than in humans²²⁴).

Early biomechanical aspects of disease development

In 2012, Favreau et al.¹⁹⁵ combined high-frequency ultrasound biomicroscopy with speckle-tracking to report circumferential wall strain evolution in 6 points along the Angiotensin II-infused aorta (3 in the thoracic and 3 in the abdominal portion). Among the three points within the abdominal aorta, the supraceliac location experienced the most *abrupt reduction of wall strain* (in other words, rapid early mechanical stiffening) after only 3 days of infusion (reduction of ~ 43%, Figure 30), prior to the formation of dissecting AAAs. Another study similarly reported a drop of ~ 50% in circumferential cyclic wall strain after 3 days²²⁵. The decrease in circumferential cyclic wall strain over the entire course of AngII infusion has been documented in other studies using ultrasound^{225,213,216} and magnetic resonance imaging¹⁹². Goergen et al. further reported that AngII-induced AAAs formed near the location of maximum aortic curvature in the abdominal aorta, and correlated the leftward direction of suprarenal aortic motion with the leftward direction of aortic expansion. Genovese et al. used a panoramic digital image correlation method to evaluate full field surface strains in pressure-distended excised abdominal aneurysms of 28 days, which also reflected underlying increases in stiffness²²⁶.

In the elastase model, after similarly identifying an abrupt early stiffening of the aneurysm-prone segment, Raaz et al. proposed the novel concept of *segmental aortic stiffening* (SAS)²²⁷. They demonstrated using finite element analysis that the localized segmental stiffening leads to axial wall stress due to the tethering of the stiffer segment to its adjacent, more compliant wall segments. After externally applying surgical glue to stiffen the more compliant AAA-adjacent segments (thus equalizing the stiffness profile along the aorta), the authors observed

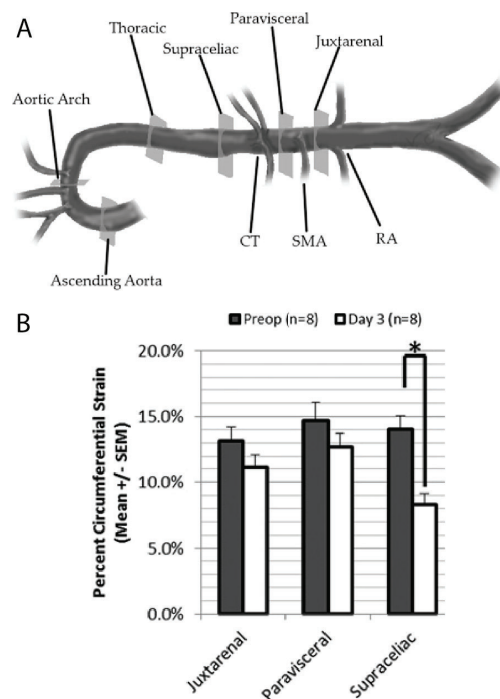


Figure 30: Early stiffening of the suprarenal aorta after AngII infusion. A. Points of interest analyzed in the AngII-infused aorta B. Reduction of circumferential (linear or Cauchy) strain in 3 points of the abdominal aorta. CT: celiac trunk, SMA: superior mesenteric artery, RA: renal arteries. The suprarenal location is 1mm proximal to the CT, paravisceral is between the CT and SMA, juxtarenal is 1mm distal to the SMA. Note that in our own experience, the left and right renal arteries do not branch off at the same level; usually the SMA and right renal artery branch off together forming a trifurcation. Adapted from¹⁹⁵.

a reduction in aneurysm growth. Albeit these findings concern another murine AAA model with disparate driving mechanisms than AngII infusion, the proposed mechanism of SAS can prove valuable in delineating early events leading to AAA formation.

The most integrating hypothesis, illustrated in Figure 31, to explain the regional differences along the aorta in response to AngII infusion was put forward by Bersi et al.¹⁸⁸.

According to their scheme, mechanical changes occur early on and precede the inflammatory response. The early increase in wall stress is induced by elevated pressure and contractility. The common pathways can yet result in regional differences: compare the mechano-adaptive response in the infrarenal aorta with the different maladaptive responses in the ascending thoracic aorta, proximal descending thoracic aorta and suprarenal abdominal aorta (the pathological outcomes of each region are aneurysmal propensity, fibrosis and dissection propensity respectively). Bersi et al. reported that regional differences are governed by different mechano-biological and immuno-biological responses¹⁸⁸. The authors hypothesized that the early rise in blood pressure increases medial stress and results in hypertrophy in the suprarenal and infrarenal aorta, while the sustained blood pressure rise also increases

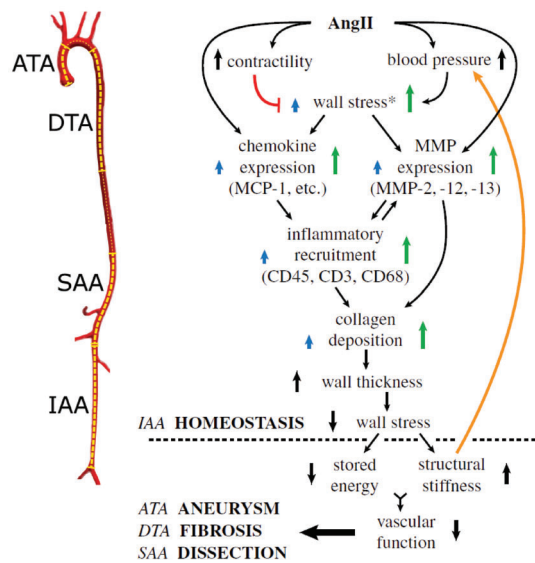


Figure 31: Left: illustration of the aortic regions, Right: scheme of AngII mediated aortic remodelling. Mechanical changes precede the inflammatory response, with positive feedback (orange line) between structural stiffness and blood pressure. Note: a red line denotes negative feedback; blue arrows represent effects on the media and green arrows represent the more pronounced effects on the adventitia. Superscript * indicates findings from^{20,228}. ATA: ascending thoracic aorta, DTA: proximal descending thoracic aorta, SAA: suprarenal abdominal aorta, IAA: infrarenal abdominal aorta. Reproduced from¹⁸⁸.

adventitial wall stress, particularly in the suprarenal aorta. The inflammation cascade is then triggered, along with maladaptive matrix turnover - the relative balance of which defines the pathological outcome of each region.

The suprarenal abdominal aorta had the smallest increase in wall thickness after 4 days of AngII infusion among the 4 regions studied (cf. Figure 31), and was the only one with a reduced percentage of the wall occupied by adventitia by day 4 - a finding in line with the concomitant increased levels of MMPs¹⁸⁸. The authors deduced that in the suprarenal aorta there is delayed collagen deposition, which is needed to stress-shield the vascular wall from pressure-induced wall stress. The authors also reported but did not show weak contractility in the suprarenal aorta.

In Bersi's proposed mechanism, a delicate balance of inflammation and matrix turnover seems to define the final outcome of the disease regionally. But what happens at the very beginning of the hypothesized cascade of Figure 31? Which exactly are the reasons for the locally elevated wall stress, which seems to devastatingly affect the suprarenal aorta?

Early on since the appearance of the AngII model, studies suggested^{189,229} and investigated^{102,218} the effect of hemodynamic loads in lesion progression, intrigued by the site-specific nature of the dissections. Mouse-specific data obtained with micro-CT and ultrasound

allowed the setup of a computation fluid dynamics model which paid particular attention to the hemodynamic conditions at 4 major branches of the abdominal aorta (celiac, superior mesenteric and renal arteries)¹⁹³. The authors found the most distinct area of disturbed flow at baseline to be located either at the branching site (trifurcation) of the superior mesenteric and right renal artery or at the bifurcation of the celiac artery, but comparison against dimensions of end-stage dissections did not lead to a conclusive message. A subsequent study performed extensive histomorphometric examination of the 4 major aortic side branches and showed that at the late stage of disease, transmural disruptions are present, with astonishing consistency, around the orifices of large branches^{194,230}. To date however, there has been no data obtained in the early-phase of the disease to indicate the potential involvement of side branches in dissection formation.

The following question therefore emerges:

What, if any, is the role of aortic side branches in disease initiation?

In order to answer this question, one needs an appropriate investigative tool. To characterize events taking place within the murine vascular wall, let alone subtle early changes of the AngII-induced pathology, and decipher the governing mechanisms of this mouse model we need a substantially powerful imaging modality. Synchrotron imaging came to address this need and has been instrumental in shedding light to open questions of this mouse model, as we will see in section 5.3. Given the imaging tool, several approaches can be followed. In this thesis, we will focus on two alternative hypotheses: the first focuses on (branch-related) biomechanics, while the second focuses on (branch-related) mechanobiology.

Thus far, from a **biomechanical** perspective, considerable work has been published on hemodynamic modelling, extending well beyond the CFD study we mentioned above¹⁹³. Ultrasound imaging has been used to set up mouse-specific hemodynamic simulations of dissecting AAAs, which did not however include any side branches²³¹. Ultrasound (~40µm) combined with in vitro optical coherence tomography(~7µm) has yielded models of hemodynamics within the false channel of a dissected murine suprarenal abdominal aorta for lesions ranging from mild to severe²³². 4D ultrasound and direct deformation estimation were also used to compute the in vivo 3D Green-Lagrange strain in heterogeneous dissecting lesions²³³. But none of these models was focused on the pre-aneurysmal stage of the abdominal aorta or on the role of aortic branching sites in lesion formation. Accurately assessing the biomechanics of the mouse abdominal aorta is a challenge. In the last part of section 5.3, we will see how synchrotron imaging can help propose a simulation approach that leverages its high resolution potential.

Transitioning to the **mechanobiological** scope, recent findings have underlined an important role for smooth muscle cell contractility in aortic disease - after all, smooth muscle cells are a crucial component of the aortic wall. Dysfunctional contractility of smooth muscle cells of the descending thoracic aorta has recently been associated with maladaptive aortic

remodelling in hypertensive AngII-infused mice (infused with subpressor doses of AngII)²³⁴. Pharmacological enhancement of contractility can help protect an otherwise vulnerable ECM by reducing pressure-induced wall stress²³⁵. In other words, increased contractility can off-load some stress from a mechanically vulnerable vascular wall; this notion is also present in the hypothesized mechanism of Figure 31. Smooth muscle cells are also known to switch from the contractile phenotype to an adverse proliferative phenotype in pathology.

In light of these findings, we deemed that assessing the suprarenal aorta's vascular function can hold important information to explain the localized pathogenesis of lesions. Alterations in vascular function of the suprarenal aorta however, especially viewed in conjunction with the local branching topology, has never been assessed. The little prior attention that has been directed towards the vascular function of the suprarenal aorta is in fact partly attributable to the branching topology itself. In myograph applications, traditionally used for vasoreactivity assessment, the arterial rings or segments need to be straight, therefore classically tests are carried out on the segments of the straight thoracic aorta, while the abdominal aorta is avoided. Notwithstanding the utility of assessing the suprarenal segment's 'bulk' properties as in the study by¹⁸⁸ (cf. Figure 31, depiction of the suprarenal segment), it is important to have in mind that aortic dissection initiates locally. With the celiac, superior mesenteric and renal arteries branching off and potentially acting as local concentrators of strain, as we are led to believe, the suprarenal abdominal aorta is hardly a homogeneous segment. It is important therefore to consider spatial distinctions within the suprarenal aorta itself, demarcated by its aortic branches, to understand its localized response to AngII (cf. for example also Figure 30). An interesting notion to mention at this point is also that of mechanobiological stability as a unifying paradigm to describe vascular behavior²³⁶ and aneurysm growth²³⁷. This concept melds strictly mechanical foundations with mechanobiological adaptive and dynamic mechanisms, underscoring the interplay between biomechanics and vascular biology.

AngII-induced ascending aneurysms

Apart from abdominal dissecting aortic aneurysms, mice infused with Angiotensin II also develop ascending aortic aneurysms, as reported by Daugherty et al. in 2010¹⁶⁵. The response of the thoracic aorta is rapid: Rateri et al. reported that within 4 days of AngII infusion, the diameter and luminal area of the aortic arch expand significantly¹⁸². The TAAs exhibit early prominent medial thickening and intramural hematoma, that preferentially forms in the outer medial aspect (Figure 32). This preferential gradient of medial pathologies towards the outer aspect of the wall has been recapitulated in other animal models, and is also the case in humans²³⁸. Rateri et al. were unable to detect an entry point of blood into the outer intralamellar units of the media¹⁸².

In the study by Rateri et al.¹⁸², a gradual decrease of circumferential cyclic Green-Lagrange strain became significant after 7 days of infusion. At the end of the 28-day infusion, elastin fragmentation had become significant and mice presented with partial medial breaks - rup-

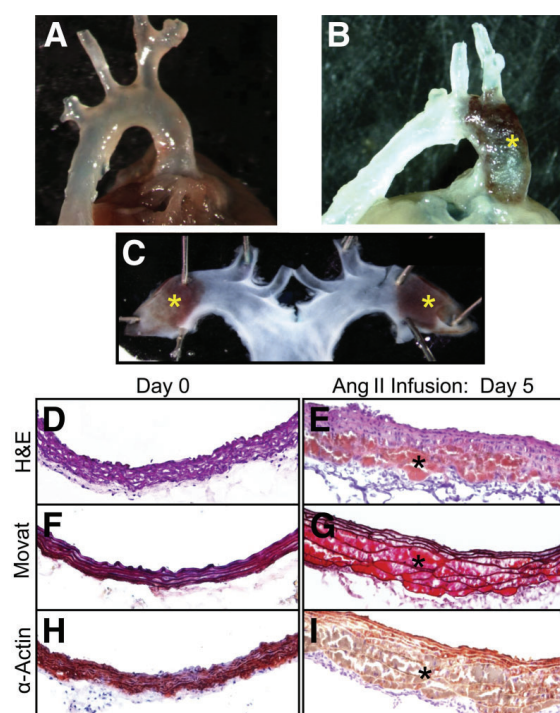


Figure 32: Interlamellar hemorrhage in the anterior aorta of AngII-infused mice. (A) Saline-infused aortic arch, (B) AngII-infused aortic arch macroscopically and (C) *en face*. (D-I) Histological evaluations of ascending aortic cross sections at day 0 and 5 of AngII infusion show interlamellar hemorrhage at the outer portion of the aortic wall. * denotes hemorrhage (A-C), presence of red blood cells within the media (D-I). Reproduced from¹⁸².

tures that did not transect but a portion of the medial layer. These medial breaks occurred in the inner layers of the wall, on the anterior aspect of the aorta, with an incidence of 56% (n=9/15). Monocyte-derived macrophages have been found to invade the media from the adventitial side, and co-localize with sites of elastin fragmentation²³⁹. The spatial variations of material and structural properties of AngII-induced ascending aneurysms have recently been characterized²⁴⁰.

The differences between ascending and thoraco-abdominal lesions in this mouse model are intriguing. In contrast to the complex branching topology of the abdominal aorta, the ascending aorta has no side branches, thus excluding any branch-related hypothesis to explain the region's disease propensity. In response to chronic infusion with AngII, the ascending aorta is the only region of the aorta that presents medial hyperplasia, contrary to hypertrophy developed in the other aortic regions¹⁸⁷. It has been postulated that this heterogeneity in AngII response within the aorta is due to the different embryonic origin of its smooth muscle cells, which may present functional differences. In the ascending aorta and the carotids, smooth muscle cells are derived from the neural crest, while in the thoracic and abdominal aorta they are derived from somite and splanchnic mesoderm lineages respectively¹⁸⁷. An in-depth analysis of the differential response to AngII along the aorta has been carried out by Bersi et

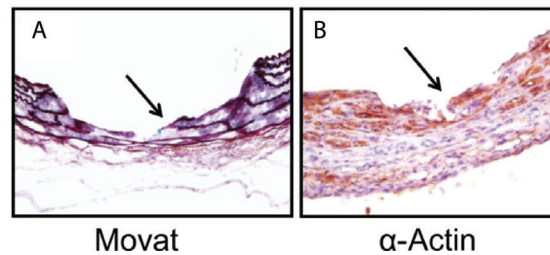


Figure 33: Limited tearing in the anterior part of the aorta after 28 days of AngII infusion. Arrows point to the disrupted inner layers of the media. A. Aortic section stained with Movat's pentachrome, B. Immunostaining for smooth muscle α -actin. Reproduced from¹⁸².

al.¹⁸⁸, as we saw in section 5.2.

The literature on ascending aortic aneurysms in AngII mouse model is much less diverse than the literature on abdominal lesions in the same model. A number of questions concerning the ascending pathology in the AngII model have remained unanswered, notably concerning the entry point of erythrocytes in the media and the role of adventitial remodelling in disease progression. As we will see in the next section, obtaining a high-resolution 3D geometry with synchrotron imaging clarified many of the obscure points of the AngII-induced ascending pathology, similar to the increased insight it offered in abdominal lesion morphology.

Before moving forward, we note here in the context of experimental ascending pathologies that mouse models of heritable TAA (contrasted to the spontaneous TAAs induced by AngII or BAPN²⁴¹ infusion) have been generated by manipulation of genes responsible for ECM integrity or SMC function, such as fibrillin-1, fibulin-4 and ACTA-2^{242,243,244,245}. These mouse studies have provided valuable insight on the genetic basis of human thoracic aortic disease, but their description is beyond the scope of our work here.

5.3 Insights from high-resolution 3D synchrotron imaging

The advent of the synchrotron imaging method has helped elucidate intricate questions concerning the Angiotensin II mouse model and provide new insight with regards to the temporal evolution, topographic patterns and morphology of these experimental lesions in the abdominal and ascending murine aorta. The studies revealed that aortic suprarenal side branches most probably play a crucial role in dissecting AAA lesion formation. Moreover, they underscored the marked difference between lesion morphology in the abdominal and the thoracic regions. The principal findings of this work, on which this dissertation has largely relied as a starting point, are described below. The first section describes findings of two studies on abdominal dissecting aneurysms, the second section focuses on ascending aneurysms, and the third section demonstrates how the increased granularity of synchrotron imaging presents a unique opportunity to advance the state-of-the-art in computational aortic biomechanics through the development of a novel computational framework.

AngII-induced abdominal dissecting aneurysms

a. The first use of synchrotron imaging in the AngII model

The first implementation of synchrotron radiation to image AngII-induced dissecting aneurysms was reported by Trachet et al¹⁹⁶. In this study lesions were induced via Angiotensin II administration, albeit not on ApoE-deficient mice: as mentioned in subsection 5.2, combination of Angiotensin II infusion with anti-transforming growth factor- β antibody administration in normocholesterolemic mice induces higher rupture rates of abdominal lesions. Male C57BL/6J mice (n=20) were implanted a 200 μ L osmotic pump delivering Angiotensin II, and received regular intraperitoneal injections of mouse anti-human TGF- β (2G7 clone, 20 mg/kg, three times a week) to achieve systemic neutralization of TGF- β . The progression of dissecting AAAs was longitudinally monitored at different time points in vivo using high-frequency ultrasound (Vevo 2100). Before sacrifice, six animals with obvious dissecting AAA formation (as confirmed by ultrasound) were injected in the lateral tail vein with 4 mL/g body weight of Exitron nano 12 000 (Miltenyi Biotec, Germany), a nanoparticle contrast agent for in vivo micro-CT scans as we saw in section 4.1. These animals were subsequently scanned in vivo with a Quantum FX micro-CT scanner. During both ultrasound and micro-CT imaging, animals were anaesthetized by inhalation of 1.5% isoflurane. At the endpoints of the experiments, the mice were sacrificed and the aorta was flushed in situ by transcardiac perfusion of PBS. In animals that died of transmural rupture of the aneurysmatic wall, the aorta was collected (without flushing) as soon as possible after finding them in the cage. The abdominal aorta of both intact and transmurally ruptured dissecting AAAs was carefully excised, and samples were fixed by immersion in 4% paraformaldehyde (PFA). The samples were scanned at the TOMCAT beamline of the Swiss Light Source (PSI, Switzerland). All reconstructed data sets (in vivo as well as PCXTM) were semi-automatically segmented into 3D models using the commercial software package Mimics (Materialise, Belgium).

5. The Angiotensin II infusion mouse model

Visualization of the aortic wall morphology at the Synchrotron using phase contrast with grating interferometry at **6.5 μm isotropic resolution** led to unprecedented insight of 3D lesion morphology and even reconsideration of previously mis- or under-interpreted literature findings. An unexpected but important by-product of this work was that the Exitron micro-CT contrast agent leaks into the arterial wall through micro-ruptures intra vitam, which are subsequently visible on both the in vivo micro-CT images and the ex vivo synchrotron images (Figure 34, green arrows). This fortuitous discovery was used for this dissertation as a means to elegantly localize early microruptures of the vascular wall of the AngII-infused mouse aorta.

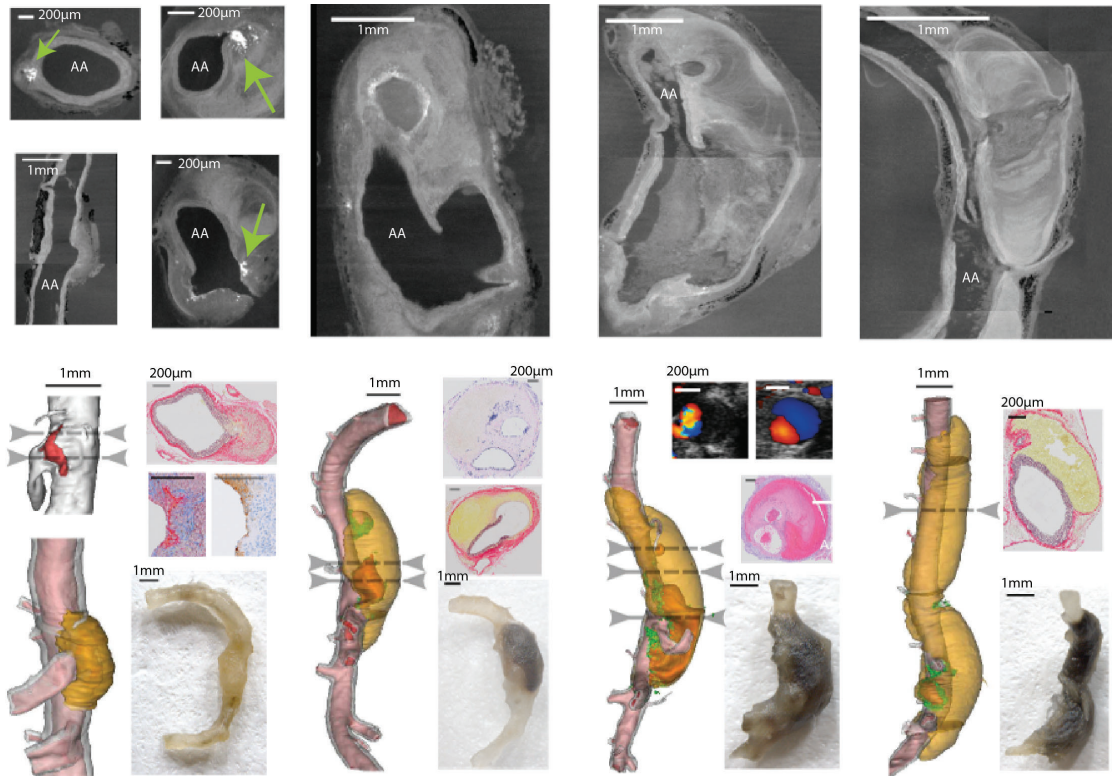


Figure 34: Ex vivo synchrotron images of aneurysmatic aortas and their resulting 3D reconstructions. Upper panels: Longitudinal and transversal images of the abdominal aorta taken with grating interferometry. Green arrows show infiltrating contrast agent at level of branching points on transversal images. Lower panels: 3D reconstructions of abdominal dissecting AAAs, with indicative histology (H&E, SR-Miller, CD31, MSB) at selected slices and color doppler ultrasound for one sample. Macroscopic gross morphology of the aorta shown for comparison. On 3D volumes, intramural hematoma is in yellow, contrast agent is in green, aortic lumen is in (transparent) red surrounded by its tunica media is (transparent) grey. AA: aortic lumen. Scale bars of histological images that are not annotated are 200 μm . Adapted from¹⁹⁶.

After PCXTM scanning, fixation in PFA and histological analysis was performed on the excised tissue. The intrinsic resolution of PCXTM (6.5 μm), i.e. the inter-slice distance between the ex-vivo images, was similar to the thickness of histological paraffin coupes (4 μm) used for histological analysis. It was therefore possible to perform **PCXTM-guided histology** and thus

Introduction

select sections of interest along the aorta in a highly precise manner for histological analysis. The exact locations of interest along the aorta can be spotted beforehand based on the ex-vivo images and allow for targeted, selective sectioning, so as to cut and stain only at the regions of interest. Knowledge of the 3D morphology also greatly facilitates the interpretation of the 2D histological images.

Leaking of contrast agent in the aortic wall

Given the particular importance that the serendipitous finding of this study on contrast agent infiltrations in the wall holds for this dissertation, we will highlight some additional information here. In the n=6 animals of this study which underwent in vivo contrast-enhanced micro-CT scans 2 hours prior to their sacrifice, the contrast agent was seen on the PCXTM images as dense white aggregates (green arrows on Figure 34). Owing to the small size of the particles (whose diameter is 0.11 μ m) and the discontinuity of the intimal/medial layers, Exitron entered the aortic wall together with erythrocytes (whose diameter is 6-7 μ m) along the edges of medial tears and ruptured branch ostia. The aortas were flushed (to remove blood from the lumen) after sacrifice and prior to imaging, hence these areas show that there was intra-vitam locally increased permeability due to the wall's disrupted continuity and loss of architecture. Histological stainings with CD31 at these regions showed focal hypertrophy of the endothelium (endothelial activation), additional stainings are shown in Figure 35.

We note here that the contrast agent infiltrations of the wall can be observed not only in the PCXTM images but also in the in vivo micro-CT scans, in cases of advanced dissections. A note on this is made in chapter 2.

Aneurysmal lesions (i.e. apparent luminal dilatation) were associated with two phenomena. On the one hand, ruptures of the tunica media near the ostia of **small suprarenal branches of the abdominal aorta** could be visualized for the first time. These resulted in a dissection and delamination of the media-adventitia interface, while stagnant blood coagulated, forming an intramural thrombus. On the other hand, a **large tear of the medial layer in the vicinity of the celiac artery** was observed on all animals. This led to an eccentric, apparent luminal dilatation as the free flowing blood entered the intramural space at the level of the tear. In certain animals, a false channel grew progressively and cranially into the previously existing hematoma.

Standard imaging modalities would not have allowed this level of acquired insight on the morphology of the AAAs. For example, in numerous instances of published data, researchers described the existence of pronounced luminal expansion adjacent to an intact media surrounded by a thickened adventitial layer, based on histological findings. Thanks to the 3D geometry obtained with PCXTM and the image-guided histology, the false channel was visualized forming parallel to the true lumen of the aorta. The risk of misinterpreting the 2D histological images was thus bypassed.

The findings on the tears in the inner aortic wall, both near the celiac artery and near intercostal

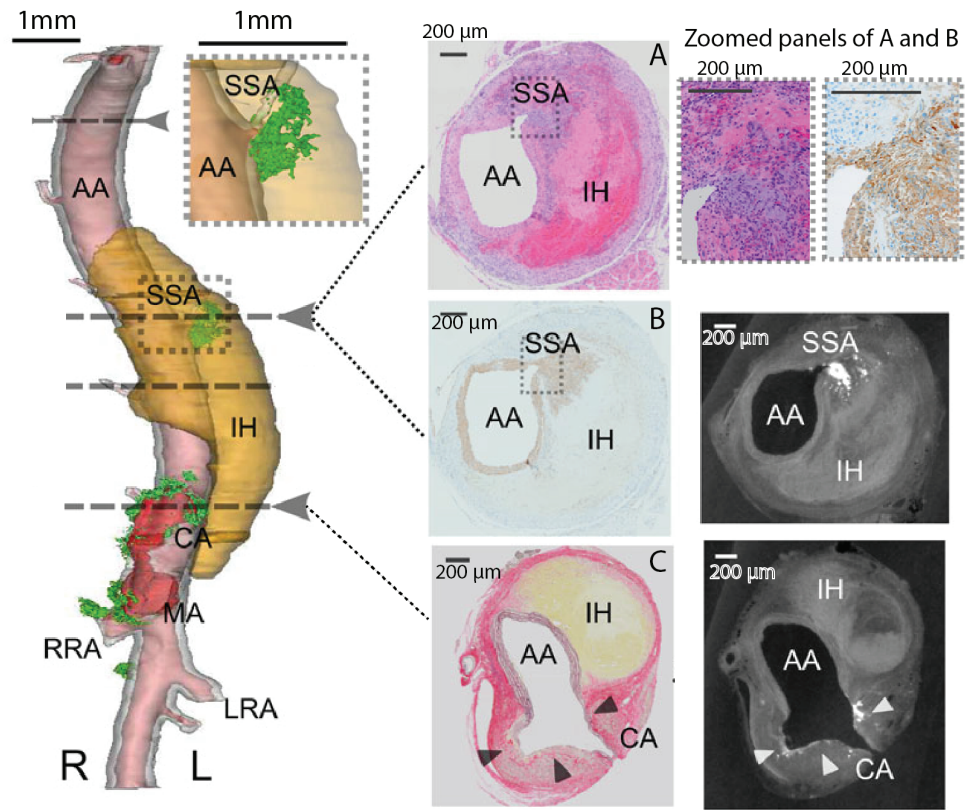


Figure 35: Histological findings at the level of Exitron infiltrations. Left: 3D representation of the aorta. Tunica media in (transparent) grey, intramural hematoma in yellow, blood-filled lumen in red, Exitron in green. Right: Stainings at the level of side branches, with Exitron infiltration along with 2D PCXTM images at the same locations. A. H&E (and its zoomed panel), Exitron particles infiltrating the wall show a typical grey-greenish discolouration of phagocytic cells. Note also the presence of erythrocytes. B. α smooth muscle actin (and its zoomed panel), showing migrating spindle cells. C. Combined SR Miller stain. R: right, L: left, SSA, superior suprarenal artery; IH, intramural haematoma; RRA, right renal artery; LRA, left renal artery. Adapted from¹⁹⁶.

side branches, revealed that the role of side branches in the onset of the disease is much more important than what was previously considered. A longitudinal study with in vivo follow-up and synchrotron imaging (phase contrast using grating interferometry) was repeated, but this time on AngII infused ApoE^{-/-} mice, the most standard genetic background for this model²¹⁵. The main findings of this study are summarized below; the observations on the early phase time mark of this study are separately presented in Chapter 2.

Introduction

b. A second study to characterize the variability in the AngII model¹

The study by Trachet et al.²¹⁵ used three objective criteria to describe the variability of thoracoabdominal lesions they observed: the presence of a transmural tear (transecting all elastic laminae of the aorta), the presence of an intramural hematoma in the vicinity of the tear, and the presence of a false channel (Figure 36). Note that the definition of false channel in this work was defined by free-flowing blood that extended beyond the axial length of the medial tear from which it originated, thus forming a channel that was parallel to the true lumen.

No intramural hematoma formed without the presence of a medial tear; in some cases the tear was contained by the adventitial layer without any hematoma formation. The axial length of the intramural hematoma positively correlated with the number of side branches whose ostium was ruptured ($r^2=0.78$). Furthermore, the volume of the hematoma was larger on the left and supraceliac aspects of the aorta (left and above the celiac artery), as compared to right and below the celiac artery. Moreover, no false channel formed without the presence of an intramural hematoma; in some cases there was just intramural hematoma without any false channel.

This study used to its advantage the serendipitous finding of contrast agent infiltration described in the previous section. The mice underwent contrast-enhanced micro-CT with Exitron so that, apart from micro-CT monitoring, Trachet et al. could also localize infiltration volumes of contrast agent in the wall, which denote the presence of microstructural damage. In animals that were sacrificed after 10, 18 or 28 days of Ang II-infusion, the highest amounts of Exitron were detected near the ostia of side branches (Figure 37A). Trachet et al. reported that the ostium of minor branches in the thoracic aorta was significantly less often infiltrated by Exitron than that of minor abdominal branches ($P<0.05$). The ostium of the celiac artery was significantly more often affected than the other major abdominal branches ($P<0.05$). Medial tears occurred only very seldom near minor branches of the thoracic or abdominal aorta (8 tears on a total of >400 minor branches that was counted across all investigated mice, Figure 37B). Contrastingly, medial tears in the abdominal aorta were significantly more frequent near **the celiac artery and the superior mesenteric artery** than near any of the other major branches (Figure 37B).

This study confirmed that the pathophysiology of this animal model is more reminiscent of aortic dissections rather than aortic aneurysms and highlighted the implication of aortic branches in lesion heterogeneity.

AngII-induced ascending aortic aneurysms

The synchrotron imaging modality was combined with in vivo imaging to also evaluate the temporal evolution of ascending aortic pathologies in AngII-infused male ApoE-deficient mice

¹Findings of this work concerning the early stage of disease in the AngII model are presented separately in Chapter 2.

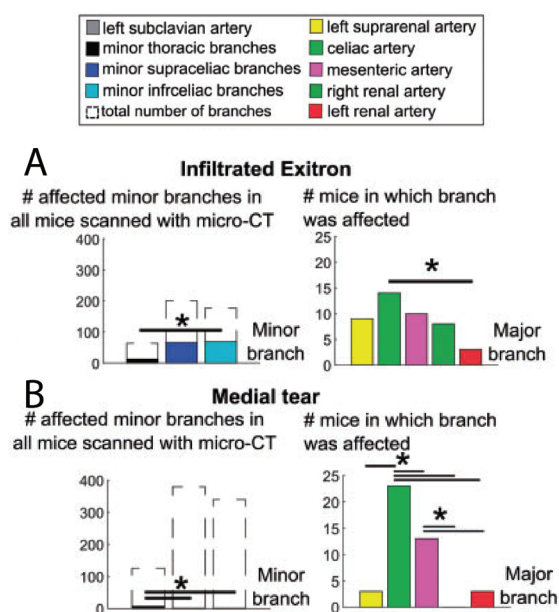


Figure 37: Medial damage near aortic side branches. A: Infiltrated Exitron contrast agent and B: medial tears around major side branches (right panels) and minor side branches (left panels). Each branch was given a color code according to the legend. For minor branches, the total number of affected branches across all mice was reported, while for major branches the number of mice in which each branch was affected is reported. * $P < 0.05$. Adapted from²¹⁵.

determined by PCXTM and PCXTM-guided histological analysis, reaffirmed previous findings that AngII infusion leads to intramural hematoma occurring on the adventitial side of the aortic wall¹⁸².

Location-specific occurrence of ascending aortic aneurysms

The *in vivo* measured axisymmetric dilatation of the ascending aorta was related to highly non-symmetric, focal lacerations in the aortic wall. The lesions appeared as abrupt losses of the medial continuity in the PCXTM images, and could be observed in the histological slides as well (Figure 38). In stark contrast to the complete absence of focal dissections in aortas from saline-infused mice, lacerations were present in 41/42 (98%) scanned aortas from AngII-infused mice - an incidence much higher than that reported by Rateri et al.¹⁸² (56%, cf. section 5.2). The lacerations were predominantly found in the outer convex aspect of the ascending aorta. Interestingly, 7/41 focal dissections occurred in bilateral pairs, with a tear on the right side of the aorta accompanied by a mirroring one on the left, downstream of the aortic valve (cf. timepoint of Day 18 in Figure 38).

Temporal evolution of ascending aortic aneurysms

Large intramural hematomas were observed after only 3 days of angiotensin II infusion, and their size was larger at 3 days of AngII infusion than at subsequent time points. The presence of contrast agent aggregates within the wall indicates an *intra vitam* locally increased permeabil-

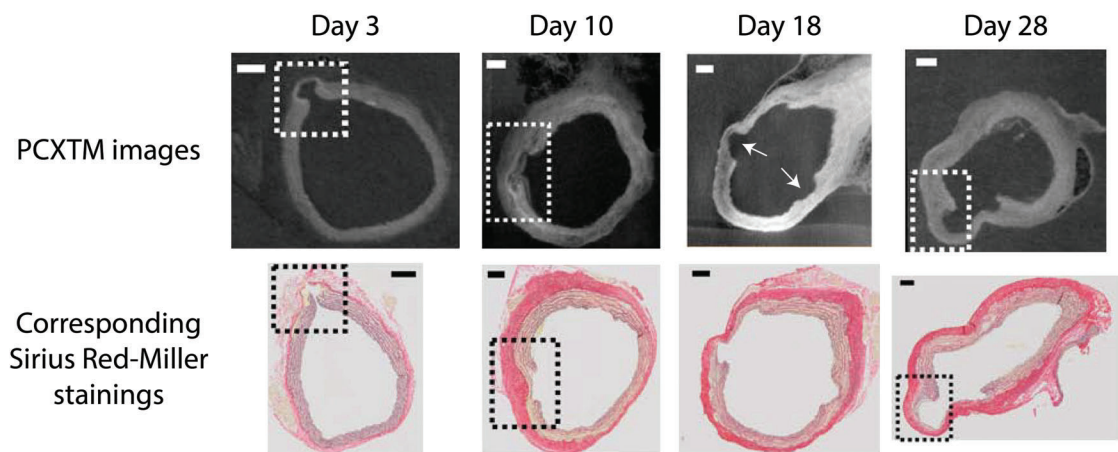


Figure 38: Focal lacerations at the ascending aorta. In the top row, 2D PCXTM transversal images of the ascending aorta at 6.5μm resolution at different time points. On day 18, arrows point to bilateral focal lacerations downstream of the aortic valve. Bottom row shows Sirius Red-Miller stains of focal dissections at sections corresponding to the images on top. Scale bars represent 200 μm. Adapted from ¹⁸³.

ity of the vessel wall or even loss of continuity of the endothelial lining. The fact that contrast agent leakage is decreased in subsequent timepoints suggests that this increased permeability is temporary and localized. In contrast to Rateri et al, who could not identify any access point for the interlamellar hematoma¹⁸², PCXTM- and PCXTM-guided histology showed the intimal defect which led to an intramural bleeding at this early time point (Figure 39).

Prussian blue staining identified hemosiderophages actively resorbing the hematoma at later time points. These data show that the rapid formation of an intramural hematoma is an early-stage event in this pathology, and is resolved at later stages of the disease. All of the 8 mice that succumbed to hemothorax in this study died between 3 and 8 days of AngII infusion. In these mice, PCXTM-guided histology confirmed a complete rupture of all laminae of the tunica media. This suggests that the focal dissection evolved too abruptly, so that the outer wall segments, which did not have the time to remodel, could not bear the rapidly increased load. Adventitial remodelling hence dictates whether the early focal lacerations result in a contained aortic dilatation or in catastrophic rupture.

A critical question that is highlighted is why the hematoma is restricted to the outer laminae. This study revealed that the highest number of laminar ruptures occurred in the central laminae (L2-L4), but the inner (L1) and outer (L7) laminae were less frequently affected. The fact of the outer lamellae being more affected in the ascending aortic pathology is not a feature exclusive to the model of AngII infusion: it has been recapitulated, as we saw in section 5.2, in several different models of ascending aortic aneurysms^{246,247}. The predominance of pathology in the outer medial layers is also a common feature in human ascending aortic aneurysm and dissection²⁴⁸.

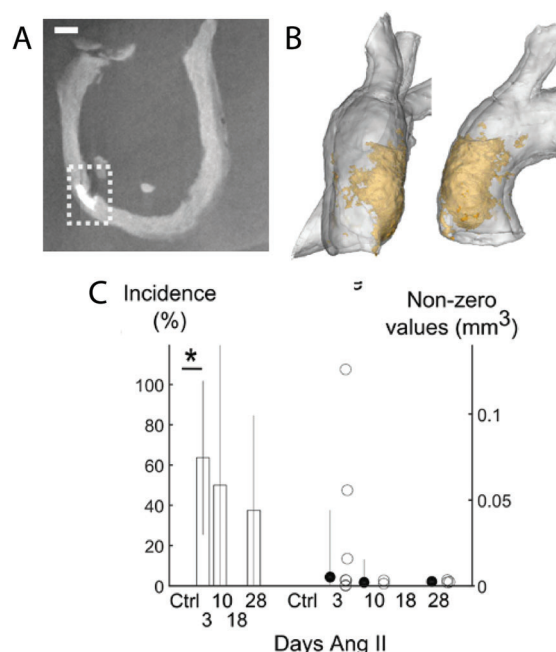


Figure 39: Temporal distribution of interlamina hematoma. A. Two-dimensional (2D) phase contrast X-ray tomographic microscopy (PCXTM) image shows the contrast agent leakage (white aggregate within box) in between the laminae through an intimal tear. B. Three-dimensional (3D) representation of a major Exitron leakage (in orange) that has percolated into the tunica media (in transparent white). C. Contrast agent volume penetrating into the tunica media over time. *P<0.05, **P<0.001. Scale bar represents 200 μm. Adapted from¹⁸³.

The combination of *in vivo* techniques with *ex vivo* synchrotron imaging allowed the identification of early events and a characterization of the progressive pathology of Angiotensin II-induced ascending aortic aneurysms.

Synchrotron-based biomechanics

In order to investigate the role of local biomechanics in the pathophysiology of branch-related ruptures in Angiotensin II infused mice, Trachet et al. presented a mouse-specific fluid–structure interaction (FSI) model of the (healthy) abdominal aorta in ApoE-/- mice that incorporates *in vivo* stresses²⁴⁹. The simulation showed zones of elevated wall stress near the ostium of the celiac artery, which coincided with the location of medial rupture as seen on another mouse imaged at synchrotron, for comparison (Figure 40).

The FSI framework incorporated some of the latest improvements in mouse-specific computational biomechanics, such as strongly coupled FSI, a material model with parameters tuned to mouse-specific *in vivo* measurements, a high quality hexahedral mesh and a backward displacement method to incorporate *in vivo* circumferential stress. However, the framework was also subject to several limitations, namely:

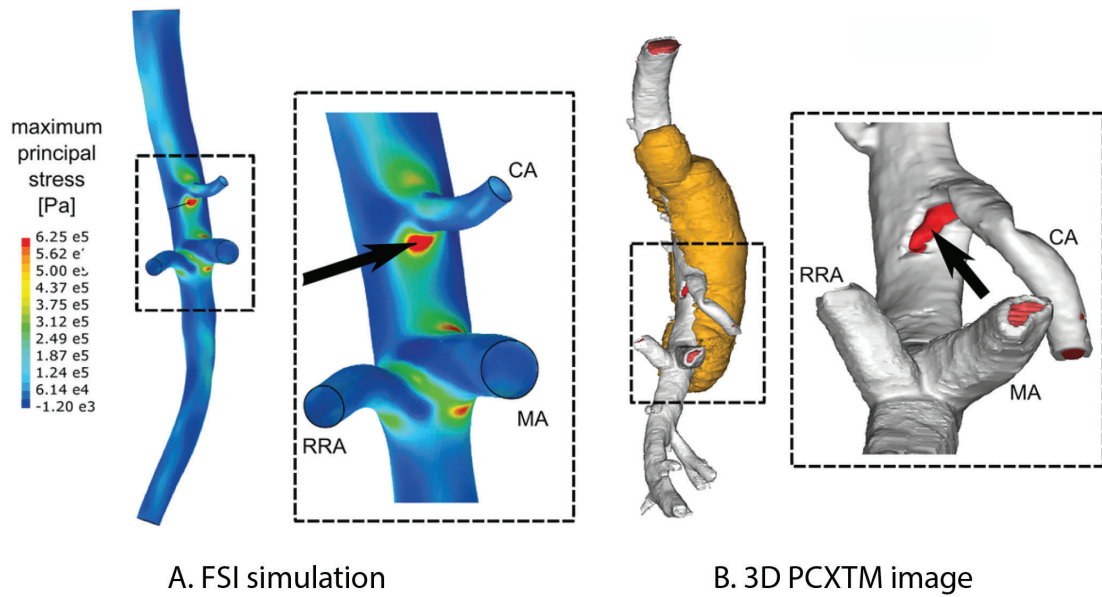


Figure 40: Left: FSI simulation of a healthy murine aorta shows zones of elevated wall stress near the ostium of the celiac artery, Right: Reconstructed 3D volume of dissected aorta from synchrotron images. The transmural rupture occurs at the level of the celiac. Mural hematoma in (transparent) orange, blood filled lumen in (transparent) red, Exitron in green. FC, false channel; AA, aortic aneurysm; IH, Intramural hematoma; CA, celiac artery; RRA, right renal artery; CA, celiac artery, MA, mesenteric artery. Scale bar represents 1mm. Adapted from^{249,196}.

- *Assumption of a uniform wall thickness.* Current in vivo imaging techniques (CT or MRI in humans, micro-CT in mice) do not yield sufficient resolution to include a detailed mouse-specific wall thickness into the model. A non-uniform thickness has been shown to have a significant influence on the outcome of numerical simulations of aneurysms^{250,251,252}.
- *Omission of minor arterial side branches.* The aortic geometry did not include minor side branches such as subcostal arteries. Similarly to the subject-specific thickness, the resolution of standard imaging approaches does not allow to visualize these minor branches. Nevertheless, it has been demonstrated that these small side branches are preferred regions for hemodynamic perturbations and vascular lesion development²⁵³.
- *Omission of axial pre-stretch.* This is a general limitation for models based on in vivo images since, unlike circumferential prestresses, the axial stretch can only be calculated if one has access to the ex vivo, zero-stretch condition of the vessel. Nevertheless, local variations in axial stretch and stress might have a significant influence in both the initiation and development of different cardiovascular diseases^{26,254}.
- *Lack of mouse-specific validation.* Simulations were only performed on a healthy, non-diseased aorta. While Trachet et al. did find stress concentrations near the same side branches where vascular damage had been observed in angiotensin II infused mice, a

mouse-specific (one on one) study in which simulations and experiments are performed on the same animal is still lacking. Mice provide a unique opportunity to compare the computational hotspot predictions, since in a clinical setting there are typically no post-mortem scans available to investigate the predicted rupture risks.

- *Arruda-Boyce material model.* The Arruda-Boyce hyperelastic constitutive model used is rather simplified, compared to the more sophisticated two-fiber³¹ or four-fiber-family model³². More complicated models generally need more parameters and are thus difficult to fit to in vivo measurements. Moreover, while the anisotropic constitutive relations and fiber directions have been established ex vivo (typically on idealized cylinder-shaped geometries), the in vivo mechanical response at the bifurcation level (which is of particular interest when investigating the role of side branches) is still unclear.

These limitations (except for the use of the material model) were addressed using synchrotron imaging and implementing synchrotron-based biomechanics.

Combination of in vivo micro-CT imaging with ex-vivo synchrotron imaging of a mouse abdominal aorta conveys a level of detailed information not yet reached with clinical images. Ferraro et al.²⁵⁵ developed a novel semi-automated framework to incorporate anatomical aspects revealed by synchrotron imaging (namely non-uniform subject specific wall thickness, minor side branches and non-uniform axial stretch) within a computational model of the mouse abdominal aorta. The algorithm maps the non-pressurized, non-stretched ex vivo synchrotron PCXTM scans (containing information on the local wall thickness and minor side branches visualized at 6.5 μm resolution) onto the pressurized, stretched in vivo micro-CT scans (only depicting the aortic lumen). Since in the biomechanical part of this dissertation we have applied this framework for different mouse geometries, we will hereby describe in detail its implementation steps for the sake of completeness. The framework, along with a sensitivity analysis to evaluate the impact of each element included in the computational model, can be found in²⁵⁵.

Experimental protocol

One male ApoE-deficient mouse on a C57Bl/6 background was implanted with a 200 μL osmotic pump, filled with a solution of angiotensin II in saline 0.9%. Prior to implantation the pump was primed for 24 h at 37°C. The mouse was sacrificed after 3 days of angiotensin II infusion to investigate the early phase of dissecting aneurysm development. Care was taken not to damage the aortic tissue during the dissection of the aorta while surrounding connective tissue was carefully removed. The following imaging modalities were used:

- (a) *In vivo contrast-enhanced micro-CT imaging after 3 days of AngII infusion.* The animal was injected intravenously in the lateral tail vein with 4 mL/g body weight of Exitron nano 12 000 (Miltenyi Biotec, Bergisch Gladbach, Germany) and subsequently underwent a micro-CT scan. During micro-CT imaging the animal was anaesthetized by

inhalation of 1.5% isoflurane. This technique provides an isotropic pixel size of 50 μm of the abdominal aorta lumen, but the tissue contrast is not sufficient to provide information about the wall thickness. The scan was not gated and the generated micro-CT segmentation represents an average between systolic and diastolic geometries.

- (b) *Ex vivo PCXTM imaging after sacrifice.* Following euthanasia, the abdominal aorta was excised and the sample was fixed by immersion in freshly prepared 4% paraformaldehyde. The samples were scanned at the TOMCAT beamline of the Swiss Light Source, Paul Scherrer Institut, Villigen, Switzerland. PCXTM computer microtomography provides volumetric data of samples in a non-destructive way with an isotropic pixel size of 6.5 μm . This novel imaging technique yields enough tissue contrast to accurately evaluate the wall thickness and to segment small subcostal side branches.

Preprocessing

Both in vivo micro-CT and ex vivo synchrotron scans were semi-automatically segmented in the software package Mimics v.17.0 (Materialise, Leuven, Belgium). For micro-CT scans this required manual intervention to separate aortic and venous segments of the contrast enhanced vasculature. The cross-sectional diameter of the smallest side branches (e.g., subcostal arteries) only consisted of 3–5 pixels in the micro-CT images. In case of doubt, the PCXTM image stack was used as a guidance to guarantee that the correct structures were identified. For PCXTM the contrast agent infiltrations within the vessel wall were segmented separately since previous observations had shown that such infiltrations represent a clear indication of early vascular damage, as described above in section 5.3. Both micro-CT and synchrotron-based masks were smoothed while taking care not to cause any shrinkage. The open-source library VMTK (ref) was subsequently used to finalize pre-processing. Inner and outer walls of PCXTM were separated in order to generate the ex vivo computational mesh, while the side branches of the PCXTM model were removed and reconstructed. Since we lack any reference on the side branches, we decided to develop a consistent extension technique. Each side branch was artificially extended by means of a branch-specific extension length proportional to the corresponding one measured in the CT model. In particular, the distance between the celiac and mesenteric bifurcation was calculated in terms of abscissa coordinate of the centerline, both in the CT and PCXTM scans. The ratio between these two quantities provided an extension coefficient which was multiplied by the PCXTM side branch length and used as extension length.

Meshing procedure

In order to generate the ex vivo mouse-specific mesh, the outer wall of the PCXTM model was discretized with an unstructured quadrilateral mesh and exported into the stereolithographic (STL) file format. This geometry file was subsequently passed on to the extended Treemesh method, a parametric interface that has been implemented in pyFormex to generate hexahedral meshes²⁵⁶. The outer mesh was then smoothed using a non-shrinking Taubin smoothing filter (passband 0.1, 100 smoothing iterations) and projected onto the mesh of the inner wall

through an in-house developed Matlab code (The Mathworks, Inc., Natick, MA, USA). The result was an unstructured hexahedral solid mesh of the ex vivo geometry (Figure 41). All meshes were auto-generated to ensure grid independency of the simulation results. The average element edge length in the converged models is $9.6 \mu\text{m}$, while the maximum and minimum lengths are 34 and $1.5 \mu\text{m}$, respectively.

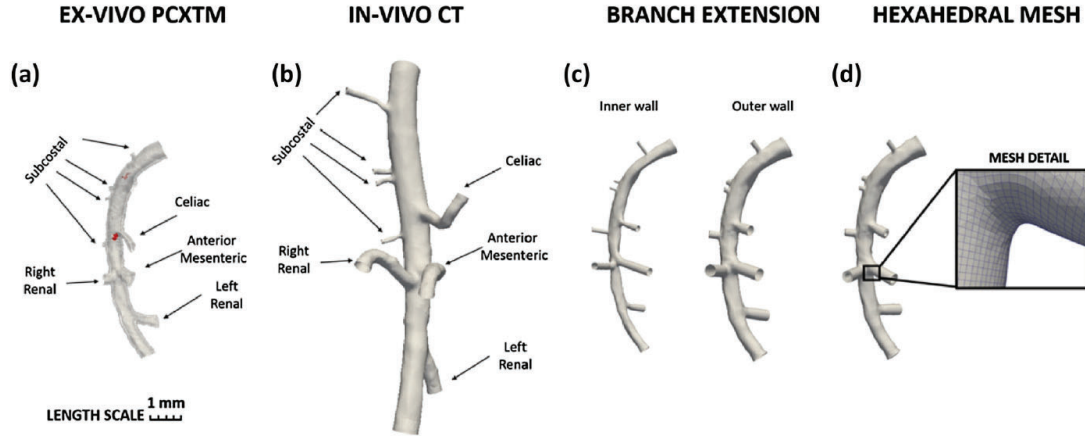


Figure 41: Preprocessing step of the morphing framework. (a) Segmented synchrotron geometry (contrast agent in red). (b) Segmented micro-CT geometry. (c) Inner and outer walls of the synchrotron model after artificial branch extension. (d) Conformal hexahedral mesh with mouse specific wall thickness (zoomed panel).

Morphing Framework Set-Up

The evaluation of the local stretch field along the abdominal aorta requires the generation of a pointwise correspondence between the ex vivo PCXTM mesh (not stretched, not pressurized) with the in vivo CT model (in vivo axial stretch, pressurized). To this end we implemented a branch-based change of coordinates. Using VMTK, branch splitting was performed on the micro-CT model and the inner wall of the PCXTM mesh (Figure 42a).

At this stage, each branch of the arterial network was topologically equivalent to a cylinder and a rectangular parametric space could be generated. In the circumferential direction, the angular position of each point on the surface mesh was parameterized with respect to the centerline following the method proposed by Antiga et al.²⁵⁷ (Figure 42b). In longitudinal direction, a parameterization was performed using the harmonic mapping method presented by Halier et al.²⁵⁸. In particular, a Laplacian partial differential equation was solved on the surface by imposing Dirichlet boundary conditions on the two open boundaries, generating a longitudinal parametric distribution (see Figure 42c). The combination of the two parametrizations can be compared between micro-CT and PCXTM models, and a standard nearest neighbor approach has been used to find the minimum distance for each PCXTM mesh node with respect to all the micro-CT nodes²⁵⁹. Once all the maps were computed, the global displacement map was generated using the element connectivity of the PCXTM model as a reference. In order to avoid mesh distortion, smoothing and projection procedures were

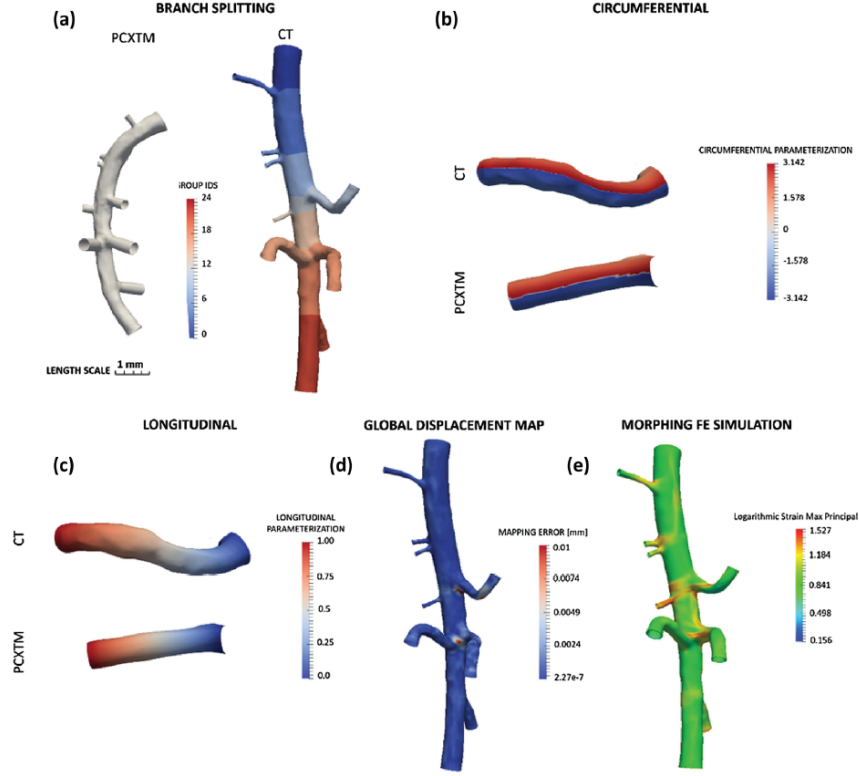


Figure 42: Setup of the morphing framework. (a) branch splitting; (b) circumferential mapping computation; (c) longitudinal mapping computation; (d) global displacement map error contour plot with respect to the original CT model; (e) max principal strain contour plot after morphing FE simulation.

performed in a similar fashion to those used during the meshing phase. The final map shows very good agreement with the original micro-CT model (Figure 42d), with maximum error of 10 μm located at the main bifurcations, which is five times less than the micro-CT pixel size. The global map, representing a surface mesh with the shape of the CT model and the mesh size and distribution of the PCXTM inner wall mesh, was employed as a set of displacement conditions to morph the latter onto the former. Both the final PCXTM model and the global displacement map were automatically embedded within an input file for the commercial FEM solver Abaqus/Standard 6.13 (Simulia, Dassault Systemes, Providence, RI, USA). The structural simulation was considered static and fully displacement controlled, under a large deformation regime (Figure 42e). A nearly incompressible Arruda–Boyce²⁶⁰ constitutive model was used. The Arruda-Boyce model, also known as the eight-chain model, is based on an eight-chain representation of the underlying macromolecular network structure of rubber and the non-Gaussian behavior of the chains in the network. The strain energy function is given below (Equation 3).

$$W = \mu \sum_{i=1}^5 \frac{\alpha_i}{\lambda_m^{2i-2}} \left(I_1^i - 3^i \right) \quad (3)$$

$$\alpha_1 = \frac{1}{2}, \alpha_2 = \frac{1}{20}, \alpha_3 = \frac{11}{1050}, \alpha_4 = \frac{19}{7000}, \alpha_5 = \frac{519}{67375\lambda_m^8}$$

In these equations W is the strain-energy function, I_1 is the first invariant of the Cauchy-Green tensor, μ is the shear modulus, μ_0 is the initial shear modulus and λ_m the locking stretch, which approximately denotes the stretch at which the slope of the stress-strain curve will rise significantly. This model captures the cooperative nature of network deformation with only two material parameters, i.e., the shear modulus μ and locking stretch λ_m . The two parameters are linked to the physics of molecular chain orientations involved in the deformation of rubbery materials and elastomers. The initial shear modulus μ_0 is related to the locking stretch λ_m by Equation 4.

$$\mu_0 = \mu \left(1 + \frac{3}{5\lambda_m^2} + \frac{99}{175\lambda_m^4} + \frac{513}{875\lambda_m^6} + \frac{42039}{67375\lambda_m^8} \right) \quad (4)$$

The material parameters ($\mu = 24,358$ Pa, $\lambda = 1.01$) were the same used in the previous FSI work²⁴⁹.

At the open boundaries, all nodes throughout the wall thickness were constrained to follow the motion of the corresponding nodes of the inner wall, in order to avoid non-physiological shearing effects. In order to facilitate the comparison of the final outcome with the location of micro-ruptures in the ex vivo synchrotron model, the strain contour plot was mapped backward onto the ex vivo undeformed configuration and the artificial extensions in side branches were removed for visualization purposes.

Qualitative comparison of structural simulation with experimental data

The distribution of the maximum principal strain was quantified at the outer wall, with particular focus on regions of high strain (termed hotspots). Looking at the full model, the values ranged from 0.3 in the most tethered regions close to the mesenteric artery to 1.66 at the orifice of the celiac artery. In addition to the main strain concentration on the ventral side of the celiac bifurcation, two hotspots were detected on the dorsal side of one of the subcostal arteries and on the left-ventral side of the mesenteric artery (Figure 43a). Two slices of the morphed model corresponding to the contrast agent infiltration regions were selected for a detailed comparison to the local strain concentrations (Figure 43c). Both the overall 3D assessment and the 2D slices show good agreement between the computed strain and the experimentally observed infiltrations of contrast agent (Figure 43c).

A sensitivity analysis was carried out to assess the impact of certain features of the morphing approach on the computed aortic strain field (Figure 44). Results showed that the constant thickness modelling assumption, which is standard in the field, may lead to incorrect results at particular bifurcations. All side branches, including the very small ones, can alter the local mechanical equilibrium of the aorta, both in axial and circumferential direction. Lastly, the axial stretch in the murine aorta is highly nonuniform, and this non-uniformity contributes to the distribution of stresses and strains along the aorta.

5. The Angiotensin II infusion mouse model

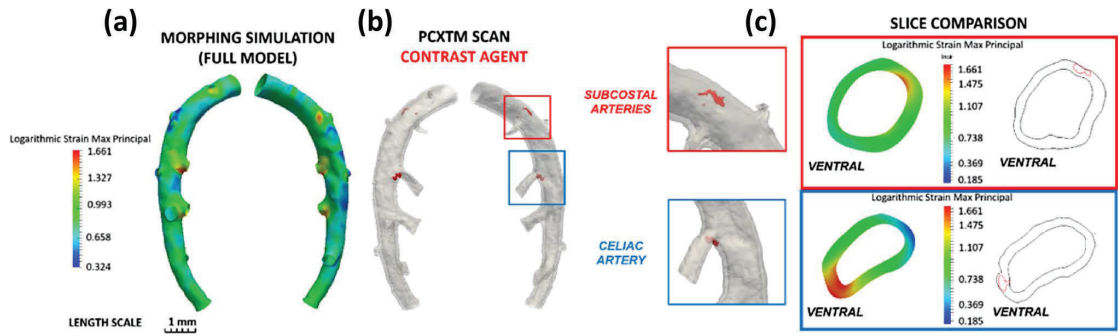


Figure 43: Qualitative comparison of computed strain and infiltrated contrast agent. (a) logarithmic strain max principal contour plot; (b) original PCXTM model (contrast agent infiltration is highlighted in red); (c) 2D slices comparison with focus on the regions of contrast agent infiltration.

The biomechanics and mechanobiology underlying the branch-related ruptures in this mouse model still remains to be demonstrated. Solid mechanics provide an approach to explain branch-related ruptures as the mechanical tension exerted on the tunica media is expected to be elevated near branch bifurcations. A thorough understanding of the biomechanics in the murine aorta, and in particular the biomechanics of abdominal side branches, is still lacking as we saw in subsection 5.2. Given the interplay of biomechanics with mechanobiology, combining these approaches can maximize our insight of the mechanisms driving disease initiation.

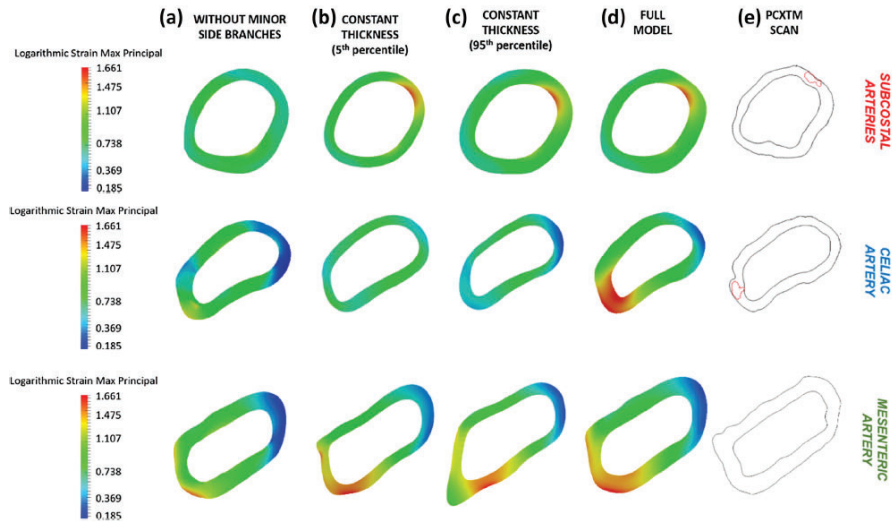


Figure 44: Sensitivity analysis: 2D slice strain max principal contour plot at the strain hotspots locations, (a) model without minor side branches; (b) 5th percentile constant thickness; (c) 95th percentile constant thickness; (d) full model; (e) PCXTM scan (contrast agent in red).

6 Aims of the thesis

Based on the knowledge gaps that exist in literature, we defined specific aims at the onset of this thesis. The first goal arose from the need to describe the hemodynamic conditions in the arterial system of the healthy mouse, the most commonly used laboratory animal today. In Chapter 1 we developed a versatile tool to predict blood pressure and flow rate waveforms in systemic and cerebral arteries of the mouse.

The next part of this thesis focused on the pathogenesis of abdominal aortic dissections in the mouse model of systemic Angiotensin II infusion. We identified the research question that emerged in the Introduction of this thesis (section 5.2):

What, if any, is the role of aortic side branches in disease initiation?

In order to answer this question, we started off from an inkling on the (previously underappreciated) importance of aortic branching sites in disease, as suggested by synchrotron images of parietal damage consistently present around the side branches in advanced-stage dissecting lesions. In Chapter 2, we set out to assess the possible implication of side branches in the early phase of the disease using dedicated synchrotron imaging of early-stage lesions.

After the important role of specific side branches, namely the celiac and superior mesenteric arteries, in disease initiation was in fact demonstrated, we focused on understanding *why* dissections are branch-related. This led to two studies, addressed from two separate standpoints. In Chapter 3, we investigated the local biomechanics around the side branches of the abdominal aorta and evaluate the association of mechanical strain with the branch-related, early microstructural damage of the aortic wall. To complement these biomechanical findings, in Chapter 4 we investigated whether regional variations in vascular function within the (diseased but not yet dissecting) suprarenal abdominal aorta and its side branches may further elucidate the branch-related nature of these lesions.

7 Summary of chapters

The chapters of this dissertation, summarized below, have been written as (parts of) manuscripts that are published or in preparation for publication.

Chapter 1

Transposition of a 1D model of the arterial circulation from humans to mice.

In this work, we developed and validated an *in silico*, one dimensional model of the murine systemic arterial tree consisting of 85 arterial segments. Detailed aortic dimensions were obtained *in vivo* from contrast-enhanced micro-computed tomography in 3 male, C57BL/6J anesthetized mice and 3 male ApoE^{-/-} mice, all 12-weeks old. Physiological input data were

gathered from a wide range of literature data. The integrated form of the Navier-Stokes equations was solved numerically to yield pressures and flows throughout the arterial network. The resulting model predictions have been validated against invasive pressure waveforms and non-invasive velocity and diameter waveforms that were measured in vivo on an independent set of 47 mice. The output of this work is a validated one-dimensional model of the anesthetized murine cardiovascular system that can serve as a versatile tool in the field of preclinical cardiovascular research.

Chapter 2

A characterization of early-stage lesion formation

Over the last years, preclinical research on aneurysms and dissections has made great use of the Angiotensin II infusion model on mice to explore the natural history of the disease. A number of intriguing questions on this mouse model remain unsolved, notably concerning the consistent localization of dissecting aneurysms in the suprarenal abdominal aorta, with attention usually directed towards the end-stage of disease development. In this work, we use synchrotron-based imaging to characterize the early stage of abdominal lesions and assess the spatial distribution of observed microstructural damage. We submit that early microstructural defects focally concentrate around the ostia of abdominal side branches, with a predilection for the celiac and superior mesenteric arteries in particular.

Chapter 3

A mechanically-mediated hypothesis for disease initiation in the Angiotensin II mouse model explored with synchrotron-based biomechanics.

In this work, we combined micro-CT and synchrotron-based imaging with computational biomechanics to estimate in vivo aortic strains in the abdominal aorta of Angiotensin II infused ApoE-deficient mice, which were compared with mouse-specific aortic microstructural damage inferred from histopathology. Targeted histology showed that the 3D distribution of micro-CT contrast agent that had been injected in vivo co-localized with precursor vascular damage in the aortic wall at 3 days of hypertension, with damage predominantly near the ostia of the celiac and superior mesenteric arteries. Computations similarly revealed higher mechanical strain in branching relative to non-branching regions, thus resulting in a positive correlation between high strain and vascular damage in branching segments that included the celiac, superior mesenteric and right renal arteries. These results suggest a mechanically-driven initiation of damage at these locations, which was supported by 3D synchrotron imaging of load-induced ex vivo delaminations of Angiotensin II infused suprarenal abdominal aortas. That is, the major intramural delamination plane in the ex vivo tested aortas was also near side branches and specifically around the celiac artery. Our findings thus support the hypothesis of an early mechanically-mediated formation of microstructural

defects at aortic branching sites that subsequently propagate into a macroscopic medial tear, giving rise to aortic dissection in Angiotensin II infused mice.

Chapter 4

A vascular function-mediated hypothesis for disease initiation in the Angiotensin II mouse model explored with wire myography.

Aortic aneurysms and dissections are clinically silent entities whose etiology is not yet fully understood. Animal models can fill important gaps of knowledge on disease pathogenesis, with a potential for clinical translation. Here, we focus on the early development of aortopathology in Angiotensin II-infused mice, which is known to develop primarily in the ascending aorta (aneurysms) and the abdominal suprarenal aorta (dissections), with a predilection for the orifice of celiac and mesenteric arteries in the latter. First, we assessed at which time point the onset of disease is manifested. We found that *in vivo* aortic volume dilatation and *ex vivo* vascular damage only become significant after 3 days of infusion, both in the ascending and the suprarenal aorta. On this time mark, we assessed the vascular reactivity of the suprarenal aorta by dividing it in 3 segments (supraceliac, paravisceral, juxtarenal). We observed that contractile capacity was severely blunted and endothelium-dependent relaxations were impaired in the aortic segment above the celiac artery, which is traditionally regarded as the most-dissection prone. The effects were less dramatic in the more distal segments; the juxtarenal segment showed no vascular dysfunction. Dysfunctional contractility was not observed for the aortic side branches tested, which included the celiac, superior mesenteric and left renal arteries. These results are the first to evaluate vascular function at the early development of disease within the suprarenal abdominal aorta of AngII infused ApoE-deficient mice. Early vascular dysfunction may conspire with previously reported biomechanical mechanisms to instigate the location-specific aortopathy of this mouse model.

Bibliography

- [1] M. Björck, M. J. Bown, E. Choke, J. Earnshaw, T. Flørenes, M. Glover, M. Kay, S. Laukontaus, T. Lees, J. Lindholt, J. T. Powell, A. van Rij, S. Svensjö, and A. Wanhainen. International update on screening for abdominal aortic aneurysms: Issues and opportunities. *European Journal of Vascular and Endovascular Surgery*, 49(2):113–115, 2015.
- [2] A. Goyal, A.R. Keramati, M.J. Czarny, J.R. Resar, and A. Mani. The genetics of aortopathies in clinical cardiology. *Clinical Medicine Insights: Cardiology*, 11, 2017. cited By 4.
- [3] J. D. Humphrey. Possible mechanical roles of glycosaminoglycans in thoracic aortic dissection and associations with dysregulated transforming growth factor-beta. *Journal of Vascular Research*, 50(1):1–10, 2013.
- [4] J.D. Humphrey. Blood vessels, mechanical and physical properties of. In K.H. Jürgen Buschow, Robert W. Cahn, Merton C. Flemings, Bernhard Ilshner, Edward J. Kramer, Subhash Mahajan, and Patrick Veyssi re, editors, *Encyclopedia of Materials: Science and Technology*, pages 748 – 751. Elsevier, Oxford, 2001.
- [5] J.D. Humphrey and G.A. Holzapfel. Mechanics, mechanobiology, and modeling of human abdominal aorta and aneurysms. *Journal of Biomechanics*, 45(5):805 – 814, 2012. Special Issue on Cardiovascular Solid Mechanics.
- [6] J.D. Humphrey and A. Baroutaji. Blood vessels, mechanical and physical properties of. In *Reference Module in Materials Science and Materials Engineering*. Elsevier, 2016.
- [7] Junyan Xu and Guo-Ping Shi. Vascular wall extracellular matrix proteins and vascular diseases. *Biochimica et Biophysica Acta (BBA) - Molecular Basis of Disease*, 1842(11):2106 – 2119, 2014.
- [8] Silvia M. Arribas, Aleksander Hinek, and M. Carmen Gonz lez. Elastic fibres and vascular structure in hypertension. *Pharmacology & Therapeutics*, 111(3):771 – 791, 2006.
- [9] J.Jeffrey Alexander. The pathobiology of aortic aneurysms. *Journal of Surgical Research*, 117(1):163 – 175, 2004.
- [10] Jaspreet K Kular, Shouvik Basu, and Ram I Sharma. The extracellular matrix: Structure, composition, age-related differences, tools for analysis and applications for tissue engineering. *Journal of Tissue Engineering*, 5:2041731414557112, 2014. PMID: 25610589.
- [11] Calum Wilson, Matthew D. Lee, and John G. McCarron. Acetylcholine released by endothelial cells facilitates flow-mediated dilatation. *The Journal of Physiology*, 594(24):7267–7307, 2016.
- [12] Robert F. Furchgott and John V. Zawadzki. The obligatory role of endothelial cells in the relaxation of arterial smooth muscle by acetylcholine. *Nature*, 288(5789):373–376, 1980.
- [13] Joerg Herrmann and Amir Lerman. The endothelium – the cardiovascular health barometer. *Herz Kardiovaskul re Erkrankungen*, 33(5):343–353, Jul 2008.
- [14] Lewis J. Kleinsmith Jeff Hardin, Gregory Paul Bertoni. *Becker’s world of the cell*. Pearson, 8 edition, 2012. Rev. ed. of: World of the cell / Wayne M. Becker ... [et al.]. 7th ed.;Includes bibliographical references and index.

Bibliography

- [15] JM Ruddy, JA Jones, FG Spinale, and JS Ikonomidis. Regional heterogeneity within the aorta: relevance to aneurysm disease. *J Thorac Cardiovasc Surg*, 136(5):1123 – 1130, 2008.
- [16] Jean Marie Ruddy, Jeffery A Jones, and John S Ikonomidis. Pathophysiology of thoracic aortic aneurysm (taa): is it not one uniform aorta? role of embryologic origin. *Prog Cardiovasc Dis*, 56(1):68–73, 2013.
- [17] Vera van de Pol, Kondababu Kurakula, Marco C. DeRuiter, and Marie-José Goumans. Thoracic aortic aneurysm development in patients with bicuspid aortic valve: What is the role of endothelial cells? *Frontiers in Physiology*, 8:938, 2017.
- [18] Chaohong Li and Qingbo Xu. Mechanical stress-initiated signal transduction in vascular smooth muscle cells in vitro and in vivo. *Cellular Signalling*, 19(5):881 – 891, 2007.
- [19] Matthias Chiquet, Laurent Gelman, Roman Lutz, and Silke Maier. From mechanotransduction to extracellular matrix gene expression in fibroblasts. *Biochimica et Biophysica Acta (BBA) - Molecular Cell Research*, 1793(5):911 – 920, 2009. Includes Special Section on Context-dependent signaling in development & disease.
- [20] Jessica E. Wagenseil and Robert P. Mecham. Vascular extracellular matrix and arterial mechanics. *Physiological Reviews*, 89(3):957–989, 2009. PMID: 19584318.
- [21] Nicolaas Westerhof, Nikos Stergiopulos, and Mark I. M. Noble. *Snapshots of Hemodynamics*. New York, springer s edition, 2010.
- [22] Michel E. Safar and Bernard I. Lévy. Chapter 13 - resistance vessels in hypertension. In Gregory Y.H. Lip and John E. Hall, editors, *Comprehensive Hypertension*, pages 145 – 150. Mosby, Philadelphia, 2007.
- [23] Bilge Guvenç Tuna, Erik N. T. P. Bakker, and Ed VanBavel. Smooth muscle biomechanics and plasticity: Relevance for vascular calibre and remodelling. *Basic & Clinical Pharmacology & Toxicology*, 110(1):35–41, 2012.
- [24] Y. C. (Yuan-cheng) Fung. *Biomechanics : motion, flow, stress, and growth*. New York : Springer-Verlag, 1990. "With 254 illustrations."
- [25] J. D. Humphrey. *Cardiovascular Solid Mechanics: Cells, Tissues, and Organs*, volume 55 of *Applied Mechanics Reviews*. ASME, 2002. 10.1115/1.1497492.
- [26] J.D. Humphrey, J.F. Eberth, W.W. Dye, and R.L. Gleason. Fundamental role of axial stress in compensatory adaptations by arteries. *Journal of Biomechanics*, 42(1):1 – 8, 2009.
- [27] J. D. Humphrey. Vascular adaptation and mechanical homeostasis at tissue, cellular, and sub-cellular levels. *Cell Biochemistry and Biophysics*, 50(2):53–78, 2008.
- [28] HARVEY WOLINSKY and SEYMOUR GLAGOV. A lamellar unit of aortic medial structure and function in mammals. *Circulation Research*, 20(1):99–111, 1967.
- [29] Raymond P. Vito and Stacey A. Dixon. Blood vessel constitutive models—1995–2002. *Annual Review of Biomedical Engineering*, 5(1):413–439, 2003. PMID: 12730083.
- [30] Gerhard A. Holzapfel and Ray W. Ogden. Constitutive modelling of arteries. *Proceedings of the Royal Society A: Mathematical, Physical and Engineering Sciences*, 466(2118):1551–1597, 2010.

- [31] Gerhard A. Holzapfel, Thomas C. Gasser, and Ray W. Ogden. A new constitutive framework for arterial wall mechanics and a comparative study of material models. *Journal of elasticity and the physical science of solids*, 61(1):1–48, Jul 2000.
- [32] S. Baek, R.L. Gleason, K.R. Rajagopal, and J.D. Humphrey. Theory of small on large: Potential utility in computations of fluid–solid interactions in arteries. *Computer Methods in Applied Mechanics and Engineering*, 196(31):3070 – 3078, 2007. Computational Bioengineering.
- [33] Laura Hansen, William Wan, and Rudolph L. Gleason. Microstructurally motivated constitutive modeling of mouse arteries cultured under altered axial stretch. *Journal of biomechanical engineering*, 131(10):101015–101015, 2009. 19831485[pmid] PMC3093188[pmcid].
- [34] Rudolph L. Gleason, Wendy W. Dye, Emily Wilson, and Jay D. Humphrey. Quantification of the mechanical behavior of carotid arteries from wild-type, dystrophin-deficient, and sarcoglycan-delta knockout mice. *Journal of biomechanics*, 41(15):3213–3218, 2008. 18842267[pmid] PMC2688405[pmcid] S0021-9290(08)00418-1[PII].
- [35] J. F. Eberth, A. I. Taucer, E. Wilson, and J. D. Humphrey. Mechanics of carotid arteries in a mouse model of marfan syndrome. *Annals of biomedical engineering*, 37(6):1093–1104, 2009. 19350391[pmid] PMC2753508[pmcid].
- [36] William Wan, Hiromi Yanagisawa, and Jr. Gleason, Rudolph L. Biomechanical and microstructural properties of common carotid arteries from fibulin-5 null mice. *Annals of biomedical engineering*, 38(12):3605–3617, 2010. 20614245[pmid] PMC3098006[pmcid].
- [37] K.Wayne Johnston, Robert B. Rutherford, M.David Tilson, Dhiraj M. Shah, Larry Hollier, and James C. Stanley. Suggested standards for reporting on arterial aneurysms. *Journal of Vascular Surgery*, 13(3):452 – 458, 1991.
- [38] *Robbins and Cotran pathologic basis of disease*. Elsevier/Saunders, Philadelphia, PA, 9th edition, 2015.
- [39] Jonathan Golledge, Juanita Muller, Alan Daugherty, and Paul Norman. Abdominal aortic aneurysm. *Arteriosclerosis, Thrombosis, and Vascular Biology*, 26(12):2605–2613, 2006.
- [40] D. E. Szilagyi, R. F. Smith, F. J. DeRusso, J. P. Elliott, and F. W. Sherrin. Contribution of abdominal aortic aneurysmectomy to prolongation of life. *Annals of surgery*, 164(4):678–699, 1966. 5924789[pmid] PMC1477299[pmcid].
- [41] Derek P. Nathan, Chun Xu, Alison M. Pouch, Krishnan B. Chandran, Benoit Desjardins, Joseph H. Gorman, Ron M. Fairman, Robert C. Gorman, and Benjamin M. Jackson. Increased wall stress of saccular versus fusiform aneurysms of the descending thoracic aorta. *Annals of Vascular Surgery*, 25(8):1129 – 1137, 2011.
- [42] Emelia J. Benjamin, Salim S. Virani, Clifton W. Callaway, Alanna M. Chamberlain, Alexander R. Chang, Susan Cheng, Stephanie E. Chiuve, Mary Cushman, Francesca N. Delling, Rajat Deo, Sarah D. de Ferranti, Jane F. Ferguson, Myriam Fornage, Cathleen Gillespie, Carmen R. Isasi, Monik C. Jiménez, Lori Chaffin Jordan, Suzanne E. Judd, Daniel Lackland, Judith H. Lichtman, Lynda Lisabeth, Simin Liu, Chris T. Longenecker, Pamela L. Lutsey, Jason S. Mackey, David B. Matchar, Kunihiro Matsushita, Michael E. Mussolino, Khurram Nasir, Martin O’Flaherty, Latha P. Palaniappan, Ambarish Pandey, Dilip K. Pandey, Mathew J. Reeves, Matthew D. Ritchey, Carlos J.

Bibliography

- Rodriguez, Gregory A. Roth, Wayne D. Rosamond, Uchechukwu K.A. Sampson, Gary M. Satou, Svati H. Shah, Nicole L. Spartano, David L. Tirschwell, Connie W. Tsao, Jenifer H. Voeks, Joshua Z. Willey, John T. Wilkins, Jason H.Y. Wu, Heather M. Alger, Sally S. Wong, and Paul Muntner. Heart disease and stroke statistics—2018 update: A report from the American Heart Association. *Circulation*, 137(12):e67–e492, 2018.
- [43] D. P. J. Howard, A. Banerjee, J. F. Fairhead, A. Handa, L. E. Silver, P. M. Rothwell, and the Oxford Vascular Study. Age-specific incidence, risk factors and outcome of acute abdominal aortic aneurysms in a defined population. *BJS*, 102(8):907–915, 2015.
- [44] Davide Carino, Timur P. Sarac, Bulat A. Ziganshin, and John A. Elefteriades. Abdominal aortic aneurysm: Evolving controversies and uncertainties. *Int J Angiol*, 27(02):058–080, 2018.
- [45] Timothy M. McGloughlin and Barry J. Doyle. New approaches to abdominal aortic aneurysm rupture risk assessment. *Arteriosclerosis, Thrombosis, and Vascular Biology*, 30(9):1687–1694, 2010.
- [46] Sourabh Aggarwal, Arman Qamar, Vishal Sharma, and Alka Sharma. Abdominal aortic aneurysm: A comprehensive review. *Experimental and clinical cardiology*, 16(1):11–15, 2011. 21523201[pmid] PMC3076160[pmcid].
- [47] Jean E. Starr and Vivienne Halpern. Abdominal aortic aneurysms in women. *Journal of Vascular Surgery*, 57(4, Supplement):3S – 10S, 2013. Vascular Disease in Women.
- [48] Jonathan Golledge and Paul E. Norman. Atherosclerosis and abdominal aortic aneurysm: Cause, response or common risk factors? *Arteriosclerosis, Thrombosis, and Vascular Biology*, 30(6):1075–1077, 2010.
- [49] D. Bhagavan, P. Di Achille, and J. D. Humphrey. Strongly coupled morphological features of aortic aneurysms drive intraluminal thrombus. *Scientific Reports*, 8(1):13273, 2018.
- [50] Ian M. Nordon, Robert J. Hinchliffe, Ian M. Loftus, and Matt M. Thompson. Pathophysiology and epidemiology of abdominal aortic aneurysms. *Nature Reviews Cardiology*, 8:92, 2011.
- [51] Helena Kuivaniemi, Evan J. Ryer, James R. Elmore, and Gerard Tromp. Understanding the pathogenesis of abdominal aortic aneurysms. *Expert Review of Cardiovascular Therapy*, 13(9):975–987, 2015. PMID: 26308600.
- [52] Alan Daugherty and Lisa A. Cassis. Mechanisms of abdominal aortic aneurysm formation. *Current Atherosclerosis Reports*, 4(3):222–227, May 2002.
- [53] Simon W. Rabkin. Chapter seven - the role matrix metalloproteinases in the production of aortic aneurysm. In Raouf A. Khalil, editor, *Matrix Metalloproteinases and Tissue Remodeling in Health and Disease: Cardiovascular Remodeling*, volume 147 of *Progress in Molecular Biology and Translational Science*, pages 239 – 265. Academic Press, 2017.
- [54] Vito Turk, Veronika Stoka, Olga Vasiljeva, Miha Renko, Tao Sun, Boris Turk, and Dušan Turk. Cysteine cathepsins: From structure, function and regulation to new frontiers. *Biochimica et Biophysica Acta (BBA) - Proteins and Proteomics*, 1824(1):68 – 88, 2012. Proteolysis 50 years after the discovery of lysosome.

- [55] Sabrina Amar, Lyndsay Smith, and Gregg B. Fields. Matrix metalloproteinase collagenolysis in health and disease. *Biochimica et Biophysica Acta (BBA) - Molecular Cell Research*, 1864(11, Part A):1940 – 1951, 2017. Matrix Metalloproteinases.
- [56] Matthew A. Dale, Melissa K. Ruhlman, and B. Timothy Baxter. Inflammatory cell phenotypes in aas. *Arteriosclerosis, Thrombosis, and Vascular Biology*, 35(8):1746–1755, 2015.
- [57] John Travis. On the origin of the immune system. *Science*, 324(5927):580–582, 2009.
- [58] C. Galle, L. Schandené, P. Stordeur, Y. Peignois, J. Ferreira, J.-C. Wautrecht, J.-P. Dereume, and M. Goldman. Predominance of type 1cd4+t cells in human abdominal aortic aneurysm. *Clinical & Experimental Immunology*, 142(3):519–527, 2005.
- [59] Toshihiro Tsuruda, Johji Kato, Kinta Hatakeyama, Kazushi Kojima, Mitsuhiro Yano, Yoshikazu Yano, Kunihide Nakamura, Fukumi Nakamura-Uchiyama, Yoshibumi Matsushima, Takuroh Imamura, Toshio Onitsuka, Yujiro Asada, Yukifumi Nawa, Tanenao Eto, and Kazuo Kitamura. Adventitial mast cells contribute to pathogenesis in the progression of abdominal aortic aneurysm. *Circulation Research*, 102(11):1368–1377, 2008.
- [60] Juliette Raffort, Fabien Lareyre, Marc Clément, Réda Hassen-Khodja, Giulia Chinetti, and Ziad Mallat. Monocytes and macrophages in abdominal aortic aneurysm. *Nature Reviews Cardiology*, 14:457, 2017.
- [61] Elena Galkina and Klaus Ley. Immune and inflammatory mechanisms of atherosclerosis. *Annual Review of Immunology*, 27(1):165–197, 2009. PMID: 19302038.
- [62] Joseph J. Boyle, Peter L. Weissberg, and Martin R. Bennett. Tumor necrosis factor- α ; promotes macrophage-induced vascular smooth muscle cell apoptosis by direct and autocrine mechanisms. *Arteriosclerosis, Thrombosis, and Vascular Biology*, 23(9):1553–1558, 2003.
- [63] Markus Leskinen, Yenfeng Wang, Dariusz Leszczynski, Ken A. Lindstedt, and Petri T. Kovanen. Mast cell chymase induces apoptosis of vascular smooth muscle cells. *Arteriosclerosis, Thrombosis, and Vascular Biology*, 21(4):516–522, 2001.
- [64] Frank M. Davis, Debra L. Rateri, and Alan Daugherty. Abdominal aortic aneurysm: novel mechanisms and therapies. *Current opinion in cardiology*, 30(6):566–573, 2015. 26352243[pmid] PMC4624089[pmcid].
- [65] Stefan W. Ryter, Hong Pyo Kim, Alexander Hoetzel, Jeong W. Park, Kiichi Nakahira, Xue Wang, and Augustine M. K. Choi. Mechanisms of cell death in oxidative stress. *Antioxidants & Redox Signaling*, 9(1):49–89, 2007. PMID: 17115887.
- [66] Natzi Sakalihasan, Jean-Baptiste Michel, Athanasios Katsargyris, Helena Kuivaniemi, Jean-Olivier Defraigne, Alain Nchimi, Janet T. Powell, Koichi Yoshimura, and Rebecka Hultgren. Abdominal aortic aneurysms. *Nature Reviews Disease Primers*, 4(1):34, 2018.
- [67] Theophilus I. Emeto, Joseph V. Moxon, Minnie Au, and Jonathan Golledge. Oxidative stress and abdominal aortic aneurysm: potential treatment targets. *Clinical Science*, 130(5):301–315, 2016.
- [68] Jonathan Golledge. Abdominal aortic aneurysm: update on pathogenesis and medical treatments. *Nature Reviews Cardiology*, 16(4):225–242, 2019.

Bibliography

- [69] Jonathan Golledge, Paul E. Norman, Michael P. Murphy, and Ronald L. Dalman. Challenges and opportunities in limiting abdominal aortic aneurysm growth. *Journal of Vascular Surgery*, 65(1):225 – 233, 2017.
- [70] T.M.M. Joergensen, K. Christensen, J.S. Lindholt, L.A. Larsen, A. Green, and K. Houliind. Editor's choice – high heritability of liability to abdominal aortic aneurysms: A population based twin study. *European Journal of Vascular and Endovascular Surgery*, 52(1):41 – 46, 2016.
- [71] Frank A. Lederle, Gary R. Johnson, Samuel E. Wilson, Edmund P. Chute, Fred N. Littooy, Dennis Bandyk, William C. Krupski, Gary W. Barone, Charles W. Acher, and David J. Ballard. Prevalence and Associations of Abdominal Aortic Aneurysm Detected through Screening. *Annals of Internal Medicine*, 126(6):441–449, 03 1997.
- [72] Koichi Sugimoto, Yoshiaki Shimamura, Chie Tezuka, Ken'ichi Tsubota, Hao Liu, Kenichiro Okumura, Yoshitada Masuda, and Hideaki Haneishi. Effects of arterial blood flow on walls of the abdominal aorta: distributions of wall shear stress and oscillatory shear index determined by phase-contrast magnetic resonance imaging. *Heart and Vessels*, 31(7):1168–1175, 2016.
- [73] Alain Nchimi, Jean-Paul Cheramy-Bien, T. Christian Gasser, Gauthier Namur, Pierre Gomez, Laurence Seidel, Adelin Albert, Jean-Olivier Defraigne, Nicos Labropoulos, and Natzi Sakalihasan. Multifactorial relationship between ^{18}F -fluoro-deoxy-glucose positron emission tomography signaling and biomechanical properties in unruptured aortic aneurysms. *Circulation: Cardiovascular Imaging*, 7(1):82–91, 2014.
- [74] S. Khosla, D. R. Morris, J. V. Moxon, P. J. Walker, T. C. Gasser, and J. Golledge. Meta-analysis of peak wall stress in ruptured, symptomatic and intact abdominal aortic aneurysms. *BJS*, 101(11):1350–1357, 2014.
- [75] Mark F. Fillinger, Steven P. Marra, M.L. Raghavan, and Francis E. Kennedy. Prediction of rupture risk in abdominal aortic aneurysm during observation: Wall stress versus diameter. *Journal of Vascular Surgery*, 37(4):724 – 732, 2003.
- [76] Vijay S. Ramanath, Jae K. Oh, Thoralf M. Sundt, and Kim A. Eagle. Acute aortic syndromes and thoracic aortic aneurysm. *Mayo Clinic Proceedings*, 84(5):465 – 481, 2009.
- [77] Jessica E. Wagenseil. Bio-chemo-mechanics of thoracic aortic aneurysms. *Current Opinion in Biomedical Engineering*, 5:50 – 57, 2018. Futures of Biomedical Engineering: Cardiovascular Bioengineering and Vascular Biomechanics.
- [78] Elisabeth Gillis, Lut Van Laer, and Bart L Loeys. Genetics of thoracic aortic aneurysm: at the crossroad of transforming growth factor- β signaling and vascular smooth muscle cell contractility. *Circ Res*, 113(3):327–40, 2013.
- [79] S. C. Siu and C. K. Silversides. Bicuspid aortic valve disease. *J Am Coll Cardiol*, 55(25):2789–800, 2010.
- [80] A.J. Brownstein, B.A. Ziganshin, H. Kuivaniemi, S.C. Body, A.E. Bale, and J.A. Elefteriades. Genes associated with thoracic aortic aneurysm and dissection: an update and clinical implications. *Aorta*, 5(1):11–20, 2017. cited By 24.

- [81] Dianna M. Milewicz, Dong-Chuan Guo, Van Tran-Fadulu, Andrea L. Lafont, Christina L. Papke, Sakiko Inamoto, Carrie S. Kwartler, and Hariyadarshi Pannu. Genetic basis of thoracic aortic aneurysms and dissections: Focus on smooth muscle cell contractile dysfunction. *Annual Review of Genomics and Human Genetics*, 9(1):283–302, 2008. PMID: 18544034.
- [82] Mark E. Lindsay and Harry C. Dietz. Lessons on the pathogenesis of aneurysm from heritable conditions. *Nature*, 473:308, 2011.
- [83] Tim McGloughlin. *Biomechanics and Mechanobiology of Aneurysms*. Springer-Verlag Berlin Heidelberg, 1 edition, 2011.
- [84] Ren-Ke Li and Richard D. Weisel. *Cardiac Regeneration and Repair*, volume 2: Biomaterials and tissue engineering. Woodhead Publishing, 2014.
- [85] S. A. LeMaire, X. Wang, J. A. Wilks, S. A. Carter, S. Wen, T. Won, D. Leonardelli, G. Anand, L. D. Conklin, X. L. Wang, R. W. Thompson, and J. S. Coselli. Matrix metalloproteinases in ascending aortic aneurysms: bicuspid versus trileaflet aortic valves. *J Surg Res*, 123(1):40–8, 2005. LeMaire, Scott A Wang, Xinwen Wilks, Jonathan A Carter, Stacey A Wen, Shixiang Won, Taehee Leonardelli, Dominic Anand, Gobind Conklin, Lori D Wang, Xing Li Thompson, Robert W Coselli, Joseph S Journal Article United States J Surg Res. 2005 Jan;123(1):40-8.
- [86] Francesco Ramirez and Harry C Dietz. Marfan syndrome: from molecular pathogenesis to clinical treatment. *Current Opinion in Genetics & Development*, 17(3):252 – 258, 2007. Genetics of disease.
- [87] Bart L. Loeys, Ulrike Schwarze, Tammy Holm, Bert L. Callewaert, George H. Thomas, Hariyadarshi Pannu, Julie F. De Backer, Gretchen L. Oswald, Sofie Symoens, Sylvie Manouvrier, Amy E. Roberts, Francesca Faravelli, M. Alba Greco, Reed E. Pyeritz, Dianna M. Milewicz, Paul J. Coucke, Duke E. Cameron, Alan C. Braverman, Peter H. Byers, Anne M. De Paepe, and Harry C. Dietz. Aneurysm syndromes caused by mutations in the $\text{tgf-}\beta$ receptor. *New England Journal of Medicine*, 355(8):788–798, 2006. PMID: 16928994.
- [88] Jay D. Humphrey, Martin A. Schwartz, George Tellides, and Dianna M. Milewicz. Role of mechanotransduction in vascular biology, focus on thoracic aortic aneurysms and dissections. *Circulation Research*, 116(8):1448–1461, 2015.
- [89] Gonzalo Albornoz, Michael A. Coady, Michele Roberts, Ryan R. Davies, Maryann Tranquilli, John A. Rizzo, and John A. Elefteriades. Familial thoracic aortic aneurysms and dissections—incidence, modes of inheritance, and phenotypic patterns. *The Annals of Thoracic Surgery*, 82(4):1400 – 1405, 2006.
- [90] Dong-Chuan Guo, Hariyadarshi Pannu, Van Tran-Fadulu, Christina L. Papke, Robert K. Yu, Nili Avidan, Scott Bourgeois, Anthony L. Estrera, Hazim J. Safi, Elizabeth Sparks, David Amor, Lesley Ades, Vivienne McConnell, Colin E. Willoughby, Dianne Abuelo, Marcia Willing, Richard A. Lewis, Dong H. Kim, Steve Scherer, Poyee P. Tung, Chul Ahn, L. Maximilian Buja, C. S. Raman, Sanjay S. Shete, and Dianna M. Milewicz. Mutations in smooth muscle α -actin (acta2) lead to thoracic aortic aneurysms and dissections. *Nature Genetics*, 39:1488, 2007.
- [91] Dianna M. Milewicz, Kathleen M. Trybus, Dong chuan Guo, H. Lee Sweeney, Ellen Regalado, Kristine Kamm, and James T. Stull. Altered smooth muscle cell force generation as a driver of thoracic aortic aneurysms and dissections. *Arteriosclerosis, Thrombosis, and Vascular Biology*, 37(1):26–34, 2017.

Bibliography

- [92] Amélie Pinard, Gregory T. Jones, and Dianna M. Milewicz. Genetics of thoracic and abdominal aortic diseases. *Circulation Research*, 124(4):588–606, 2019.
- [93] Jay D. Humphrey, Dianna M. Milewicz, George Tellides, and Martin A. Schwartz. Dysfunctional mechanosensing in aneurysms. *Science*, 344(6183):477–479, 2014.
- [94] ISIDRE VILACOSTA and JOSÉ ALBERTO SAN ROMÁN. Acute aortic syndrome. *Heart*, 85(4):365–368, 2001.
- [95] W. Darrin Clouse, John W. Hallett, Hartzell V. Schaff, Peter C. Spittell, Charles M. Rowland, Duane M. Ilstrup, and L. Joseph Melton. Acute aortic dissection: Population-based incidence compared with degenerative aortic aneurysm rupture. *Mayo Clinic Proceedings*, 79(2):176 – 180, 2004.
- [96] Christoph A. Nienaber, Rachel E. Clough, Natzi Sakalihasan, Toru Suzuki, Richard Gibbs, Firas Mussa, Michael P. Jenkins, Matt M. Thompson, Arturo Evangelista, James S. M. Yeh, Nicholas Cheshire, Ulrich Rosendahl, and John Pepper. Aortic dissection. *Nature Reviews Disease Primers*, 2:16053, 2016.
- [97] Christoph A. Nienaber and Janet T. Powell. Management of acute aortic syndromes. *European Heart Journal*, 33(1):26–35, 08 2011.
- [98] Maya J Salameh and Elizabeth V Ratchford. Aortic dissection. *Vascular Medicine*, 21(3):276–280, 2016. PMID: 26989169.
- [99] Christoph A. Nienaber, Rachel E. Clough, Natzi Sakalihasan, Toru Suzuki, Richard Gibbs, Firas Mussa, Michael P. Jenkins, Matt M. Thompson, Arturo Evangelista, James S. M. Yeh, Nicholas Cheshire, Ulrich Rosendahl, and John Pepper. Aortic dissection. *Nature Reviews Disease Primers*, 2:16053, 2016.
- [100] G. Marinov, R. Guidoin, L. W. Tse, A. A. Ruthrauff, T. Yao, and M. W. King. *21 - Endovascular prostheses for aortic aneurysms: a new era for vascular surgery*, pages 640–675. Woodhead Publishing, 2013.
- [101] P. M. Treuting, S. M. Dintzis, and K. S. Montine. *Introduction. In Comparative Anatomy and Histology - A Mouse and Human Atlas, (1–6)*. Elsevier Inc, London, 2012.
- [102] Craig J. Goergen, Kyla N. Barr, Diem T. Huynh, Jeffrey R. Eastham-Anderson, Gilwoo Choi, Maj Hedehus, Ronald L. Dalman, Andrew J. Connolly, Charles A. Taylor, Philip S. Tsao, and Joan M. Greve. In vivo quantification of murine aortic cyclic strain, motion, and curvature: Implications for abdominal aortic aneurysm growth. *Journal of Magnetic Resonance Imaging*, 32(4):847–858, 2010.
- [103] K. Namdee, M. Carrasco-Teja, M. B. Fish, P. Charoenphol, and O. Eniola-Adefeso. Effect of variation in hemorheology between human and animal blood on the binding efficacy of vascular-targeted carriers. *Scientific Reports*, 5:11631, 2015.
- [104] Fabian Kiessling and Pichler Bernd. *Small Animal Imaging: Basics and Practical Guide*. Springer, Berlin, Heidelberg, 2011.
- [105] Douglass H. Howry and William Bliss. Ultrasonic visualization of soft tissue structures of the body. *The Journal of laboratory and clinical medicine*, 40 4:579–92, 1952.

- [106] C.T. Badea and D. Panetta. 2.09 - high-resolution ct for small-animal imaging research. In Anders Brahme, editor, *Comprehensive Biomedical Physics*, pages 221 – 242. Elsevier, Oxford, 2014.
- [107] Joel D. Boerckel, Devon E. Mason, Anna M. McDermott, and Eben Alsberg. Microcomputed tomography: approaches and applications in bioengineering. *Stem Cell Research & Therapy*, 5(6):144, Dec 2014.
- [108] Darin P. Clark and Cristian T. Badea. Micro-ct of rodents: state-of-the-art and future perspectives. *Physica medica : PM : an international journal devoted to the applications of physics to medicine and biology : official journal of the Italian Association of Biomedical Physics*, 30 6:619–34, 2014.
- [109] Jeffrey R. Ashton, Jennifer L. West, and Cristian T. Badea. In vivo small animal micro-ct using nanoparticle contrast agents. *Frontiers in pharmacology*, 6:256–256, 2015. 26581654[pmid] PMC4631946[pmcid].
- [110] Xiang Li, Nicolas Anton, Guy Zuber, and Thierry Vandamme. Contrast agents for preclinical targeted x-ray imaging. *Advanced Drug Delivery Reviews*, 76:116 – 133, 2014. Targeted imaging.
- [111] Laura Nebuloni, Gisela A. Kuhn, and Ralph Müller. A comparative analysis of water-soluble and blood-pool contrast agents for in vivo vascular imaging with micro-ct. *Academic Radiology*, 20(10):1247–1255, 2013.
- [112] David P. Cormode, Pratap C. Naha, and Zahi A. Fayad. Nanoparticle contrast agents for computed tomography: a focus on micelles. *Contrast Media & Molecular Imaging*, 9(1):37–52, 2014.
- [113] C T Badea, M Drangova, D W Holdsworth, and G A Johnson. In vivosmall-animal imaging using micro-CT and digital subtraction angiography. *Physics in Medicine and Biology*, 53(19):R319–R350, aug 2008.
- [114] Liberato De Caro, Cinzia Giannini, Roberto Bellotti, and Sabina Tangaro. A theoretical study on phase-contrast mammography with thomson-scattering x-ray sources. *Medical Physics*, 36(10):4644–4653, 2009.
- [115] T.E. Clark, M.A. Lillie, A.W. Vogl, J.M. Gosline, and R.E. Shadwick. Mechanical contribution of lamellar and interlamellar elastin along the mouse aorta. *Journal of Biomechanics*, 48(13):3599 – 3605, 2015.
- [116] Darren Haskett, Jefferson J. Doyle, Connie Gard, Hwudaurw Chen, Corbie Ball, Mark A. Estabrook, Alejandra C. Encinas, Harry C. Dietz, Urs Utzinger, Jonathan P. Vande Geest, and Mohamad Azhar. Altered tissue behavior of a non-aneurysmal descending thoracic aorta in the mouse model of marfan syndrome. *Cell and Tissue Research*, 347(1):267–277, Jan 2012.
- [117] Xunjie Yu, Raphaël Turcotte, Francesca Seta, and Yanhang Zhang. Micromechanics of elastic lamellae: unravelling the role of structural inhomogeneity in multi-scale arterial mechanics. *Journal of The Royal Society Interface*, 15(147):20180492, 2018.
- [118] N. Yagi. 8.02 - synchrotron radiation. In Anders Brahme, editor, *Comprehensive Biomedical Physics*, pages 17 – 33. Elsevier, Oxford, 2014.
- [119] D. Iwanenko and I. Pomeranchuk. On the maximal energy attainable in a betatron. *Phys. Rev.*, 65:343–343, Jun 1944.

Bibliography

- [120] F. R. Elder, A. M. Gurewitsch, R. V. Langmuir, and H. C. Pollock. Radiation from electrons in a synchrotron. *Phys. Rev.*, 71:829–830, Jun 1947.
- [121] A. Isenegger G. Mikuljan Q. Chen A. Bertrand S. Henein R. Betemps U. Frommherz P. Böhler D. Meister M. Lange R. Abela M. Stampanoni, A. Groso. Trends in synchrotron-based tomographic imaging: the sls experience. 6318, 2006.
- [122] Kevin Mader, Federica Marone, Christoph Hintermüller, Gordan Mikuljan, Andreas Isenegger, and Marco Stampanoni. High-throughput full-automatic synchrotron-based tomographic microscopy. *Journal of Synchrotron Radiation*, 18(2):117–124, Mar 2011.
- [123] Bram Trachet, Goran Lovric, Pablo Villanueva-Perez, Lydia Aslanidou, Mauro Ferraro, Gerlinde Logghe, Nikolaos Stergiopulos, and Patrick Segers. Synchrotron-based phase contrast imaging of cardiovascular tissue in mice—grating interferometry or phase propagation? *Biomedical Physics & Engineering Express*, 5(1):015010, nov 2018.
- [124] D. Paganin, S. C. Mayo, T. E. Gureyev, P. R. Miller, and S. W. Wilkins. Simultaneous phase and amplitude extraction from a single defocused image of a homogeneous object. *Journal of Microscopy*, 206(1):33–40.
- [125] Timur Gureyev, Sara Mohammadi, Yakov Nesterets, Christian Dullin, and Giuliana Tromba. Accuracy and precision of reconstruction of complex refractive index in near-field single-distance propagation-based phase-contrast tomography. *Journal of Applied Physics*, 114(14):144906, 2013.
- [126] Gerlinde Logghe, Bram Trachet, Lydia Aslanidou, Pablo Villanueva-Perez, Julie De Backer, Nikolaos Stergiopulos, Marco Stampanoni, Hiroki Aoki, and Patrick Segers. Propagation-based phase-contrast synchrotron imaging of aortic dissection in mice: from individual elastic lamella to 3d analysis. *Scientific Reports*, 8(1):2223, 2018.
- [127] Fabien Lareyre, Marc Clément, Juliette Raffort, Stefanie Pohlod, Meghana Patel, Bruno Esposito, Leanne Master, Alison Finigan, Marie Vandestienne, Nikolaos Stergiopulos, Soraya Taleb, Bram Trachet, and Ziad Mallat. Tgf β 2; (transforming growth factor- β 2;) blockade induces a human-like disease in a nondissecting mouse model of abdominal aortic aneurysm. *Arteriosclerosis, Thrombosis, and Vascular Biology*, 37(11):2171–2181, 2017.
- [128] Bram Trachet, Mauro Ferraro, Goran Lovric, Lydia Aslanidou, Gerlinde Logghe, Patrick Segers, and Nikolaos Stergiopulos. Synchrotron-based visualization and segmentation of elastic lamellae in the mouse carotid artery during quasi-static pressure inflation. *Journal of The Royal Society Interface*, 16(155):20190179, 2019.
- [129] Andrea Acuna, Alycia G. Berman, Frederick W. Damen, Brett A. Meyers, Amelia R. Adelsperger, Kelsey C. Bayer, Melissa C. Brindise, Brittani Bungart, Alexander M. Kiel, Rachel A. Morrison, Joseph C. Muskat, Kelsey M. Wasilczuk, Yi Wen, Jiacheng Zhang, Patrick Zito, and Craig J. Goergen. Computational fluid dynamics of vascular disease in animal models. *Journal of Biomechanical Engineering*, 140(8):080801–080801–14, 2018. 10.1115/1.4039678.
- [130] Tianwu Xie and Habib Zaidi. Development of computational small animal models and their applications in preclinical imaging and therapy research. *Medical Physics*, 43(1):111–131, 2016.
- [131] Yubing Shi, Patricia Lawford, and Rodney Hose. Review of zero-d and 1-d models of blood flow in the cardiovascular system. *BioMedical Engineering OnLine*, 10(1):33, Apr 2011.

- [132] Nikos Stergiopoulos, D. F. Young, and T. R. Rogge. Computer simulation of arterial flow with application to arterial and aortic stenoses. *Journal of biomechanics*, 25(12):1477–1488, 1992.
- [133] Philippe Reymond, Fabrice Merenda, Fabienne Perren, Daniel Rüfenacht, and Nikos Stergiopoulos. Validation of a one-dimensional model of the systemic arterial tree. *American journal of physiology. Heart and circulatory physiology*, 297(1):H208–H222, 2009.
- [134] J. P. Mynard and J. J. Smolich. One-dimensional haemodynamic modeling and wave dynamics in the entire adult circulation. *Annals of Biomedical Engineering*, 43(6):1443–60, 2015.
- [135] Nicolaas Westerhof, Frederik Bosman, Cornelis J. De Vries, and Abraham Noordergraaf. Analog studies of the human systemic arterial tree. *Journal of Biomechanics*, 2(2):121 – 143, 1969.
- [136] Natalija Bogunovic, Jorn P. Meekel, Dimitra Micha, Jan D. Blankensteijn, Peter L. Hordijk, and Kak K. Yeung. Impaired smooth muscle cell contractility as a novel concept of abdominal aortic aneurysm pathophysiology. *Scientific Reports*, 9(1):6837, 2019.
- [137] Il Murtada, Sae, Jay D. Humphrey, and Gerhard A. Holzapfel. Multiscale and multiaxial mechanics of vascular smooth muscle. *Biophysical Journal*, 113(3):714–727, 2017.
- [138] Alexander W. Caulk, Jay D. Humphrey, and Sae-Il Murtada. Fundamental roles of axial stretch in isometric and isobaric evaluations of vascular contractility. *Journal of Biomechanical Engineering*, 141(3):031008–031008–10, 2019. 10.1115/1.4042171.
- [139] Denmark Danish Myo Technology A/S, Aarhus. www.dmt.dk.
- [140] Steven K. Burke, Karen Bingham, Emma Moss, Daniel P. Gottlieb, Marco D. Wong, Kimberly S. Bland, and F. Nicholas Franano. Recombinant human elastase alters the compliance of atherosclerotic tibial arteries after ex vivo angioplasty. *Journal of cardiovascular pharmacology*, 67(4):305–311, 2016. 26745001[pmid] PMC4827324[pmcid].
- [141] M J Mulvany and W Halpern. Contractile properties of small arterial resistance vessels in spontaneously hypertensive and normotensive rats. *Circulation Research*, 41(1):19–26, 1977.
- [142] Lara del Campo and Mercedes Ferrer. *Wire Myography to Study Vascular Tone and Vascular Structure of Isolated Mouse Arteries*, pages 255–276. Springer New York, New York, NY, 2015.
- [143] Alan Daugherty and Lisa A. Cassis. Mouse models of abdominal aortic aneurysms. *Arteriosclerosis, Thrombosis, and Vascular Biology*, 24(3):429–434, 2004.
- [144] Jean Sénémaud, Giuseppina Caligiuri, Harry Etienne, Sandrine Delbosc, Jean-Baptiste Michel, and Raphaël Coscas. Translational relevance and recent advances of animal models of abdominal aortic aneurysm. *Arteriosclerosis, Thrombosis, and Vascular Biology*, 37(3):401–410, 2017.
- [145] A. Daugherty and L. A. Cassis. Mouse models of abdominal aortic aneurysms. *Arterioscler Thromb Vasc Biol*, 24(3):429–34, 2004.
- [146] Alexandra Trollope, Joseph V. Moxon, Corey S. Moran, and Jonathan Golledge. Animal models of abdominal aortic aneurysm and their role in furthering management of human disease. *Cardiovascular Pathology*, 20(2):114 – 123, 2011.
- [147] Frank M Davis, Debra L Rateri, and Alan Daugherty. Mechanisms of aortic aneurysm formation: translating preclinical studies into clinical therapies. *Heart*, 100(19):1498–1505, 2014.

Bibliography

- [148] J. Lysgaard Poulsen, J. Stubbe, and J.S. Lindholt. Animal models used to explore abdominal aortic aneurysms: A systematic review. *European Journal of Vascular and Endovascular Surgery*, 52(4):487 – 499, 2016.
- [149] Colleen M. Brophy, Joan E. Tilson, Irwin M. Braverman, and M. David Tilson. Age of onset, pattern of distribution, and histology of aneurysm development in a genetically predisposed mouse model. *Journal of Vascular Surgery*, 8(1):45–48, 1988.
- [150] Jeffrey M. Reilly, Edward B. Savage, Colleen M. Brophy, and M. David Tilson. Hydrocortisone Rapidly Induces Aortic Rupture in a Genetically Susceptible Mouse. *JAMA Surgery*, 125(6):707–709, 06 1990.
- [151] Harry C. Dietz, Garry R. Cutting, Reed E. Pyeritz, Cheryl Maslen, Lynn Sakai, Glen M. Corson, Erik G. Puffenberger, Ada Hamosh, Elizabeth J. Nanthakumar, Sheila M. Curristin, Gail Stetten, Deborah A. Meyers, and Clair A. Francomano. Marfan syndrome caused by a recurrent de novo missense mutation in the fibrillin gene. *Nature*, 352(6333):337–339, 7 1991.
- [152] Andrew S. Plump, Jonathan D. Smith, Tony Hayek, Katriina Aalto-Setälä, Annemarie Walsh, Judy G. Verstuyft, Edward M. Rubin, and Jan L. Breslow. Severe hypercholesterolemia and atherosclerosis in apolipoprotein e-deficient mice created by homologous recombination in es cells. *Cell*, 71(2):343–353, 1992.
- [153] SH Zhang, RL Reddick, JA Piedrahita, and N Maeda. Spontaneous hypercholesterolemia and arterial lesions in mice lacking apolipoprotein e. *Science*, 258(5081):468–471, 1992.
- [154] A Fukamizu, K Sugimura, E Takimoto, F Sugiyama, M S Seo, S Takahashi, T Hatae, N Kajiwar, K Yagami, and K Murakami. Chimeric renin-angiotensin system demonstrates sustained increase in blood pressure of transgenic mice carrying both human renin and human angiotensinogen genes. *Journal of Biological Chemistry*, 268(16):11617–11621, 1993.
- [155] S Ishibashi, J L Goldstein, M S Brown, J Herz, and D K Burns. Massive xanthomatosis and atherosclerosis in cholesterol-fed low density lipoprotein receptor-negative mice. *The Journal of Clinical Investigation*, 93(5):1885–1893, 5 1994.
- [156] Peter J. Kuhlencordt, Robert Gyurko, Fred Han, Marielle Scherrer-Crosbie, Thomas H. Aretz, Roger Hajjar, Michael H. Picard, and Paul L. Huang. Accelerated atherosclerosis, aortic aneurysm formation, and ischemic heart disease in apolipoprotein e/endothelial nitric oxide synthase double-knockout mice. *Circulation*, 104(4):448–454, 2001.
- [157] J. Silence, D. Collen, and H.R. Lijnen. Reduced atherosclerotic plaque but enhanced aneurysm formation in mice with inactivation of the tissue inhibitor of metalloproteinase-1 (<i>timp-1</i>) gene. *Circulation Research*, 90(8):897–903, 2002.
- [158] Kati Takaluoma, Marjo Hyry, Juha Lantto, Raija Sormunen, Ruud A. Bank, Kari I. Kivirikko, Johanna Myllyharju, and Raija Soininen. Tissue-specific changes in the hydroxylysine content and cross-links of collagens and alterations in fibril morphology in lysyl hydroxylase 1 knock-out mice. *Journal of Biological Chemistry*, 282(9):6588–6596, 2007.
- [159] Marion Hofmann Bowman, Jeannine Wilk, Ahlke Heydemann, Gene Kim, Jalees Rehman, Joseph A. Lodato, Jai Raman, and Elizabeth M. McNally. S100a12 mediates aortic wall remodeling and aortic aneurysm. *Circulation Research*, 106(1):145–154, 2010.

- [160] S Anidjar, J L Salzmman, D Gentric, P Lagneau, J P Camilleri, and J B Michel. Elastase-induced experimental aneurysms in rats. *Circulation*, 82(3):973–981, 1990.
- [161] Robert Pyo, Jason K. Lee, J. Michael Shipley, John A. Curci, Dongli Mao, Scott J. Ziporin, Terri L. Ennis, Steven D. Shapiro, Robert M. Senior, and Robert W. Thompson. Targeted gene disruption of matrix metalloproteinase-9 (gelatinase b) suppresses development of experimental abdominal aortic aneurysms. *The Journal of Clinical Investigation*, 105(11):1641–1649, 6 2000.
- [162] S D Gertz, A Kurgan, and D Eisenberg. Aneurysm of the rabbit common carotid artery induced by periarterial application of calcium chloride in vivo. *The Journal of Clinical Investigation*, 81(3):649–656, 3 1988.
- [163] Andy C. Chiou, Bill Chiu, and William H. Pearce. Murine aortic aneurysm produced by periarterial application of calcium chloride. *Journal of Surgical Research*, 99(2):371–376, 2001.
- [164] Alan Daugherty, Michael W. Manning, and Lisa A Cassis. Angiotensin ii promotes atherosclerotic lesions and aneurysms in apolipoprotein e–deficient mice. *The Journal of Clinical Investigation*, 105(11):1605–1612, 2000.
- [165] Alan Daugherty, Debra L. Rateri, Israel F. Charo, A. Phillip Owens, Deborah A. Howatt, and Lisa A. Cassis. Angiotensin ii infusion promotes ascending aortic aneurysms: attenuation by ccr2 deficiency in apoe^{-/-} mice. *Clinical Science*, 118(11):681–689, 2010.
- [166] Gary G. Deng, Baby Martin-McNulty, Drew A. Sukovich, Ana Freay, Meredith Halks-Miller, Therese Thinnies, David J. Loskutoff, Peter Carmeliet, William P. Dole, and Yi-Xin Wang. Urokinase-type plasminogen activator plays a critical role in angiotensin ii-induced abdominal aortic aneurysm. *Circulation Research*, 92(5):510–517, 2003.
- [167] Yu Wang, Hafid Ait-Oufella, Olivier Herbin, Philippe Bonnin, Bhama Ramkhalawon, Soraya Taleb, Jin Huang, Georges Offenstadt, Christophe Combadière, Laurent Rénia, Jason L. Johnson, Pierre-Louis Tharaux, Alain Tedgui, and Ziad Mallat. Tgf- β activity protects against inflammatory aortic aneurysm progression and complications in angiotensin ii–infused mice. *The Journal of Clinical Investigation*, 120(2):422–432, 2 2010.
- [168] M. J. Collins, M. Bersi, E. Wilson, and J. D. Humphrey. Mechanical properties of suprarenal and infrarenal abdominal aorta: implications for mouse models of aneurysms. *Medical engineering & physics*, 33(10):1262–1269, 2011. 21742539[pmid] PMC3235688[pmcid] S1350-4533(11)00131-7[PII].
- [169] Irene Cuadrado, Jesus Egido, JL Zamorano, and Carlos Zaragoza. *Preclinical Models*. 2016.
- [170] A. J. Schriebl, M. J. Collins, D. M. Pierce, G. A. Holzapfel, L. E. Niklason, and J. D. Humphrey. Remodeling of intramural thrombus and collagen in an ang-ii infusion apoe^{-/-} model of dissecting aortic aneurysms. *Thrombosis Research*, 130(3):e139–e146, 2012.
- [171] Debra L. Rateri, Jessica J. Moorleggen, Anju Balakrishnan, A. Phillip Owens, Deborah A. Howatt, Venkateswaran Subramanian, Aruna Poduri, Richard Charnigo, Lisa A. Cassis, and Alan Daugherty. Endothelial cell-specific deficiency of ang ii type 1a receptors attenuates ang ii-induced ascending aortic aneurysms in ldl receptor^{-/-} mice. *Circulation Research*, 108(5):574–581, 2011.

Bibliography

- [172] Yan Sun, Suli Zhang, Mingming Yue, Yang Li, Jing Bi, and Huirong Liu. Angiotensin ii inhibits apoptosis of mouse aortic smooth muscle cells through regulating the circnrg-1/mir-193b-5p/nrg-1 axis. *Cell Death & Disease*, 10(5):362, 2019.
- [173] Steven J. Forrester, George W. Booz, Curt D. Sigmund, Thomas M. Coffman, Tatsuo Kawai, Victor Rizzo, Rosario Scalia, and Satoru Eguchi. Angiotensin ii signal transduction: An update on mechanisms of physiology and pathophysiology. *Physiological Reviews*, 98(3):1627–1738, 2018.
- [174] Lilach O. Lerman, Theodore W. Kurtz, Rhian M. Touyz, David H. Ellison, Alejandro R. Chade, Steven D. Crowley, David L. Mattson, John J. Mullins, Jeffrey Osborn, Alfonso Eirin, Jane F. Reckelhoff, Costantino Iadecola, Thomas M. Coffman, and null null. Animal models of hypertension: A scientific statement from the american heart association. *Hypertension*, 73(6):e87–e120, 2019.
- [175] Godfrey S. Getz and Catherine A. Reardon. *Use of Mouse Models in Atherosclerosis Research*, pages 1–16. Springer New York, New York, NY, 2015.
- [176] Minako Ishibashi, Kensuke Egashira, Qingwei Zhao, Ken ichi Hiasa, Kisho Ohtani, Yoshiko Ihara, Israel F. Charo, Shinobu Kura, Teruhisa Tsuzuki, Akira Takeshita, and Kenji Sunagawa. Bone marrow-derived monocyte chemoattractant protein-1 receptor ccr2 is critical in angiotensin ii-induced acceleration of atherosclerosis and aneurysm formation in hypercholesterolemic mice. *Arteriosclerosis, Thrombosis, and Vascular Biology*, 24(11):e174–e178, 2004.
- [177] Yutaka Nakashima, Andrew S Plump, Elaine W Raines, Jan L Breslow, and Russell Ross. Apoe-deficient mice develop lesions of all phases of atherosclerosis throughout the arterial tree. *Arteriosclerosis and thrombosis: a journal of vascular biology*, 14(1):133–140, 1994.
- [178] ALAN DAUGHERTY and LISA CASSIS. Chronic angiotensin ii infusion promotes atherogenesis in low density lipoprotein receptor -/- mice. *Annals of the New York Academy of Sciences*, 892(1):108–118, 1999.
- [179] Daiana Weiss, John J. Kools, and W. Robert Taylor. Angiotensin ii-induced hypertension accelerates the development of atherosclerosis in apoe-deficient mice. *Circulation*, 103(3):448–454, 2001.
- [180] Bram Trachet, Rodrigo A. Fraga-Silva, Philippe A. Jacquet, Nikolaos Stergiopoulos, and Patrick Segers. Incidence, severity, mortality, and confounding factors for dissecting AAA detection in angiotensin II-infused mice: a meta-analysis. *Cardiovascular Research*, 108(1):159–170, 08 2015.
- [181] Hong Lu, Deborah A. Howatt, Anju Balakrishnan, Jessica J. Moorlegghen, Debra L. Rateri, Lisa A. Cassis, and Alan Daugherty. Subcutaneous angiotensin ii infusion using osmotic pumps induces aortic aneurysms in mice. *JoVE*, (103):e53191, 2015.
- [182] Debra L. Rateri, Frank M. Davis, Anju Balakrishnan, Deborah A. Howatt, Jessica J. Moorlegghen, William N. O'Connor, Richard Charnigo, Lisa A. Cassis, and Alan Daugherty. Angiotensin ii induces region-specific medial disruption during evolution of ascending aortic aneurysms. *The American Journal of Pathology*, 184(9):2586–2595, 2014.
- [183] Bram Trachet, Alessandra Piersigilli, Rodrigo A. Fraga-Silva, Lydia Aslanidou, Jessica Sordet-Dessimoz, Alberto Astolfo, Marco F.M. Stampanoni, Patrick Segers, and Nikolaos Stergiopoulos. Ascending aortic aneurysm in angiotensin ii-infused mice. formation, progression, and the role of focal dissections. *Arteriosclerosis, Thrombosis, and Vascular Biology*, 36(4):673–681, 2016.

- [184] Sara B. Police, Sean E. Thatcher, Richard Charnigo, Alan Daugherty, and Lisa A. Cassis. Obesity promotes inflammation in periaortic adipose tissue and angiotensin ii-induced abdominal aortic aneurysm formation. *Arteriosclerosis, Thrombosis, and Vascular Biology*, 29(10):1458–1464, 2009.
- [185] Sara B. Police, Kelly Putnam, Sean Thatcher, Frederique Batifoulier-Yiannikouris, Alan Daugherty, and Lisa A. Cassis. Weight loss in obese c57bl/6 mice limits adventitial expansion of established angiotensin ii-induced abdominal aortic aneurysms. *American Journal of Physiology-Heart and Circulatory Physiology*, 298(6):H1932–H1938, 2010. PMID: 20304811.
- [186] Kiran Saraff, Fjoralba Babamusta, Lisa A. Cassis, and Alan Daugherty. Aortic dissection precedes formation of aneurysms and atherosclerosis in angiotensin ii-infused, apolipoprotein e-deficient mice. *Arteriosclerosis, Thrombosis, and Vascular Biology*, 23(9):1621–1626, 2003.
- [187] A. Phillip Owens, Venkateswaran Subramanian, Jessica J. Moorleggen, Zhenheng Guo, Coleen A. McNamara, Lisa A. Cassis, and Alan Daugherty. Angiotensin ii induces a region-specific hyperplasia of the ascending aorta through regulation of inhibitor of differentiation 3. *Circulation Research*, 106(3):611–619, 2010.
- [188] M. R. Bersi, R. Khosravi, A. J. Wujciak, D. G. Harrison, and J. D. Humphrey. Differential cell-matrix mechanoadaptations and inflammation drive regional propensities to aortic fibrosis, aneurysm or dissection in hypertension. *Journal of The Royal Society Interface*, 14(136):20170327, 2017.
- [189] Yi-Xin Wang, Baby Martin-McNulty, Ana D. Freay, Drew A. Sukovich, Meredith Halks-Miller, Wei-Wei Li, Ronald Vergona, Mark E. Sullivan, John Morser, William P. Dole, and Gary G. Deng. Angiotensin ii increases urokinase-type plasminogen activator expression and induces aneurysm in the abdominal aorta of apolipoprotein e-deficient mice. *The American Journal of Pathology*, 159(4):1455–1464, 2001.
- [190] A Daugherty, MW Manning, and LA Cassis. Antagonism of at2 receptors augments angiotensin ii-induced abdominal aortic aneurysms and atherosclerosis. *British journal of pharmacology*, 134(4):865–870, October 2001.
- [191] Yasuhisa Kanematsu, Miyuki Kanematsu, Chie Kurihara, Tsung-Ling Tsou, Yoshitsugu Nuki, Elena I. Liang, Hiroshi Makino, and Tomoki Hashimoto. Pharmacologically induced thoracic and abdominal aortic aneurysms in mice. *Hypertension*, 55(5):1267–1274, 2010.
- [192] Craig J. Goergen, Junya Azuma, Kyla N. Barr, Lars Magdefessel, Dara Y. Kallop, Alvin Gogineni, Amarjeet Grewall, Robby M. Weimer, Andrew J. Connolly, Ronald L. Dalman, Charles A. Taylor, Philip S. Tsao, and Joan M. Greve. Influences of aortic motion and curvature on vessel expansion in murine experimental aneurysms. *Arteriosclerosis, thrombosis, and vascular biology*, 31(2):270–279, 2011. 21071686[pmid] *Arterioscler Thromb Vasc Biol*.
- [193] Bram Trachet, Marjolijn Renard, Gianluca De Santis, Steven Staelens, Julie De Backer, Luca Antiga, Bart Loeys, and Patrick Segers. An integrated framework to quantitatively link mouse-specific hemodynamics to aneurysm formation in angiotensin ii-infused apoe -/- mice. *Annals of Biomedical Engineering*, 39(9):2430, 2011.
- [194] Lilach Gavish, Chen Rubinstein, Yacov Berlatzky, Leah Y. Gavish, Ronen Beeri, Dan Gilon, Atila Bulut, Mickey Harlev, Petachia Reissman, and S. David Gertz. Low level laser arrests abdominal aortic aneurysm by collagen matrix reinforcement in apolipoprotein e-deficient mice. *Lasers in Surgery and Medicine*, 44(8):664–674, 2012.

Bibliography

- [195] John T. Favreau, Binh T. Nguyen, Ian Gao, Peng Yu, Ming Tao, Jacob Schneiderman, Glenn R. Gaudette, and C. Keith Ozaki. Murine ultrasound imaging for circumferential strain analyses in the angiotensin ii abdominal aortic aneurysm model. *Journal of Vascular Surgery*, 56(2):462–469, 2012.
- [196] Bram Trachet, Rodrigo A. Fraga-Silva, Alessandra Piersigilli, Alain Tedgui, Jessica Sordet-Dessimoz, Alberto Astolfo, Carole Van der Donckt, Peter Modregger, Marco F. M. Stampanoni, Patrick Segers, and Nikolaos Stergiopoulos. Dissecting abdominal aortic aneurysm in Ang II-infused mice: suprarenal branch ruptures and apparent luminal dilatation. *Cardiovascular Research*, 105(2):213–222, 12 2014.
- [197] Prediman K. Shah. Inflammation, metalloproteinases, and increased proteolysis. *Circulation*, 96(7):2115–2117, 1997.
- [198] Y. X. Wang. Cardiovascular functional phenotypes and pharmacological responses in apolipoprotein e deficient mice. *Neurobiology of aging*, 26(3):309–16, 2005.
- [199] Dan Gavrilu, Wei Gen Li, Michael L. McCormick, Manesh Thomas, Alan Daugherty, Lisa A. Cassis, Francis J. Miller, Larry W. Oberley, Kevin C. Dellsperger, and Neal L. Weintraub. Vitamin e inhibits abdominal aortic aneurysm formation in angiotensin ii-infused apolipoprotein e-deficient mice. *Arteriosclerosis, Thrombosis, and Vascular Biology*, 25(8):1671–1677, 2005.
- [200] Matthew J. Eagleton, Nicole Ballard, Erin Lynch, Sunita D. Srivastava, Jr. Upchurch, Gilbert R., and James C. Stanley. Early increased mt1-mmp expression and late mmp-2 and mmp-9 activity during angiotensin ii induced aneurysm formation. *Journal of Surgical Research*, 135(2):345–351, 2006.
- [201] Michael W. Manning, Lisa A. Cassis, and Alan Daugherty. Differential effects of doxycycline, a broad-spectrum matrix metalloproteinase inhibitor, on angiotensin ii-induced atherosclerosis and abdominal aortic aneurysms. *Arteriosclerosis, Thrombosis, and Vascular Biology*, 23(3):483–488, 2003.
- [202] Yanwen Qin, Xu Cao, Jun Guo, Yaozhong Zhang, Lili Pan, Hongjia Zhang, Huihua Li, Chaoshu Tang, Jie Du, and Guo-Ping Shi. Deficiency of cathepsin S attenuates angiotensin II-induced abdominal aortic aneurysm formation in apolipoprotein E-deficient mice. *Cardiovascular Research*, 96(3):401–410, 08 2012.
- [203] Y. Qin, Y. Wang, O. Liu, L. Jia, W. Fang, J. Du, and Y. Wei. Tauroursodeoxycholic acid attenuates angiotensin ii induced abdominal aortic aneurysm formation in apolipoprotein e-deficient mice by inhibiting endoplasmic reticulum stress. *European Journal of Vascular and Endovascular Surgery*, 53(3):337 – 345, 2017.
- [204] Dai Yamanouchi, Stephanie Morgan, Kaori Kato, Justin Lengfeld, Fan Zhang, and Bo Liu. Effects of caspase inhibitor on angiotensin ii-induced abdominal aortic aneurysm in apolipoprotein e-deficient mice. *Arteriosclerosis, Thrombosis, and Vascular Biology*, 30(4):702–707, 2010.
- [205] Fjoralba Babamusta, Debra L. Rateri, Jessica J. Moorleghe, Deborah A. Howatt, Xiang-An Li, and Alan Daugherty. Angiotensin ii infusion induces site-specific intra-laminar hemorrhage in macrophage colony-stimulating factor-deficient mice. *Atherosclerosis*, 186(2):282 – 290, 2006.
- [206] Florent Ginhoux and Steffen Jung. Monocytes and macrophages: developmental pathways and tissue homeostasis. *Nat Rev Immunol*, 14(6):392–404, 2014.

- [207] Safa Mellak, Hafid Ait-Oufella, Bruno Esposito, Xavier Loyer, Maxime Poirier, Thomas F. Tedder, Alain Tedgui, Ziad Mallat, and Stéphane Potteaux. Angiotensin ii mobilizes spleen monocytes to promote the development of abdominal aortic aneurysm in apoe^{-/-} mice. *Arteriosclerosis, Thrombosis, and Vascular Biology*, 35(2):378–388, 2015.
- [208] Stéphane Potteaux and Alain Tedgui. Monocytes, macrophages and other inflammatory mediators of abdominal aortic aneurysm. *Current Pharmaceutical Design*, 21(28):4007–4015, 2015.
- [209] Victoria L. King, Darshini B. Trivedi, Jonathan M. Gitlin, and Charles D. Loftin. Selective cyclooxygenase-2 inhibition with celecoxib decreases angiotensin ii-induced abdominal aortic aneurysm formation in mice. *Arteriosclerosis, Thrombosis, and Vascular Biology*, 26(5):1137–1143, 2006.
- [210] Tracy A. Henriques, Jing Huang, Susan S. D’Souza, Alan Daugherty, and Lisa A. Cassis. Orchidectomy, But Not Ovariectomy, Regulates Angiotensin II-Induced Vascular Diseases in Apolipoprotein E-Deficient Mice. *Endocrinology*, 145(8):3866–3872, 08 2004.
- [211] Tracy Henriques, Xuan Zhang, Frederique B. Yiannikouris, Alan Daugherty, and Lisa A. Cassis. Androgen increases at1a receptor expression in abdominal aortas to promote angiotensin ii-induced aas in apolipoprotein e-deficient mice. *Arteriosclerosis, Thrombosis, and Vascular Biology*, 28(7):1251–1256, 2008.
- [212] Sofia Xanthoulea, Melanie Thelen, Chantal Pöttgens, Marion J. J. Gijbels, Esther Lutgens, and Menno P. J. de Winther. Absence of p55 tnfr receptor reduces atherosclerosis, but has no major effect on angiotensin ii induced aneurysms in ldl receptor deficient mice. *PLOS ONE*, 4(7):1–10, 07 2009.
- [213] Amelia R. Adelsperger, Evan H. Phillips, Hilda S. Ibriga, Bruce A. Craig, Linden A. Green, Michael P. Murphy, and Craig J. Goergen. Development and growth trends in angiotensin ii-induced murine dissecting abdominal aortic aneurysms. *Physiological Reports*, 6(8):e13668, 2018. 29696811[pmid]PHY213668[PII]Physiol Rep.
- [214] Practical assessment of the quantification of atherosclerotic lesions in apoe^{-/-} mice. *Molecular Medicine Reports*, 12(4):5298–5306, 2015.
- [215] Bram Trachet, Lydia Aslanidou, Alessandra Piersigilli, Rodrigo A. Fraga-Silva, Jessica Sordet-Dessimoz, Pablo Villanueva-Perez, Marco F.M. Stampanoni, Nikolaos Stergiopoulos, and Patrick Segers. Angiotensin II infusion into ApoE^{-/-} mice: a model for aortic dissection rather than abdominal aortic aneurysm? *Cardiovascular Research*, 113(10):1230–1242, 06 2017.
- [216] Evan H. Phillips, Adam H. Lorch, Abigail C. Durkes, and Craig J. Goergen. Early pathological characterization of murine dissecting abdominal aortic aneurysms. *APL Bioengineering*, 2(4):046106, 2018.
- [217] Dating Sun, Mingxi Zhang, Yuanyuan Li, Shuai Mei, Jin Qin, and Jiangtao Yan. c-jun/ap-1 is upregulated in an ang ii-induced abdominal aortic aneurysm formation model and mediates chop expression in mouse aortic smooth muscle cells. *Molecular medicine reports*, 19(5):3459–3468, 2019. 30864718[pmid] PMC6472129[pmcid].
- [218] Richard Y. Cao, Tim Amand, Matthew D. Ford, Ugo Piomelli, and Colin D. Funk. The murine angiotensin ii-induced abdominal aortic aneurysm model: Rupture risk and inflammatory progression patterns. *Frontiers in Pharmacology*, 1:9, 2010. 21713101[pmid] Front Pharmacol.

Bibliography

- [219] Manesh Thomas, Dan Gavrilu, Michael L. McCormick, Jr. Miller, Francis J., Alan Daugherty, Lisa A. Cassis, Kevin C. Dellsperger, and Neal L. Weintraub. Deletion of p47phox attenuates angiotensin ii-induced abdominal aortic aneurysm formation in apolipoprotein e-deficient mice. *Circulation*, 114(5):404–413, 2006. 16864727[pmid] PMC3974117[pmcid] *Circulation*.
- [220] Jun-o Deguchi, Hayden Huang, Peter Libby, Elena Aikawa, Peter Whittaker, Jeremy Sylvan, Richard T. Lee, and Masanori Aikawa. Genetically engineered resistance for mmp collagenases promotes abdominal aortic aneurysm formation in mice infused with angiotensin ii. *Laboratory Investigation*, 89:315, 2009.
- [221] Catherine Rush, Moses Nyara, Joseph V. Moxon, Alexandra Trollope, Bradford Cullen, and Jonathan Golledge. Whole genome expression analysis within the angiotensin ii-apolipoprotein e deficient mouse model of abdominal aortic aneurysm. *BMC Genomics*, 10(1):298, Jul 2009.
- [222] Lisa A. Cassis, Debra L. Rateri, Hong Lu, and Alan Daugherty. Bone marrow transplantation reveals that recipient at1a receptors are required to initiate angiotensin ii-induced atherosclerosis and aneurysms. *Arteriosclerosis, Thrombosis, and Vascular Biology*, 27(2):380–386, 2007.
- [223] Debra L. Rateri, Jessica J. Moorlegghen, Victoria Knight, Anju Balakrishnan, Deborah A. Howatt, Lisa A. Cassis, and Alan Daugherty. Depletion of endothelial or smooth muscle cell-specific angiotensin ii type 1a receptors does not influence aortic aneurysms or atherosclerosis in ldl receptor deficient mice. *PLOS ONE*, 7(12):1–8, 12 2012.
- [224] Smbat Amirbekian, Robert C. Long, Michelle A. Consolini, Jin Suo, Nick J. Willett, Sam W. Fielden, Don P. Giddens, W. Robert Taylor, and John N. Oshinski. In vivo assessment of blood flow patterns in abdominal aorta of mice with mri: implications for aaa localization. *American Journal of Physiology-Heart and Circulatory Physiology*, 297(4):H1290–H1295, 2009. PMID: 19684182.
- [225] Evan H. Phillips, Alexa A. Yrineo, Hilary D. Schroeder, Katherine E. Wilson, Ji-Xin Cheng, and Craig J. Goergen. Morphological and biomechanical differences in the elastase and angii apoe-/- rodent models of abdominal aortic aneurysms. *BioMed Research International*, 2015:12, 2015.
- [226] K. Genovese, M. J. Collins, Y. U. Lee, and J. D. Humphrey. Regional finite strains in an angiotensin-ii induced mouse model of dissecting abdominal aortic aneurysms. *Cardiovascular Engineering and Technology*, 3(2):194–202, 2012.
- [227] Uwe Raaz, Alexander M. Zöllner, Isabel N. Schellinger, Ryuji Toh, Futoshi Nakagami, Moritz Brandt, Fabian C. Emrich, Yosuke Kayama, Suzanne Eken, Matti Adam, Lars Maegdefessel, Thomas Hertel, Alicia Deng, Ann Jagger, Michael Buerke, Ronald L. Dalman, Joshua M. Spin, Ellen Kuhl, and Philip S. Tsao. Segmental aortic stiffening contributes to experimental abdominal aortic aneurysm development. *Circulation*, 131(20):1783–1795, 2015.
- [228] Matthew R. Bersi, Chiara Bellini, Jing Wu, Kim R.C. Montaniel, David G. Harrison, and Jay D. Humphrey. Excessive adventitial remodeling leads to early aortic maladaptation in angiotensin-induced hypertension. *Hypertension*, 67(5):890–896, 2016.
- [229] Eiketsu Sho, Mien Sho, Hiroshi Nanjo, Koichi Kawamura, Hirotake Masuda, and Ronald L. Dalman. Hemodynamic regulation of cd34⁺ cell localization and differentiation in experimental aneurysms. *Arteriosclerosis, Thrombosis, and Vascular Biology*, 24(10):1916–1921, 2004.

-
- [230] Lilach Gavish, Ronen Beeri, Dan Gilon, Chen Rubinstein, Yacov Berlatzky, Leah Y. Gavish, Atila Bulut, Mickey Harlev, Petachia Reissman, and S. David Gertz. Inadequate reinforcement of transmural disruptions at branch points subtends aortic aneurysm formation in apolipoprotein-e-deficient mice. *Cardiovascular Pathology*, 23(3):152–159, 2014.
 - [231] Matthew D. Ford, Ariel T. Black, Richard Y. Cao, Colin D. Funk, and Ugo Piomelli. Hemodynamics of the mouse abdominal aortic aneurysm. *Journal of Biomechanical Engineering*, 133(12):121008–121008–9, 2011. 10.1115/1.4005477.
 - [232] E. H. Phillips, P. Di Achille, M. R. Bersi, J. D. Humphrey, and C. J. Goergen. Multi-modality imaging enables detailed hemodynamic simulations in dissecting aneurysms in mice. *IEEE Transactions on Medical Imaging*, 36(6):1297–1305, 2017.
 - [233] Hannah L. Cebull, Arvin H. Soepriatna, John J. Boyle, Sean M. Rothenberger, and Craig J. Goergen. Strain mapping from four-dimensional ultrasound reveals complex remodeling in dissecting murine abdominal aortic aneurysms. *Journal of Biomechanical Engineering*, 141(6):060907–060907–8, 2019. 10.1115/1.4043075.
 - [234] Arina Korneva and Jay D. Humphrey. Maladaptive aortic remodeling in hypertension associates with dysfunctional smooth muscle contractility. *American Journal of Physiology-Heart and Circulatory Physiology*, 316(2):H265–H278, 2019. PMID: 30412437.
 - [235] Jacopo Ferruzzi, Sae-Il Murtada, Guangxin Li, Yang Jiao, Selen Uman, Magdalene Y.L. Ting, George Tellides, and Jay D. Humphrey. Pharmacologically improved contractility protects against aortic dissection in mice with disrupted transforming growth factor- β signaling despite compromised extracellular matrix properties. *Arteriosclerosis, Thrombosis, and Vascular Biology*, 36(5):919–927, 2016.
 - [236] C. J. Cyron and J. D. Humphrey. Vascular homeostasis and the concept of mechanobiological stability. *International journal of engineering science*, 85:203–223, 2014. 25308990[pmid] Int J Eng Sci.
 - [237] C. J. Cyron, J. S. Wilson, and J. D. Humphrey. Mechanobiological stability: a new paradigm to understand the enlargement of aneurysms? *Journal of The Royal Society Interface*, 11(100), 2014.
 - [238] Hisashi Sawada, Jeff Z. Chen, Bradley C. Wright, Mary B. Sheppard, Hong S. Lu, and Alan Daugherty. Heterogeneity of aortic smooth muscle cells: A determinant for regional characteristics of thoracic aortic aneurysms? *Journal of translational internal medicine*, 6(3):93–96, 2018. 30425944[pmid] PMC6231305[pmcid] jtim-2018-0023[PII].
 - [239] Brian C. Tieu, Chang Lee, Hong Sun, Wanda LeJeune, Adrian Recinos 3rd, Xiaoxi Ju, Heidi Spratt, Dong-Chuan Guo, Dianna Milewicz, Ronald G. Tilton, and Allan R. Brasier. An adventitial il-6/mcp1 amplification loop accelerates macrophage-mediated vascular inflammation leading to aortic dissection in mice. *The Journal of Clinical Investigation*, 119(12):3637–3651, 12 2009.
 - [240] Matthew R. Bersi, Chiara Bellini, Jay D. Humphrey, and Stéphane Avril. Local variations in material and structural properties characterize murine thoracic aortic aneurysm mechanics. *Biomechanics and Modeling in Mechanobiology*, 18(1):203–218, Feb 2019.
 - [241] Weihong Ren, Yan Liu, Xuerui Wang, Lixin Jia, Chunmei Piao, Feng Lan, and Jie Du. beta-aminopropionitrile monofumarate induces thoracic aortic dissection in c57bl/6 mice. *Scientific Reports*, 6:28149, 2016.

Bibliography

- [242] Daniel P. Judge, Nancy J. Biery, Douglas R. Keene, Jessica Geubtner, Loretha Myers, David L. Huso, Lynn Y. Sakai, and Harry C. Dietz. Evidence for a critical contribution of haploinsufficiency in the complex pathogenesis of marfan syndrome. *The Journal of Clinical Investigation*, 114(2):172–181, 7 2004.
- [243] Precious J. McLaughlin, Qiuyun Chen, Masahito Horiguchi, Barry C. Starcher, J. Brett Stanton, Thomas J. Broekelmann, Alan D. Marmorstein, Brian McKay, Robert Mecham, Tomoyuki Nakamura, and Lihua Y. Marmorstein. Targeted disruption of fibulin-4 abolishes elastogenesis and causes perinatal lethality in mice. *Molecular and Cellular Biology*, 26(5):1700–1709, 2006.
- [244] Dianna M. Milewicz, John R. Østergaard, Leena M. Ala-Kokko, Nadia Khan, Dorothy K. Grange, Roberto Mendoza-Londono, Timothy J. Bradley, Ann Haskins Olney, Lesley Adès, Joseph F. Maher, Dongchuan Guo, L. Maximilian Buja, Dong Kim, James C. Hyland, and Ellen S. Regalado. De novo acta2 mutation causes a novel syndrome of multisystemic smooth muscle dysfunction. *American Journal of Medical Genetics Part A*, 152A(10):2437–2443.
- [245] Jiyuan Chen, Andrew Peters, Christina L. Papke, Carlos Villamizar, Lea-Jeanne Ringuette, Jiumei Cao, Shanzhi Wang, Shuangtao Ma, Limin Gong, Katerina L. Byanova, Jian Xiong, Michael X. Zhu, Rosalinda Madonna, Patrick Kee, Yong-Jian Geng, Allan R. Brasier, Elaine C. Davis, Siddharth Prakash, Callie S. Kwartler, and Dianna M. Milewicz. Loss of smooth muscle α -actin leads to nf- κ b-dependent increased sensitivity to angiotensin ii in smooth muscle cells and aortic enlargement. *Circulation Research*, 120(12):1903–1915, 2017.
- [246] Jason R. Cook, Nicholas P. Clayton, Luca Carta, Josephine Galatioto, Emily Chiu, Silvia Smaldone, Carol A. Nelson, Seng H. Cheng, Bruce M. Wentworth, and Francesco Ramirez. Dimorphic effects of transforming growth factor- β signaling during aortic aneurysm progression in mice suggest a combinatorial therapy for marfan syndrome. *Arteriosclerosis, Thrombosis, and Vascular Biology*, 35(4):911–917, 2015.
- [247] Jie Hong Hu, Hao Wei, Mia Jaffe, Nathan Airhart, Liang Du, Stoyan N. Angelov, James Yan, Julie K. Allen, Inkyung Kang, Thomas N. Wight, Kate Fox, Alexandra Smith, Rachel Enstrom, and David A. Dichek. Postnatal deletion of the type ii transforming growth factor- β receptor in smooth muscle cells causes severe aortopathy in mice. *Arteriosclerosis, Thrombosis, and Vascular Biology*, 35(12):2647–2656, 2015.
- [248] Hiroaki Osada, Masahisa Kyogoku, Motonori Ishidou, Manabu Morishima, and Hiroyuki Nakajima. Aortic dissection in the outer third of the media: what is the role of the vasa vasorum in the triggering process? *European Journal of Cardio-Thoracic Surgery*, 43(3):e82–e88, 12 2012.
- [249] Bram Trachet, Joris Bols, Joris Degroote, Benedict Verhegghe, Nikolaos Stergiopulos, Jan Vierendeels, and Patrick Segers. An animal-specific fsi model of the abdominal aorta in anesthetized mice. *Annals of Biomedical Engineering*, 43(6):1298–1309, Jun 2015.
- [250] Samarth S. Raut, Anirban Jana, Victor De Oliveira, Satish C. Muluk, and Ender A. Finol. The importance of patient-specific regionally varying wall thickness in abdominal aortic aneurysm biomechanics. *Journal of Biomechanical Engineering*, 135(8):081010–081010–10, 2013. 10.1115/1.4024578.
- [251] Eric K. Shang, Derek P. Nathan, Edward Y. Woo, Ronald M. Fairman, Grace J. Wang, Robert C. Gorman, Joseph H. Gorman, and Benjamin M. Jackson. Local wall thickness in finite element

- models improves prediction of abdominal aortic aneurysm growth. *Journal of Vascular Surgery*, 61(1):217 – 223, 2015.
- [252] S. Voß, S. Glaßer, T. Hoffmann, O. Beuing, S. Weigand, K. Jachau, B. Preim, D. Thévenin, G. Janiga, and P. Berg. Fluid-structure simulations of a ruptured intracranial aneurysm: Constant versus patient-specific wall thickness. *Computational and Mathematical Methods in Medicine*, 2016:8, 2016.
- [253] Andrew R. Bond, Chih-Wen Ni, Hanjoong Jo, and Peter D. Weinberg. Intimal cushions and endothelial nuclear elongation around mouse aortic branches and their spatial correspondence with patterns of lipid deposition. *American Journal of Physiology-Heart and Circulatory Physiology*, 298(2):H536–H544, 2010. PMID: 19933414.
- [254] Stéphane Avril, Pierre Badel, Mohamed Gabr, Michael A. Sutton, and Susan M. Lessner. Biomechanics of porcine renal arteries and role of axial stretch. *Journal of Biomechanical Engineering*, 135(8):081007–081007–10, 2013. 10.1115/1.4024685.
- [255] Mauro Ferraro, Bram Trachet, Lydia Aslanidou, Heleen Fehervary, Patrick Segers, and Nikolaos Stergiopoulos. Should we ignore what we cannot measure? how non-uniform stretch, non-uniform wall thickness and minor side branches affect computational aortic biomechanics in mice. *Annals of Biomedical Engineering*, 46(1):159–170, Jan 2018.
- [256] Joris Bols, L. Taelman, G. De Santis, J. Degroote, B. Verhegghe, P. Segers, and J. Vierendeels. Unstructured hexahedral mesh generation of complex vascular trees using a multi-block grid-based approach. *Computer Methods in Biomechanics and Biomedical Engineering*, 19(6):663–672, 2016. PMID: 26208183.
- [257] L. Antiga and D. A. Steinman. Robust and objective decomposition and mapping of bifurcating vessels. *IEEE Transactions on Medical Imaging*, 23(6):704–713, June 2004.
- [258] S. Halier, S. Angenent, A. Tannenbaurn, and R. Kikinis. Nondistorting flattening maps and the 3-d visualization of colon ct images. *IEEE Transactions on Medical Imaging*, 19(7):665–670, July 2000.
- [259] Jerome H. Friedman, Jon Louis Bentley, and Raphael Ari Finkel. An algorithm for finding best matches in logarithmic expected time. *ACM Trans. Math. Softw.*, 3(3):209–226, September 1977.
- [260] Ellen M. Arruda and Mary C. Boyce. A three-dimensional constitutive model for the large stretch behavior of rubber elastic materials. *Journal of the Mechanics and Physics of Solids*, 41(2):389 – 412, 1993.

Chapter 1

A 1D model of the arterial circulation in mice

Lydia Aslanidou¹, Bram Trachet^{1,2}, Philippe Reymond¹, Rodrigo A. Fraga-Silva¹, Patrick Segers², Nikos Stergiopoulos¹

¹ Institute of Bioengineering, École Polytechnique Fédérale de Lausanne, Switzerland

² IBiTech-bioMMeda, Ghent University-IMinds Medical IT, Ghent, Belgium

Published in Altex (Alternatives to Animal Experimentation) 2016

1 Introduction

Cardiovascular disease is often studied in a preclinical setting since small animal models offer more flexibility, easier access to in and ex vivo tissues, and faster disease progression than humans. Mice in particular are a common model in hypothesis-driven cardiovascular research¹ due to their short lifespan, their small size, the similarity of their well-decoded genome with the human one and, most importantly, the possibility to induce genetic modifications². Genetically or pharmacologically altered mouse models have provided insight into (amongst many other cardiovascular applications) abdominal aortic aneurysm³ (see section 5.3 of the Introduction), stable and unstable atherosclerotic plaque^{4,5}, diabetes⁶, hypertrophy⁷ and Marfan syndrome⁸. However, since mice have a much smaller (aortic dimensions are 10x smaller, Table 2) and faster (average, non-anesthetized heart rate is 10x higher) cardiovascular system, the interpretation of these results requires a cautious translation between murine and human systems. Striking similarities between human and murine aortic flow velocity and pressure waveforms⁹, as well as a highly similar branching pattern of the aortic arch¹⁰, have been reported in literature. However, in-depth research on aortic anatomy and physiology is not straightforward since, both in humans and mice, (non-)invasive measurements are (i) technically difficult to obtain, (ii) limited to a restricted number of aortic locations, and (iii) need to be justified from an ethical perspective. In a human setting, these limitations can be circumvented since reference data for both anatomy and physiology are readily available for many arterial locations. The development of a wide range of 1D models of the human arterial circulation^{11,12,13,14,15,16} has allowed researchers to study the effect of alterations in anatomy

or physiology¹⁷ without the ethical and technical limitations of *in vivo* measurements. In mice, the available data are focused on arterial physiology rather than anatomy. To the best of our knowledge, the most complete computational model of the murine arterial tree is the FSI model of Cuomo et al.¹⁸. They set up a 3D model to investigate the effect of invasive pressure measurements on local hemodynamics, while accounting for ventricular-vascular coupling. However, their 3D model was based on a single mouse and only included the major branches. An extensive description of the ‘reference’ murine arterial anatomy and physiology has, to the best of our knowledge, never been reported and a validated *in silico* model describing the average murine systemic tree and its hemodynamics is lacking. A validated numerical model of the murine circulation could facilitate the implementation of the 3R’s principle (Refine, Reduce, Replace) in small animal research and contribute to minimize the use of animals by providing valuable insight into murine hemodynamics without animal suffering.

In this work, we used high-resolution, contrast-enhanced micro-CT to obtain reference data on the *in vivo* anatomy of the entire systemic arterial tree in mice. We subsequently combined these measurements with a wide range of literature data to translate an existing one-dimensional model of the human systemic arterial tree¹⁹ into a murine setting. The resulting *in silico* model of the anesthetized murine systemic arterial tree includes 85 arterial segments and predicts pressure and velocity waveforms at all arterial locations without the need for arduous invasive measurements. We demonstrated the validity of the model by comparing its predicted pressure, velocity and diameter waveforms to those measured *in vivo* in a large sample of young, male laboratory mice.

2 Methods

In vivo measurements

Mice

All procedures were approved by the Ethical Committee of Canton Vaud, Switzerland (EC 2647.1 for the wild type mice, EC 2647.2 for the apolipoprotein E gene-deleted [ApoE-/-] mice) and performed according to the guidelines from Directive 2010/63/EU of the European Parliament on the protection of animals used for scientific purposes. Male wild type C57BL6/J and male ApoE-/- mice on a C57BL6/J background were purchased from Janvier (Saint-Berthevin, France). All surgery and measurements were performed under isoflurane anesthesia, and all efforts were made to minimize suffering. The 3R (refine, reduce, replace) principle was applied to minimize the number of laboratory animals. Initial micro-CT, invasive pressure and ultrasound measurements were performed on five wild type, male C57BL/6J mice, 12-15 weeks old, that served as control animals in a study on murine abdominal aortic aneurysms (AAA)³. Subsequent micro-CT ($n = 3$) and ultrasound ($n = 47$) measurements were performed on male ApoE-/- mice on a C57BL/6J background, 12 weeks old, that served as baseline data in a follow-up study on murine AAA²⁰. Mice were housed in the controlled environment of

the EPFL animal facility, which is a part of the Lemanic animal facility network, and had ad libitum access to water and food (standard rodent chow). The overall well-being of the animals was inspected twice per day. Both wild type and ApoE^{-/-} mice were euthanized at humane endpoints defined by their respective studies (just after micro-CT for wild types, after 10, 18 or 28 days of angiotensin II-infusion for ApoE^{-/-} mice).

Contrast-enhanced micro-CT

Animals were anesthetized by inhalation of 1.5% isoflurane and injected intravenously in the lateral tail vein with 100 μ l/25 g body weight of Exitron (Miltenyi Biotec, Germany). The animals were subsequently scanned in vivo in dorsal recumbency with a Quantum FX micro-CT scanner (Caliper Life Sciences, Hopkinton, Massachusetts), which has been optimized for longitudinal studies owing to its low radiation dose. Acquisition was performed with a 90 kVp tube voltage and a current of 160 μ A. Each animal underwent 5 consecutive scans, with region of interest focused on the head, thorax, abdomen, legs and tail, respectively. Each scan lasted for 2 minutes, and images were obtained with a 24 mm transverse field of view and a theoretical spatial pixel size of 50 μ m. Micro-CT images were reconstructed using an in-house method based on the iterative maximum-likelihood polychromatic algorithm²¹.

Invasive pressure

In five wild type mice, a 1.2 F Scisense catheter (Transonic, Maastricht, The Netherlands) with two pressure sensors spaced 2 cm apart was inserted via an incision in the femoral artery. The catheter was guided into the correct position using simultaneous long axis BMode ultrasound, and allowed to settle for 10 minutes. Continuous pressure waveforms were recorded with the tip of the catheter (i.e., the first pressure sensor) at the descending, thoracic and abdominal aorta.

High-frequency ultrasound

Ultrasound imaging was performed with a high-frequency ultrasound device (Vevo 2100, VisualSonics, Toronto, Canada). During the procedure animals were anesthetized by inhalation of 1.5% isoflurane and fixed on the imaging table in dorsal position. Physiological function (respiration and heart rate obtained from ECG) was monitored while the animal was positioned on the heated handling table. All measurements were performed by a single, experienced operator. In 5 wild type mice and 47 ApoE^{-/-} mice, pulsed Doppler measurements were obtained in the ascending, descending, and 5 locations along the thoraco-abdominal aorta: the thoracic aorta, the supraceliac region just cranial to the bifurcation of the celiac artery, the paravisceral region cranial to the trifurcation of the mesenteric and right renal arteries, the pararenal region caudal to the trifurcation of the mesenteric and right renal arteries and the infrarenal region caudal to the bifurcation of the left renal artery. Pulsed Doppler

measurements were also obtained in the celiac, mesenteric and renal (left and right) arteries. In the 5 wild type mice additional pulsed Doppler measurements were obtained prior to pressure probe insertion in the brachiocephalic trunk, common, internal and external carotid arteries (left and right), caudal and iliac arteries. Ultrasound Pulsed Doppler waveforms were traced within a custom-made environment in Matlab. For each measurement location, the average of three different waveforms was calculated. The resulting waveform vectors were subsampled to 501 points and filtered using a Savitsky-Golay filter of an order 3 and window width 51. All blood flow velocity ultrasound measurements were divided by a factor of 2, assuming that the ultrasound velocity measurements correspond to the maximum centerline velocity of a parabolic velocity profile²².

In wild type mice RF (radio frequency) diameter waveforms were obtained with long axis MMode imaging at the same locations as invasive pressure measurements, while in ApoE^{-/-} mice RF diameter waveforms were measured with MMode at the ascending aorta and at 2 locations in the abdominal aorta (cranial to the celiac and caudal to the left renal artery). A custom-written platform in Matlab, based on the algorithm described by Rabben et al.²³, was used to reconstruct the complete MMode image from RF data as described in previous work²⁰. For each measurement, 3 cardiac cycles were subsequently selected and plotted as a reference for semi-automatic wall segmentation guided by the user. The tracked aortic wall movement yielded highly accurate in vivo diameter waveforms (Figure 1.4).

In silico model

For an in-depth description of the governing equations and assumptions that were made in the modelling approach, we refer to a previous manuscript describing the human model¹⁹. Here, a synopsis of the most important modelling assumptions is given, with emphasis on the aspects in which the murine modelling assumptions differ from the human ones.

Arterial tree

As literature data on murine anatomy are scarce and restricted to the main aorta, we based the arterial tree only on dedicated in vivo measurements. For $n = 3$ C57BL/6J mice, reconstructed micro-CT images were converted into TIFF format and imported into the 3D segmentation software package Mimics (Materialise, Leuven, Belgium). Arterial branches were segmented when micro-CT resolution allowed so, and when their inclusion was judged physiologically relevant for future applications. This resulted in an averaged tree consisting of 85 segments (Table 2). For each segment, inlet and outlet areas were measured perpendicular to and segment length was measured along the centerline that was calculated in Mimics. To account for variation due to differences in genetic background, the detailed data from 3 wild type mice were complemented with diameters and lengths of the main aorta and its major branches (carotids, celiac, mesenteric and renal arteries) from micro-CT scans of the thorax and abdomen in 3 ApoE^{-/-} mice. The schematic representation of the resulting arterial tree is shown

in Figure 1.1. The 8 pairs of intercostal arteries were accounted for by introducing a single vessel with a blood flow equivalent of the set of the 8 intercostal pairs, similar to what was done in the human model¹⁹.

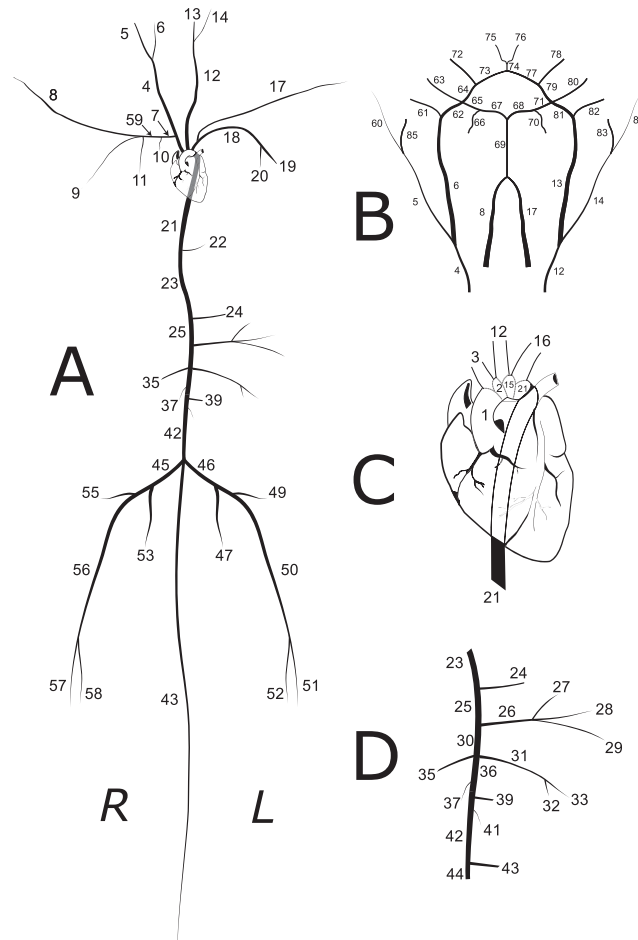


Figure 1.1: Schematic representation of arterial tree. A: main systemic arterial tree, B: cerebral vasculature, connected via the carotids (segments 4, 12) and the vertebrals (segments 8, 17) to the main arterial tree shown in A, C: detail of the heart, ascending aorta and carotid branches, D: detail of the principal abdominal aortic branches. R: right; L: left.

Chapter 1. A 1D model of the arterial circulation in mice

Table 1.1: Arterial tree segments and dimensions

Arterial segment name	Arterial Segment Number (Right/Left)	Length, mm	Prox. lum. diam., mm	Dist. lum. diam., mm	Dist., 10^{-3} 1/mmHg	TR, mmHg·s·ml ⁻¹	TC, 10^{-8} ml/mmHg
Ascending aorta	1	2.6	1.41	1.54	2.95		
Aortic arch A	2	0.7	1.33	1.33	2.79		
Brachiocephalic trunk	3	2.1	0.80	0.71	1.97		
Common carotid	4	10.2	0.52	0.49	1.52		
Right external carotid	5	2.6	0.42	0.36	1.27		
Right internal carotid	6	1.8	0.41	0.39	1.42		
Right subclavian A	7	1.2	0.55	0.53	1.68		
Right vertebral	8	13.3	0.40	0.27	1.13		
Right axillary	9	7.8	0.35	0.27	1.11	1,015.7	9.8
Costocervical trunk	10	2.7	0.26	0.23	0.93	4,962.3	6.0
internal mammary	11	5.1	0.25	0.23	0.93	2,198.4	6.0
Left common carotid	12	13.3	0.63	0.52	1.55		
Left internal carotid	13	1.8	0.44	0.41	1.43		
Left external carotid	14	2.6	0.43	0.40	1.27		
Aortic arch B	15	1.2	1.20	1.18	2.58		
Left subclavian A	16	1.8	0.61	0.55	1.58		
Left vertebral	17	13.2	0.34	0.26	1.12		
Left subclavian B	18	6.1	0.40	0.32	1.36		
Left axillary	19	3.0	0.25	0.22	0.92	2,079.2	5.5
Left cervical trunk	20	2.4	0.32	0.30	1.10	948.1	11.9
Thoracic aorta A	21	12.2	1.16	1.11	2.45		
Intercostals	22	1.6	0.51	0.51	1.42	592.8	973.3
Thoracic aorta B	23	12.2	1.11	1.07	2.39		
Left suprarenal	24	3.0	0.33	0.31	1.04	4,414.0	133.3
Thoracic aorta C	25	2.3	1.06	1.06	2.34		
Coeliac	26	3.1	0.46	0.43	1.32		
Hepatic	27	3.4	0.24	0.24	0.86	2,955.8	66.7
Lieno-gastric	28	5.1	0.31	0.27	0.98	1,680.4	110.0
Lieno-pancreatic	29	6.9	0.29	0.27	0.96	1,777.2	124.3
Abdominal aorta A	30	1.8	1.00	0.97	2.26		
Superior mesenteric	31	4.7	0.60	0.56	1.56		
Ileocolic	32	1.3	0.31	0.24	0.94	2,439.5	674.1
Ileac and jejunal branches	33	2.6	0.55	0.53	1.48	319.3	1099.6
Abdominal aorta B	34	0.4	0.93	0.93	2.14		
Right renal	35	2.9	0.51	0.49	1.40	641.3	666.6
Abdominal aorta C	36	1.9	0.88	0.87	2.06		
Right Spermatic artery	37	5.1	0.26	0.23	0.87	21,346.7	4.3
Abdominal aorta D	38	1.2	0.85	0.83	2.00		
Left renal	39	1.5	0.47	0.45	1.33	862.3	400.0

Table 1.1: Arterial tree segments and dimensions

Arterial segment name	Arterial Segment Number (Right/Left)	Length, mm	Prox. lum. diam., mm	Dist. lum. diam., mm	Dist., 10^{-3} l/mmHg	TR, mmHg·s·ml ⁻¹	TC, 10^{-8} ml/mmHg
Abdominal aorta E	40	1.0	0.80	0.80	1.94		
Left Spermatic artery	41	5.3	0.23	0.22	0.83	46,939.9	3.9
Abdominal aorta F	42	9.0	0.78	0.70	1.85		
Middle Caudal	43	28.1	0.34	0.22	0.96	20,303.3	4.5
Abdominal aorta G	44	0.7	0.70	0.70	1.77		
Common iliac	45/46	3.4	0.51	0.47	1.41/1.41		
Inner iliac	47/53	4.0	0.23	0.18	0.77/0.77	37,180.5	2.4
External iliac	48/54	1.5	0.48	0.47	1.36/1.36		
Pudic-epigastric trunk	49/55	1.3	0.27	0.23	0.88/0.88	20,430.5	4.6
Femoral	50/56	8.6	0.47	0.43	1.32/1.32		
Posterior tibial	51/57	4.3	0.30	0.23	0.98/0.98	6,807.5	6.0
Anterior tibial	52/58	3.0	0.35	0.26	0.98/0.98	6,761.8	5.8
Right subclavian B	59	0.7	0.53	0.53	1.62		
Maxillary	60/84	8.3	0.26	0.20	1.23/1.24	2,373.8/ 1,797.9	31.4/ 32.3
Ophthalmic	61/82	3.2	0.33	0.21	1.13/1.22	3,203.2/ 1,988.3	16.5/ 22.4
Internal carotid sinus	62/81	4.8	0.35	0.30	1.36/1.37		
Anterior choroidal	63/80	1.3	0.19	0.14	0.78/0.83	10,443.2/ 8,857.9	5.6/ 7.4
ICA distal	64/79	1.5	0.28	0.25	1.12/1.20		
Posterior cerebral C	65/71	2.7	0.22	0.20	0.84/0.90		
Posterior cerebral B	66/70	3.5	0.22	0.18	2.00/1.83	839.5/ 898.5	249.4/ 173.6
Posterior cerebral A	67/68	2.6	0.19	0.17	1.01/1.01		
Basilar artery	69	4.8	0.23	0.24	1.33		
Middle cerebral	72/7	2.2	0.19	0.16	0.86/1.82	6,068.4/ 4,812.6	57.9
Anterior Cerebral	73/77	2.6	0.24	0.21	1.00/2.07		
Supraorbital	74	2.1	0.31	0.23	2.00		
Naso-frontal	75	2.0	0.19	0.16	1.59	2,427.7	95.1
Anterior facial	76	3.2	0.18	0.13	1.47	3,464.2	58.9
fac. occ. left sup. thy. asc. ph. lyng. fac.	83/85	3.2	0.19	0.16	1.05/1.04	3,865.4/ 5,087.7	16.8/ 16.3

Prox.lum.diam.: proximal lumen diameter, Dist.lum.diam.: distal lumen diameter, Dist: distensibility, TR: terminal resistance, TC: terminal compliance.

Governing equations

The murine systemic arteries were modelled as compliant tapering cylindrical vessels with a viscoelastic wall. The 1-D formulation of the continuity equation and the incompressible, axisymmetric Navier-Stokes equations for a Newtonian fluid governed the propagation of blood flow and pressure in the model (while taking into account the Fåhræus-Lindqvist effect on viscosity, see below). A third, constitutive equation was used to relate the distending pressure to the local cross-sectional area, thus describing the viscoelastic properties of the arterial wall. The system of three equations with three unknowns (pressure, flow and area) was solved numerically with an implicit finite difference scheme over 8 cardiac cycles, using an in-house MATLAB code previously developed for the human arterial tree¹⁹. The Witzig Womersley theory was implemented to approximate the pulsatile effects on the velocity profile, which was needed to calculate convective acceleration and wall shear stresses in the momentum equation.

Viscoelastic modelling of the wall

Holenstein's model²⁴ was implemented to describe the viscoelastic wall behavior. The instantaneous lumen area under a distending pressure P was expressed as the sum of a nonlinear elastic and a viscoelastic component:

$$A(t) = A^e[P(t)] + A^v(t)$$

The elastic component of the local area, A_e relates to the distending pressure by its elastic compliance, C_A^e . To account for both pressure and location dependence, we assumed that elastic area compliance was the product of a pressure-dependent function, termed $C_p^e(P)$, and a location-dependent function, termed $C_d^e(\bar{d}, P_{ref})$. As Langewouters^{25,26} proposed for the pressure dependency of the static compliance:

$$C_p^e(P) = \frac{C_m}{1 + \left[\frac{P - P_{maxC}}{P_{width}} \right]^2}$$

Fitting of the parameters was based on literature³⁶ as well as in house pressure-diameter measurements on excised C57BL/6 murine aortas, which resulted in the following values: $C_m = 17.3 \text{ m}^2/\text{mmHg}$, $P_{maxC} = 27.2 \text{ mmHg}$ and $P_{width} = 20 \text{ mmHg}$. The local diameter-dependent variation of the elastic area compliance was derived from the following equation:

$$C_d^e(\bar{d}, P_{ref}) = \frac{A}{\rho P W V^2(\bar{d}, P_{ref})}$$

In order to model the location-dependent compliance, local aortic stiffness data were gathered from a wide range of literature data^{27,28,29,30,37,31,32,22,35,34,33}. If local ex vivo pressure-diameter

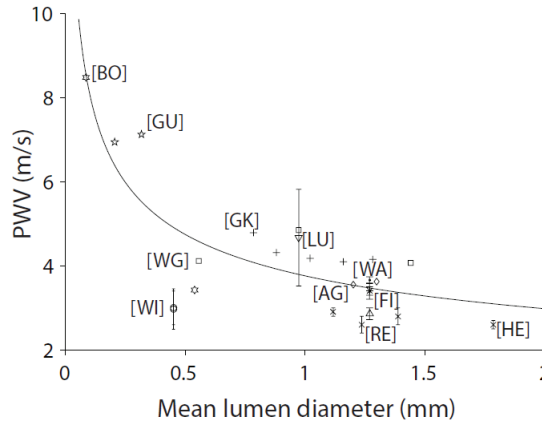


Figure 1.2: Pulse wave velocity (PWV) values reported in literature for different arterial sites as a function of lumen diameter. Acronyms refer to the publication reporting the values (AG: Agianniotis and Stergiopoulos, 2012²⁷; BO: Bolduc et al., 2012²⁸; FI: Fitch et al., 2006²⁹; GK: Guo and Kassab, 2003³⁰; GU: Guo et al., 2006; HE: Herold et al., 2009³¹; LU: Luo et al., 2009³²; RE: Reddy et al., 2003²²; WI: Williams et al., 2007³³; WA: Wang, 2005³⁴; WG: Wagenseil et al., 2005³⁵). Standard deviations are shown where available.

curves or distensibility values were reported, these were converted into local pulse wave velocities (PWV) using the Bramwell-Hill equation. To allow for comparison with the human model, PWV values were subsequently plotted against lumen area (Figure 1.2). In spite of some well anticipated dispersion, we found an inverse relation between artery size and PWV:

$$PWV(\bar{d}) = \frac{a}{\bar{d}^b}$$

The coefficients obtained for the best fit (PWV in m/s, diameter in m) were $\alpha = 0.3693$ and $b = 0.3359$, with $R^2 = 0.6$, which is a better fit than what was obtained in the human model¹⁹. The viscoelastic area component, $A_v(t)$, was calculated by the convolution product between the elastic area, A_e , and the derivative of a creep function, $J(t)$:

$$A^v(t) = \int_0^\infty j(\tau) A^e[P(t - \tau)] d\tau$$

$$j(\tau) = \tilde{\alpha} \frac{e^{-t/\tau_2} - e^{-t/\tau_1}}{t}$$

Measurements on visco-elastic properties of mouse arterial tissues were kindly provided by Tian et al.³⁸, but as there was much scattering in the data we did not manage to obtain a physiologically reasonable fit. Following Reymond et al.¹⁹, we used Holenstein's fitted values for τ_1 (0.00081s) and τ_2 (0.41s), which had been fit on canine data from Bergel³⁹. Further, we assumed that the viscoelastic coefficient $\tilde{\alpha}$ increases linearly from the heart to the distal beds:

$$\tilde{\alpha} \cong a_1 \cdot \bar{d} + b_1$$

Since the dimensions of the human brain vasculature (0.5- 4 mm) are approximately of the same order of magnitude as the murine systemic arteries (0.13 to 1.54 mm), we decided to apply the fit obtained for the human brain vasculature in the murine systemic arteries. This resulted in values of $a_1 = -0.0062 \text{ mm}^{-1}$ and $b_1 = 0.34$.

Fåhræus-Lindqvist effect

The Fåhræus-Lindqvist effect describes a significant decrease of apparent blood viscosity in tubes of diameters less than $300 \mu\text{m}$ ⁴⁰ and down to approximately $10 \mu\text{m}$ ⁴¹. In the murine anatomy obtained for our model, 26 arterial segments out of 85 were of a diameter below the critical $300 \mu\text{m}$. We therefore implemented an empirical relationship to account for the dependence of relative apparent viscosity on tube diameter and hematocrit, based on in vitro and in vivo observations, for a hematocrit equal to 45%⁴².

Distal vasculature model and boundary conditions at terminal vessels

A three-element windkessel model was used to account for the cumulative resistance and compliance of all vessels distal to the terminal segments. Following Reymond et al.¹⁹, the windkessel compliance C_T^i was assumed to be proportional to the area compliance C_A^i of the terminal vessel at its distal end:

$$C_T^i \cong C_T \frac{C_A^i}{\sum C_A^i}$$

where $C_T = \sum_i C_T^i$ is the part of the total volume compliance attributed to peripheral vessels beyond the termination sites. The addition of the segments' volume compliance and the compliance of the peripheral beds yielded the total systemic vascular compliance:

$$C_v = \sum_i^n C_{v,i} + \sum_i^m C_{T,i}$$

where $n = 85$ is the total number of arterial segments and $m = 39$ is the total number of terminal beds. The volume compliance for each segment was calculated by integrating the area compliance over the segment length. Volume compliances (and, in order to preserve consistency, distensibilities) were adjusted to match the literature value of $2.67 \times 10^{-4} \text{ ml/mmHg}$ for the compliance of the murine central aorta including some of its major branches³⁰. For the estimation of the total terminal compliances, we followed the assumption that 20% of the total systemic compliance lies in the terminal beds^{19,15}. Terminal resistances were calculated based on flow rates into major branches that were reported by Trachet et al.⁴³. At locations where no experimental data were available, we completed the values assuming that the mean wall shear stress (given by Poiseuille's law) was the same as for nearby arteries. Unlike the human model, where the entire mean pressure drop was assumed to occur in the distal beds, we accounted for losses within the system by subtracting the pressure drop predicted by Poiseuille's law prior

to calculating the terminal resistances.

Arterial bifurcations

Continuity of pressure and flow were imposed across each branching point. To minimize forward wave reflections, the characteristic impedances of all segments were adapted so that the absolute value of the reflection coefficient was <0.1 at all bifurcations.

Heart model

At its proximal end, the arterial tree was coupled to a varying elastance model of the left ventricle⁴⁴. Following the argumentation of Reymond et al.¹⁹, we imposed the following expression for the varying elastance of an ejecting heart:

$$E(t) = E^*(t)[1 - kQ(t)]$$

where E^* represents the elastance that would be measured during an isovolumic (non-ejecting) contraction, and k a constant relating the internal resistance of the left ventricle to the ventricular pressure during an isovolumic contraction. We derived the isovolumic elastance E^* from the global normalized elastance curve reported by Senzaki et al.⁴⁵, given the striking similarity in normalized elastance curves between humans and mice⁴⁶. This required the use of a “standard” aortic flow waveform, which we obtained from averaged flow velocity and aortic diameter waveforms at the ascending aorta in 47 ApoE-/- mice. The value of k was derived iteratively, by minimizing the difference between the elastance resulting from the 1-D model and the original one from Senzaki et al.⁴⁵. The final k -value was 0.42 s/ml. Other parameter values for the heart model were obtained from literature and, where needed, calculated from reported P-V loops. Due to the large variety of measurement methods for mice of different strains under different anesthesia methods, the mean literature values of minimum^{47,46,48,49,50} and maximum^{47,51,52,48,49} elastance as well as dead volume^{47,46,53} were subsequently tuned to yield a physiological pulse pressure and velocity waveform at the proximal aorta. The final values were 0.1 μ l for the dead volume, 0.09 mmHg/ μ l for the minimum elastance and 6.2 mmHg/ μ l for the maximum elastance. End-diastolic pressure was taken equal to the mean of the literature values^{47,54,48,49,50}, which was 4.6 mmHg. Given the lack of reports on venous resistance values for mice, we decided on a value of 0.23 mmHg·s·ml⁻¹, which yielded physiological heart parameters (presented in the results section). Anesthetized heart rate was set equal to 445 bpm, i.e., the average of the measured heart rate values (during ultrasound acquisition) of the 47 ApoE-/-, and was close to the mean heart rate of 480 bpm of several literature reports^{47,54,48,49,50}. The time to maximum elastance was set equal to 59 ms for a heart cycle of 0.135 s.

Lumped parameter windkessel model

Global arterial properties can be estimated by coupling the time-varying elastance heart model to a lumped parameter windkessel model representing the whole arterial tree^{55,56,57,58}. For an overall validation for the model, we coupled the heart model to a four-element windkessel model so as to compare the arterial model parameters of total systemic resistance, total compliance and aortic characteristic impedance to values reported by Segers et al.⁵⁹.

Cerebral circulation

The carotid arteries are expected to be susceptible to returning waves from the highly resistant cerebral sites¹⁹. We therefore investigated the effect of the presence of the cerebral vasculature on the blood flow and pressure estimates in the right carotid artery. In order to ensure a fair comparison, the distal sites of the carotids and vertebral arteries were terminated with lumped three-element WK models appropriately tuned to account for the same total terminal resistance and compliance as with the presence of the brain model.

Pressure in the tail

The mouse tail is a specific region of interest, since tail-cuff pressure measurements are the most common noninvasive method to determine arterial blood pressure in mice. Yet, thermoregulatory vasomotion in the tail of the mouse can cause a significant variance in tail blood flow⁶⁰ and, hence, in tail-cuff pressure measurements⁶¹. The modelled percentage of proximal aortic blood flow to the caudal artery was 3%. In order to simulate different thermoregulatory states, a parameter study was performed in which the blood flow to the caudal artery was varied between 1% and 5% of the proximal aortic blood flow.

3 Results

General physiological parameters

Main hemodynamic parameters estimated from the 1D model are presented in Table 1.3, along with values of the 3D model published by Cuomo et al.¹⁸. Cardiac output was 14 ml/min, stroke volume was 31.4 μ l, heart ejection fraction was 61% and mean blood pressure in the proximal aorta was 98 mmHg. The aortic PWV was calculated with the transit time method between the proximal ascending aorta and the distal abdominal aorta just before the iliac bifurcation and was found equal to 4.44 m/s. In the proximal aorta, systolic pressure was 121 mmHg and diastolic pressure was 79 mmHg, with the mean flow equal to 0.23 ml/s. Modelling of the entire murine arterial tree with the four-element lumped parameter windkessel model yielded the parameters reported in Table 1.3. Maximum values of Womersley and Reynolds numbers within the murine circulation were 2.5 and 175, respectively.

Model predictions vs in vivo measurements

Model predictions of blood flow velocity, mean blood pressure and pulse pressure as well as the mean value of the validation set of 47 in vivo measurements are summarized for all major arterial sites in Table 1.2.

Table 1.2: Quantification of pressure and blood flow velocity model predictions and corresponding in vivo measurements at different locations along the aortic tree.

	In vivo measurements	Model	In vivo measurements	Model
Ascending aorta	0.17 ± 0.24	0.15	NA	98.2
Descending aorta	0.09 ± 0.12	0.15	96.5 ± 18.6	97.3
Thoracic aorta	0.09 ± 0.07	0.15	99.6 ± 17.4	95.5
Supraceliac region	0.12 ± 0.08	0.15	104.9 ± 16.2	95.2
Coeliac artery	0.12 ± 0.03	0.11	NA	94.4
Paravisceral region	0.13 ± 0.08	0.13	NA	94.9
Mesenteric artery	0.13 ± 0.05	0.13	NA	94.2
Right renal	0.11 ± 0.04	0.11	NA	94.2
Pararenal region	0.08 ± 0.07	0.11	107.2 ± 31.4	94.6
Left renal	0.10 ± 0.04	0.09	NA	94.0
Infrarenal aortic region	0.06 ± 0.06	0.07	NA	94.1

Table 1.3: Modelled hemodynamic parameters, compared against the 3D model of Cuomo et al.¹⁸ and a range of reported physiological values.

	CO, ml/min	SV, μl	EF %	MAP, mmHg	aPWV, m/s	R, mmHg·μl ⁻¹ ·s	C, μl·mmHg ⁻¹	Z, mmHg·μl ⁻¹ ·s
1D model	13.96	31.4	61	98	4.44	0.42	0.54	0.021
Cuomo et al. ¹⁸	12.03	27.1	47	75	4.42	NA	NA	NA
Literature values	8-16 ^{1,2}	17-36 ^{1,2}	55-72 ¹	81-105 ¹	2.86-4.28 ^{3,4,5}	0.41 ± 0.13^6	0.50 ± 0.15^6	0.021 ± 0.005^6

CO: cardiac output, SV: stroke volume, EF: ejection fraction, MAP: mean arterial pressure, aPWV: aortic pulse wave velocity, R: total systemic vascular resistance, C: total arterial compliance, Z: aortic characteristic impedance. Values for R, C, Z are means \pm SD. Numbers refer to the publications reporting the values, i.e. 1:⁴⁷, 2:⁶², 3:⁶³, 4:²², 5:⁶⁴, 6:⁵⁹. *values refer to both adult C57BL/6 WT mice and ApoE^{-/-} mice.

Figure 1.3 displays the modelled blood flow velocity waveforms against in vivo measurements performed on a set of 47 ApoE^{-/-} mice at 6 sites along the arterial tree. Due to the great variability in heart rate among different measurements, the duration of the cardiac cycle has been normalized to allow for comparison between different measurements and the model prediction. The bottom panel of Figure 1.3 shows the model blood flow velocity waveforms along the aorta, starting from the proximal ascending aorta and ending in the infrarenal aortic part, before the iliac bifurcation. The mean waveform of in vivo velocity measurements performed on the same aortic locations is also displayed separately in the bottom panel. A good overall agreement in amplitude and waveform can be noted. The only arterial sites where the model prediction presents a similar waveform but different amplitude from the in vivo

measurements are the descending and thoracic aorta.

In Figure 1.4, the modelled diameter and pressure waveforms are compared with the corresponding *in vivo* measurements. Similar to the flow velocity waveforms of Figure 1.3, the heart cycle duration has been normalized in order to facilitate the comparison between the diameter waveforms. The mean pressure of the model prediction falls within the range of the measured pressure waveforms at all locations, yet the latter suffer from high inter-subject variability (cf. Table 1.2). The modelled pulse pressure is 41.7 mmHg in the ascending aorta and drops to 40.2 mmHg in the infrarenal aorta. The *in vivo* diameter waveforms are similar in shape to the *in vivo* pressure waveforms (e.g., panel C). The modelled inner lumen diameter change from diastole to systole (Δd) in the ascending aorta is 0.22 mm, whereas in the supraceliac aortic region it is 0.13 mm and 0.08 in the infrarenal aortic region. This corresponds very well to the *in vivo* diameter measurements which yielded mean Δd values of 0.23 ± 0.07 mm in the ascending aorta, 0.15 ± 0.03 mm in the supraceliac aortic region and 0.09 ± 0.02 in the infrarenal part of the aorta.

Parameter studies

Figure 1.5a displays the effect of inclusion of the brain vasculature on the model flow velocity and pressure waveform prediction in the right external carotid artery. In the first panel (i) the modelled flow velocity waveform compares relatively well to *in vivo* measurements performed in the right external carotid artery. Middle (ii) and right (iii) panels show that considerable differences occur in the carotid flow and pressure waveforms with and without inclusion of the cerebral vasculature into the model. In the absence of the cerebral tree, there is non-physiological backflow and a substantially altered waveform. Figure 1.5b shows the Fåhræus-Lindqvist effect in the posterior cerebral segment, which has a mean diameter equal to 220 μm . Inclusion of the Fåhræus-Lindqvist effect into the model results in a 0.6% decrease in mean pressure and a 2.1% decrease in mean flow velocity at this location. The effect of the Witzig-Womersley formulation for wall shear stress and convective acceleration is small on predicted pressure and flow: in the common iliac artery, use of the Witzig-Womersley formulation leads to a 0.1% decrease in the mean pressure and marks no change in the mean flow rate prediction, while in the thoracic artery it leads to a 0.1% decrease in mean pressure and a 0.2% decrease in mean flow rate. When the inflow rate at the tail was reduced from 3% to 1%, central pressure slightly increased from 98 to 99 mmHg, while the mean blood pressure in the tail increased from 83 mmHg to 90 mmHg. In this case, the systolic and diastolic blood pressure in the tail were 109 mmHg and 74 mmHg, respectively. When the flow in the caudal artery was increased to 5%, central pressure slightly decreased to 97 mmHg, while the mean blood pressure in the tail dropped to 77 mmHg. The systolic and diastolic blood pressure in the tail decreased to 93 mmHg and 64 mmHg, respectively.

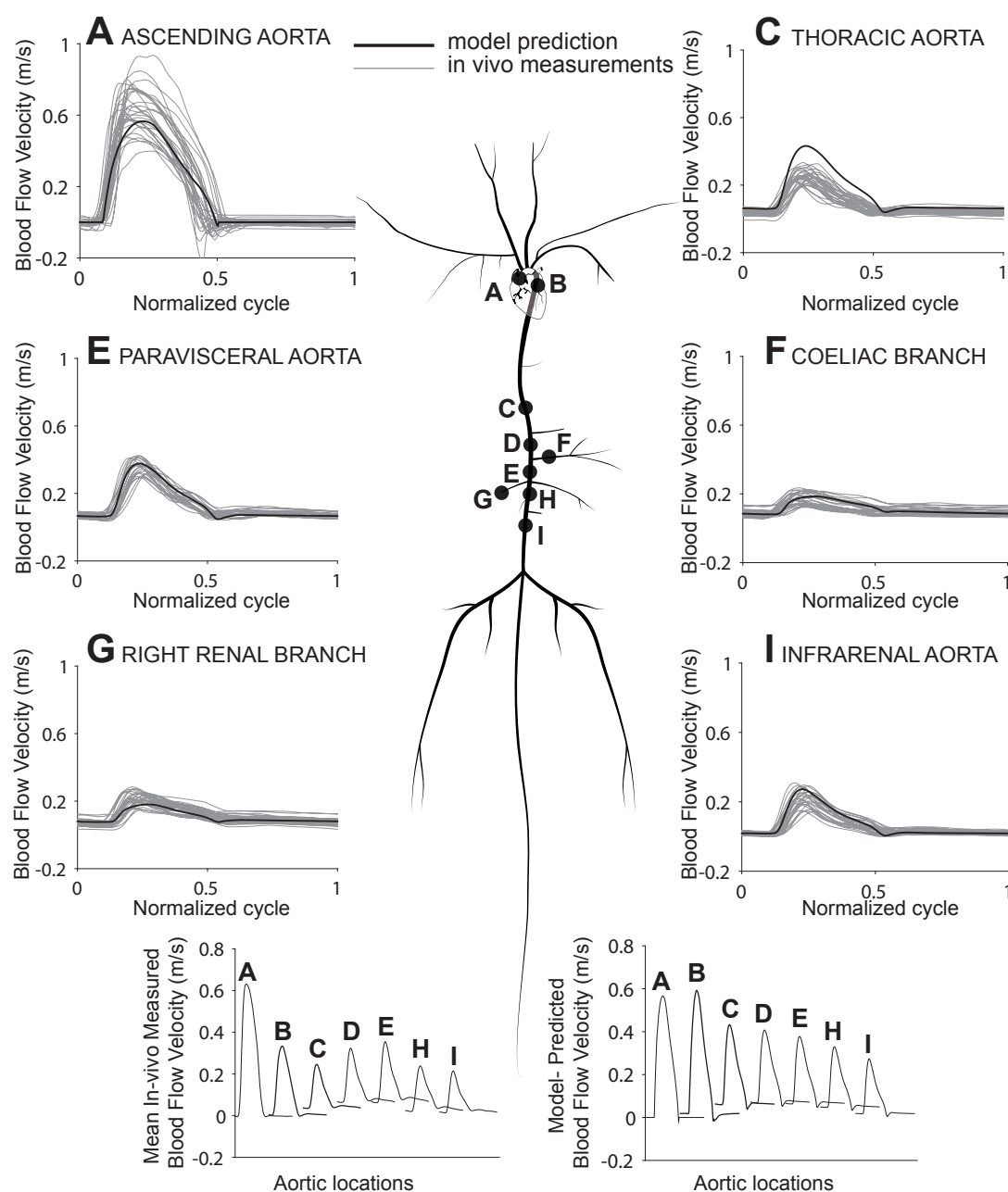


Figure 1.3: Model flow velocity predictions against in vivo flow velocity measurements over a normalized timescale at six locations along the arterial tree. The bottom panel depicts model flow velocity predictions at 7 aortic locations extending from proximal to distal abdominal aorta and the mean flow velocity waveform of the in vivo measurements performed on the same locations. A: ascending aorta, B: descending aorta, C: thoracic aorta, D: supraceliac aorta, E: paravisceral region, F: coeliac branch, G: right renal branch, H: I: infrarenal aorta.

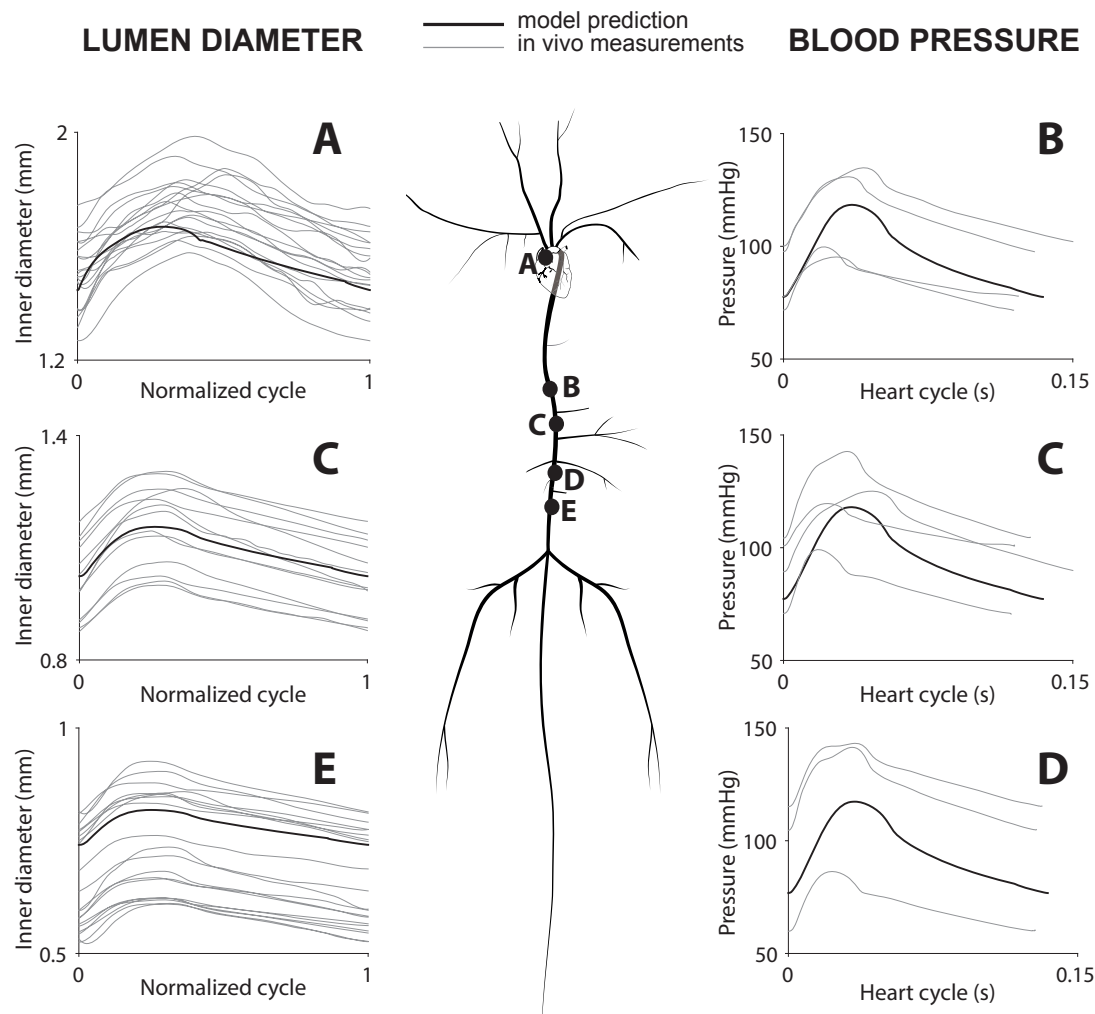


Figure 1.4: In vivo pressure and diameter measurements compared to model results at different aortic sites. The left panels show the model prediction of inner lumen diameter change over a normalized cardiac cycle against ultrasound MMode measurements performed at locations A, C and E. The right panels show the modelled prediction of aortic pressure over a normalized cardiac cycle against invasive pressure measurements at sites B, C and D. A: ascending, B: thoracic, C: supraceliac region, D: pararenal region, E: infrarenal region.

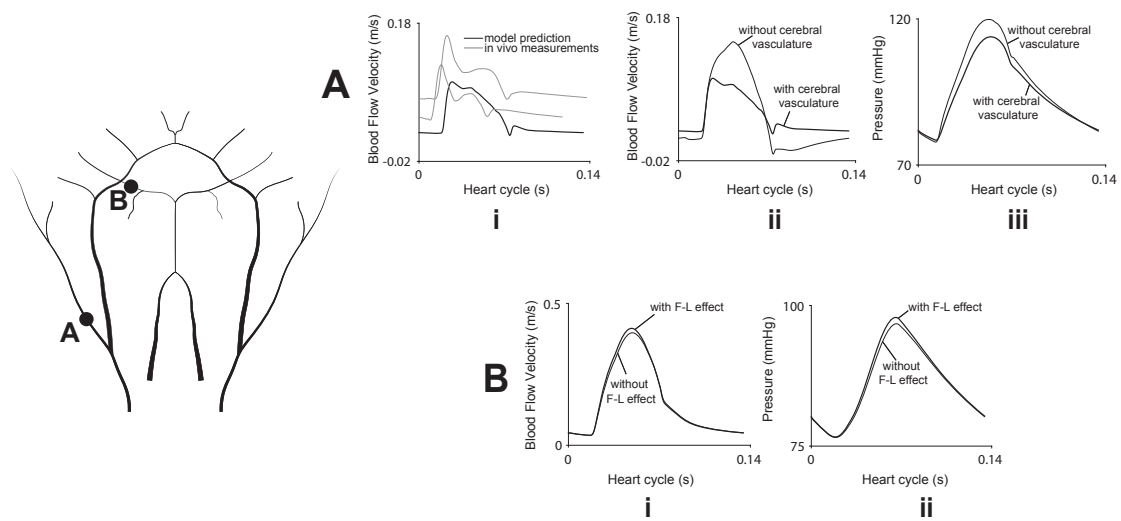


Figure 1.5: Influence of cerebral vasculature on model predictions. A. Influence of cerebral vasculature on model predictions in the right external carotid artery: i) model flow velocity prediction against in vivo velocity measurements in the same location, ii) Effect of brain vasculature omission on blood flow velocity waveform, iii) Effect of brain vasculature omission on pressure waveform. B. Fåhræus-Lindqvist (F-L) effect on blood flow velocity and pressure waveform in posterior cerebral C segment.

4 Discussion

The original 1D model of the human systemic arterial tree that formed the basis of this work was developed¹⁵ and improved¹⁹ in our lab, and has been successfully used as a research tool in a number of subsequent studies^{17,65}. Due to the fact that it includes a heart model, ventricular-vascular coupling, a detailed description of the cerebral circulation, and a detailed description of shear stress and wall viscoelasticity, the original model can be considered the most complete model available in literature. The effect of separate features on model predictions are demonstrated and discussed in detail in the original publication by Reymond et al.¹⁹. Combining data from a wide range of literature with a detailed description of the murine arterial anatomy, we have managed to translate the model into a murine setting, and to validate its predictions with in vivo flow velocity, pressure and diameter waveforms measured in a large sample of mice. Despite its generic character, the resulting in silico model provides pressure and flow velocity waveforms that faithfully reproduce the actual wave characteristics at all arterial locations.

Overall model validation

To the best of our knowledge, the most elaborate model of the murine vasculature is the recent FSI model of an anesthetized mouse by Cuomo et al.¹⁸. This model was developed based on data from one single animal and incorporates the central aorta and its major branches. Table 1.3 compares our 1D model output to values predicted by Cuomo et al.¹⁸ and literature

values. Cardiac output, stroke volume, ejection fraction and mean central pressure of the 1D model are within the range of published values. The central aPWV in both our 1D model and the 3D model of¹⁸ were above the range of aPWV values that have been measured with transit time methods. The reason is that in the 1D model we adapted the initial distensibility of the central aortic segments (Figure 1.2) to match the central aortic compliance obtained by Guo and Kassab³⁰. Transit time aPWV is not the most reliable measurement in mice since the relative measurement error on the transit distance is much larger than in humans^{18,20}. Therefore, we judged that the global value of accumulated local in vivo pressure-diameter loops performed by Guo and Kassab³⁰ yielded a more accurate and trustworthy value for central aortic compliance. This hypothesis is further corroborated by the close match of our total volume compliance with the value that was obtained by Segers et al. using ventricular pressure-volume loops in $n = 17$ anesthetized mice⁵⁹, while the latter was not used as an input for the model.

Model validation at major arterial locations

When interpreting the model validation, it is important to keep in mind that the model is based on averaged data and by definition provides generic pressure and flow waveforms. While these aim to be representative for the average young, male laboratory mouse on a C57BL/6J background, they can only be compared qualitatively, and not quantitatively, to individual measurements. Ideally, full validation would require a mouse-specific approach, where all input parameters defining the model (geometry, elastic properties, peripheral resistances, varying elastance of the heart) would be tuned to each specific animal, after which predicted pressures and flows could be compared quantitatively with the measured waveforms in the same animal. Clearly, this is an impossible task, as the technical limitations hampering such precise measurements are the very reason we need an *in silico* model. Instead, we opted to compare the model predictions to measurements obtained in mice that were not used to define the input for the model (i.e., the local flow split, pressure and distensibility) at these locations.

In general, modelled flow velocities correspond well to the *in vivo* measurements (Figure 1.3). However, while the modelled flow velocity predictions exhibit a gradual dampening along the main aortic segment, the *in vivo* measurements show a drop in the descending and thoracic aortic mean flow velocities, which is then followed by an increase of mean flow velocity in the abdominal aorta. Since there is no physiological reason for the velocity to drop locally, we believe that this discrepancy is due to a systematic underestimation of the measured velocity at the descending and thoracic arteries, rather than an error in the model. Given the curvature and branching of the local geometry in the descending aspects of the aortic arch, it is likely that the ultrasound measurements at these locations did not correspond to the centerline velocity. Another possibility is that, because of the spatially skewed velocity profile at the descending aorta⁶⁶, the ultrasound measurement at the center of the vessel did not correspond to the peak velocity of an ideal, perfectly parabolic velocity profile. Both effects would lead to an

underestimation of the measured velocities.

It is important to remark that the diameters shown in Figure 1.4 were not a direct output of the model, but were calculated a posteriori based on the nonlinear elastic instantaneous lumen area change under a distending pressure. Nevertheless, the diameter waveforms predicted by the model showed very good agreement with measured MMode diameter waveforms. Moreover, the general morphology of diameter and pressure waveforms was highly similar, as could be expected from literature⁶⁷. The pressure measurements were obtained in a set of C57BL/6J animals ($n = 5$). Despite the similar genetic background, age, gender and diet of the used experimental mice, pressure measurements showed significantly more inter and intra mice variability than the velocities or diameters (Table 1.2, Figure 1.4). As discussed in previous work²⁰, we hypothesize that this was most likely induced by (i) the invasive nature of the pressure measurements, as the inserted pressure probe alters local hemodynamics¹⁸ since it blocks the femoral artery and significantly obstructs the flow in the distal part of the abdominal aorta, and (ii) the long period of anesthesia (around 45 min) required for the combination of surgery (probe insertion) and pressure measurements. Therefore, we judged the velocity and diameter model validations most trustworthy for validation purposes. The modelled blood pressure in the tail was lower than the central blood pressure, and was found to be dependent on the amount of blood flow in the caudal artery. Higher blood flow to the caudal artery leads to higher viscous losses, resulting in a decrease of the mean blood pressure in the tail. As mice regulate the blood flow in the tail during thermoregulation, especially during anesthesia, these results confirm earlier findings that tail-cuff blood pressure measurements in anesthetized mice are to be interpreted with caution^{60,68}.

Model validation in small side branches

Model predictions in smaller branches could not be validated, since such measurements are technically very challenging: a rigid invasive pressure probe with a diameter of 0.4 mm cannot be inserted into the small side branches^{18,20}, while high-frequency ultrasound flirts with the limits of the achievable resolution at these locations. Nevertheless, confirming previous results in the human 1D model¹⁹, we found that inclusion of the cerebral tree is necessary for the accuracy of model predictions in the carotid arteries (Figure 1.5, panel A). Moreover, as we will see in Chapter 2, there seems to be a previously undetected role of small branches in the early phase of cardiovascular pathology. Therefore, we decided to include the cerebral tree and other small branches in the model, despite the lack of proper validation. In the near future, improvements in imaging technology might lead to a more extensive validation that would include physiological measurements at these locations.

Anesthesia

All in vivo experiments (micro-CT, high-frequency ultrasound as well as invasive pressures) were performed under anesthesia, and so were all flow rates, cardiac parameters and local

stiffness data that were extracted from literature. We did not attempt to convert all input and validation data into values that are representative for conscious mice. Instead, we chose to restrict the input of the model to measurements obtained under anesthesia, and thus de facto construct an *in silico* model representing the average anesthetized mouse. This choice was partly made for practical reasons, as it is neither possible nor ethically acceptable to perform *in vivo* measurements in conscious mice. Moreover a conversion of anesthetized to conscious data would have induced additional uncertainty and variability into the model. But we also believe that a model of anesthetized mice will prove more useful for the research community than a model for conscious mice, as it allows to investigate the influence of changes in anatomy or physiology *in silico* and compare the outcome to actual values measured *in vivo* (i.e., under anesthesia). Anesthesia slows down heart rate, reduces cardiac output⁶⁹, and reduces pulse pressure, and it is important to take these factors into account when interpreting model predictions.

Genetic background

Model predictions were initially compared to a limited number ($n = 5$) of non-invasive flow velocity and invasive pressure measurements in C57BL/6J mice. To account for the biological variation in our initial validation data, we complemented them with velocity and diameter measurements from $n = 47$ ApoE^{-/-} that were readily available as baseline data from a study on abdominal aortic aneurysm⁷⁰. This strategy enabled a more extensive, accurate and ethically justifiable validation of the model predictions since (i) many more animals and arterial locations could be included in the validation, and (ii) no additional animals needed to be sacrificed, which was after all the final goal of developing an *in silico* model. It is, however, important to keep in mind that ApoE^{-/-} mice are genetically different from wild type C57BL/6J mice. These hypercholesterolemic mice develop atherosclerotic plaques when they are put on a Western diet, and aneurysms when they are infused with angiotensin II. At the time of the measurements, they were on a normal diet, at a young age, and had not yet been subjected to any surgical or pharmacological intervention. To account for any variability induced by the different genetic background, we compared micro-CT measurements of the main aorta and major branches of 3 ApoE^{-/-} mice with the arterial tree obtained in wild type mice. Since no significant difference in segment diameters or segment lengths could be detected, dimensions from both groups were combined in the final arterial tree. Since we did not observe any morphological differences between diameter and flow velocity waveforms obtained from both strains, and since genetic background, age, gender and diet were similar in both groups, we decided to combine all data into one single model.

Of mice and men

Despite the many similarities between human and murine arterial anatomy, it would be wrong to simply dismiss the murine cardiovascular system as a smaller and faster version of the human one, which is also the reason why we acquired mouse-specific input for the entire

geometry and all boundary conditions, rather than downscaling the existing human model. For instance, while murine dimensions are much lower and murine heart rate is much higher, both blood viscosity and blood flow velocity are similar in mice and men. This has a number of implications.

First of all, mice have a much lower Reynolds and Womersley number^{71,72} and thus murine flow is more laminar and organized than human flow⁴³. In the numerical model of the human arterial tree, the Womersley number falls below 2.5 only in the radial, tibial and cerebral arteries. The Reynolds number drops below 175, which is the highest value it attains in the murine arterial tree, in the human cerebral segments, vertebral and external carotid arteries, as well as in the coronary arteries, the inner iliac and the inferior mesenteric artery. The Fåhræus-Lindquist effect has been included in our model to account for the drop in apparent blood viscosity in small vessels, but appears to have no significant effect on our results, even in the smallest vessels of the cerebral arterial network.

Arterial pulse wave velocity values in mice are slightly lower but in the same order of magnitude as values measured in humans⁷³, which means that pulse wave travels at similar speed in a much shorter system. In the human 1D model that formed the basis for this work, the aPWV was equal to 5.66 m/s⁷⁴ and the heart rate was 75 bpm (1.25 Hz), resulting in a wavelength of 4.5 meters predicted by the wave equation. At the same time the central aorta in the human model measured 0.51 m, which is only 11.3% of the wavelength. In our murine model, the aPWV value of 4.44 m/s and a heart rate of 445 bpm (7.4 Hz) result in a wavelength of approximately 0.6 m. The central aorta in the murine model equals 47.3 mm, which corresponds to 7.9% of wavelength. Since the ratio of wavelength to total aortic length is similar in the two cases, we would expect similar wave propagation behavior. However, there is no pulse pressure amplification in the mouse model as we move from the proximal aorta (PP = 41.7 mmHg) to the iliac bifurcation (PP = 40.2 mmHg). Instead, the pulse pressure is gradually dampened from the heart to the periphery. At the same time the model yields a drop in mean pressure of 5.5 mmHg from the proximal aorta to the distal abdominal part. On the other hand, when assuming inviscid flow, the model does exhibit a pulse pressure amplification of 36 mmHg in the proximal aorta to 42 mmHg at the iliac bifurcation, which is similar to the pulse pressure amplification observed in the human model. The high frictional losses thus override the effect of pulse pressure amplification in the mouse.

Model limitations and possibilities for improvement

Limitations related to the in vivo measurements (anesthesia, inter-mouse variability, genetic background) have been discussed above. From a modelling point of view, we believe that our model is state-of-the-art, as we managed to translate all features of the state-of-the-art 1D-model of the human arterial tree into a murine setting. Both the assets and the limitations of our model are therefore comparable to those of the human 1D model. The model neglects the venous circulation, the pulmonary circulation and the circulation of cerebrospinal fluid

surrounding intracranial arteries. Windkessel models employed in the cerebral circulation are based on assumptions and should be investigated in more detail. The varying elastance curve may not be invariant in the presence of cardiovascular disease⁷⁵, and the varying elastance model may not be the most appropriate to account for changes in pressure and volume during the cardiac cycle in anesthetized mice⁷⁶. Viscoelastic parameters were obtained from a limited number of canine arteries³⁹, and additional datasets on aortic wall viscoelasticity are needed to refine this aspect for both the human and the murine model. Finally, the input and validation of the model have been restricted to young male mice, while the cardiovascular anatomy and physiology change significantly with age as well as gender²². Future work will focus on the development of dedicated age- and gender dependent models, in which arterial dimensions, wall properties, peripheral impedances and cardiac function will be appropriately adjusted.

Conclusions and future work

We presented a versatile numerical model of the systemic arterial tree in mice. Detailed measurements of anatomy (obtained from *in vivo* micro-CT measurements) and physiology (obtained from high-frequency ultrasound measurements and literature data) were combined with a 1-D implementation of the Navier-Stokes equations to predict pressure and flow waveforms in 85 different branches. The output of the model has been shown to correspond well with pressure, diameter as well as velocity measurements obtained in mice that were not used as an input for the model. At a time of strong ethical considerations over animal testing, we believe that computational models have an important role to play. While specific biological experiments can and will obviously never be replaced by generic modelling results, our versatile 1D model is perfectly suited to serve as an alternative for *in vivo* proof-of-concept studies. Rather than performing cumbersome invasive measurements that often require to sacrifice the animals in order to gain insight into the physiology of altered experimental conditions (e.g., in case of the ligation of a specific artery or the increase of aortic stiffness), a wide range of different physiological conditions can be simulated in the model without sacrificing a single animal. The ability to simulate cardiovascular pathology (e.g., aortic valve insufficiency, aortic aneurysm, stenosis, hypertension) or operative measures affecting the arterial anatomy (e.g., aortic ligation, castration, amputation) prior to or instead of sacrificing animals, can lead to the reduction and ultimate replacement of the amount of sacrificed animals in (the pilot stage of) newly developed experimental techniques and thus facilitate the implementation of the 3R's principle in research practice. The model could also lead to the derivation of central pressures from tail cuff measurements, through a transfer function.

Bibliography

- [1] P. M. Treuting, S. M. Dintzis, and K. S. Montine. *Introduction. In Comparative Anatomy and Histology - A Mouse and Human Atlas, (1–6)*. Elsevier Inc, London, 2012.
- [2] L. a Pennacchio. Insights from human/mouse genome comparisons. *mammalian genome: official journal. of the International Mammalian Genome Society*, 14(7):429–36, 2003.
- [3] Bram Trachet, M. Renard, C. Van der Donckt, S. Deleye, J. Bols, G. R. Y. De Meyer, S. Staelens, B. L. Loeys, and P. Segers. Longitudinal follow-up of ascending versus abdominal aortic aneurysm formation in angiotensin ii-infused apoe^{-/-} mice. *Artery Research*, 8(1):16–23, 2014.
- [4] C. Van der Donckt, J. L. Van Herck, and D. M. Schrijvers. *Elastin Fragmentation in Atherosclerotic Mice Leads to Intraplaque Neovascularization, Plaque Rupture, Myocardial Infarction, Stroke, and Sudden Death*. 2014.
- [5] D. De Wilde, B. Trachet, and C. Van der Donckt. Vulnerable plaque detection and quantification with gold particle-enhanced computed tomography in atherosclerotic mouse models. *Molecular imaging*, 14:9–19, 2015.
- [6] J. C. Reed and K. C. Herold. Thinking bedside at the bench: The nod mouse model of t1dm. *Nature Reviews Endocrinology*, 11(5):308–14, 2015.
- [7] N. Yamaguchi, N. Takahashi, and L. Xu. Early cardiac hypertrophy in mice with impaired calmodulin regulation of cardiac muscle ca²⁺ release channel. *The Journal of Clinical Investigation*, 117(5):1344–53, 2007.
- [8] L. Campens, M. Renard, and B. Trachet. Intrinsic cardiomyopathy in marfan syndrome: Results from inand ex-vivo studies of the fbn1(c1039g/+) model and longitudinal findings in humans. *pediatric research*, 2015 2015.
- [9] W. Nichols, M. O’Rourke, and C. Vlachopoulos. *Contours of Pressure and Flow Waves in Arteries. In McDonald’s Blood Flow in Arteries - Theoretical, experimental and clinical principles*. CRC Press, Taylor & Francis Group, Boca Raton, 2011.
- [10] C. Casteleyn, B. Trachet, and D. Van Loo. Validation of the murine aortic arch as a model to study human vascular diseases. *Journal of anatomy*, 216(5):563–71, 2010.
- [11] A. P. Avolio. Multi-branched model of the human arterial system. *Medical & biological engineering & computing*, 18:709–18, 1980.
- [12] D. Bessems, M. Rutten, and F. Van De Vosse. A wave propagation model of blood flow in large vessels using an approximate velocity profile function. *Journal of fluid mechanics*, 580:145–68, 2007.

Bibliography

- [13] J. P. Mynard and J. J. Smolich. One-dimensional haemodynamic modeling and wave dynamics in the entire adult circulation. *Annals of Biomedical Engineering*, 43(6):1443–60, 2015.
- [14] S. J. Sherwin, V. Franke, and J. Peiro. One-dimensional modelling of a vascular network in space-time variables. *Journal of engineering mathematics*, 47:217–50, 2003.
- [15] Nikos Stergiopoulos, D. F. Young, and T. R. Rogge. Computer simulation of arterial flow with application to arterial and aortic stenoses. *Journal of biomechanics*, 25(12):1477–1488, 1992.
- [16] R. R. Wemple and L. Mockros. Pressure and flow in the systemic arterial system. *Journal of biomechanics*, 5:629–41, 1972.
- [17] O. Vardoulis, E. Coppens, and B. Martin. Impact of aortic grafts on arterial pressure: A computational fluid dynamics study. *European Journal of Vascular and Endovascular Surgery*, 42(5):704–10, 2011.
- [18] F. Cuomo, J. Ferruzzi, and J. Humphrey. An experimental–computational study of catheter induced alterations in pulse wave velocity in anesthetized mice. *annals of biomedical engineering*. D., et al, 2015.
- [19] Philippe Reymond, Fabrice Merenda, Fabienne Perren, Daniel Rüfenacht, and Nikos Stergiopoulos. Validation of a one-dimensional model of the systemic arterial tree. *American journal of physiology. Heart and circulatory physiology*, 297(1):H208–H222, 2009.
- [20] B. Trachet, R. A. Fraga-Silva, and F. J. Londono. Performance comparison of ultrasound-based methods to assess aortic diameter and stiffness in normal and aneurysmal mice. *PLoS ONE*, 10(5):0129007, 2015.
- [21] B. De Man, J. Nuyts, and P. Dupont. An iterative maximum-likelihood polychromatic algorithm for ct. *IEEE transactions on medical imaging*, 20(10):999–1008, 2001.
- [22] A. K. Reddy, Y. H. Li, and T. T. Pham. Measurement of aortic input impedance in mice: Effects of age on aortic stiffness. *American journal of physiology. Heart and circulatory physiology*, 285(4):1464–70, 2003.
- [23] S. I. Rabben, S. Bjærum, and V. Sørhus. Ultrasound-based vessel wall tracking: An auto-correlation technique with rf center frequency estimation. *Ultrasound in Medicine and Biology*, 28(4):507–17, 2002.
- [24] R. Holenstein, P. Niederer, and M. Anliker. A viscoelastic model for use in predicting arterial pulse waves. *Journal of biomechanical engineering*, 102:318–25, 1980.
- [25] G. J. Langewouters. Visco-elasticity of the human aorta in vitro in relation to pressure and age. *Free*, 1982.

-
- [26] G. J. Langewouters, K. H. Wesseling, and W. J. Goedhard. The static elastic properties of 45 human thoracic and 20 abdominal aortas in vitro and the parameters of a new model. *Journal of biomechanics*, 17(6):425–35, 1984.
- [27] A. Agianniotis and N. Stergiopoulos. Wall properties of the apolipoprotein e-deficient mouse aorta. *Atherosclerosis*, 223(2):314–20, 2012.
- [28] V. Bolduc, E. Baraghis, and N. Duquette. Catechin prevents severe dyslipidemia-associated changes in wall biomechanics of cerebral arteries in *ldlr*^{-/-}:*hapob*^{+/+} mice and improves cerebral blood flow. *American journal of physiology. Heart and circulatory physiology*, 302(6):1330–39, 2012.
- [29] R. M. Fitch, J. C. Rutledge, and Y. X. Wang. Synergistic effect of angiotensin ii and nitric oxide synthase inhibitor in increasing aortic stiffness in mice. *American journal of physiology. Heart and circulatory physiology*, 290(3):1190–98, 2006.
- [30] Xiaomei Guo and Ghassan S. Kassab. Variation of mechanical properties along the length of the aorta in *c57bl/6* mice. *American Journal of Physiology-Heart and Circulatory Physiology*, 285(6):H2614–H2622, 2003. PMID: 14613915.
- [31] V. Herold, M. Parczyk, and P. Mörchel. *In Vivo Measurement of Local Aortic Pulse-Wave Velocity in Mice with MR Microscopy at 17.6 Tesla. Magnetic resonance in medicine: official journal*, volume 61, pages 1293–99. 2009.
- [32] J. Luo, K. Fujikura, and L. S. Tyrie. Pulse wave imaging of normal and aneurysmal abdominal aortas in vivo. *IEEE transactions on medical imaging*, 28(4):477–86, 2009.
- [33] R. Williams, A. Needles, and E. Cherin. Noninvasive ultrasonic measurement of regional and local pulse-wave velocity in mice. *Ultrasound in medicine & biology*, 33(9):1368–75, 2007.
- [34] Y. X. Wang. Cardiovascular functional phenotypes and pharmacological responses in apolipoprotein e deficient mice. *Neurobiology of aging*, 26(3):309–16, 2005.
- [35] J. E. Wagenseil, N. L. Nerurkar, and R. H. Knutsen. Effects of elastin haploinsufficiency on the mechanical behavior of mouse arteries. *American journal of physiology. Heart and circulatory physiology*, 289(3):1209–17, 2005.
- [36] V. P. Le, R. H. Knutsen, and R. P. Mecham. Decreased aortic diameter and compliance precedes blood pressure increases in postnatal development of elastin-insufficient mice, 2011 2011.
- [37] X. Guo, M. J. Oldham, and M. T. Kleinman. Effect of cigarette smoking on nitric oxide, structural, and mechanical properties of mouse arteries. *American journal of physiology. Heart and circulatory physiology*, 291(5):2354–61, 2006.

Bibliography

- [38] L. Tian, Z. Wang, and R. S. Lakes. Comparison of approaches to quantify arterial damping capacity from pressurization tests on mouse conduit arteries. *Journal of biomechanical engineering*, 135(5):54504, 2013.
- [39] D. H. Bergel. The dynamic elastic properties of the arterial wall. *The Journal of Physiology*, 156(3):458–69, 1961.
- [40] R. Fahraeus and T. Lindqvist. The viscosity of the blood in narrow capillary tubes. *American journal of physiology*, 96:562–68, 1930.
- [41] M. Sugihara-Seki and B. M. Fu. Blood flow and permeability in microvessels. *Fluid Dynamics Research*, 37(1-2):"SPEC." "82–132.", 2005.
- [42] T. W. Secomb and A. R. Pries. Blood viscosity in microvessels: Experiment and theory. *Comptes Rendus Physique*, 14(6):470–78, 2013.
- [43] Bram Trachet, Marjolijn Renard, Gianluca De Santis, Steven Staelens, Julie De Backer, Luca Antiga, Bart Loeys, and Patrick Segers. An integrated framework to quantitatively link mouse-specific hemodynamics to aneurysm formation in angiotensin ii-infused apoe^{-/-} mice. *Annals of Biomedical Engineering*, 39(9):2430, 2011.
- [44] K. Sagawa. The end-systolic pressure-volume relation of the ventricle: Definition, modifications and clinical use. *Circulation*, 63(6):1223–27, 1981.
- [45] H. Senzaki, C. Chen, and D. Kass. Single-beat estimation of end-systolic pressure-volume relation in humans. a new method with the potential for noninvasive application. *Circulation*, 94(10):2497–2506, 1996.
- [46] D. Georgakopoulos, W. A. Mitzner, and C. H. Chen. In vivo murine left ventricular pressure-volume relations by miniaturized conductance micromanometry. *The American journal of physiology*, 274(4):1416–22, 1998.
- [47] O. H. Cingolani and D. a Kass. Pressure-volume relation analysis of mouse ventricular function. *American journal of physiology. Heart and circulatory physiology*, 301(6):2198–2206, 2011.
- [48] P. Pacher, T. Nagayama, and P. Mukhopadhyay. Measurement of cardiac function using pressure-volume conductance catheter technique in mice and rats. *Nature protocols*, 3(9):1422–34, 2008.
- [49] K. M. Shioura, D. L. Geenen, and P. H. Goldspink. Assessment of cardiac function with the pressure-volume conductance system following myocardial infarction in mice. *American journal of physiology. Heart and circulatory physiology*, 293(5):2870–77, 2007.
- [50] B. Yang, D. F. Larson, and R. Watson. Age-related left ventricular function in the mouse: Analysis based on in vivo pressure-volume relationships. *The American journal of physiology*, 277(5):1906–13, 1999.

-
- [51] D. J. Lips, T. van der Nagel, and P. Steendijk. Left ventricular pressure-volume measurements in mice: Comparison of closed-chest versus open-chest approach. *Basic research in cardiology*, 99(5):351–59, 2004.
- [52] S. Nemoto, G. DeFreitas, and D. L. Mann. Effects of changes in left ventricular contractility on indexes of contractility in mice. *American journal of physiology. Heart and circulatory physiology*, 283(6):2504–10, 2002.
- [53] D. J. Grieve, A. C. Cave, and J. a Byrne. Analysis of ex vivo left ventricular pressure-volume relations in the isolated murine ejecting heart. *Experimental physiology*, 89(5):573–82, 2004.
- [54] I. L. Grupp, a Subramaniam, and T. E. Hewett. Comparison of normal, hypodynamic, and hyperdynamic mouse hearts using isolated work-performing heart preparations. *The American journal of physiology*, 265(4):1401–10, 1993.
- [55] P. Segers, N. Stergiopulos, and N. Westerhof. Quantification of the contribution of cardiac and arterial remodeling to hypertension, 2000 2000.
- [56] P. Segers, N. Stergiopulos, and N. Westerhof. Relation of effective arterial elastance to arterial system properties, 2002 2002.
- [57] N. Stergiopulos, B. E. Westerhof, and N. Westerhof. Total arterial inertance as the fourth element of the windkessel model, 1999 1999.
- [58] N. Westerhof, J. W. Lankhaar, and B. Westerhof. The arterial windkessel. *Medical & Biological Engineering & Computing*, 47(2):131–41, 2009.
- [59] P. Segers, D. Georgakopoulos, and M. Afanasyeva. Conductance catheter-based assessment of arterial input impedance, arterial function, and ventricular-vascular interaction in mice. *American journal of physiology. Heart and circulatory physiology*, 288(3):1157–64, 2005.
- [60] C. J. Gordon. *Temperature Regulation in Laboratory Rodents*. Cambridge University Press, 1993.
- [61] R. E. Hoyt, J. V. Hawkins, and M. B. St Clair. *Mouse Physiology*, volume 3, pages 23–90. Elsevier Inc, 2007.
- [62] Michael A. Laflamme, Manu M. Sebastian, and Bernard S. Buetow. 10 - cardiovascular. In Piper M. Treuting and Suzanne M. Dintzis, editors, *Comparative Anatomy and Histology*, pages 135 – 153. Academic Press, San Diego, 2012.
- [63] Craig J. Hartley, Anilkumar K. Reddy, Sridhar Madala, Baby Martin-McNulty, Ronald Vergona, Mark E. Sullivan, Meredith Halks-Miller, George E. Taffet, Lloyd H. Michael, Mark L. Entman, and Yi-Xin Wang. Hemodynamic changes in apolipoprotein e-knockout mice. *American Journal of Physiology-Heart and Circulatory Physiology*, 279(5):H2326–H2334, 2000. PMID: 11045969.

Bibliography

- [64] Yi-Xin Wang, Meredith Halks-Miller, Ron Vergona, Mark E. Sullivan, Richard Fitch, Cornell Mallari, Baby Martin-McNulty, Valdecil da Cunha, Ana Freay, Gabor M. Rubanyi, and Katalin Kauser. Increased aortic stiffness assessed by pulse wave velocity in apolipoprotein e-deficient mice. *American Journal of Physiology-Heart and Circulatory Physiology*, 278(2):H428–H434, 2000. PMID: 10666072.
- [65] O. Vardoulis, T. G. Papaioannou, and N. Stergiopoulos. On the estimation of total arterial compliance from aortic pulse wave velocity. *Annals of Biomedical Engineering*, 1(8):10–1007, 2012.
- [66] A. Feintuch, P. Ruengsakulrach, and A. Lin. Hemodynamics in the mouse aortic arch as assessed by mri, ultrasound, and numerical modeling. 884–92, 2007 2007.
- [67] C. Hartley, A. Reddy, and M. Entman. Characterization of arterial wave propagation and reflection in mice. conference proceedings. *IEEE Engineering in Medicine and Biology Society. IEEE Engineering in Medicine and Biology Society. Conference*, 1:601–4, 2005.
- [68] X. Zhao, D. Ho, and S. Gao. Arterial pressure monitoring in mice. current protocols in mouse. *biology*, 1:105–22, 2011.
- [69] B. J. a Janssen, T. De Celle, and J. J. M. Debets. Effects of anesthetics on systemic hemodynamics in mice. *American journal of physiology. Heart and circulatory physiology*, 287(4):1618–24, 2004.
- [70] Bram Trachet, Rodrigo A. Fraga-Silva, Alessandra Piersigilli, Alain Tedgui, Jessica Sordet-Dessimoz, Alberto Astolfo, Carole Van der Donckt, Peter Modregger, Marco F. M. Stampanoni, Patrick Segers, and Nikolaos Stergiopoulos. Dissecting abdominal aortic aneurysm in Ang II-infused mice: suprarenal branch ruptures and apparent luminal dilatation. *Cardiovascular Research*, 105(2):213–222, 12 2014.
- [71] J. Suo, D. E. Ferrara, and D. Sorescu. Hemodynamic shear stresses in mouse aortas: Implications for atherogenesis. *Arteriosclerosis, Thrombosis, and Vascular Biology*, 27(2):"346–51." "ATV.0000253492.45717.46.", 2007.
- [72] B. Trachet, A. Swillens, and D. Van Loo. The influence of aortic dimensions on calculated wall shear stress in the mouse aortic arch. *Computer methods in biomechanics and biomedical engineering*, 12(5):491–99, 2009.
- [73] W. Nichols, M. O'Rourke, and C. Vlachopoulos. *McDonald's Blood Flow in Arteries: Theoretical, Experimental and Clinical Principles*. Oxford University Press, New York, 4th ed edition, 1998.
- [74] P. Boutouyrie and S. J. Vermeersch. Determinants of pulse wave velocity in healthy people and in the presence of cardiovascular risk factors: Establishing normal and reference values. *European Heart Journal*, 31(19):2338–50, 2010.

- [75] D. Jegger, A. S. Mallik, and M. Nasratullah. The effect of a myocardial infarction on the normalized time-varying elastance curve. *Journal of applied physiology*, 102(3):1123–29, 2007.
- [76] T. E. Claessens, D. Georgakopoulos, and M. Afanasyeva. Nonlinear isochrones in murine left ventricular pressure-volume loops: How well does the time-varying elastance concept hold? *American journal of physiology. Heart and circulatory physiology*, 290(4):1474–83, 2006.

Chapter 2

Early characterization of Angiotensin II-induced dissections: do side branches hold the key?

Bram Trachet^{1,2}, Lydia Aslanidou^{*2}, Alessandra Piersigilli³, Rodrigo A. Fraga-Silva², Jessica Sordet-Dessimoz⁴, Pablo Villanueva-Perez⁵, Marco F.M. Stampanoni^{5,6}, Nikos Stergiopoulos², Patrick Segers¹

¹ *bioMMeda, Ghent University, Ghent, Belgium*

² *Institute of Bioengineering, École Polytechnique Fédérale de Lausanne, Switzerland*

³ *Pathology and Laboratory Medicine, Weill Medicine Cornell New York, NY, USA*

⁴ *Histology Core Facility, École Polytechnique Fédérale de Lausanne, Lausanne, Switzerland*

⁵ *Swiss Light Source, Paul Scherrer Institute, Villigen, Switzerland*

⁶ *Institute for Biomedical Engineering, University and ETH Zürich, Zürich, Switzerland*

Published in Cardiovascular Research (2017) 113, 1230–1242 doi:10.1093/cvr/cvx128

*In comparison to the original published manuscript, the work presented in this chapter has been restricted to the findings relevant to onset of disease, which were also the contribution of LA to the study. Other findings of this study, focused on more advanced stages of Angiotensin II-induced dissections, have been summarized in section 5.3 in of the Introduction.

1 Introduction

Ever since its first appearance, Angiotensin II (Ang II) infusion into hypercholesterolemic ApoE-/- mice has been a mainstay in the study abdominal aortic aneurysm (AAA)^{1,2,3}. Despite reproducing several clinical features of human AAA such as elastin degradation, macrophage infiltration, thrombus formation and re-endothelialization, other observations have remained unexplained, such as the suprarenal location of lesions and the role of aortic side branches in

disease evolution^{4,5,6,7}. As we saw in the Introduction (section 5.3), Trachet et al. have used a novel synchrotron-based imaging technique (phase contrast X-ray tomographic microscopy; PCXTM) to show that the luminal dilatation in Ang II-infused, anti-TGF-beta injected C57Bl6 mice is the result of a medial tear, occurring near the ostium of suprarenal side branches. This tear was sometimes accompanied by a false channel with varying degrees of severity, and in some cases it resulted in the formation of an intramural (but not intraluminal) hematoma (IMH)⁸. Differently from human aortic dissection (AD), the medial tear transected all of the elastic laminae and no re-entry into the true lumen was observed. They therefore described these lesions as dissecting AAAs, a term previously coined by other researchers^{9,10}. In a follow-up review article, they showed that synchrotron-based findings on dissecting aneurysms were compatible with virtually all existing (2D-imaging based) literature on the abdominal lesions of Ang II-infused ApoE-/- mice, and that the luminal dilatation in these models (if present at all) was more reminiscent of AD than of AAA^{11,12}. But while these observations provided new insights into the model, a number of intriguing research questions have remained unsolved. Why do dissecting aneurysms primarily develop near suprarenal side branches? And why are some branches more affected than others⁷? A better understanding of the interaction between side branches and the initiation of disease in Ang II-infused mice could substantially improve our understanding of the mechanisms leading to the formation of AAA and AD in humans¹³.

To answer the lingering questions of this mouse model, appropriate imaging has to be used able to capture early changes within the murine vascular wall. Accurate morphologic evaluation at microscopic level can be achieved through histopathology, but this relies on two-dimensional sections that make 3D reconstruction and analysis challenging if not impossible⁹. In vitro (vascular casting) as well as in vivo (contrast enhanced) micro-CT offer an isotropic pixel size up to 50 μm but are restricted to the blood-filled aortic lumen and do not allow for visualization of the aortic wall⁵. In vivo micro-MRI provides soft tissue contrast visualizing the aortic wall, but the typical through-plane distance is too coarse (order of magnitude 100–200 μm) for detailed 3D analyses^{14,15,16}. Finally, 3D ultrasound offers a detailed in-plane pixel size (up to 15 μm) and through-plane distance (up to 35 μm) as well as limited soft tissue contrast, but it is a highly operator-dependent technique that is often subject to interpretation¹⁷. Differential phase contrast X-ray tomographic microscopy (PCXTM) uses synchrotron radiation to overcome all these limitations as it combines detailed soft tissue contrast (obtained through grating interferometry) with an isotropic pixel size of 6.5 μm ¹⁸ (cf. section 4.1 of the Introduction).

Here, we present an observational study in which we intend to characterize the early stage of lesion formation in this model. The thoraco-abdominal aorta of Ang II-infused ApoE-/- mice was studied in vivo with high-frequency ultrasound and contrast-enhanced micro-CT, and ex vivo with PCXTM and PCXTM-guided histology. In this study, the use of contrast-enhanced micro-CT has been done intentionally, as opposed to incidentally in the first synchrotron study we described in section 5.3 of the Introduction. Following the incidental discovery of micro-CT contrast agent infiltrations in the aortic wall, here we have used the same contrast agent Exitron for two reasons. Its infiltrations in the aortic wall can point us to the exact

location of primary damage after short-term AngII infusion, while it also serves for the in vivo follow-up of animals with micro-CT.

2 Methods

Animals

All the procedures were approved by the Ethical Committee of Canton Vaud, Switzerland (EC 2647.2) and performed according to the guidelines from Directive 2010/63/EU of the European Parliament on the protection of animals used for scientific purposes. Male ApoE ^{-/-} mice on a C57Bl/6J background were purchased from Janvier (Saint Berthevin, France). At the age of 12 weeks, n=12 mice were implanted with a 200 µl osmotic pump (model Alzet 2004; Durect Corp, Cupertino, CA) filled with a solution of angiotensin II in sterile saline 0.9% (Bachem, Bubendorf, Switzerland), on the right flank via an incision in the scapular region. During the implantation mice were anesthetized with 1.5% isoflurane. For every administration of isoflurane mentioned throughout this dissertation for induction and maintenance of anesthesia, we note that we have used compressors that concentrate room air to oxygen levels between 85% and 91% (model: Sequal Integra E-Z Oxygen concentrator), and deliver this concentrated air to the inhalation anesthesia system. To avoid interference with the micro-CT images, the metal flow divider inside the pump was replaced by a PEEK alternative (Durect Corp, Cupertino, CA). Each pump infused Angiotensin II at 1000 ng/kg/ min¹⁹, for a total duration of 3 days. Prior to implantation the animals received buprenorphine (0.08mg/kg, subcutaneous) as analgesic. Water and regular mouse diet were available ad libitum and animals were observed daily after the implantation of pumps.

One animal died with hemothorax after in vivo imaging on day 3, but prior to sacrifice. Another animal of the study experienced a medial tear and intramural hematoma formation in the abdominal aorta during the micro-CT scan at day 3. This animal was treated separately, as a special case of this study. The remaining n=10 animals were sacrificed after 3 days of AngII infusion and studied for the occurrence of micro-ruptures.

In vivo ultrasound and micro-CT imaging

Animals were anesthetized with 1.5% isoflurane during the in vivo scans (in concentrated air with oxygen levels 85% and 91%, see above). Ultrasound imaging was performed with a high-frequency ultrasound device (Vevo 2100, VisualSonics, Toronto, Canada) using a linear array probe (MS 550D, frequency 22–55MHz). Animals that were followed up in vivo with a contrast-enhanced, non-gated micro-CT were injected in the lateral tail vein with 4µl/gram body weight of ExiTron nano 12000 (Miltenyi Biotec, Bergisch Gladbach, Germany) (cf. section 4.1 of the Introduction). After the experiments, mice were anesthetized with Ketamine/Xylazine (100 mg/kg and 15 mg/kg, respectively) and the aortic tissue was carefully harvested post mortem.

Ex vivo PCXTM imaging

After sacrifice, the aorta was flushed in situ by transcardiac perfusion of PBS (pH 7.4) through the left ventricle. The abdominal aorta of both intact and transmurally ruptured dissecting AAAs was carefully excised, and samples were fixed by immersion in 4% paraformaldehyde (PFA) in 0.15 mMPBS. The samples were scanned at the TOMCAT beamline of the Swiss Light Source, Paul Scherrer Institut, Villigen, Switzerland for imaging. Differential phase contrast X-ray tomographic microscopy (PCXTM) uses synchrotron radiation combines detailed soft tissue contrast (obtained through grating interferometry) with an isotropic pixel size of 6.5 μm (as described in section 4.1 of the Introduction).

PCXTM-guided histology

After PCXTM scanning, the samples were fixed as mentioned above, processed, and embedded in paraffin according to standard histological procedures. Four micrometre thick paraffin sections were carefully compared with the corresponding PCXTM images under a Leica DM750 bright field microscope to spot the exact rupture sites. Selected slides were stained with Hematoxylin-Eosin (H&E) to assess general morphology. Miller stain and Sirius red F3B (CI35782, Direct red 80) were combined to specifically highlight elastic fibers and collagen on the same section. All slides were photographed using an automated slide scanner (VI20-L100, Olympus).

Statistics

Since only a limited number of animals was sacrificed, the ex vivo PCXTM-based results had too few samples to ascertain normality. The measurements were analysed using a Kruskal-Wallis analysis, followed by a post-hoc Dunn's test for pairwise comparisons. P-value < 0.05 was considered significant (*).

Micro-CT and PCXTM image processing

All reconstructed 3D datasets were semi-automatically segmented into 3D models using the commercial software package Mimics (Materialise, Leuven, Belgium). As a first segmentation step, the aorta was manually thresholded and segmented where necessary. When the resulting segmentation was judged sufficiently accurate, a separate threshold was applied for the contrast agent infiltrations on the vascular wall. The volume of exitron surrounding the orifice of each branch was then quantified separately for each branch. Perpendicular planes were imposed as shown on Figure 2.1 at branching points to define circumferential quadrants. The number of minor side branches (meaning besides the celiac, superior mesenteric, right and left renal) which had contrast agent infiltration around their orifice were also quantified.

3 Results

Early microstructural damage around side branches

Ex vivo PCXTM images revealed that in $n=8/10$ animals sacrificed after 3 days of AngII infusion, despite a gross normal appearance of the aortic samples, the contrast agent had infiltrated the tunica media of the vascular wall (Figure 2.1a). These infiltrated aggregates, denoting focal microstructural damage, were predominantly found at the orifice of major abdominal side branches, with a high preference for the celiac and superior mesenteric arteries in particular (Figure 2.1b).

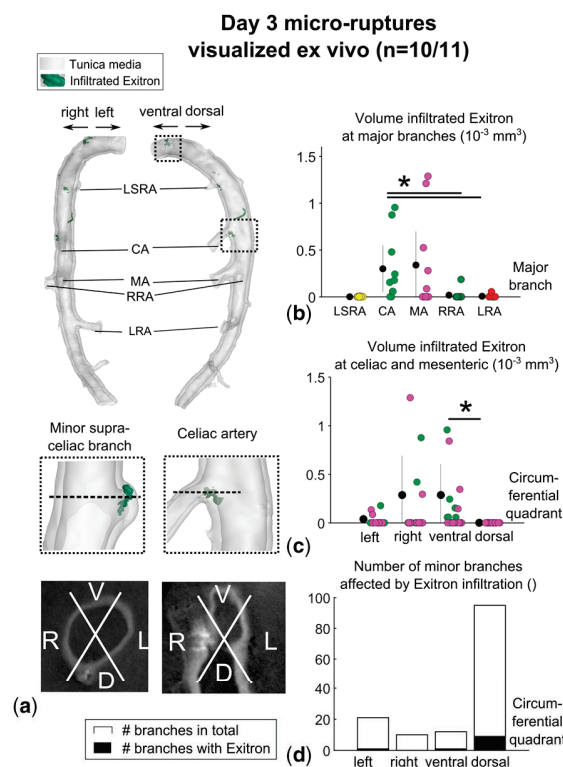


Figure 2.1: Early events in Angiotensin II-infused mice ($n=10/11$, since $n=1/11$ animal presented in vivo rupture). (a) 3D (segmented) and 2D PCXTM images of early-stage damage as visualized with Exitron. (b) Scatter plot showing the volume of Exitron infiltration at each of the five major branches. (c) Scatter plot showing the circumferential variation of Exitron infiltration at the level of the celiac and superior mesenteric arteries (quadrants shown in panel a, bottom right). (d) Bar plot showing how the number of minor branches affected by Exitron infiltration varies across the circumference (quadrants as in panel a, bottom left). * $P < 0.05$. V: ventral, D: dorsal, R: right, L: left, LSRA: left suprarenal artery, CA: celiac artery, MA: mesenteric artery, RRA: right renal artery, LRA: left renal artery.

Circumferential distribution of vascular damage

We separated the aortic wall in quadrants to capture trends in the distribution of contrast agent infiltrates along the circumference of the aorta. At the level of the most affected abdominal branches, the celiac and the superior mesenteric arteries, the infiltration was most pronounced in the ventral aspect of the aorta and sometimes left and right of the orifice, but never in the dorsal aspect (Figure 2.1c).

Given the resolution of the imaging technique, we further assessed the circumferential variation in microstructural damage at the level of smaller suprarenal branches (such as minor subcostal arteries). Exitron infiltration occurred predominantly around the ostia of dorsal branches, which were also the most abundant (Figure 2.1d).

In vivo and ex vivo imaging of an ongoing aortic dissection

We serendipitously witnessed an aortic dissection play out in vivo during the micro-CT scan of an animal on the third day of AngII infusion. Figure 2.2 shows how the free-flowing blood outside the media and the resulting intramural hematoma evolved over time. A false channel with a large volume of free-flowing blood was visible on the initial micro-CT scan (Figure 2.2a). Imaging with Color Doppler 1 hour after the first microCT scan showed absence of blood flow within the intramural hematoma. The 2D images of the follow-up micro-CT scan performed just 2.5 hours later show how most of the free-flowing blood had already coagulated, evidenced further by Exitron infiltration as dense white clusters within the false channel (Figure 2.2b). The animal was sacrificed 4 hours after the initial micro-CT scan and imaged with PCXTM, which showed that the adventitial dissection and IMH had extended even further cranial and caudal of the medial tear. The medial tear that had been the source of free-flowing blood could be visualized, and the coagulation patterns around the initial tear could also be seen on the ex vivo PCXTM images (Figure 2.2c, also the 2D panels in e). PCXTM image-guided histology (Figure 2.2e, bottom) with SR-Miller and H&E showed how coagulation had taken place at the level of the tear, but not yet as organized at the cranial and caudal ends of the hematoma 4 hours after the live dissection.

4 Discussion

The suprarenal location of dissecting aneurysms: do side branches hold the key?

Motivated by previous observations of outstandingly frequent medial tears around side branches of fully dissected abdominal mouse aortas, as evidenced by histomorphometry^{6,7} and high-resolution imaging⁸, we set out to assess whether branches may also be implicated in the early stage of disease process. Here we have made use of a previous serendipitous finding of contrast agent percolations in the aortic wall, and have used contrast agent as a marker for vascular damage. We report that microstructural damage in the abdominal aorta occurs as

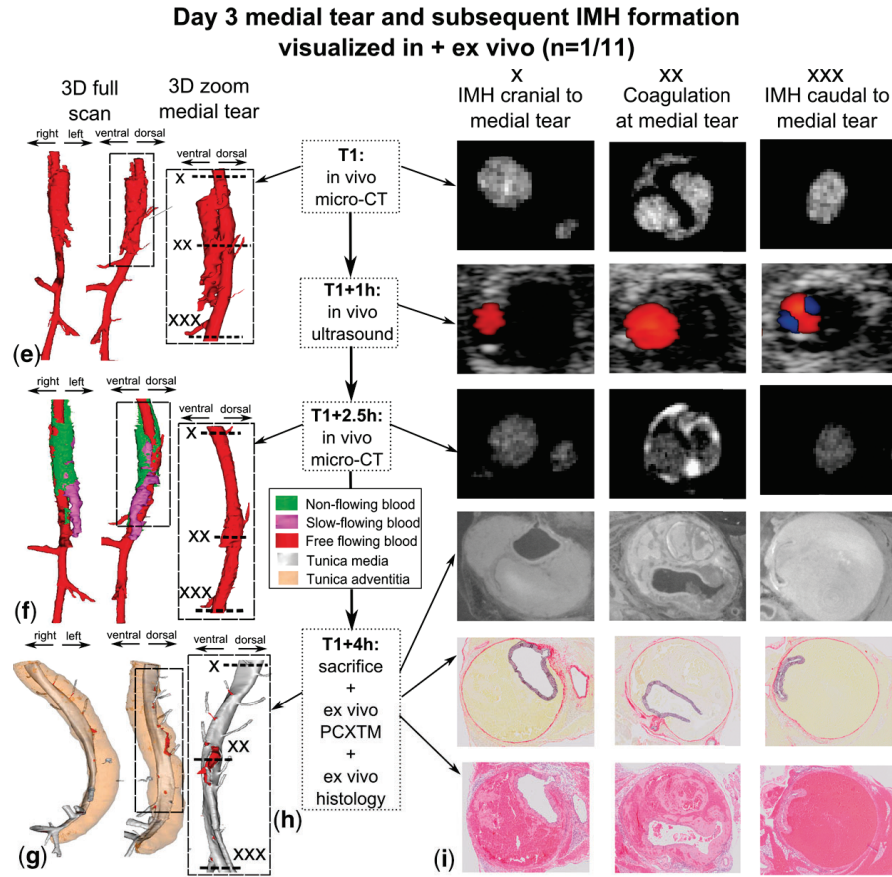


Figure 2.2: (a-c) 3D (segmented) micro-CT (top, middle) and PCXTM (bottom) showing how the free-flowing blood outside the media and the resulting IMH evolved over time in the case of a live rupture. (d) Timeline of in and ex vivo scans performed on the case of live rupture. (e) Top-bottom: micro-CT images at T1, Color Doppler at T1+1h, micro-CT at T1+2.5h (notice the dense white clustering of the Exitron), PCXTM at T1+4h, SR-Miller and H&E stains at T1+4h. * P< 0.05. V: ventral, D: dorsal, R: right, L: left, LSRA: left suprarenal artery, CA: celiac artery, MA: mesenteric artery, RRA: right renal artery, LRA: left renal artery.

early as 3 days post-implantation (compared to previous observations made after 28 days), with a spatial preference for the orifice of aortic side branches. The most frequently affected side branches were the celiac and superior mesenteric arteries. Given the identical topology of medial tears around the same branching regions in fully developed dissecting aneurysms (cf. Figure 37), this finding demonstrates unequivocally that side branches, particularly the celiac and superior mesenteric, are implicated in the onset of dissection in this mouse model.

An in vivo dissecting aneurysm

While early events in response to AngII such as macrophage medial migration and dissection have been captured within days of infusion²⁰, how fast these events progress once they have been initiated has not been reported. Within the context of this study, we serendipitously

Chapter 2. Characterization of early-stage lesion formation

imaged an aortic dissection occurring in vivo during micro-CT imaging. Follow-up of the animal using Color Doppler ultrasound and further imaging with micro-CT showed remarkable propagation of the adventitial dissection and coagulation of the intramural hematoma within only 2.5 hours. The synchrotron-imaged aorta of the mouse at the time mark of its sacrifice, 4 hours after the in vivo dissection, showed further propagation of the dissection cranially and caudally in the 1.5 hours that elapsed between the second micro-CT scan and the final sacrifice of the animal. This remarkable case shows how that, once initiated, these lesions evolve in a matter of hours and is, to our knowledge, the first instance of such a dissection extensively characterized during in vivo imaging.

Is contrast agent visible also on in vivo micro-CT, besides PCXTM?

The Exitron contrast agent was, exceptionally, visible not only on the PCXTM images but also on micro-CT scans in the case of the in vivo imaged dissecting aneurysm presented in Figure 2.2 (2D micro-CT images at panel e, timepoint T1+2.5h). However in most of the aortas that underwent short-term AngII infusion and did not dissect (n=10/11 animals presented in this study), such is not the case. In the intact-appearing aortas such as the ones we harvest after 3 days of infusion, the resolution of the microCT does not suffice to distinguish the small contrast agent quantities found within the wall. An example of a contrast agent aggregate (3D rendering from a Synchrotron scan) is shown below on the left, with its dimensions in x, y and z. On the right is the microCT image of the aorta at the corresponding level of the celiac bifurcation (noted with arrow is the expected point of exitron appearance). No contrast agent is visible on the microCT outside the lumen however. The contrast agent aggregate is 1.9-2.2 times the pixel size of 50 μm , thus barely at the Nyquist theorem limit of detectable objects for the given pixel size. Especially considering that during in vivo scans, the animal is breathing and the aorta is pulsating, the wall motion during the non-gated scan makes it near impossible to resolve details within the wall. Thus microCT-based approaches to evaluate Exitron infiltrations may be used for late-stage disease investigations, but the method is not well-suited for early-stage studies.

It is important to point out that the findings presented in this observational study mainly explain *what* is happening near side branches at an early stage of Ang II infusion. The question *why* this is the case remains unanswered and requires further investigation. While intuitively such consistent localization around the aortic side branches can be attributed to biomechanical forces, within the dynamic and constantly mechanoregulated environment that is the aorta more factors may be at play at the cellular or molecular level.

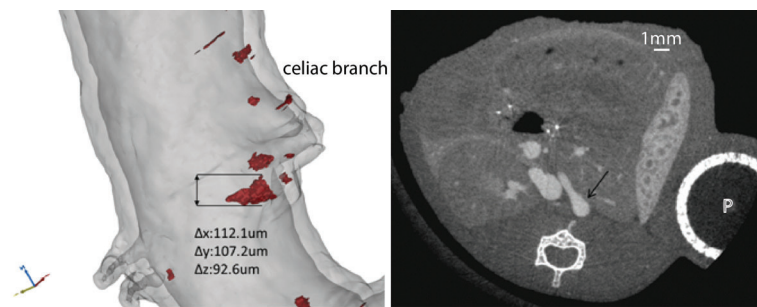


Figure 2.3: Exitron infiltrations are not visible on a micro-CT scan after 3 days of AngII infusion. Left: 3D rendering of the aorta (grey) and local contrast agent infiltration (red) around the celiac branch. Dimensions of the contrast agent infiltrate are annotated. Left: Transversal micro-CT image at the level of the celiac bifurcation (arrow points at the aorta, at expected site of Exitron visualization). P: Alzet pump, whose metal flow divider has been replaced with a micro-CT compatible alternative, as explained in the Methods section.

Bibliography

- [1] Alan Daugherty, Michael W. Manning, and Lisa A Cassis. Angiotensin ii promotes atherosclerotic lesions and aneurysms in apolipoprotein e-deficient mice. *The Journal of Clinical Investigation*, 105(11):1605–1612, 2000.
- [2] Bram Trachet, Rodrigo A. Fraga-Silva, Philippe A. Jacquet, Nikolaos Stergiopoulos, and Patrick Segers. Incidence, severity, mortality, and confounding factors for dissecting AAA detection in angiotensin II-infused mice: a meta-analysis. *Cardiovascular Research*, 108(1):159–170, 08 2015.
- [3] Jean Sénémaud, Giuseppina Caligiuri, Harry Etienne, Sandrine Delbosc, Jean-Baptiste Michel, and Raphaël Coscas. Translational relevance and recent advances of animal models of abdominal aortic aneurysm. *Arteriosclerosis, Thrombosis, and Vascular Biology*, 37(3):401–410, 2017.
- [4] A Daugherty, MW Manning, and LA Cassis. Antagonism of at2 receptors augments angiotensin ii-induced abdominal aortic aneurysms and atherosclerosis. *British journal of pharmacology*, 134(4):865—870, October 2001.
- [5] Bram Trachet, Marjolijn Renard, Gianluca De Santis, Steven Staelens, Julie De Backer, Luca Antiga, Bart Loeys, and Patrick Segers. An integrated framework to quantitatively link mouse-specific hemodynamics to aneurysm formation in angiotensin ii-infused apoe *-/-* mice. *Annals of Biomedical Engineering*, 39(9):2430, 2011.
- [6] Lilach Gavish, Chen Rubinstein, Yacov Berlatzky, Leah Y. Gavish, Ronen Beeri, Dan Gilon, Atila Bulut, Mickey Harlev, Petachia Reissman, and S. David Gertz. Low level laser arrests abdominal aortic aneurysm by collagen matrix reinforcement in apolipoprotein e-deficient mice. *Lasers in Surgery and Medicine*, 44(8):664–674, 2012.
- [7] Lilach Gavish, Ronen Beeri, Dan Gilon, Chen Rubinstein, Yacov Berlatzky, Leah Y. Gavish, Atila Bulut, Mickey Harlev, Petachia Reissman, and S. David Gertz. Inadequate reinforcement of transmural disruptions at branch points subtends aortic aneurysm formation in apolipoprotein-e-deficient mice. *Cardiovascular Pathology*, 23(3):152–159, 2014.
- [8] Bram Trachet, Rodrigo A. Fraga-Silva, Alessandra Piersigilli, Alain Tedgui, Jessica Sordet-Dessimoz, Alberto Astolfo, Carole Van der Donckt, Peter Modregger, Marco F. M. Campanoni, Patrick Segers, and Nikolaos Stergiopoulos. Dissecting abdominal aortic aneurysm in Ang II-infused mice: suprarenal branch ruptures and apparent luminal dilatation. *Cardiovascular Research*, 105(2):213–222, 12 2014.
- [9] A. J. Schriebl, M. J. Collins, D. M. Pierce, G. A. Holzapfel, L. E. Niklason, and J. D. Humphrey. Remodeling of intramural thrombus and collagen in an ang-ii infusion apoe-/- model of dissecting aortic aneurysms. *Thrombosis Research*, 130(3):e139–e146, 2012.

-
- [10] Sofia Xanthoulea, Melanie Thelen, Chantal Pöttgens, Marion J. J. Gijbels, Esther Lutgens, and Menno P. J. de Winther. Absence of p55 tnf receptor reduces atherosclerosis, but has no major effect on angiotensin ii induced aneurysms in ldl receptor deficient mice. *PLOS ONE*, 4(7):1–10, 07 2009.
- [11] B Trachet, R Fraga-Silva, A Piersigilli, P Segers, and N Stergiopoulos. Dissecting abdominal aortic aneurysm in angiotensin ii-infused mice: the importance of imaging. *Current Pharmaceutical Design*, 21(28):4049.
- [12] Loren F. Hiratzka, George L. Bakris, Joshua A. Beckman, Robert M. Bersin, Vincent F. Carr, Donald E. Casey, Kim A. Eagle, Luke K. Hermann, Eric M. Isselbacher, Ella A. Kazerooni, Nicholas T. Kouchoukos, Bruce W. Lytle, Dianna M. Milewicz, David L. Reich, Souvik Sen, Julie A. Shinn, Lars G. Svensson, and David M. Williams. 2010 accf/aha/aats/acr/asa/sca/scai/sir/sts/svm guidelines for the diagnosis and management of patients with thoracic aortic disease. *Circulation*, 121(13):e266–e369, 2010.
- [13] Jay D. Humphrey, Martin A. Schwartz, George Tellides, and Dianna M. Milewicz. Role of mechanotransduction in vascular biology, focus on thoracic aortic aneurysms and dissections. *Circulation Research*, 116(8):1448–1461, 2015.
- [14] A. Klink, J.L.M. Heynens, B. Herranz, M.E. Lobatto, T. Arias, H.M.H.F. Sanders, G.J. Strijkers, M. Merckx, K. Nicolay, V. Fuster, A. Tedgui, Z. Mallat, W.J.M. Mulder, and Z.A. Fayad. In vivo characterization of a new abdominal aortic aneurysm mouse model with conventional and molecular magnetic resonance imaging. *Journal of the American College of Cardiology*, 58(24):2522–2530, 2011.
- [15] Craig J. Goergen, Kyla N. Barr, Diem T. Huynh, Jeffrey R. Eastham-Anderson, Gilwoo Choi, Maj Hedehus, Ronald L. Dalman, Andrew J. Connolly, Charles A. Taylor, Philip S. Tsao, and Joan M. Greve. In vivo quantification of murine aortic cyclic strain, motion, and curvature: Implications for abdominal aortic aneurysm growth. *Journal of Magnetic Resonance Imaging*, 32(4):847–858, 2010.
- [16] Gregory H. Turner, Alan R. Olzinski, Roberta E. Bernard, Karpagam Aravindhan, Heather W. Karr, Rosanna C. Mirabile, Robert N. Willette, Peter J. Gough, and Beat M. Jucker. In vivo serial assessment of aortic aneurysm formation in apolipoprotein e-deficient mice via mri. *Circulation: Cardiovascular Imaging*, 1(3):220–226, 2008.
- [17] Matthew D. Ford, Ariel T. Black, Richard Y. Cao, Colin D. Funk, and Ugo Piomelli. Hemodynamics of the mouse abdominal aortic aneurysm. *Journal of Biomechanical Engineering*, 133(12):121008–121008–9, 2011. 10.1115/1.4005477.
- [18] Samuel Alan McDonald, Federica Marone, Christoph Hintermüller, Gordan Mikuljan, Christian David, Franz Pfeiffer, and Marco Stampanoni. Advanced phase-contrast imaging using a grating interferometer. *Journal of Synchrotron Radiation*, 16(4):562–572, Jul 2009.

Bibliography

- [19] Yu Wang, Hafid Ait-Oufella, Olivier Herbin, Philippe Bonnin, Bhama Ramkhelawon, Soraya Taleb, Jin Huang, Georges Offenstadt, Christophe Combadière, Laurent Rénia, Jason L. Johnson, Pierre-Louis Tharaux, Alain Tedgui, and Ziad Mallat. Tgf- β activity protects against inflammatory aortic aneurysm progression and complications in angiotensin ii-infused mice. *The Journal of Clinical Investigation*, 120(2):422–432, 2 2010.
- [20] Kiran Saraff, Fjoralba Babamusta, Lisa A. Cassis, and Alan Daugherty. Aortic dissection precedes formation of aneurysms and atherosclerosis in angiotensin ii-infused, apolipoprotein e-deficient mice. *Arteriosclerosis, Thrombosis, and Vascular Biology*, 23(9):1621–1626, 2003.

Chapter 3

Co-Localization of Microstructural Damage and Excessive Mechanical Strain at Aortic Branches in Angiotensin-II Infused Mice

Lydia Aslanidou¹, Mauro Ferraro¹, Goran Lovric^{2,3}, Matthew Bersi^{4,5}, Jay D Humphrey⁴,
Patrick Segers⁶, Bram Trachet^{1,6}, Nikos Stergiopoulos¹

¹ Institute of Bioengineering, École Polytechnique Fédérale de Lausanne, Switzerland

² Centre d'Imagerie BioMédicale, École Polytechnique Fédérale de Lausanne, Switzerland

³ Swiss Light Source, Paul Scherrer Institute, Villigen, Switzerland

⁴ Department of Biomedical Engineering, Yale University, New Haven, USA

⁵ Department of Biomedical Engineering, Vanderbilt University, Nashville, USA

⁶ bioMMeda, Ghent University, Ghent, Belgium

Published in the Journal Biomechanics and modelling in Mechanobiology 2019

1 Introduction

Degenerative conditions of the aorta, such as progressive aneurysmal dilatation, acute dissection, or catastrophic rupture, are influenced strongly by the biomechanical loads that act on the vessel wall. Importantly, dissection and rupture occur when the intramural mechanical stress exceeds the strength of the wall^{1,2}, with dissections involving a tearing of intimal / medial layers that allows blood to enter the wall. An associated progressive separation within the medial layer can create a false channel parallel to the true lumen that may or may not re-enter the aorta. Mechanical stimuli are thought to be key contributors to the initiation of aneurysms and dissections, not just their progression³. Estimation of the mechanical stresses/strains within the vessel wall via biomechanical simulations thus represents a promising approach for risk stratification^{4,5} and patient-specific interventional management^{6,7,8}. Simulations can also help enhance our hitherto limited understanding of the pathogenesis and early arterial remodelling that is characteristic of aneurysms and dissections, thus leading to an improved

prognostic capability and therapeutic design. Computational models of the biosolid and biofluid mechanics suggest, for example, that pressure-induced hotspots of elevated normal wall stress⁹ and flow-induced hotspots of elevated wall shear stress¹⁰ occur around the branching regions of the aortic arch, where initial dissecting tears often manifest. A continuing limitation of computational models, however, is the lack of validation due to the paucity of longitudinal patient data, particularly during early stages of the disease. Animal models can therefore serve as invaluable complements to human studies.

Chronic infusion of the vasoconstrictive peptide angiotensin II (AngII) in atherosclerosis-prone mice is a well-accepted model for dissecting aortic aneurysms^{11,12}. The observed lesions develop within hours to days in the suprarenal abdominal aorta and are caused by a medial tear that is often accompanied by marked dissection and intramural hematoma^{13,14}. A number of studies investigated roles of hemodynamic loads in this AngII-induced model of dissection^{15,16,17}, motivated by earlier suggestions of the likely importance of mechanical stresses in the etiology^{18,19}. An important subsequent experimental finding, however, was the histomorphometric identification of transmural disruptions in the vicinity of orifices at major side branches in late stages of the disease, namely after 28 days of AngII infusion^{20,21}. Although this finding focused subsequent attention on the potential biomechanical vulnerability of branch points^{22,23} the precise role of biomechanics in the initiation and early progression of AngII-induced lesions has remained elusive. Our continuing search for biomechanical mechanisms must nevertheless build on prior studies. Numerous imaging modalities, including in vivo magnetic resonance imaging, high frequency ultrasound and ex vivo panoramic digital image correlation, have been used to estimate regional biomechanics in the AngII-infused murine abdominal aorta^{24,25,26,27}. Biaxial mechanical testing has also shed light on the solid mechanics of the mouse aortic wall prior to and during AngII infusion^{28,29}. Mouse-specific fluid dynamics simulations have been used to understand flow patterns in the true aortic lumen either prior to AngII infusion¹⁷ or in the late stages of disease development when a false lumen is present^{30,31}. Mouse-specific fluid-solid-interaction (FSI) simulations have shown the distribution of principal stresses in a healthy mouse aorta³², but computational efforts focusing on the early stage of AngII-induced lesions with appropriate mouse-specific validation are lacking.

We have previously performed ex vivo synchrotron-based imaging of AngII-induced dissecting aneurysms by means of phase contrast X-ray tomographic microscopy (PCXTM), which yielded 3D datasets of the aortic wall at 6.5 μm isotropic resolution^{22,23,33}. We found that dissections starting as medial microruptures can be visualized ex vivo due to a fortuitous discovery: the micro-computed tomography (micro-CT) contrast agent injected into the mice in vivo (prior to euthanasia) infiltrated the aortic wall intra vitam to form microleaks that appeared as white aggregates. The advantage of such microleaks is that they can be analyzed in 3D along the entire vessel, and therefore offer a much more accurate and complete assessment of vascular damage than what can be obtained by traditional slice-by-slice 2D histology - an arduous, expensive, and invasive procedure. Consistent with earlier histological findings^{20,21}, the microleaks occurred mainly near the ostia of suprarenal side branches, with a particularly

high incidence around the celiac and superior mesenteric arteries. It is expected that the preferential localization of these microruptures are intricately linked to the regional mechanics. Aiming to test this hypothesis, we introduced a custom automated morphing framework to map the non-pressurized, non-axially-stretched, PCXTM geometry onto the pressurized, axially-stretched in vivo micro-CT geometry³⁴. The output of this morphing scheme is a mouse-specific structural finite element simulation under pressurization and axial stretch. In this way, this synchrotron-based biomechanical modelling considers often-overlooked aspects of the native geometry - namely mouse-specific aortic wall thickness, minor aortic side branches and local axial stretch – that impact the location of hotspots in the computed in vivo aortic strain field³⁴. This morphing framework was only tested for a single mouse, however, thus its general validity remained to be demonstrated.

The aim of this work is to test the hypothesis that the local mechanics at major abdominal side branches drive disease initiation in AngII-infused mice. To that end, we present an experimental-computational approach that was used to compare histopathological, imaging, and computational results regionally for AngII-infused and saline-infused control mice. We first verified that the infiltrated contrast agent can be used as a precursor for vascular damage, and then compared the 3D distribution of infiltrated contrast agent to spatial hotspots of mechanical strain (obtained with synchrotron-based biomechanics). Importantly, the associated mechanical strains were computed by comparing unloaded and temporally averaged loaded configurations of the abdominal aortic wall, not in vivo diastolic and systolic configurations. Finally, we further tested the hypothesis that load-induced delamination of the wall initiates at or near branch sites via synchrotron imaging of aortas that were mechanically tested ex vivo in the absence of complicating mechanical factors such as complex hemodynamics^{30,31} and perivascular tissue support³⁵, thus focusing on the effect of material and geometric heterogeneities at branch sites.

2 Methods

Animals

All procedures were approved by the Ethical Committee of Canton Vaud, Switzerland (EC 2647.2) and performed according to Directive 2010/63/EU of the European Parliament on the protection of animals used for scientific purposes. Twelve-week old male ApoE-deficient mice on a C57BL/6J background (n=10) were infused for 3 days with AngII at a rate of 1000ng/kg/min, as described in the method section 2 of Chapter 2. Age-, sex- and strain-matched controls (n=6) were infused for 3 days with 0.9% normal saline. All mice underwent a micro-CT scan (detailed below) just prior to euthanasia with a ketamine/xylazine cocktail (100 mg/kg and 15 mg/kg, respectively) and aortic tissue was collected immediately after euthanasia.

Imaging

In vivo. The abdominal region was imaged using contrast-enhanced non-gated micro-CT on the third day of AngII infusion. The contrast agent (ExiTron nano 12000; Miltenyi Biotect, Germany) was injected into the lateral caudal vein at 4 mL/g body mass and imaging was achieved using a Quantum FX micro-CT scanner (Caliper Life Sciences, USA). Anesthesia was maintained throughout scanning with an inhalation of 1.5% isoflurane. We used compressors that concentrate room air to oxygen levels between 85% and 91% (model: Sequal Integra E-Z Oxygen concentrator), which then deliver this concentrated air to the inhalation anesthesia system. The resulting DICOM images had an isotropic voxel size of 50 μm . The soft-tissue contrast of this technique delineates the blood-filled aortic lumen but is not sufficient for visualization of the aortic wall thickness. Resulting segmentations of the aorta from these (non-gated) scans represent an average of the systolic and diastolic geometries.

Ex vivo. The abdominal aortas of the 10 AngII-infused and 6 saline-infused control mice were excised and fixed in 4% paraformaldehyde (PFA). The samples were then imaged at the TOMCAT beamline of the Swiss Light Source in the Paul Scherrer Institut, Villigen, Switzerland. Images were acquired in stacked scans with 6.5 μm isotropic resolution using differential phase contrast X-ray tomographic microscopy (PCXTM) with grating interferometry, as we described in section 4.1 of the Introduction. This complementary imaging modality enables tissue contrast sufficient to quantify wall thickness and to segment small side branches off the aorta³⁶.

Histology

The reliability of local contrast agent distribution as a marker of vascular damage was first validated against targeted 2D histology. Briefly, after ex vivo PCXTM scanning, samples were fixed again in 4% PFA and embedded in paraffin using standard histological procedures. We then followed procedures for PCXTM-guided histology that we introduced previously²². Namely, upon examination of the PCXTM dataset for each sample, we identify sites of contrast agent infiltration and serially section the embedded samples to obtain desired locations, including those with and without contrast agent as well as with and without branches. Slides were stained with Haematoxylin-Eosin (H&E) to assess general morphology: 214 slides from the 10 AngII-infused mice and 157 from the saline-infused control mice. Whereas eosin also stains erythrocytes red, a Martius, Scarlet and Blue (MSB) stain was used to assess fibrin within coagulated blood. Immunostaining identified macrophages (F4/80), continuity of the endothelial cell layer (CD31), and smooth muscle cells (α -smooth muscle actin, α -SMA). Pathophysiological observations in each slide were assessed by an investigator blinded from the PCXTM guided histology.

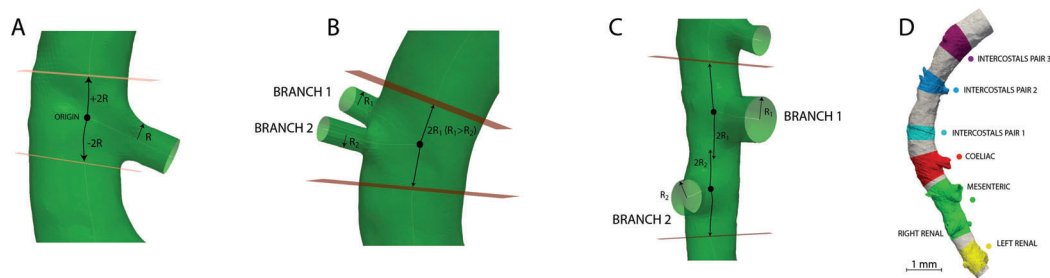


Figure 3.1: Schematic depiction of aortic partitioning at the level of ramifications. a: Ramification with one daughter branch. Cutting planes intercept the abscissae at a distance of $\pm 2R$ with respect to the origin of the bifurcation. b: Ramification with more than one daughter branch (from a common origin). Cutting planes intercept the abscissae at a distance of $\pm 2R$, where R is the maximal of the daughter branches' radii. c: Neighboring ramifications. If cutting planes applied for each ramification yield overlapping neighboring branching zones, the aortic regions are merged into a single branching segment. d: Illustration of partitioned aorta in branching (colored) and non-branching (gray) segments.

Computational Analyses

We sought to assess mechanical strains locally along the abdominal aorta by comparing the loaded (micro-CT) and unloaded (PCXTM) configurations. Toward this end, semi-automatic segmentations of paired *in vivo* micro-CT and *ex vivo* PCXTM scans were performed using the image processing software Mimics (Materialise NV, Belgium). Preprocessing, meshing and morphing were achieved using an integrated framework that has been described in detail in section 5.3 of the Introduction, and in³⁴.

Preprocessing

Precise lengths of the aortic side branches could not be estimated from the micro-CT images, hence we developed a consistent extension technique to mitigate effects of artificial stretching during the morphing simulation. Each side branch was numerically extended in proportion to a related length measured in the micro-CT model. For example, the distance between the celiac and superior mesenteric bifurcations was calculated in terms of the abscissa coordinate of the centerline in both the micro-CT and PCXTM scans (see Figure 3.1d), which was clearly identifiable with both imaging modalities. The ratio between these two quantities provided an extension coefficient that multiplied the PCXTM side branch length to yield an extension length.

Meshing

The outer vascular surface in each PCXTM segmentation was discretized with an unstructured quadrilateral mesh. This mesh was then smoothed using a non-shrinking Taubin filter (pass-

Table 3.1: Mesh size and edge lengths for the geometrical models.

Case	Elements	Average edge length	Maximum edge length [μm]	Minimum edge length [μm]
AngII-infused				
1	713952	10.1	45.0	1.0
2	267808	17.2	113.0	1.7
3	275464	18.4	59.3	2.4
4	303740	15.4	152.0	4.2
5	245692	20.3	60.0	6.1
6	332784	13.9	84.8	4.5
7	833212	9.6	39.3	0.9
8	254472	19.6	89.4	4.5
9	916660	9.6	34.0	1.5
Saline-infused				
1	611208	10.1	81.4	1.3
2	220000	21.1	72.1	1.3

band 0.1, 100 smoothing iterations) and projected onto the mesh of the inner wall using a custom Matlab code (The Mathworks, Inc., Natick, MA, USA, code available in the supplementary material for³⁴). The final result was an unstructured hexahedral solid mesh of the ex vivo geometry. Several meshes were auto-generated to ensure that the simulations were independent of the grids used; details of the final converged meshes, including the average, maximum, and minimum element edge lengths, are in Table 3.1. Convergence could not be reached for only 1 of the 10 AngII-infused mice, mainly due to element distortions related to poor local element quality. Conversely, the collapsed ex vivo geometry hindered mesh generation for 4 of 6 control mice. All of the 5 cases of poor mesh quality are shown in Figure 3.8 of this chapter's Appendix.

Morphing simulation set-up

In order to estimate strains along the abdominal aorta, we developed a pointwise mapping scheme between the ex vivo PCXTM mesh (not stretched, not pressurized) and the in vivo micro-CT model (in vivo axial stretch and pressurized). To this end, we introduced a branch-based coordinate transformation in which a cylindrical parametrization was generated from a rectangular parametric space for each branch. This transformation was applied to both the micro-CT and PCXTM models, and a global displacement map was obtained by subtracting each nearest neighbour node in the micro-CT and PCXTM models, respectively.

The output of this novel method thus synthesized the hexahedral PCXTM mesh and the computed displacement map into a single structural finite element method (FEM) based simulation of morphing. The morphing simulation was static and fully displacement controlled, allowing finite deformations. A nearly incompressible Arruda–Boyce constitutive model was used, with material parameters ($\mu = 24.358$ kPa, $\lambda_m = 1.01$) consistent with those used in a prior fluid-solid-interaction simulation³².

In order to co-localize results of the simulation with locations of micro-ruptures that were

identified using PCXTM imaging, the computed Eulerian strains were mapped back onto the ex vivo undeformed configuration while artificial extensions of side branches were removed for visualization and excluded from the analysis.

Partitioning of the abdominal aorta

To allow consistent region-matched comparisons between aortic strains (computed from the FEM simulations) and vascular damage (observed from contrast infiltrations in PCXTM scans), the aorta was sub-divided into branching and non-branching zones. Post-processing of data was achieved using the vascular modelling toolkit (VMTK, Orobix, Bergamo, Italy³⁷, Matlab (The MathWorks Inc., Natick, MA, USA) and the open-source code Paraview³⁸. The VMTK subroutine `vmtkbifurcationreferencesystems` was used to compute reference systems for the ramifications of the aortic tree, and Frenet-Serret tangents and abscissas were subsequently computed along the smoothed and resampled centerline of the simulated vessel geometry (subroutines `vmtkcenterlinenormals` and `vmtkcenterlineattributes`).

In the regions containing bifurcations, the aortic zone corresponding to a branch of radius R was delimited by two planes at a curvilinear centerline distance of $\pm 2R$ from the origin of the bifurcation (Figure 3.1a). Planes laterally demarcating the branching segment were placed perpendicular to the centerline as defined by local Frenet-Serret tangents. In the case of multiple bifurcating branches from a common origin, the planes delimiting the segment were placed at a distance $2R_{\max}$ above and below the origin, where R_{\max} was the maximum radius of the side branches (Figure 3.1b). Adjacent ramifications were grouped with a single branching aortic segment if the curvilinear centerline distance between the originating points was not sufficient to define two separate segments without any overlap (Figure 3.1c). Straight segments were then, by inference, defined as those lying between branching segments. Identical cutting planes were imposed on the ex vivo PCXTM scans to divide them into branching and non-branching segments. In most geometries, the sectioning yielded 7 straight and 6 branching aortic segments, which are depicted in Figure 3.1d.

Quantification of strain and 3D microstructural vascular damage

Quantification of strain and 3D microstructural vascular damage For each simulation, high values of strain were defined as $\geq 80\%$ of the maximal principal strain. For each aortic segment, the surface area A_1 of high strain and the total surface area A_2 of the aortic segment was exported into Paraview. We used a nondimensional metric defined as the percentage of the A_1 / A_2 ratio as a high strain index.

Microleaks of contrast agent within the aortic wall were segmented in the Mimics software. The quantified volume of contrast agent was subsequently partitioned using the same aortic segment definitions – hence a volume of contrast agent, if present, was assigned to each aortic segment.

Load-induced intramural delaminations ex vivo

Ex vivo biaxial mechanical testing can also be used to explore biomechanical mechanisms of aortic dissection in mouse models. In particular, load-induced intramural delaminations have been observed in aortas of mice that have a propensity to dissect in vivo^{39,29}. Here, for the first time, we use synchrotron imaging (PCXTM at 6.5 μm isotropic resolution) to examine the abdominal aorta from male ApoE-deficient mice (n=4) that were infused with AngII for 4 days (1000ng/kg/min) and underwent ex vivo biaxial testing with concurrent optical coherent tomography (OCT) imaging, as previously described³⁹. The biaxial tests were carried out on freshly excised, non-fixed samples. Because the delaminations were observed in different regions (1 proximal descending aorta, 2 suprarenal abdominal aortas, and 1 infrarenal abdominal aorta), we used these data to further evaluate the role of branching regions as potential nucleation sites for dissection.

Statistical analysis

Differences in both mechanical strain and contrast agent infiltration between straight and branching segments were assessed with the nonparametric Mann-Whitney U test. Differences between AngII and saline-infused mice in a given aortic region were evaluated with multiple t-tests between the two groups with post-hoc Sidak-Bonferroni correction. For AngII-infused mice, a Kruskal Wallis test with post-hoc Dunn's testing for multiple comparisons was used to compare strain and contrast agent volumes between aortic locations and circumferential quadrants. Linear relationships between variables were assessed by the Pearson correlation.

3 Results

Contrast agent infiltration in the wall is a proxy for microstructural damage

A 3D rendering of the abdominal aortic wall of a representative AngII-infused mouse shows regions of infiltrated contrast agent in red (Figure 3.2a). Contrast agent was found in the aortic wall of all 10 AngII-infused mice but was absent in all aortic regions within the saline-infused control animals (cf. Figure 3.3c). Despite the near normal gross morphology, H&E and immuno-staining revealed a compromised structural integrity of the wall of the AngII-infused aortas in multiple locations (Figure 3.2b). Intimal and intramural defects in the AngII-infused animals included a fragmented internal elastic lamina accompanied by subintimal cellular infiltration, intramural accumulation of red blood cells and fibrin, macrophage infiltration, and loss of vascular smooth muscle cells. In stark contrast, no histopathological findings arose in the saline-infused animals (Figure 3.2d).

We also found good agreement between contrast agent localization and histopathological findings, as quantified in Figure 3.2c. In 64% of the examined slides, absence of contrast agent matched the absence of histopathological features (termed 'true negatives') while in 24% of the

cases, contrast agent infiltration co-localized with histopathological findings (true positives). The main histological findings of the true positive cases were subintimal cellular infiltration and intramural hematoma (52% and 35% of true positives, respectively). False positives and false negatives, that is, a mismatch between contrast agent infiltration and microstructural damage, represented only 5% and 6% of the total cases, respectively. The finding that went mostly undetected with PCXTM was medial VSMC loss (82% of all histologically identified instances were not accompanied by contrast agent infiltration).

In the intercostal region of AngII-infused mice, the most prevalent histopathological feature was disruption of the intimal layer accompanied by subintimal cellular infiltration (46%), followed by loss of medial smooth muscle cells (24%). Intramural hematoma (i.e., accumulation of red blood cells in the wall) was found in the outer lamellar layers at 7% of the branching sites but in none of the non-branching ones. In non-branching sites of the intercostal region, there was no lesion in 78% of the sections analyzed; this is in contrast to 61% absence for the branching sites. In the paravisceral aortic region, extending from above the celiac down to the right renal artery, the most prevalent lesions were intramural hematoma (50% of the observed lesions), followed by subintimal cellular infiltration (42%). The incidence of hematomas was similar in branching and non-branching sites (15% and 19% respectively, Figure 3.2d). We observed that 50% and 55% of intramural hematomas in the intercostal and the paravisceral regions co-localized with medial macrophages. No macrophage infiltration was observed in the more distal aortic region, extending from above the left renal artery to the infrarenal aorta. The only observed lesion in this region was fibrin accumulation (4% of sections from AngII-infused mice).

Strain and contrast agent infiltration in the aorta: a macro-comparison

The structural FEM calculations of in vivo aortic strain obtained by implementing the morphing framework for 9 AngII and 2 saline-infused mice are shown in Figure 3.3a. The corresponding ex vivo segmentations of the abdominal aortic wall and corresponding contrast agent microleaks - which serve as indicators of vascular damage - are shown in Figure 3.3b. The mean value as well as the range of predicted values of strain was similar between those for the AngII and saline infused mice (Figure 3.3c). There was also no significant correlation between minimum or maximum strain values and the total volume of contrast agent in the wall (Figure 3.3d).

Strain and contrast agent infiltration in the aorta: branching and non-branching regions

In order to evaluate the distribution of strain - rather than its range of values - and to consistently assess the implication of branching regions on the strain map, we divided the aorta into branching and straight (non-branching) regions. Representative analysis of the abdominal aortic branching topology resulted in the partitioned geometry shown in Figure 3.4 (center).

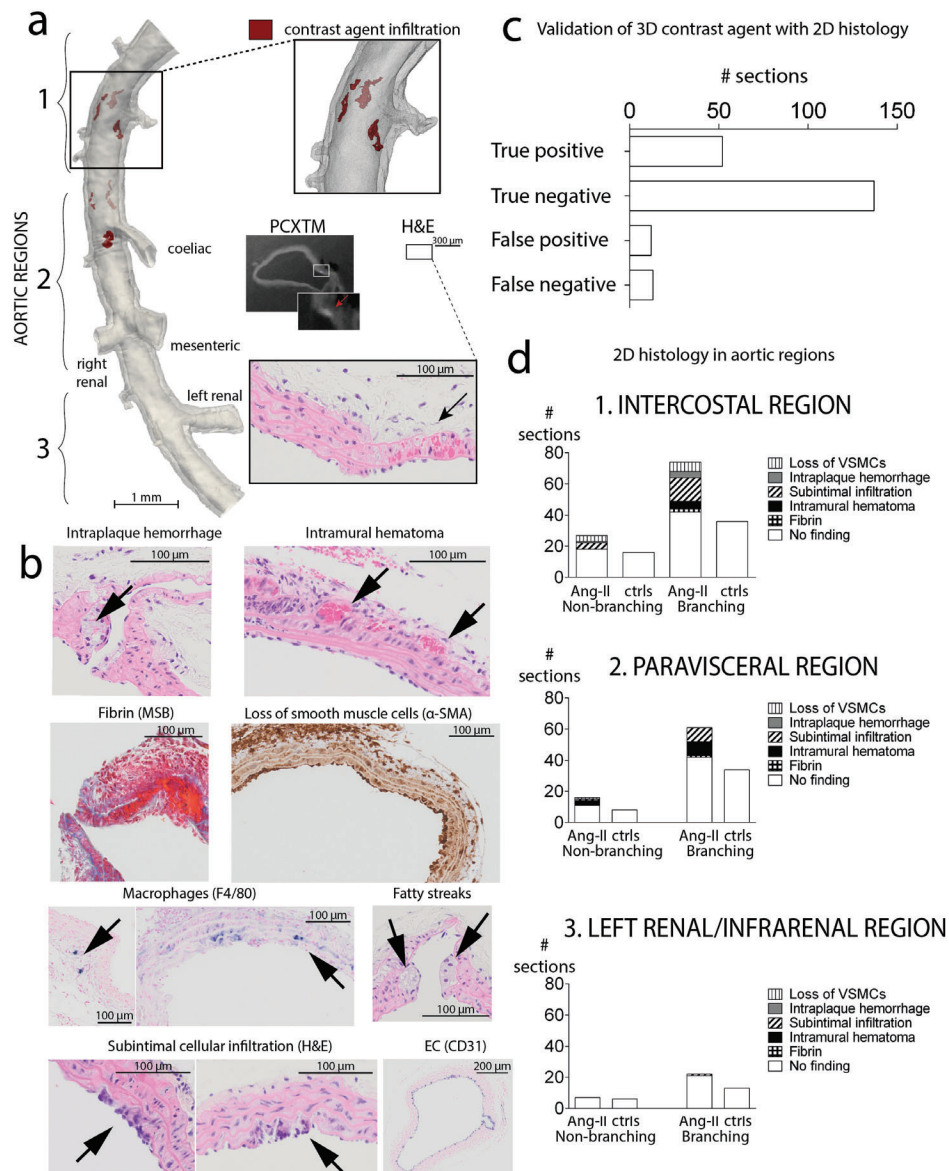


Figure 3.2: Targeted image-guided histology. **a**. 3D volume rendering of an abdominal aorta after 3 days of AngII infusion with zoomed suprarenal region (contrast agent in red). Note the correspondence between the ex vivo PCXTM image and targeted H&E section. The infiltrated contrast agent (red arrow) co-localizes in the zoomed H&E image with an intramural accumulation of red blood cells. This zoomed image also shows a transition of elastic laminae from 5 to 2 in the branching region. **b**. Zoomed images of lesions (arrows) located on H&E, MSB and immunostained slides (α -SMA, CD31, F4/80). **c**. Bar plot showing correspondence between the presence or absence of contrast agent in the wall and histopathological findings in AngII-infused mice. **d**. Bar plots showing histopathological findings in AngII and saline-infused animals, in branching and non-branching sites of each aortic region shown in **a**.

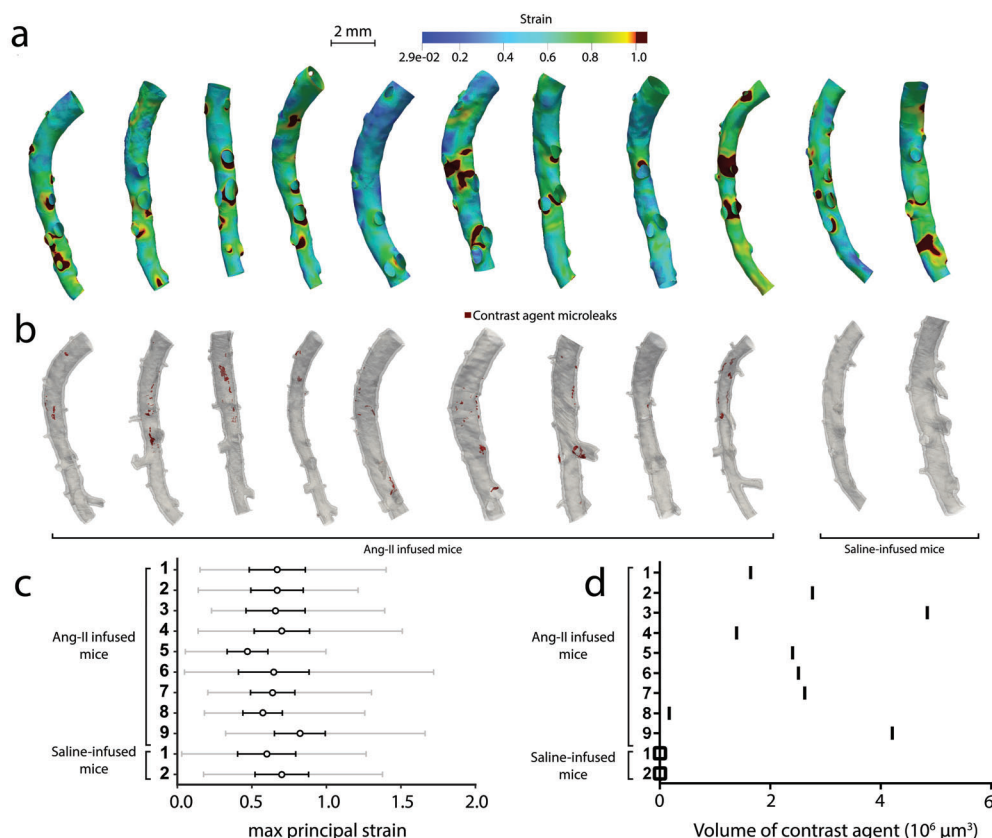


Figure 3.3: a. Structural FEM simulations of 9 AngII-infused and 2 saline-infused murine abdominal aortas. The strain contour plot was projected back onto the ex vivo undeformed configuration to enable direct comparisons of strain concentrations and contrast agent microleaks in the aortic wall. b. 3D aortic wall renderings corresponding to geometries presented in A with contrast agent microleaks shown in red. c. Error bar plot of principal strain. The thick black line shows the mean \pm SD. Grey line shows range of strain values from minimum to maximum. d. A scatter plot shows total volume of infiltrated contrast agent per aorta.

For each mouse, the high strain index and volume of contrast agent infiltration was quantified within each straight and branching segment. Overall, the high strain index in the branching regions was significantly greater than in the straight regions ($P < 0.0001$, Figure 3.4a). Similarly, the volume of contrast agent was significantly lower in straight regions than in branching regions ($P = 0.0028$, Figure 3.4b).

For AngII-infused mice, the aortic zone around the first pair of intercostal arteries cranial to the celiac artery had significantly higher strain than the control mice (Figure 3.4a, bottom). The volume of contrast agent in the vicinity of the (i) celiac artery and (ii) superior mesenteric and right renal artery was significantly higher than in corresponding regions in saline-infused mice ($P = 0.00001$ and $P = 0.0002$ respectively, Figure 3.4b bottom). Moreover, the aortic region around the celiac artery had more extensive microleaks of contrast agent than did the zone around the left renal artery ($P = 0.0419$). No contrast agent was found in 67% of the straight

regions, whereas this percentage dropped to 35% for the branching zones.

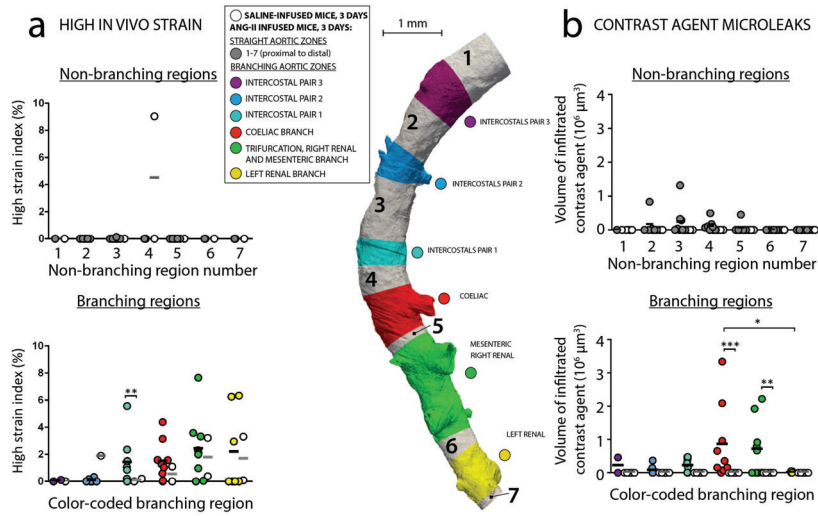


Figure 3.4: Center: Color-coded division of the aorta in branching and straight zones. a. Scatter plots show the computed high strain index (percentage of segment's surface area with strain values exceeding 80% of maximal strain) in straight and branching aortic regions in AngII-infused (n=9) and saline-infused (n=2) animals b. Scatter plots show the volume of infiltrated contrast agent in straight and branching aortic regions in AngII-infused and saline-infused animals. Bold horizontal lines denote the mean of each group; grey lines denote the mean for saline-infused animals. * $P < 0.05$, ** $P < 0.001$, *** $P < 0.0001$.

In order to compare regions of high strain to high contrast agent more directly, we plotted the high strain index versus contrast agent volume for all aortic segments, delineating between straight and branching regions (Figure 3.5a, top and bottom respectively). Most straight segments had low strain values, but among the clustered points around the origin of the axes some had non-zero contrast agent volumes. Discordant pairs – defined by predictions of low strain accompanied by high volumes of contrast agent and vice versa - were found among branching regions as well. Upon closer examination of these cases, however, we found that most could be classified in one of two categories (Figure 3.5b, cases 1 and 2). First, in a number of cases, the cutting planes used to partition the aortic geometry into segments intercepted a continuous volume of contrast agent that extended between two consecutive zones. This infiltrated volume resulted from the propagation of a single initial microleak (one point of entry) in the vessel wall. Thus, identifying two neighboring segments with a continuous volume of contrast agent as contrast agent-positive potentially led to an overestimation of the number of damage events suffered by the aortic wall. Second, in a number of cases, a minor aortic branch visualized on the PCXTM images was excluded in the FEM simulation due to difficulties in implementing the morphing framework. Omission of the side branches could have altered (either over- or under-estimated) the computed local strain, as previously shown in section 5.3 of the Introduction. In Figure 3.5b, the data belonging to the aforementioned cases have been color-coded for straight (top) and branching regions (bottom). After eliminating them from the analysis, no significant correlation was found

between high strain and contrast agent infiltration for straight segments (Figure 3.5c, top). Conversely, a significant positive correlation between high strain and contrast agent volume emerged for branching segments (Figure 3.5c bottom, $P < 0.0001$ with Pearson's correlation). These branching regions are color-coded and the data driving the correlation arise mainly from the celiac and superior mesenteric/right renal arteries.

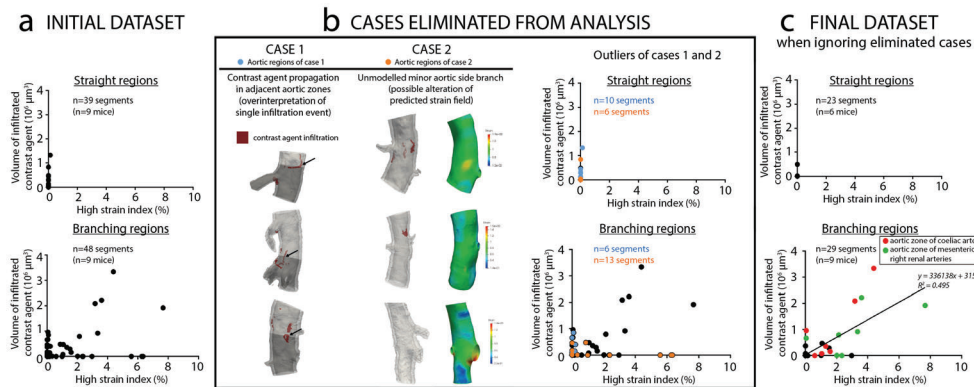


Figure 3.5: a. Scatter plots show the correlation between high strain calculation and volume of contrast agent infiltration for straight and branching segments. b. Outlier cases 1 and 2 were eliminated from the analysis (left) and color-coded on the scatter plots (right). The number of segments classified as case 1 (18% of all segments) or case 2 (22% of all segments) is in blue and orange, respectively. c. Final scatter plots with data from cases 1 and 2 excluded from the analysis. For branching regions (bottom), color-coded data denote aortic regions (red for celiac artery region, green for superior mesenteric/right renal artery region)

Circumferential distribution of contrast agent and strain around branch arteries

In order to assess circumferential variations in strain and vascular damage, and their relation to one another, we divided the most affected aortic segments - including the celiac branching region and superior mesenteric/right renal branching region - into four quadrants (Figure 3.6, right). Both the volume of contrast agent and the computed strain were significantly higher in the ventral than in the dorsal aorta (Kruskal Wallis test with post-hoc Dunn's test for multiple comparisons, $P=0.0008$ and $P=0.0164$). The strain was also significantly higher in the ventral quadrant than in the left quadrant ($P=0.0128$). A significant positive correlation was observed between ventral high strain index and ventral contrast agent accumulation (Figure 3.6c, $P=0.0191$).

Load-induced intramural delaminations ex vivo: the role of side branches

PCXTM-based 3D representations of 4 aortic samples that underwent ex vivo biaxial mechanical testing and presented with intramural delaminations can be seen in Figure 3.7 (a-c). In all 4 samples, small side branches were damaged within the delaminated regions. The number of ruptured branches as well as the total number of branches found within the delaminated

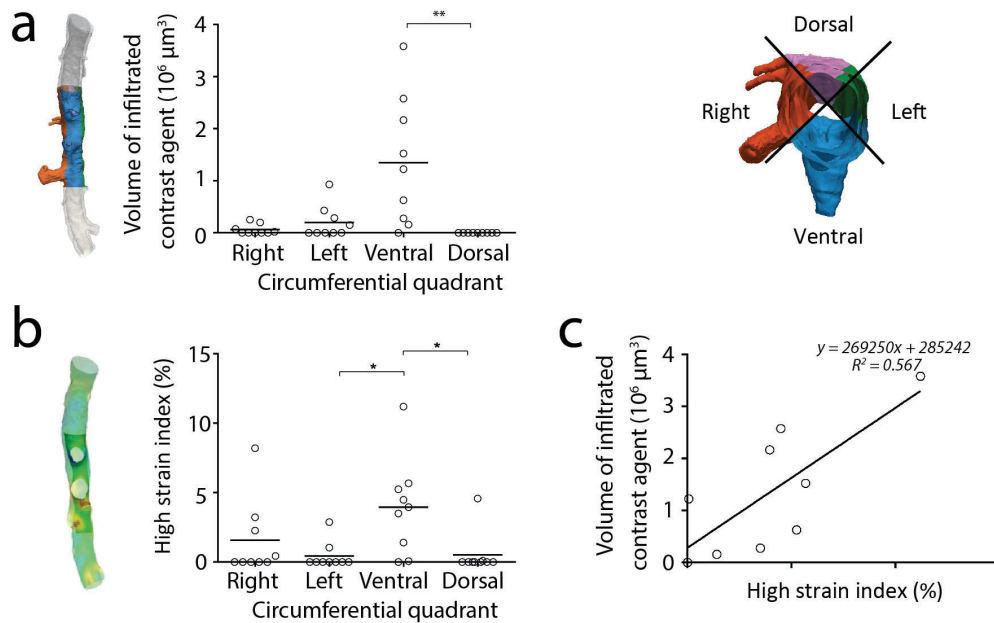


Figure 3.6: Scatter plots showing a. the volume of contrast agent microleaks and b. computed high strain variations along the circumference of the aortic region extending from the celiac to the right renal artery (quadrants as shown on right side). Bold horizontal line denotes mean value. * $P < 0.05$, ** $P < 0.001$.

region of each sample are summarized in Table 3.2. Medial tears - defined as discontinuities of the tunica media across all elastic lamellae - were found in the vicinity of a side branch in the suprarenal and infrarenal aortas (Figure 3.7d, zoomed panels). The celiac artery was the branch around which the medial tear appeared in the only sample that included this ramification. In the proximal descending aorta, the major delamination plane was found in a non-branching region (Figure 3.7d). All delaminations were contiguous with a ruptured or unruptured side branch. Correlative histology validated the observations of the 3D PCXTM images (Figure 3.7e).

Table 3.2: Quantification of ruptured and total side branches found within the delaminated region of 4 aortic samples subjected to ex vivo biaxial testing.

Sample	Aortic region	Total number of branches	Ruptured branch ostia [% of total branches]
1	Proximal descending thoracic aorta	7	3[43%]
2	Suprarenal abdominal aorta	8	6 [75%]
3	Suprarenal abdominal aorta	6	4[67%]
4	Infrarenal aorta	5	2[40%]

4 Discussion

To the best of our knowledge, this study is the first to use synchrotron-based biomechanics to predict in vivo aortic strains and to correlate strain concentrations with mouse-specific 3D

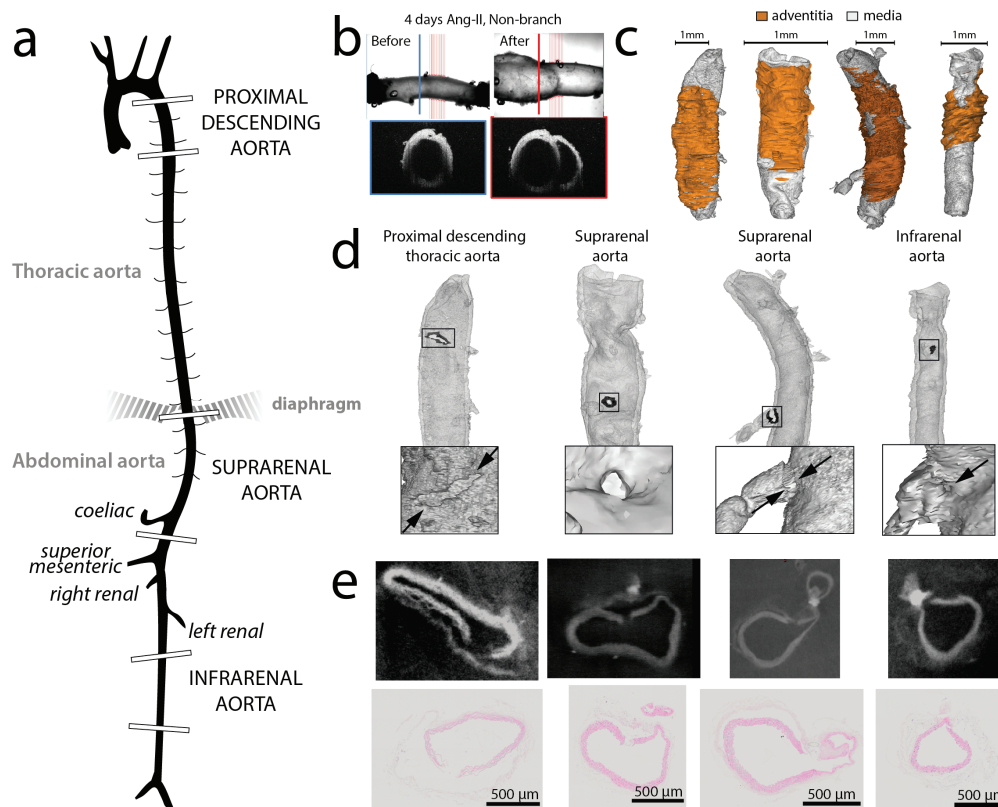


Figure 3.7: a. Illustration of the aortic regions for the four ex vivo tested samples. b. Aortic delamination of the suprarenal aorta after 4 days of AngII infusion. Optical coherence tomography during biaxial mechanical testing shows spontaneous delamination of medial and adventitial layers. c. 3D representations of the 4 samples that were subsequently scanned with PCXTM. The separated adventitial layer is shown in orange. d. 3D representations of the media (adventitia not shown). Zoomed images show the major medial tear for each sample. e. PCXTM images and targeted H&E histology in the locations of major medial tears shown in d.

intramural histopathology in the abdominal aorta. Toward this end, we used a common animal model of aortic dissection, the AngII-infused ApoE-deficient mouse²³. Histopathological findings were similar to those reported by others. There was an early cellular infiltration in the sub-intima, accumulation of macrophages in the media, and evident hematoma in the outer lamellar units in the suprarenal aorta of the AngII-infused mice, but a lack of overt morphological or histopathological changes in the aortas of saline-infused animals^{16,14}. There was also protection of the infrarenal aorta from pathological findings²⁸.

Contrast agent as a surrogate marker for precursor vascular injury

We first confirmed that infiltration of an intravenously injected micro-CT contrast agent into the aortic lumen co-localizes with vascular damage. Comparative histology showed that this contrast agent served as a reliable indicator of vascular damage in 88% of the histological

sections examined (Figure 2c). Regarding the preferential detection of certain wall defects over others, we found that contrast agent infiltration is better suited to detect subintimal cellular infiltration and intramural hematoma, but less so the loss of medial VSMCs. Moreover, localization of infiltrated contrast agent, combined with an ability to measure its distribution non-invasively in full 3D-datasets, provides an added advantage that arduous, arbitrarily located 2D histology cannot achieve. Thus, we submit that the 3D distribution of contrast infiltration along the aorta is a suitable alternative to certain aspects of 2D histology for the purpose of computational validation.

Initiating events in AngII induced abdominal pathology: branching sites are biomechanically vulnerable

Aortic dissections occur almost exclusively in the suprarenal abdominal aorta in the AngII infusion model¹⁵ and typically present within 3-10 days after the onset of AngII administration¹². Telemetric blood pressure assessment shows that the mice experience a +25 mmHg rise in mean blood pressure within 24 hours from the onset of AngII infusion, with pressure increasing continuously to +31 mmHg at 3 days of infusion⁴⁰. Elevated blood pressure can differentially increase wall stress in the media and adventitia⁴¹, and it is expected that wall damage occurs when wall stress exceeds wall strength. Within 24 hours after dissection, neutrophil accumulation is much more pronounced than macrophage infiltration and very little collagen has yet to be deposited despite focal elastin breakage in the media⁴². It has been suggested that cellular targets of AngII also exert injurious effects to the aortic wall, independent of blood pressure⁴³.

Using 2D histology Gavish and colleagues identified transmural disruptions at branch points in the abdominal aorta after 28 days of AngII infusion^{21,20}. Using 3D synchrotron imaging, we subsequently observed similar microruptures in the tunica media after 28 days of infusion, not only near major but also near minor suprarenal side branches, and this without the need for serial sectioning²². Follow-up research revealed that medial defects already arise around the ostia of major and minor abdominal aortic side branches by 3 days of AngII infusion, thus suggesting involvement in initiation, not just outcome²³. In addition to revealing local sites of intramural damage, we have shown that ex vivo synchrotron-based imaging can be combined with in vivo micro-CT-based imaging to provide geometric and kinematic information sufficient for informing biomechanical calculations of mean strain fields along the mouse aorta³⁴. In the present study we (i) validated our synchrotron-based biomechanics in a unique pre-clinical setting and (ii) investigated the role of biomechanics in disease initiation after only 3 days of AngII infusion, when lesions begin to form. As expected, we found that branching regions act as geometric and material discontinuities that can give rise to strain hotspots and sites of precursor vascular damage (Figure 3.4). That is, a positive correlation was found between high mechanical strain and contrast agent infiltration in branching, but not in straight, regions of the suprarenal aorta (Figure 3.5c). These findings thus support further the importance of side branches in the initiation of aortic dissection in mice resulting from AngII

infusion²⁰.

Due to the correlative nature of our experiments, we cannot establish an unequivocal causal link between high mechanical strain and vascular damage. In order to establish such a link, we would need to estimate the mechanical strain using synchrotron biomechanics on a healthy mouse, then follow the same animal after 3 days of AngII-infusion and compare sites of wall injury to locations of elevated mechanical strain. This is currently not technically feasible since PCXTM is an *ex vivo* technique and the animal is sacrificed before the images are taken. Yet, the strain concentrations we observe at branching regions of control animals would be expected to increase markedly at high pressures (i.e., with pressure elevation due to AngII infusion), thus increasing the likelihood of vascular damage at these sites. Indeed, there does not appear to be sufficient mechano-adaptation of the aortic wall via increased matrix deposition within the first 3 to 4 days of AngII infusion^{28,29}, hence leaving sites of high stress/strain potentially more vulnerable to mechanical damage. In the suprarenal aorta in particular, there is an early and persistent increase in elastically stored energy at systolic pressure after 4 days of AngII infusion that is consistent with an increased circumferential strain, which may arise due to an early increase in MMP13 expression in the absence of collagen synthesis^{28,29}. This concept is consistent with the suggestion by Gavish et al.²⁰ that dissections occur when vulnerable sites are not reinforced properly by collagen remodelling. The present results suggest further that following the AngII-induced rise in blood pressure, the first intimal and intramural defects in the suprarenal aorta may nucleate at branch sites that constitute strain hotspots that precede vascular damage.

Dorsal protection and circumferential variation

AngII-induced lesions not only occur preferentially in the suprarenal aorta of the mouse, they also form on the left side of the suprarenal aorta^{24,16,44}. Several hypotheses have been offered to explain this circumferential specificity^{16,27}, but a clear explanation remains wanting. Despite having the highest strain index values and the highest volumes of contrast agent infiltration of all branching regions, there was no evidence of significant microstructural damage or strain hotspots in the dorsal quadrant of the celiac and superior mesenteric/right renal segments (Figure 3.6b). Mechanical protection of the dorsal aorta is consistent with the lower stored energy density computed in the dorsal compared to the ventral half of the healthy ApoE-deficient suprarenal aorta⁴⁵ and the 3-fold lower expansion of the posterior compared to the anterior abdominal wall⁴⁶. The posterior perivascular support of the aorta⁴⁷ - such as the dorsal musculature and spinal tethering - could also explain its mechanical shielding.

Another striking observation is that microstructural damage preferentially occurs on the ventral and left quadrants of the celiac and superior mesenteric/right renal aortic segment. Interestingly, these segments also experience high strain on the ventral and (to a lesser extent) right quadrants (Figure 3.6) – the quadrants with prominent branch ostia. When it comes to strain and vascular damage, the ventral quadrants of the celiac and superior mesenteric/right

renal segments thus seem to be at the highest risk. This may at first seem contradictory to previous findings, which point to medial tears in the left and ventral, but not in the right, quadrant²³. It is important to note, however, the difference between initiation and propagation. Indeed, the propagation of microruptures into medial tears, and the subsequent dissection of the left side of the tunica adventitia, may be driven by additional mechanical factors.

Hypothesis on tear propagation

We previously conjectured that medial microruptures, occurring after 3 days of AngII infusion around the celiac and superior mesenteric branches but sometimes at the ostia of intercostal or left renal arteries, constitute the initial insult to the aortic wall in this mouse model of dissection²³. These microruptures subsequently propagate to form a medial tear, previously termed by Gavish and colleagues^{21,20} as a transmural or transmural disruption and found after 4 weeks of AngII infusion in the vicinity of the orifices of major abdominal branches. This theory is not in conflict with our current findings, which suggest that microruptures may form in locations that experience the highest strain and then propagate to form larger medial defects. We further hypothesized that the transition from microrupture to medial tear is dictated by the local mechanics near the small side branches, which may or may not be torn as the medial tear propagates in the aorta.

This general concept is supported further by the synchrotron-based images of spontaneous delaminations that occurred in 4-day AngII-infused aortas during ex vivo biaxial testing (Figure 3.7). Importantly, these vessels are tested in the absence of additional mechanical factors such as complex hemodynamics and perivascular support, hence allowing one to focus on discontinuities near branches. The medial tear that appeared to act as an entry point for saline to enter between media and adventitia was found near a side branch for the suprarenal and infrarenal aortas, specifically around the celiac artery in the sample that included this bifurcation (sample 3). Moreover, all of the delaminations observed ex vivo coincided with small side branches suggesting that the latter may have acted as originating sites or anchoring points to sustain the propagating delamination. Though we do not know whether these samples would have progressed to aortic dissection in vivo had they not been harvested at 4 days, our ex vivo observations suggest that the use of precisely controlled supra-physiological loading conditions in the absence of in vivo perivascular support may reveal an intrinsic predisposition to strain-induced delamination at branch sites following AngII infusion.

Limitations and future work

Our validation of contrast agent as an indicator of future vascular damage yielded a modest number of false positives and false negatives ($\leq 6\%$ of all measurements; Figure 3.2c). Nevertheless, these mismatches between contrast agent and histopathological lesion presence constitute a potential source of uncertainty. It is important to emphasize, however, that histological preparations inherently induce cutting artifacts, particularly in structurally vulnerable

samples and mismatches can occur due to errors in mapping histological slides to the corresponding ex vivo synchrotron image. Hence, using infiltrating contrast agent as an in vivo marker of vulnerability is promising.

We used a custom semi-automated morphing framework to compute the in vivo strain field of murine abdominal aortas. This framework combines ex vivo PCXTM and in vivo micro-CT to provide morphological information on local axial stretch, minor aortic side branches, and mouse-specific aortic wall thickness. A sensitivity analysis shows that all of these features can significantly alter the computed strain hotspots in the FEM simulations³⁴ and are thus critical to measure. Some limitations of the framework have been described previously, and include (amongst others) shrinkage of the sample due to the dehydrating fixation process for the PCXTM, the absence of pre-stress, and the use of a simplistic material model³⁴. Additional limitations of our morphing approach include the assumption of material homogeneity (which disregards possible mechanical homeostasis near branches) and the difficulty of modelling small side branches or a collapsed aortic geometry. Due to problems with collapsed (non-pressured) geometries - leading to poor mesh element quality - we were unable to model 4 cases of saline-infused animals and 1 case of an AngII-infused mouse (Figure 3.8). A similar problem did not arise for the rest of the AngII-infused vessels, which appeared to be structurally stiffer. The impact of this work would have been greater had we managed to include more saline-infused control cases. We were also not able to model some of the smallest branches, which may have influenced the results (Figure 3.5b).

In the context of computational-experimental studies, more sophisticated approaches have been proposed for identifying correlations between indices of hemodynamic simulations and plaque-related damage⁴⁷. We did not implement such approaches here because we did not expect to find an exact match between voxels with high strain and voxels with contrast agent infiltration. Indeed, our synchrotron images do not allow an unequivocal determination of the point of entry of contrast agent into the wall. Upon entering the wall, contrast agent can spread due to the transmural pressure gradient and diffusion. The choice for larger, branch- versus straight-segment defined regions thus allowed more robust comparisons. In this context, it is important that our post-hoc outlier removal (Figure 3.5b) was based on clear criteria - binary variables of presence/absence of contrast agent and aortic side branches - that were not subject to interpretation, thus avoiding observer bias.

Finally, it has been postulated that non-uniform distributions of collagen fiber orientation near branch sites lead to local material heterogeneities that could generate intramural shear stresses sufficient to initiate a delamination event which subsequently propagates into a dissection⁴⁸. Such effects were not considered in our current modelling and simulation strategy. Conversely, studies on porcine aortas have recently suggested that a strain-driven collagen fiber rearrangement mechanism may exist⁴⁹. In future work we intend to extend our current methodology to include more sophisticated imaging and material models that account for local fiber orientation. This might also allow us to gain a better understanding of the role of biomechanics in the regional variations in contrast agent infiltration that was observed within

the AngII-infused group (Figure 3.2d). More sophisticated material models will also allow better computations of wall stress, not just wall strain, noting that it is yet unknown whether intramural damage leading to dissection or rupture follow a stress-, strain-, or energy-based failure criterion. Correlations of damage with strain have the added advantage, however, of potential measurement without detailed understanding of the evolving, likely anisotropic and heterogeneous material properties.

Conclusions

We have used synchrotron-based biomechanics to study initiating events in the AngII-infusion mouse model of aortic dissection. We predicted in vivo aortic strains and correlated strain concentrations with mouse-specific 3D histopathological defects in the abdominal aortas of Ang-II infused mice. We submit that branching sites sustain significantly higher strain and wall injury compared to non-branching regions, and that the dorsal aorta is mechanically protected. Ex-vivo load-induced aortic delaminations further point towards branching regions as nucleating sites for aortic dissections in AngII-infused mice.

5 Appendix

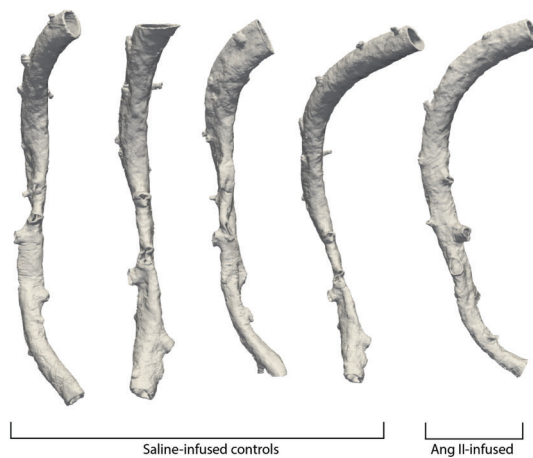


Figure 3.8: Collapsed geometries in undeformed configurations for $n=4$ saline-infused and $n=1$ AngII-infused mice.

Bibliography

- [1] J.D. Humphrey and G.A. Holzapfel. Mechanics, mechanobiology, and modeling of human abdominal aorta and aneurysms. *Journal of Biomechanics*, 45(5):805 – 814, 2012. Special Issue on Cardiovascular Solid Mechanics.
- [2] David A. Vorp. Biomechanics of abdominal aortic aneurysm. *Journal of Biomechanics*, 40(9):1887–1902, 2007.
- [3] Christos Manopoulos, Ioannis Karathanasis, Ilias Kouerinis, Dimitrios C. Angouras, Andreas Lazaris, Sokrates Tsangaris, and Dimitrios P. Sokolis. Identification of regional/layer differences in failure properties and thickness as important biomechanical factors responsible for the initiation of aortic dissections. *Journal of Biomechanics*, 80:102 – 110, 2018.
- [4] Dario Farotto, Patrick Segers, Bart Meuris, Jos Vander Sloten, and Nele Famaey. The role of biomechanics in aortic aneurysm management: requirements, open problems and future prospects. *Journal of the Mechanical Behavior of Biomedical Materials*, 77:295–307, 2018.
- [5] Eva L. Leemans, Tineke P. Willems, Maarten J. van der Laan, Cornelis H. Slump, and Clark J. Zeebregts. Biomechanical indices for rupture risk estimation in abdominal aortic aneurysms. *Journal of Endovascular Therapy*, 24(2):254–261, 2016.
- [6] Mirko Bonfanti, Stavroula Balabani, John P. Greenwood, Sapna Puppala, Shervanthi Homer-Vanniasinkam, and Vanessa Díaz-Zuccarini. Computational tools for clinical support: a multi-scale compliant model for haemodynamic simulations in an aortic dissection based on multi-modal imaging data. *Journal of The Royal Society Interface*, 14(136), 2017.
- [7] H. Y. Chen, S. V. Peelukhana, Z. C. Berwick, J. Kratzberg, J. F. Krieger, B. Roeder, S. Chambers, and G. S. Kassab. Editor’s choice – fluid–structure interaction simulations of aortic dissection with bench validation. *European Journal of Vascular and Endovascular Surgery*, 52(5):589–595, 2016.
- [8] David Perrin, Pierre Badel, Laurent Orgeas, Christian Geindreau, Sabine rolland du Roscoat, Jean-Noël Albertini, and Stéphane Avril. Patient-specific simulation of endovascular repair surgery with tortuous aneurysms requiring flexible stent-grafts. *Journal of the Mechanical Behavior of Biomedical Materials*, 63:86–99, 2016.
- [9] Derek P. Nathan, Chun Xu, Alison M. Pouch, Krishnan B. Chandran, Benoit Desjardins, Joseph H. Gorman, Ron M. Fairman, Robert C. Gorman, and Benjamin M. Jackson. Increased wall stress of saccular versus fusiform aneurysms of the descending thoracic aorta. *Annals of Vascular Surgery*, 25(8):1129 – 1137, 2011.

Bibliography

- [10] Qingzhuo Chi, Ying He, Yong Luan, Kairong Qin, and Lizhong Mu. Numerical analysis of wall shear stress in ascending aorta before tearing in type a aortic dissection. *Computers in Biology and Medicine*, 89:236–247, 2017.
- [11] Bram Trachet, Rodrigo A. Fraga-Silva, Philippe A. Jacquet, Nikolaos Stergiopoulos, and Patrick Segers. Incidence, severity, mortality, and confounding factors for dissecting AAA detection in angiotensin II-infused mice: a meta-analysis. *Cardiovascular Research*, 108(1):159–170, 08 2015.
- [12] Alan Daugherty and Lisa A. Cassis. Mouse models of abdominal aortic aneurysms. *Arteriosclerosis, Thrombosis, and Vascular Biology*, 24(3):429–434, 2004.
- [13] Alan Daugherty, Michael W. Manning, and Lisa A Cassis. Angiotensin ii promotes atherosclerotic lesions and aneurysms in apolipoprotein e-deficient mice. *The Journal of Clinical Investigation*, 105(11):1605–1612, 2000.
- [14] Kiran Saraff, Fjoralba Babamusta, Lisa A. Cassis, and Alan Daugherty. Aortic dissection precedes formation of aneurysms and atherosclerosis in angiotensin ii-infused, apolipoprotein e-deficient mice. *Arteriosclerosis, Thrombosis, and Vascular Biology*, 23(9):1621–1626, 2003.
- [15] Richard Y. Cao, Tim Amand, Matthew D. Ford, Ugo Piomelli, and Colin D. Funk. The murine angiotensin ii-induced abdominal aortic aneurysm model: Rupture risk and inflammatory progression patterns. *Frontiers in Pharmacology*, 1:9, 2010. 21713101[pmid] Front Pharmacol.
- [16] Craig J. Goergen, Kyla N. Barr, Diem T. Huynh, Jeffrey R. Eastham-Anderson, Gilwoo Choi, Maj Hedehus, Ronald L. Dalman, Andrew J. Connolly, Charles A. Taylor, Philip S. Tsao, and Joan M. Greve. In vivo quantification of murine aortic cyclic strain, motion, and curvature: Implications for abdominal aortic aneurysm growth. *Journal of Magnetic Resonance Imaging*, 32(4):847–858, 2010.
- [17] Bram Trachet, Marjolijn Renard, Gianluca De Santis, Steven Staelens, Julie De Backer, Luca Antiga, Bart Loeys, and Patrick Segers. An integrated framework to quantitatively link mouse-specific hemodynamics to aneurysm formation in angiotensin ii-infused apoe -/- mice. *Annals of Biomedical Engineering*, 39(9):2430, 2011.
- [18] Yi-Xin Wang, Baby Martin-McNulty, Ana D. Freay, Drew A. Sukovich, Meredith Halks-Miller, Wei-Wei Li, Ronald Vergona, Mark E. Sullivan, John Morser, William P. Dole, and Gary G. Deng. Angiotensin ii increases urokinase-type plasminogen activator expression and induces aneurysm in the abdominal aorta of apolipoprotein e-deficient mice. *The American Journal of Pathology*, 159(4):1455–1464, 2001.
- [19] Eiketsu Sho, Mien Sho, Hiroshi Nanjo, Koichi Kawamura, Hirotake Masuda, and Ronald L. Dalman. Hemodynamic regulation of cd34⁺ cell localization and differentiation in experimental aneurysms. *Arteriosclerosis, Thrombosis, and Vascular Biology*, 24(10):1916–1921, 2004.

- [20] Lilach Gavish, Ronen Beeri, Dan Gilon, Chen Rubinstein, Yacov Berlatzky, Leah Y. Gavish, Atilla Bulut, Mickey Harlev, Petachia Reissman, and S. David Gertz. Inadequate reinforcement of transmedial disruptions at branch points subtends aortic aneurysm formation in apolipoprotein-e-deficient mice. *Cardiovascular Pathology*, 23(3):152–159, 2014.
- [21] Lilach Gavish, Chen Rubinstein, Yacov Berlatzky, Leah Y. Gavish, Ronen Beeri, Dan Gilon, Atilla Bulut, Mickey Harlev, Petachia Reissman, and S. David Gertz. Low level laser arrests abdominal aortic aneurysm by collagen matrix reinforcement in apolipoprotein e-deficient mice. *Lasers in Surgery and Medicine*, 44(8):664–674, 2012.
- [22] Bram Trachet, Rodrigo A. Fraga-Silva, Alessandra Piersigilli, Alain Tedgui, Jessica Sordet-Dessimoz, Alberto Astolfo, Carole Van der Donckt, Peter Modregger, Marco F. M. Stampanoni, Patrick Segers, and Nikolaos Stergiopoulos. Dissecting abdominal aortic aneurysm in Ang II-infused mice: suprarenal branch ruptures and apparent luminal dilatation. *Cardiovascular Research*, 105(2):213–222, 12 2014.
- [23] Bram Trachet, Lydia Aslanidou, Alessandra Piersigilli, Rodrigo A. Fraga-Silva, Jessica Sordet-Dessimoz, Pablo Villanueva-Perez, Marco F.M. Stampanoni, Nikolaos Stergiopoulos, and Patrick Segers. Angiotensin II infusion into ApoE^{-/-} mice: a model for aortic dissection rather than abdominal aortic aneurysm? *Cardiovascular Research*, 113(10):1230–1242, 06 2017.
- [24] Amelia R. Adelsperger, Evan H. Phillips, Hilda S. Ibriga, Bruce A. Craig, Linden A. Green, Michael P. Murphy, and Craig J. Goergen. Development and growth trends in angiotensin ii-induced murine dissecting abdominal aortic aneurysms. *Physiological Reports*, 6(8):e13668, 2018. 29696811[pmid]PHY213668[PII]Physiol Rep.
- [25] John T. Favreau, Binh T. Nguyen, Ian Gao, Peng Yu, Ming Tao, Jacob Schneiderman, Glenn R. Gaudette, and C. Keith Ozaki. Murine ultrasound imaging for circumferential strain analyses in the angiotensin ii abdominal aortic aneurysm model. *Journal of Vascular Surgery*, 56(2):462–469, 2012.
- [26] K. Genovese, M. J. Collins, Y. U. Lee, and J. D. Humphrey. Regional finite strains in an angiotensin-ii induced mouse model of dissecting abdominal aortic aneurysms. *Cardiovascular Engineering and Technology*, 3(2):194–202, 2012.
- [27] Craig J. Goergen, Junya Azuma, Kyla N. Barr, Lars Magdefessel, Dara Y. Kallop, Alvin Gogineni, Amarjeet Grewall, Robby M. Weimer, Andrew J. Connolly, Ronald L. Dalman, Charles A. Taylor, Philip S. Tsao, and Joan M. Greve. Influences of aortic motion and curvature on vessel expansion in murine experimental aneurysms. *Arteriosclerosis, thrombosis, and vascular biology*, 31(2):270–279, 2011. 21071686[pmid] Arterioscler Thromb Vasc Biol.
- [28] M. R. Bersi, R. Khosravi, A. J. Wujciak, D. G. Harrison, and J. D. Humphrey. Differential cell-matrix mechanoadaptations and inflammation drive regional propensities to aortic

- fibrosis, aneurysm or dissection in hypertension. *Journal of The Royal Society Interface*, 14(136):20170327, 2017.
- [29] Fanny Laroumanie, Arina Korneva, Matthew R. Bersi, Matthew R. Alexander, Liang Xiao, Xue Zhong, Justin P. Van Beusecum, Yuhang Chen, Mohamed A. Saleh, William G. McMaster, Kyle A. Gavulic, Bethany L. Dale, Shilin Zhao, Yan Guo, Yu Shyr, Daniel S. Perrien, Nancy J. Cox, John A. Curci, Jay D. Humphrey, and Meena S. Madhur. Lnk deficiency promotes acute aortic dissection and rupture. *JCI insight*, 3(20):e122558, 2018. 30333305[pmid] PMC6237478[pmcid] 122558[PII] JCI Insight.
 - [30] Matthew D. Ford, Ariel T. Black, Richard Y. Cao, Colin D. Funk, and Ugo Piomelli. Hemodynamics of the mouse abdominal aortic aneurysm. *Journal of Biomechanical Engineering*, 133(12):121008–121008–9, 2011. 10.1115/1.4005477.
 - [31] E. H. Phillips, P. Di Achille, M. R. Bersi, J. D. Humphrey, and C. J. Goergen. Multi-modality imaging enables detailed hemodynamic simulations in dissecting aneurysms in mice. *IEEE Transactions on Medical Imaging*, 36(6):1297–1305, 2017.
 - [32] Bram Trachet, Joris Bols, Joris Degroote, Benedict Verhegghe, Nikolaos Stergiopulos, Jan Vierendeels, and Patrick Segers. An animal-specific fsi model of the abdominal aorta in anesthetized mice. *Annals of Biomedical Engineering*, 43(6):1298–1309, Jun 2015.
 - [33] Bram Trachet, Goran Lovric, Pablo Villanueva-Perez, Lydia Aslanidou, Mauro Ferraro, Gerlinde Logghe, Nikolaos Stergiopulos, and Patrick Segers. Synchrotron-based phase contrast imaging of cardiovascular tissue in mice—grating interferometry or phase propagation? *Biomedical Physics & Engineering Express*, 5(1):015010, nov 2018.
 - [34] Mauro Ferraro, Bram Trachet, Lydia Aslanidou, Heleen Fehervary, Patrick Segers, and Nikolaos Stergiopulos. Should we ignore what we cannot measure? how non-uniform stretch, non-uniform wall thickness and minor side branches affect computational aortic biomechanics in mice. *Annals of Biomedical Engineering*, 46(1):159–170, Jan 2018.
 - [35] Jacopo Ferruzzi, Paolo Di Achille, George Tellides, and Jay D. Humphrey. Combining in vivo and in vitro biomechanical data reveals key roles of perivascular tethering in central artery function. *PLOS ONE*, 13(9):e0201379, 2018.
 - [36] B Trachet, R Fraga-Silva, A Piersigilli, P Segers, and N Stergiopulos. Dissecting abdominal aortic aneurysm in angiotensin ii-infused mice: the importance of imaging. *Current Pharmaceutical Design*, 21(28):4049.
 - [37] Luca Antiga, Marina Piccinelli, Lorenzo Botti, Bogdan Ene-Iordache, Andrea Remuzzi, and David A. Steinman. An image-based modeling framework for patient-specific computational hemodynamics. *Medical & Biological Engineering & Computing*, 46(11):1097, Nov 2008.
 - [38] Utkarsh Ayachit. *The ParaView Guide: A Parallel Visualization Application*. Kitware, Inc., 2015.

- [39] Jacopo Ferruzzi, Sae-Il Murtada, Guangxin Li, Yang Jiao, Selen Uman, Magdalene Y.L. Ting, George Tellides, and Jay D. Humphrey. Pharmacologically improved contractility protects against aortic dissection in mice with disrupted transforming growth factor- β signaling despite compromised extracellular matrix properties. *Arteriosclerosis, Thrombosis, and Vascular Biology*, 36(5):919–927, 2016.
- [40] Christopher M. Haggerty, Andrea C. Mattingly, Ming C. Gong, Wen Su, Alan Daugherty, and Brandon K. Fornwalt. Telemetric blood pressure assessment in angiotensin ii-infused apoe-/- mice: 28 day natural history and comparison to tail-cuff measurements. *PLOS ONE*, 10(6):e0130723, 2015.
- [41] C. Bellini, J. Ferruzzi, S. Roccabianca, E. S. Di Martino, and J. D. Humphrey. A microstructurally motivated model of arterial wall mechanics with mechanobiological implications. *Annals of Biomedical Engineering*, 42(3):488–502, 2014.
- [42] Evan H. Phillips, Adam H. Lorch, Abigail C. Durkes, and Craig J. Goergen. Early pathological characterization of murine dissecting abdominal aortic aneurysms. *APL Bioengineering*, 2(4):046106, 2018.
- [43] Lisa A. Cassis, Manisha Gupte, Sarah Thayer, Xuan Zhang, Richard Charnigo, Deborah A. Howatt, Debra L. Rateri, and Alan Daugherty. Ang ii infusion promotes abdominal aortic aneurysms independent of increased blood pressure in hypercholesterolemic mice. *American Journal of Physiology-Heart and Circulatory Physiology*, 296(5):H1660–H1665, 2009.
- [44] Xiaojie Xie, Hong Lu, Jessica J. Moorleghen, Deborah A. Howatt, Debra L. Rateri, Lisa A. Cassis, and Alan Daugherty. Doxycycline does not influence established abdominal aortic aneurysms in angiotensin ii-infused mice. *PLOS ONE*, 7(9):e46411, 2012.
- [45] Matthew R. Bersi, Chiara Bellini, Paolo Di Achille, Jay D. Humphrey, Katia Genovese, and Stéphane Avril. Novel methodology for characterizing regional variations in the material properties of murine aortas. *Journal of Biomechanical Engineering*, 138(7):071005–071005, 2016. 10.1115/1.4033674.
- [46] Craig J. Goergen, Bonnie L. Johnson, Joan M. Greve, Charles A. Taylor, and Christopher K. Zarins. Increased anterior abdominal aortic wall motion: Possible role in aneurysm pathogenesis and design of endovascular devices. *Journal of Endovascular Therapy*, 14(4):574–584, 2007.
- [47] David De Wilde, Bram Trachet, Guido R. Y. De Meyer, and Patrick Segers. Shear stress metrics and their relation to atherosclerosis: An in vivo follow-up study in atherosclerotic mice. *Annals of Biomedical Engineering*, 44(8):2327–2338, 2016.
- [48] C. Bellini, N. J. Kristofik, M. R. Bersi, T. R. Kyriakides, and J. D. Humphrey. A hidden structural vulnerability in the thrombospondin-2 deficient aorta increases the propensity to intramural delamination. *Journal of the Mechanical Behavior of Biomedical Materials*, 71:397–406, 2017.

Bibliography

- [49] R. T. Gaul, D. R. Nolan, and C. Lally. The use of small angle light scattering in assessing strain induced collagen degradation in arterial tissue ex vivo. *Journal of Biomechanics*, 81:155–160, 2018.

Chapter 4

Early alterations in vascular function of the suprarenal aorta in AngII-infused ApoE-deficient mice

Lydia Aslanidou¹, Bram Trachet^{1,2}, Linda Sasset³, Goran Lovric^{4,5}, Annarita di Lorenzo³, Nikos Stergiopoulos¹

¹ *Institute of Bioengineering, École Polytechnique Fédérale de Lausanne, Switzerland*

² *bioMMeda, Ghent University, Ghent, Belgium*

³ *Center for Vascular Biology, Weill Cornell Medical College, New York, USA*

⁴ *Centre d'Imagerie BioMédicale, École Polytechnique Fédérale de Lausanne, Switzerland*

⁵ *Swiss Light Source, Paul Scherrer Institute, Villigen, Switzerland*

Manuscript in preparation for publication

1 Introduction

Aortic dissections and aneurysms constitute a leading cause of morbidity and mortality in the aging Western population¹. Aortic dissection (AD) is an acute and often lethal condition characterized by a medial disruption which leads to the formation of a false lumen and/or intramural hematoma². The resulting compression of the true lumen can lead to end-organ ischemia³, while breach of structural wall integrity can lead to catastrophic rupture. Contrastingly, aortic aneurysm (AA) is a progressive focal dilatation of the vessel wall to more than 50% of the normal diameter, which can also culminate to aortic rupture⁴. In humans, aneurysms manifest in the thoracic (ascending) and in the abdominal aorta. Despite sharing similar gross characteristics, ascending and abdominal aneurysms constitute disparate diseases driven by contrasting mechanisms^{5,6}. Inflammation contributes to the development of AD - inflammatory cells induce medial degradation and predispose to dissection⁷. Human data on the etiology of these aortopathies are scarce, making animal models all the more useful to elucidate the nascent stage of lesions that mimic the human condition.

Chronic systemic infusion of Angiotensin II (AngII) in mice is a well-known mouse model used in preclinical research of aortic dissection and aneurysm. Phenotypically distinct lesions

appear in the ascending and the abdominal murine aorta^{8,9}. AngII-induced ascending aortic aneurysms are associated with progressive uniform lumen expansion^{10,11}, while their abdominal counterparts chiefly mimic aortic dissection: focal medial ruptures lead to the formation of a false channel^{12,13}. Intriguingly, while AngII is administered systemically, the pathologies inflicted on the mouse aorta are highly location-specific: aneurysms consistently form in the ascending aorta⁹ and dissections occur almost exclusively in the suprarenal region of the abdominal aorta^{8,12,14}. The time course of events in the formative stage of the AngII-induced disease is not yet fully understood.

Delineating the effects of exogenous AngII which lead to aortopathy in this mouse model can be a challenge due to the diverse actions of AngII signaling. Besides being a potent vasoconstrictor of peripheral vascular beds through the contractile AT1 receptor^{15,16,17}, and hence a key regulator of blood pressure¹⁸, AngII also induces vascular inflammation and remodelling^{19,20}. In AngII-induced dissections, the NF- κ B-IL-6 pathway leads to macrophage accumulation and activation as well as ROS production, while the TGF- β -Smad pathway elicits myofibroblast transition and ECM remodelling^{19,20}.

Bersi and colleagues recently propounded a comprehensive hypothesis to disentangle AngII-induced events in the ApoE-deficient mouse and link spatially varying responses of the aorta to region-specific pathological outcomes²¹. In their view, AngII infusion initially increases blood pressure and contractility. Blood pressure elevation increases the biaxial stress on the aortic wall, an effect counteracted by the protective action of increased contractility²². The increased wall stress then triggers the expression of chemokines and MMPs, which drive an inflammatory and remodelling response involving medial and adventitial collagen deposition but also degradation. The evolving balance of matrix deposition and degradation determines the pathological outcome in each aortic region. Their findings suggest that the ascending aorta's intramural cells are unable to homeostatically respond to the rapidly increased circumferential stiffness and hence aneurysmal dilatation ensues. In the suprarenal region, a transient imbalance in collagen turnover leaves the vessel unduly exposed to increased stress and contributes to the region's unique dissection propensity²¹.

Previously studied AngII-induced thoraco-abdominal dissections by means of synchrotron-based grating interferometry phase-contrast imaging have shed new light on the disease evolution (discussed in section 5.3 of the Introduction). A fortuitous discovery of white aggregates on images of the aortic wall at 6.5 μ m resolution revealed that the micro-computed tomography (micro-CT) contrast agent injected into the mice in vivo (prior to euthanasia) infiltrates the aortic wall *intra vitam*, to form microleaks visible on the *ex vivo* synchrotron scans. Sites of intramural contrast agent infiltration correspond to locations of vascular damage and offer the advantage of 3D localization along the entire vessel compared to traditional 2D histology. This serendipitous finding allowed us to observe that dissections start with medial microruptures mainly near the ostia of suprarenal side branches, with a particularly high incidence around the celiac and superior mesenteric arteries (chapter 2). Motivated by the location-specific insults to the aortic wall, we found, as we saw in chapter 3, that the excessive

aortic strain at branching sites of the abdominal aorta may intrinsically predispose them as nucleating sites for dissection. This strain-driven hypothesis is potentially complementary with the mechano-mediated hypothesis put forward by Bersi et al.²¹ (described in section 5.2 of the Introduction), whereby reduced collagen deposition in the suprarenal region renders it alone dissection-prone within the abdominal aorta. On the other hand, these hypotheses do not preclude the (synergistic) action of other mechanisms *in vivo* that may mediate the maladaptive response of the suprarenal aorta to AngII.

In subpressor AngII doses, dysfunctional smooth muscle contractility strongly correlates with maladaptive aortic remodelling and fibrosis in the mouse thoracic aorta²³. Moreover, restored smooth muscle contractility protects the otherwise vulnerable thoracic aorta from dissection in a conditional knockout mouse model²². There is thus accumulating evidence that contractile capacity and overall vascular function may play a role in dictating the aorta's local response to exogenous AngII. It is known that long-term exposure to pressor AngII doses leads to altered vascular reactivity in the mouse thoracic aorta²⁴, and more recent findings have suggested altered properties in the same location after 1 week of AngII infusion²⁵. In this work, we aim to assess early alterations in vascular function induced by AngII within the dissection-prone abdominal suprarenal aorta.

The first question to address when studying disease initiation, is which time point one should focus on. The ideal time point should occur late enough for meaningful changes to have transpired with respect to the baseline, but early enough so that such findings are not the result of complex and inter-dependent pathways of the AngII-elicited inflammatory cascade or matrix turnover. This is why in the first part of our study we determined *in vivo* and *ex vivo*, both in the ascending and the abdominal region, how long after the onset of AngII infusion the aorta sustains initial vascular damage. In the second part, this temporal information was subsequently used to evaluate spatial differences in the vascular function of the dissection-prone suprarenal aorta (and its side branches) in response to AngII.

2 Methods

Animals

Imaging study

All procedures were approved by the Ethical Committee of Canton Vaud, Switzerland (EC 2647.3) and performed according to Directive 2010/63/EU of the European Parliament on the protection of animals used for scientific purposes. Twelve-week old male wildtype C57BL/6J mice (n=19) and ApoE-deficient mice on a C57BL/6J background (n=19) were infused with AngII at a rate of 1000ng/kg/min as previously described in the method section 2 of the Chapter 2. For each animal, the duration of the infusion was 1 (n=6 of each strain), 2 (n=6 of each strain) or 3 (n=7 of each strain) days. All mice underwent one contrast-enhanced micro-CT scan at baseline and one just prior to euthanasia with a ketamine/xylazine cocktail

(100 mg/kg and 15 mg/kg, respectively). Age- and sex- matched ApoE-deficient controls (n=6) not implanted with an osmotic mini-pump underwent the same imaging protocol. Aortic tissue was collected following euthanasia.

Micro-CT imaging

All mice underwent one contrast-enhanced non-gated micro-CT scan at baseline (prior to pump implantation) and another one at end stage (prior to euthanasia). The contrast agent (ExiTron nano 12000; Miltenyi Biotech, Germany) was injected directly into the lateral caudal vein at 4 mL/g body mass. In each scan, the thorax and abdomen were scanned with a Quantum FX micro-CT scanner (Caliper Life Sciences, USA), while anesthesia was maintained with inhalation of 1.5% isoflurane in concentrated room air with oxygen levels between 85% and 91% (compressor Sequal Integra E-Z Oxygen concentrator). The resulting DICOM images had an isotropic voxel size of 50 μ m. Aortic volumes were quantified using the Mimics software (Materialise, Leuven, Belgium). In the ascending aorta, we considered the region from the aortic root to the beginning of left subclavian artery (Figure 4.2). In the abdominal aorta, the proximal landmark was fixed at 5mm above the celiac artery and 2.5 mm below the left renal artery (Figure 4.2).

PCXTM imaging

Harvested aortic tissue was fixed in 4% PFA and imaged at the Paul Scherrer Institute (Villigen, Switzerland) using propagation-based phase-contrast imaging at a 1.625 μ m isotropic resolution, as we saw in section 4.1 of the Introduction. Indicative 2D images of this modality are shown in Figure 4.1. The contrast agent used for the micro-CT scan percolated the aortic wall intra vitam and was visible in PCXTM scans, as previously described in section 5.3 and Chapters 2 and 3. The volume of contrast agent was quantified in the ascending and abdominal aorta using the Mimics software (Materialise, Leuven, Belgium).

In order to facilitate comparison of the contrast agent distribution with vascular reactivity findings, we set the axial length of the supraceliac segment as 2 mm above the celiac artery bifurcation, corresponding to the maximal vascular ring length that can be tested on the wire myograph setup.

Vascular reactivity study

N=25 male ApoE-deficient mice on a C57BL/6J background 12-14 weeks old were purchased from Jackson labs. Micro-osmotic Alzet 1003D pumps were left to prime overnight at 37°C before implantation. Mice were sacrificed with ketamine/xylazine after 3 days of AngII (Millipore) administration at 1000 ng/kg/min. Following transcardiac perfusion with PBS through the left ventricle at 40mmHg, the abdominal aorta was carefully cleaned in situ from surrounding fat and excised.

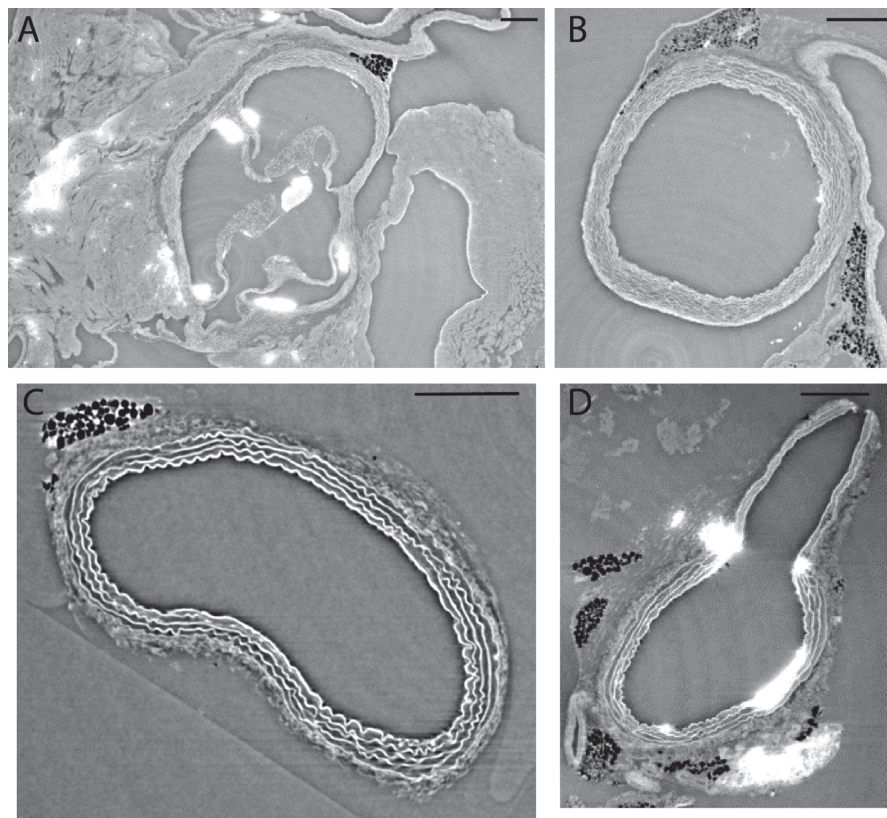


Figure 4.1: Examples of 2D images obtained in this study with propagation-based phase-contrast synchrotron imaging. A: aortic valve, B: ascending aorta, C: abdominal aorta, D: abdominal aorta at the celiac artery branching site. Note the bright contrast agent percolation in A and D. Scale bar is 300 μm .

In order to capture not only inter-subject alterations of vascular function between control and AngII-infused ApoE-deficient mice, but also intra-subject differences between aortic regions of different dissection propensities, an unaffected contralateral region was needed as a natural control. The ascending aorta, from which only one aortic ring can be obtained, offered no straight counter-segment as control in vicinity to the susceptible ascending segment. Conversely, in the abdominal aorta and in proximity to the susceptible suprarenal segment, the infrarenal segment is well-known to be protected from catastrophic events such as dissection, fibrosis or aneurysm. This region instead achieves a homeostatic response following AngII administration^{21,26,27}, which is why it can effectively serve as a control region. We chose the juxtarenal segment, between the right and left renal arteries, since it is located even closer to the affected region. Note that in the study by Bersi et al.²¹, their infrarenal segment extended from above the left renal artery (what we call juxtarenal segment here) down to the 'truly' infrarenal aorta (under both renal arteries) (cf. Figure 31). For the aortic side branches, since the celiac and superior mesenteric arteries are the most affected by microstructural damage, one of the renal arteries had to serve as control. We chose the left renal as control, since the right renal often branches off at the same level as the superior mesenteric and is hence directly

involved in the disease onset.

Briefly, the following intact aortic rings were isolated from the abdominal suprarenal aorta (cf. Figure 4.3): (i) a ring proximal to the celiac artery bifurcation (supraceliac segment), (ii) a ring in-between the bifurcations of the celiac and the superior mesenteric/right renal artery (paravisceral segment) and (iii) a ring in-between the right and left renal artery (juxtarenal segment). The maximum length of these arterial segments was 2 mm, equal to the gap of the wire myograph support system; the smaller length of the other two aortic rings was imposed by the bifurcating landmarks of the aorta which bound each segment. Arterial rings were also obtained from the celiac, superior mesenteric and left renal arteries, taken as proximally as possible close to the aorta.

Table 4.1: Mean lengths of arterial rings.

Arterial ring	Mean length [mm] \pm SD
<u>Aorta</u>	
Supraceliac	1.9 \pm 0.3
Paravisceral	1.0 \pm 0.3
Juxtarenal	1.1 \pm 0.3
<u>Side branches</u>	
Celiac	1.7 \pm 0.2
Superior mesenteric	1.8 \pm 0.2
Left renal	1.4 \pm 0.1

Two 40 μ m-diameter tungsten wires were passed through the lumen of each ring except the ring of the celiac artery, for which we used thinner 20 μ m-diameter wires to avoid damage of the inner endothelial cell layer. The vascular rings were mounted on a DMT620M wire myograph (Danish Myo Technology A/S, Denmark) and kept with carboxygenated physiological Krebs solution at 36.8°C. They were allowed to equilibrate in their optimal resting tension evaluated in preliminary experiments (0.45g for the aortic segments and superior mesenteric artery, 0.3g for the celiac and left renal arteries, Figure A1), for at least 30 minutes before the start of the protocol. Vasorelaxation was assessed with acetylcholine (Ach) and isoproterenol (ISO) (Sigma) on vessels precontracted with serotonin at concentrations adjusted to yield submaximal tension. Vasoconstriction was induced with phenylephrine (PE), and U-46619, a TXA2 mimetic (Cayman Chem). The contraction of the vessels following incubation with 60mM KCl for 20 minutes was used to normalize vasoconstriction responses (the contraction values to KCl were also assessed separately). We additionally tested Angiotensin II and endothelin-1 as vasoconstrictors but neither produced contractions in the segments, consistent with earlier reports^{28,17,24}, presumably due to the low expression of contractile AT1b receptors in the aorta. While such contractions are expected in the peripheral beds, we note that the superior mesenteric and celiac branches we test here are of a larger size than peripheral vessels (compared for example with first or second order mesenteric arteries typically used in studies of the periphery). Data were recorded on LabChart. The length of the aortic rings was

measured under a brightfield microscope following each experiment.

Histology

After imaging, samples were again fixed in % PFA. Paraffin-sections corresponding to the 3 suprarenal segments of the vascular reactivity study (supraceliac, paravisceral and juxtarenal) were stained for smooth muscle α -actin and Hematoxylin-Eosin. The samples were taken from the animals used in the imaging study. The quantification of α SMA was performed using the ImagePro software (Media Cybernetics). The aortic wall was segmented manually and the same intensity threshold was applied on all images.

Statistics

Changes in micro-CT aortic volume between baseline and endpoint geometry were evaluated with Wilcoxon matched-pairs signed rank tests. Changes in contrast agent volume infiltration between timepoints were assessed using Kruskal-Wallis tests with Dunn's multiple comparisons. For the vascular reactivity study, statistical significance was determined using two-way ANOVA with Bonferroni's multiple comparisons post-hoc test. Statistical significance was indicated by P values ≤ 0.05 .

3 Results

Temporal aspects: Aortic volume increase and vascular damage evolution over the first three days of AngII infusion

In ApoE^{-/-} mice, we observed a significant increase in the volume of the ascending and the abdominal aorta after 3 days of AngII infusion, but not after 1 or 2 days (Figure 4.2A, C and Suppl. Table A1). For wildtype mice, the volumetric increase of the ascending aorta was pronounced from day 1 of the AngII infusion leading up to day 3 (Figure 4.2B), while in the abdominal aorta the increase did not become significant until day 3, similarly to the ApoE-deficient mice (Figure 4.2D and Suppl. Table A1).

The volumetric enlargement of the ascending and abdominal aorta in vivo was paralleled by intramural contrast agent infiltration over the first 3 days of AngII infusion (Figure 4.3, Table A2), corresponding to aortic vascular damage as previously described in section 5.3 of the Introduction as well as in chapter 3. In the ascending aorta of ApoE^{-/-} mice, contrast agent leaks were present (non-zero) by day 1 of AngII infusion but only reached a significant difference with controls by day 3 ($P=0.0053$, Figure 4.3A), as was the case for WT mice ($P=0.0231$). Similarly, in the abdominal aorta of ApoE^{-/-} mice increases in contrast agent infiltration did not become significant until day 3 (Figure 4.3B). This observation was consistent for all three investigated suprarenal regions, but the amount of infiltrated contrast agent was higher in the

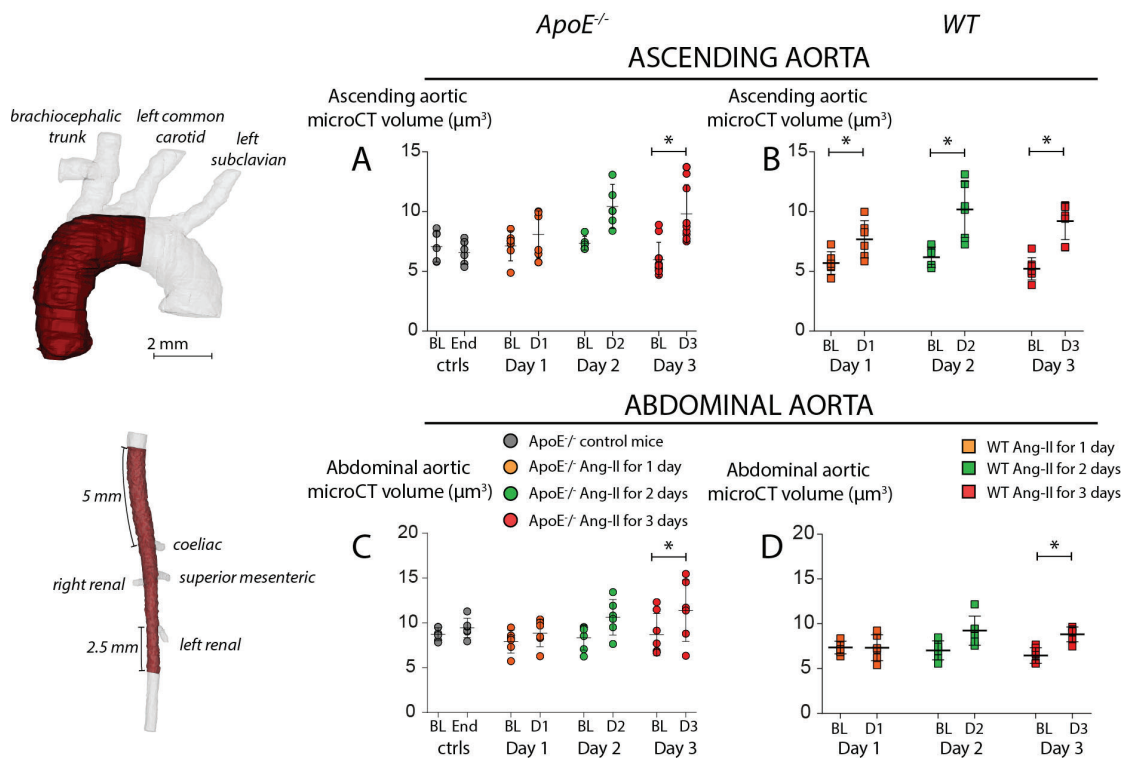


Figure 4.2: Ascending and abdominal aortic volumetric increase measured with micro-CT after 1, 2 and 3 days of AngII infusion compared to baseline, for ApoE^{-/-} (panels A,C) and WT (panels B,D) mice. Landmarks for the volumetric quantification of each region are illustrated on the left: ascending aortic volume was quantified from the aortic valve until after the bifurcation of the left common carotid. The abdominal region extended from 5-mm above the middle of the celiac bifurcation to 2.5-mm distal to the middle of the left renal bifurcation. Black line depicts mean±SD. BL: baseline, D1, D2, D3: day 1, day 2, day 3 of AngII infusion. Overbar denotes statistical significance between groups, *: P≤0.05. Values of comparisons are reported in Table A1.

supraceliac and paravisceral segments than in the juxtarenal segment. In the abdominal aorta of wildtype mice, no significant increase in microleaks could be observed by day 3.

Spatial aspects: impaired vascular endothelium-dependent relaxation and contractility in decreasing severity along the abdominal aorta

In the second part of this study we focused on the role of aortic reactivity in the propensity of the suprarenal aorta to aortic dissection. Since increases in micro-CT volume dilatation and intramural contrast agent volume infiltration did not become apparent until day 3 of AngII infusion, we set the timepoint for vascular reactivity assessment at the 3-day mark.

After 3 days of infusion we observed different degrees of impaired endothelium-mediated relaxation in the three abdominal aortic segments. In the supraceliac segment relaxation was

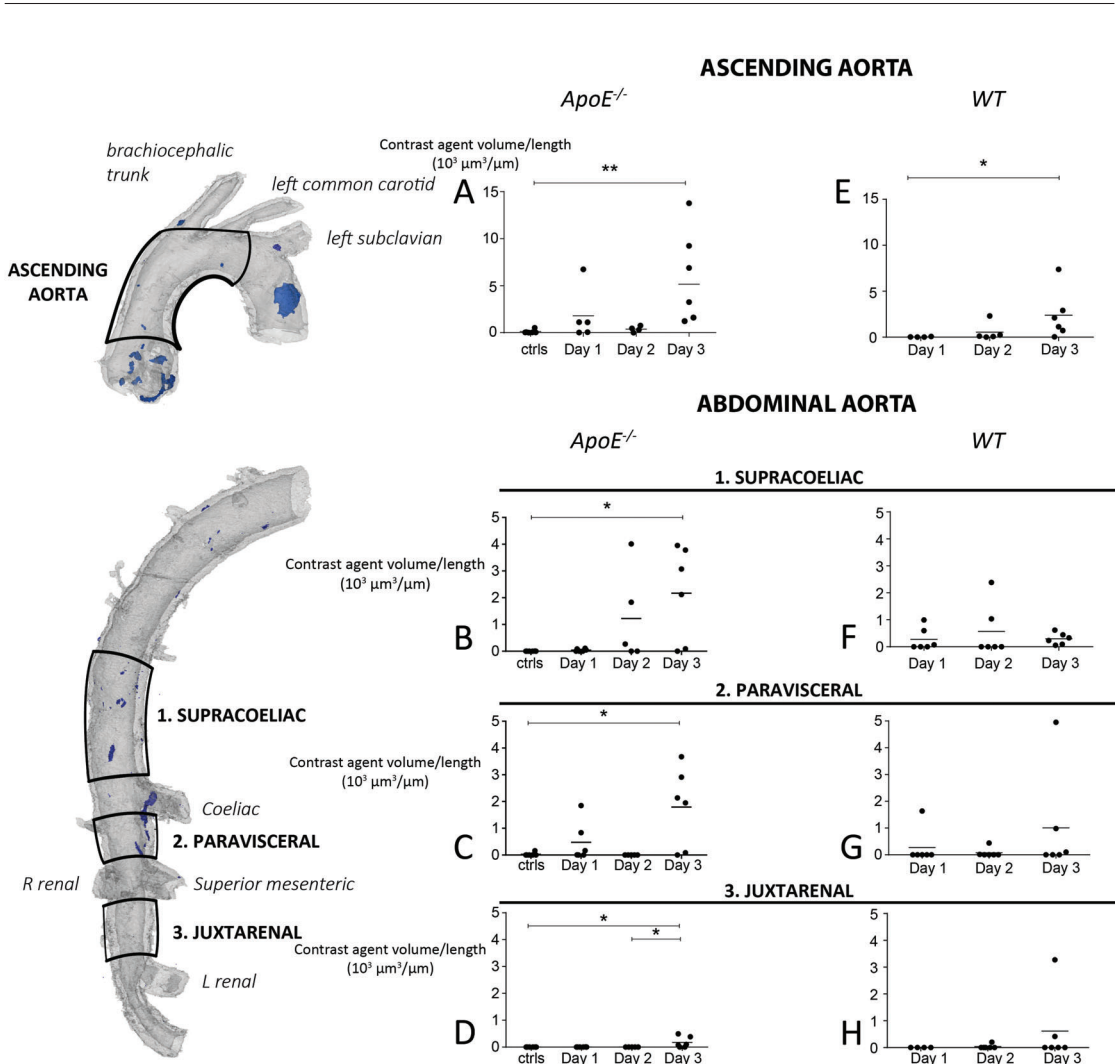


Figure 4.3: Quantification of contrast agent infiltration within the major aortic segments. Schematic depiction of the aortic segments tested is shown on the left. Contrast agent volume has been normalized to the axial length of each segment ($\mu\text{m}^3/\mu\text{m}$). Line denotes mean of group. Overbar denotes statistical significance between groups, where *, **: $P \leq 0.05$, 0.01 .

strongly impaired and in the paravisceral segment relaxation was compromised, whereas in the most distal juxtarenal segment there was no difference with control mice (Figure 4.4A). The most dramatic change occurred in the contractile response to phenylephrine, a selective $\alpha 1$ -adrenoreceptor agonist, which was severely impaired in the supraceliac segment (Figure 4.4B). In the paravisceral and juxtarenal segments, the PE agonist elicited a response that was blunted with respect to controls, but not zero.

We additionally assessed responses to other agonists. The isoproterenol-induced relaxation was significantly decreased in the supraceliac segment (Figure 4.6A). Contractile responses to U46619 (a stable thromboxane-A2 mimetic and thus an agonist for the TXA2 prostanoid receptor) reached the same maximal value in control and AngII-infused animals

but the half-maximally effective concentration shifted to larger values for the AngII mice (Figure 4.6, Table 4.2).

Table 4.2: Shift of half-maximally effective concentrations for dose-response curves to TXA2.

Aortic segment	Control EC50 [10^{-7} M]	AngII-infused EC50 [10^{-7} M]
Supraceliac	1.14	4.82
Paravisceral	1.8	6.84
Juxtarenal	1.6	3.72

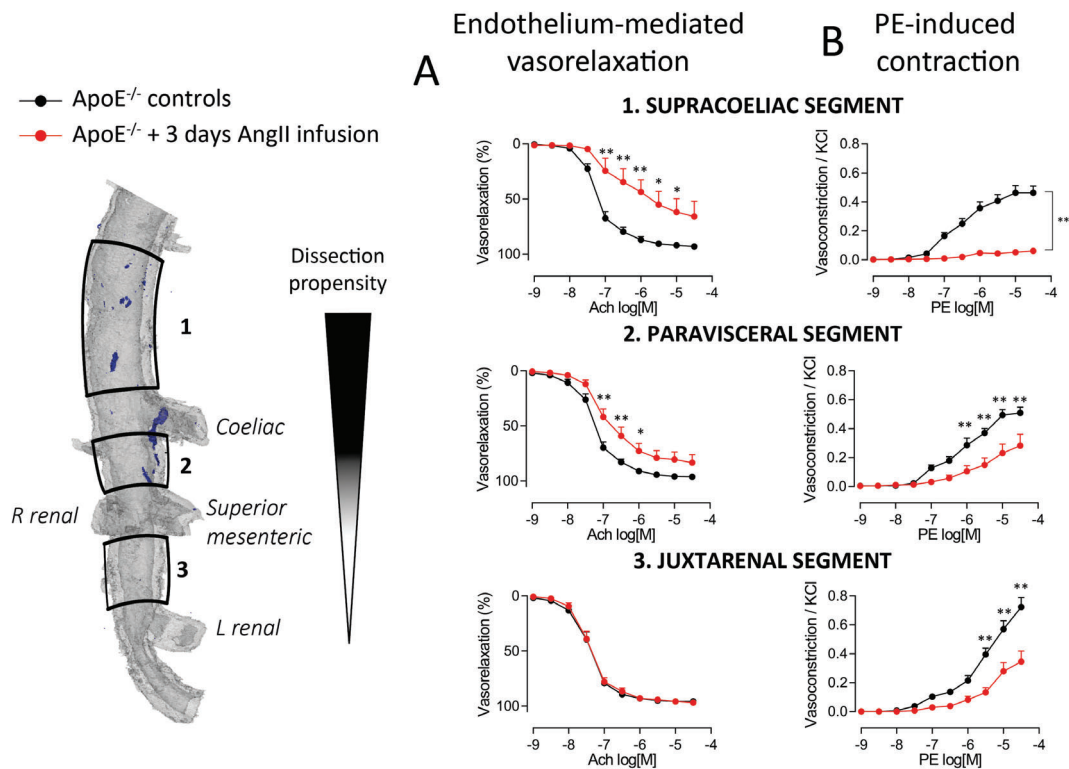


Figure 4.4: Vascular reactivity of 3 aortic segments. A. Dose-response curves of acetylcholine on vessels precontracted with serotonin [10^{-6} M]. B. Dose-response curves to phenylephrine. n=5-7 per group.

The most pronounced change in response among the vasoconstrictors tested was observed for phenylephrine, we therefore aimed to identify the underlying cause of this modulation. In order to assess whether the impaired contraction to PE stemmed from a local change in the smooth muscle contractile apparatus, we compared the rings' contractions to KCl (non-receptor-mediated response) (Figure 4.6D) but only observed a significant decrease in the paravisceral segment of AngII-infused animals. We further assessed whether receptor levels of phenylephrine were downregulated but instead found them to be upregulated in all

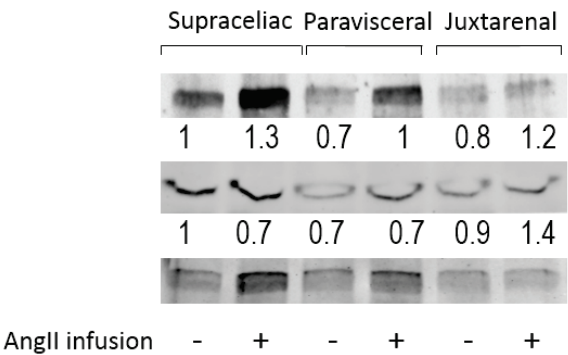


Figure 4.5: Western blot of control and AngII-infused aortic segments ($\alpha 1$ AR: adrenergic $\alpha 1$ receptor, TR: thromboxane receptor).

three abdominal segments (Figure 4.5). To further evaluate whether the $\alpha 1$ -adrenoreceptor-mediated contractility loss was due to loss of alpha smooth muscle-actin (a corollary of a possible phenotypic switch smooth muscle cells from the contractile to the synthetic type), we quantified the α -SMA content in the corresponding abdominal aortic regions but found no significant differences between time points in any of the three regions (Figure 4.7).

We then assessed the vasoreactivity of aortic side branches (Figure 4.8). No remarkable differences were found in endothelium-mediated relaxations, or responses to the vasoconstrictors phenylephrine, thromboxane-A2 or potassium chloride. These findings suggested that the overall vascular function of the branches was not compromised but generally preserved.

4 Discussion

Numerous studies have been published on the pathogenesis of ascending^{11,29} and abdominal lesions²¹ in the AngII infusion mouse model, however the temporal and spatial aspects of disease initiation still remain the subject of debate. It is known that lesion development in the abdominal aorta is rapid, spanning from hours to days^{13,30,31}. Mean blood pressure is already elevated by 20mmHg after the first day of AngII infusion, an elevation sustained over the first 3 days of infusion before further increasing³². After 2 days of AngII infusion to ApoE-deficient mice, Saraff et al. observed elastin fragmentation associated with macrophage migration in the aortic media of the suprarenal aorta¹². In our previous work we reported micro-ruptures after 3 days of AngII infusion, while Bersi et al. reported a significant increase in MMP-2 and MMP-13 expression in the suprarenal aorta (and non-significant increase in the ascending aorta) 4 days post-implantation²¹. These findings suggest that by day 4 the signaling cascade of AngII inciting inflammation and remodelling is already in effect. Here, we used synchrotron imaging to reveal that intramural infiltration of contrast agent, which serves as a proxy for intramural vascular damage, appears as early as 1 day post-implantation in the ascending and abdominal aorta of ApoE-/- mice. However, it does not increase significantly until day

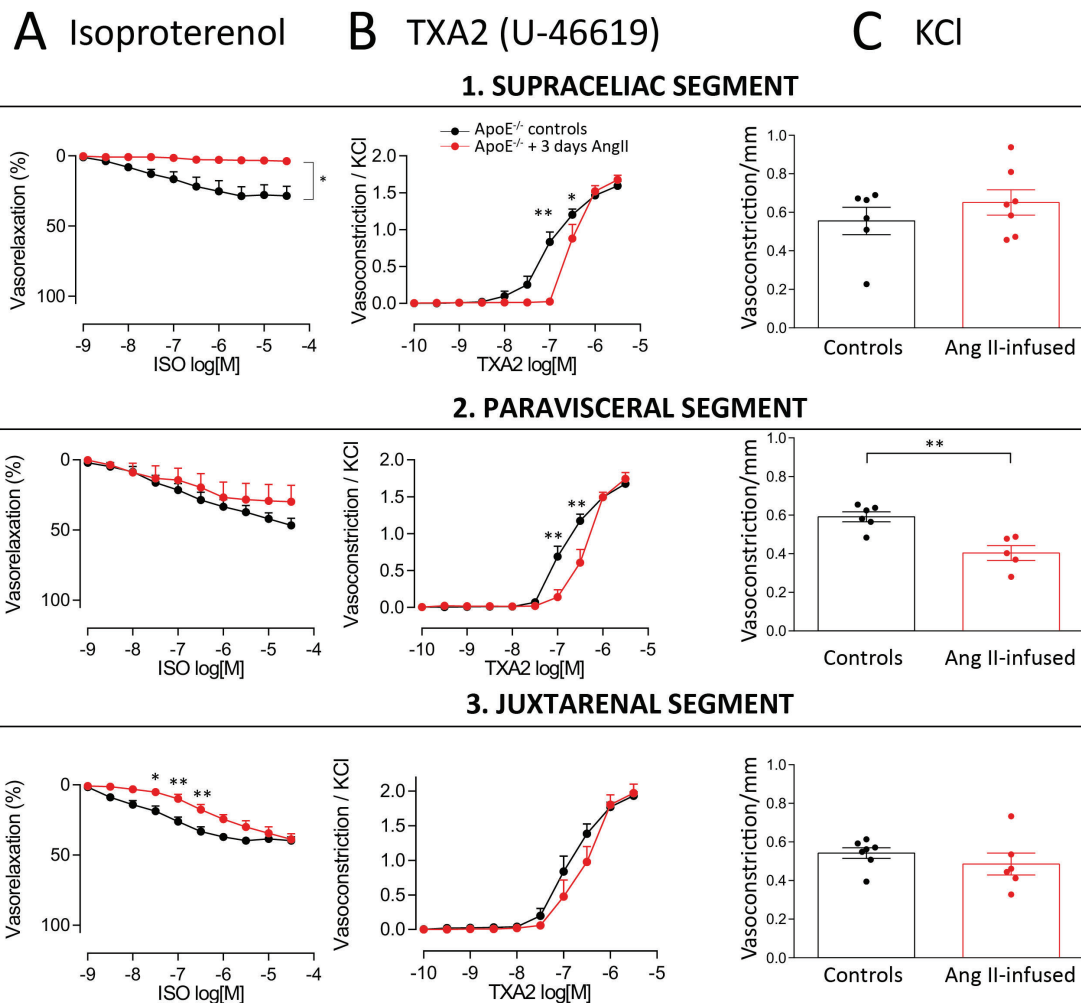


Figure 4.6: Vascular reactivity of the aortic segments. Dose-response curves of abdominal aortic segments to (A) isoproterenol, (B) U-46619, (C) KCl. In (C), the vessel's contraction to KCl has been normalized to each ring's axial length (g/mm). Mean \pm SEM, *: $P \leq 0.05$; **: $P \leq 0.01$, $n=5-7$ per group.

3 of AngII infusion (Figure 4.3). Similarly, in vivo assessment of aortic volumes based on contrast-enhanced micro-CT showed that a significant increase in the ascending and the abdominal aorta does not occur earlier than day 3 post-implantation (Figure 4.2). Based on these observations and those in literature, we determined day 3 of AngII infusion as the ideal time point to assess vascular reactivity in the abdominal aorta.

Despite the fact that AngII is administered in a systemic way, aortic dissections are almost exclusively localized in the suprarenal abdominal aorta of AngII-infused mice^{8,12,14}. We previously found that excessive aortic strain around the celiac and superior mesenteric branches of the abdominal aorta co-localized with microstructural wall damage after 3 days of AngII infusion (cf. chapter 3), suggesting a mechano-driven initiation mechanism. Bersi et al.²¹

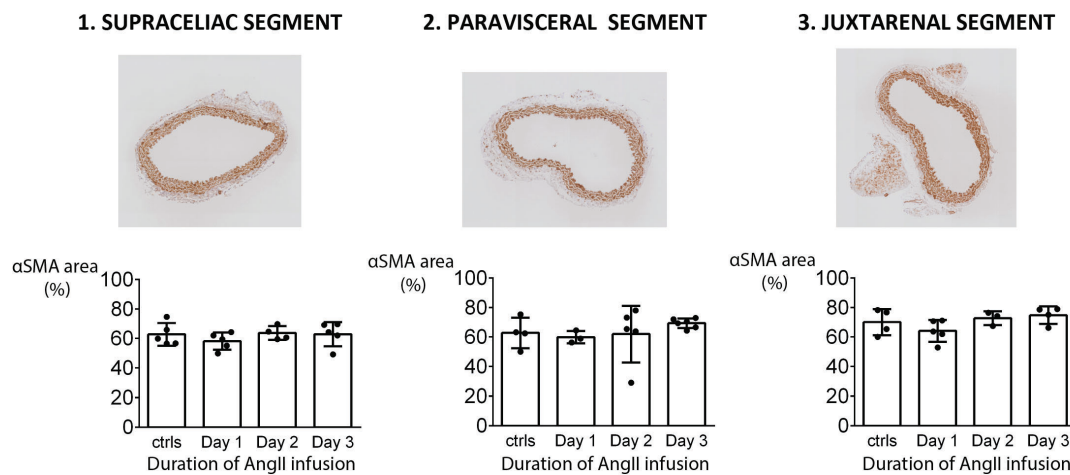


Figure 4.7: Alpha-smooth muscle actin quantification for 3 abdominal aortic regions. The area of α SMA has been normalized to the vessel area (%).

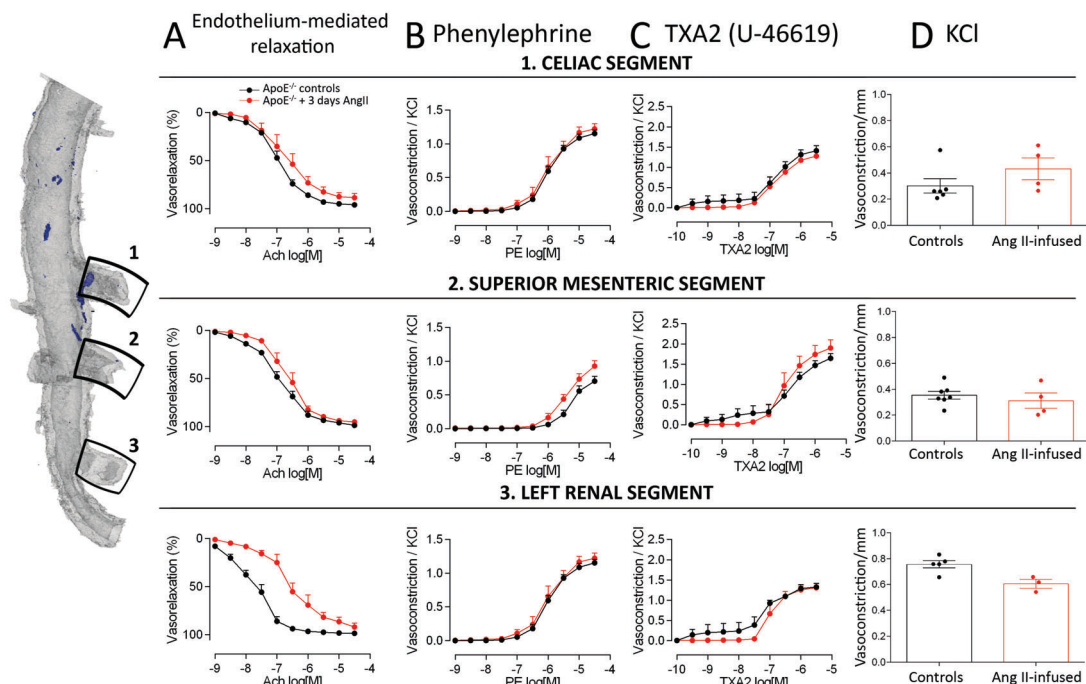


Figure 4.8: Vasoreactivity of aortic side branches. $n=5-7$ per group, except for: left renal KCl/length ($n=3$ AngII infused, length values not available for all segments tested) and left renal relaxation to acetylcholine ($n=3$ AngII infused, response not tested due to experimental conditions).

recently conjectured that the suprarenal aorta is at dissection risk because it does not manage to deposit sufficient collagen to stress shield the region against increased wall stress (previously described in section 5.2 of the Introduction). However, such reduced stress shielding could also occur due to a local alteration of vascular function, particularly at an early stage

of the disease. Taking into account the particular vulnerability of the aortic region in the vicinity of the celiac and superior mesenteric arteries, ascertained in chapter 2, we focused our vascular reactivity assessment on the abdominal suprarenal aorta in the early stage of the disease. Specifically, we investigated differences within the suprarenal region, which Bersi et al. previously considered homogeneous²¹, as well as its side branches.

Spatial differences in relaxation responses

Quantification of ex vivo contrast agent volume infiltration indicated that among the three investigated suprarenal segments, the supraceliac segment underwent the greatest wall damage (Figure 4.3, Table A3). This segment was also the one where the vascular endothelium-dependent vasorelaxation to acetylcholine was most severely compromised. Similarly to acetylcholine, relaxations through membrane hyperpolarization induced by isoproterenol were abrogated in the supraceliac segment (Figure 4.6). Endothelial dysfunction has been identified in previous isometric tension studies of AngII infused mice, albeit at later time points and different aortic regions: marked impairment was found after 14³³ and 28²⁴ days of infusion in the thoracic aorta, and in the femoral²⁴ artery of ApoE-deficient mice as well as in carotid arteries of C57BL/6 mice³⁴. No endothelial dysfunction was found in the adjacent arterial side branches, however.

Spatial differences in contraction responses

The biomechanical findings of chapter 3 have highlighted the vulnerability of side branches, particularly the celiac and superior mesenteric arteries, due to focal concentrations of strain around their ostia in the early stage of AngII infusion, thus demonstrating that AngII-induced dissections are branch-related. Here, the most dramatic change we observed in contractile response before and after brief AngII infusion was the abolished contraction to phenylephrine in the supraceliac segment of the suprarenal aorta, which borders with the coeliac side branch. This segment has been identified as the most dissection-prone within the suprarenal aorta³⁵. The compromised contractile capacity followed a tapering trend becoming less severe towards the distal end of the aorta, however side branches were spared of any dysfunction. Our present findings suggest that there is a local 'discontinuity' of vascular function properties around the ostia of side branches, as we transition from the aorta, whose endothelial function and contractile capacity have been impaired- to the -healthy- side branch, which has largely preserved its endothelial and contractile function.

The reasons behind the loss of phenylephrine-induced contractility in the suprarenal aorta are unclear. Cross-talk of alpha 1-adrenergic receptors and AngII has been reported in rats³⁶, rabbits^{37,38} but not in mice. It has been argued that the degree of sympathetic innervation could be a contributing factor in the pathophysiology of AngII-induced vascular changes in alpha adrenergic receptors³⁹. Other studies have reported that the C57BL/6 thoracic aorta showed no change in phenylephrine-induced contractions after 21 days of infusion⁴⁰, whereas

the ApoE-deficient thoracic aorta exhibited a leftward shift of the concentration response curve to phenylephrine after 14 days of AngII³³. However, those studies focused on later time points.

A possible explanation for the loss of contractility after 3 days of AngII infusion is the smooth muscle cell apoptosis, or switch of smooth muscle cells from the contractile to the synthetic phenotype. While we found no significant change in the content of α -smooth muscle actin (a smooth muscle cell marker protein customarily used to define the contractile phenotype⁴¹) over the first 3 days of AngII infusion, further histological investigation is needed to clarify whether a phenotypic switch occurs early on, similar to what has been reported in humans^{42,43}. No straightforward answer was obtained by observation of the change in responses to KCl, either. Contractions through KCl are classically used to bypass G protein-coupled receptors and activate smooth muscle by voltage-operated Ca^{2+} channels⁴⁴. KCl-elicited contractions were reduced in the (middle) paravisceral segment but not in the supraceliac or juxtarenal segment. Reduced contractile responses have been reported in thoracic aortic rings exposed to KCl after high-dose (1250 ng/kg/min for 2 weeks)⁴⁵ and low-dose AngII infusion (490 ng/kg/min for 2-4 weeks)²³, however both of these studies were focused on a different aortic region at a much later point in the time course of the disease and used different techniques. Interestingly, subpressor AngII doses in rats increased both phenylephrine and KCl contractions in the aorta^{46,47}, however important differences in inter-species vascular reactivity and response to AngII impede interpretations from rats to mice^{48,49}. Western blotting revealed a surprising upregulation of $\alpha 1$ -receptors in the aortic segments where we would have anticipated the opposite effect, given the blunted $\alpha 1$ -receptor-mediated contractions. This upregulation however could indicate that a compensatory mechanism is already at place, if the molecular pathway of $\alpha 1$ -R is inhibited by a target upstream or downstream of the receptor.

Finally, we note that our results clearly indicate an early modulation of $\alpha 1$ -adrenergic receptor-mediated contractility in the AngII infusion model. Numerous studies designed to determine whether AngII lesions are dependent or not on blood pressure use norepinephrine or phenylephrine to induce hypertension in absence^{50,51} or presence⁵² of AngII infusion. Given that both norepinephrine and phenylephrine are neurotransmitters which bind to $\alpha 1$ -adrenergic receptors, our present findings suggest that replicating the AngII-mediated hypertensive setting with signal transduction through $\alpha 1$ -adrenoreceptors may be more perplexing than it is elucidating.

5 Limitations and future work

Despite its encouraging results this is only an initial characterization study; there is a need for both more data and further analyses to determine the precise mechanisms that mediate the regional loss of endothelial and contractile function within the suprarenal abdominal aorta. Temporally refining our results can further elucidate whether changes in vascular function may occur even earlier than the 3-day mark.

One of the limitations of our study was the assumption that the preload was the same on the infused and non-infused samples. A different optimal stretch of aortic rings following 3 days of AngII infusion with respect to controls, given that aortic stiffening occurs after 3 days of AngII infusion³⁵, may influence vascular reactivity findings⁵³. Moreover, an inherent limitation of wire myography is the omission of axial stretch^{54,55}, which may alter the in vitro response of smooth muscle. In addition, the in vivo presence of perivascular adipose tissue may alter the aortic contractile function with respect to in vitro observations⁵⁶.

In future work, we plan to use calyculin A, an inhibitor of protein phosphatases PP1 and PP2A, to determine the inhibition of PE-mediated contraction is due to a target upstream or downstream of the $\alpha 1$ -R in the PP1/PP2A pathway.

6 Conclusions

Our results demonstrate that microstructural defects in the ascending and abdominal mouse aorta as well as in vivo increase of the aortic volume become apparent only after 3 days of AngII infusion. A spatially refined assessment of vascular reactivity within the suprarenal abdominal aorta revealed regional differences in vascular function at the early stage of AngII induced dissections. Specifically, we found severe endothelial and contractile dysfunction in the supraceliac segment. Alterations of vascular function elsewhere were either milder, as in the more distal, dissection-protected aortic segments, or did not occur at all, as was the case for the major arterial side branches. The focal transition of endothelial and contractile function properties from dysfunctional (aorta) to functional (branch) may further add to the mechanical burden that branch orifices have recently been shown to endure in this mouse model, to give rise to branch-related dissections. To the best of our knowledge, these results are the first to evaluate the vascular function of the suprarenal abdominal aorta and its side branches at the early phase of AngII-infusion.

Appendix

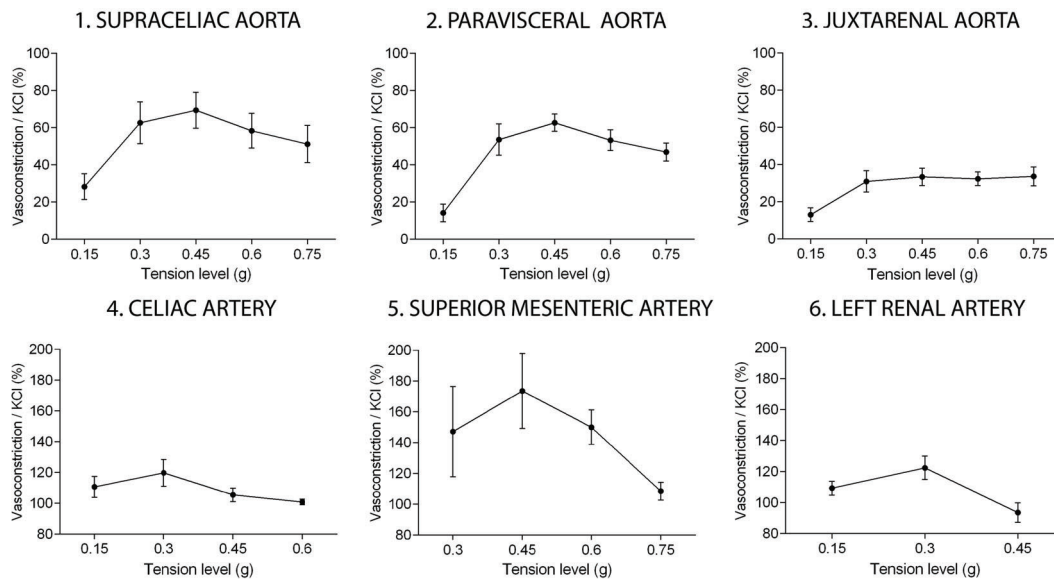


Figure A1: Panels 1-3: Optimal tension of the 3 aortic suprarenal segments, determined by vasoconstriction to PE [10^{-6}] M for incremental tension levels. Panels 4-6: Optimal tension of the 3 aortic branches, determined by vasoconstriction to SER [10^{-6}] M for incremental tension levels. Note the difference in scale for the arterial branches.

Pair	p-values	
	WT	ApoE-/-
Ascending aorta		
Baseline – Day 1	0.0313	ns
Baseline – Day 2	0.0313	ns
Baseline – Day 3	0.0156	0.0156
Abdominal aorta		
Baseline – Day 1	ns	ns
Baseline – Day 2	ns	ns
Baseline – Day 3	0.0313	0.0313

Table A1: Statistical significance for Wilcoxon matched-pairs signed rank tests of ascending aortic volume shown in Figure 4.2.

Table A2: Multiple comparisons between normalized contrast agent volumes in the abdominal aorta of control and day 1, 2, 3 animals (Kruskal-Wallis with Dunn's correction). S: significance, P-value: multiplicity-adjusted P-value for each comparison; ns: no significance; *: $P \leq 0.05$; **: $P \leq 0.01$.

Pair	Aortic region															
	IC		Suprace		Celiac		Paravisc		Mes/rren		Juxtaren		Lren		Postlren	
	S	P-value	S	P-value	S	P-value	S	P-value	S	P-value	S	P-value	S	P-value	S	P-value
AP ctrls vs AP D1	ns	> 0.9999	ns	> 0.9999	ns	> 0.9999	ns	0.8712	ns	> 0.9999	ns	> 0.9999	ns	0.8539	ns	> 0.9999
AP ctrls vs AP D2	*	0.0273	ns	0.4007	ns	> 0.9999	ns	> 0.9999	ns	> 0.9999	ns	> 0.9999	ns	> 0.9999	ns	> 0.9999
AP ctrls vs AP D3	*	0.0149	*	0.0310	*	0.0306	*	0.0445	**	0.0051	*	0.0281	ns	0.1666	ns	0.5780
AP D1 vs AP D2	ns	0.0584	ns	> 0.9999	ns	> 0.9999	ns	0.4387	ns	> 0.9999	ns	> 0.9999	ns	> 0.9999	ns	> 0.9999
AP D1 vs AP D2	*	0.0330	ns	0.5753	ns	0.7106	ns	> 0.9999	ns	0.2841	ns	0.1396	ns	> 0.9999	ns	> 0.9999
AP D2 vs AP D3	ns	> 0.9999	ns	> 0.9999	ns	0.3020	*	0.0187	*	0.0297	*	0.0420	ns	0.2819	ns	> 0.9999

Table A3: Mean and standard error of the mean of contrast agent volume infiltration normalized to axial length ($\mu\text{m}^3/\mu\text{m}$) in segments of the abdominal region.

Group	IC		suprace		celiac		paravisceral		Mes/rren		Juxtaren		Lren		Postlren	
	Mean	SEM	Mean	SEM	Mean	SEM	Mean	SEM	Mean	SEM	Mean	SEM	Mean	SEM	Mean	SEM
	Aortic region															
AP ctrls	0.0	0.0	0.7	0.7	16.1	16.1	26.8	26.8	54.9	54.9	0.0	0.0	0.0	0.0	0.0	0.0
AP day 1	52.6	52.6	40.2	19.5	305.5	155.5	476.0	304.6	419.7	203.6	0.9	0.9	714.0	675.0	430.8	430.8
AP day 2	3525.0	2013.0	1222.0	775.6	146.9	103.3	0.0	0.0	253.5	253.5	0.0	0.0	0.0	0.0	0.0	0.0
AP day 3	5204.0	4155.0	2170.0	722.0	7661.0	3832.0	1792.0	607.4	4649.0	2123.0	176.1	86.4	479.0	305.1	257.7	172.4
WT day 1	0.0	0.0	277.2	172.2	1434.1	1387.1	272.4	272.4	223.5	223.5	0.0	0.0	0.0	0.0	0.0	0.0
WT day 2	126.8	124.5	570.6	400.7	1298.0	810.1	75.5	72.75	88.5	75.0	33.66	33.66	0.0	0.0	0.0	0.0
WT day 3	412.7	343.0	296.1	87.85	2112.0	1653.5	1006.0	804.4	2714.0	2548.3	615.2	536.2	46.71	40.36	0.0	0.0

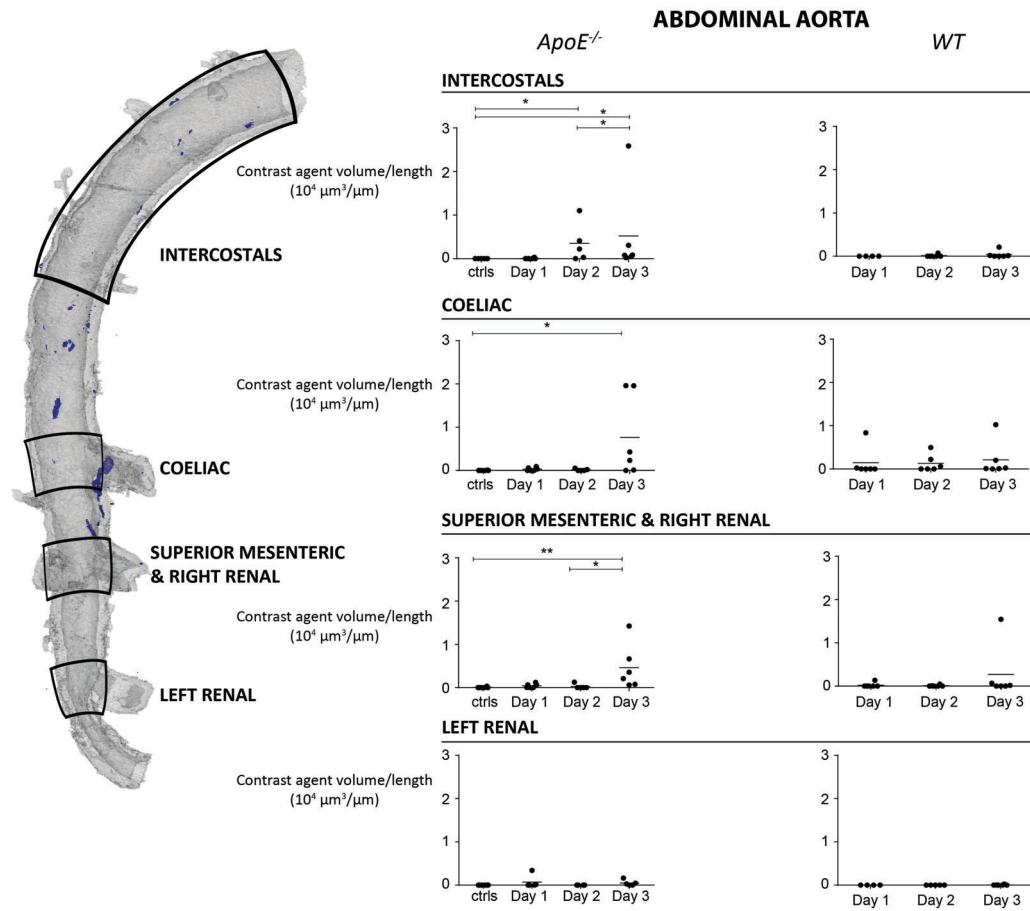


Figure A2: Contrast agent infiltration along the abdominal aorta after AngII infusion for 1, 2 and 3 days for ApoE-deficient and WT mice. Line denotes mean per group. Overbar denotes statistical significance between groups, * : $P \leq 0.05$; ** : $P \leq 0.01$.

Bibliography

- [1] Deaths, percent of total deaths, and death rates for the 15 leading causes of death in 5-year age groups, by race, and sex: United states, 2015, 2015.
- [2] Marvin D. Atkins, James H. Black, and Richard P. Cambria. Aortic dissection: Perspectives in the era of stent-graft repair. *Journal of Vascular Surgery*, 43(2, Supplement):A30–A43, 2006.
- [3] Todd C. Crawford, Robert J. Beaulieu, Bryan A. Ehlert, Elizabeth V. Ratchford, and 3rd Black, James H. Malperfusion syndromes in aortic dissections. *Vascular medicine (London, England)*, 21(3):264–273, 2016. 26858183[pmid] PMC4876056[pmcid] 1358863X15625371[PII] Vasc Med.
- [4] M. Singh, B. A. Ziganshin, and J. A. Elefteriades. *Aortic Aneurysm*, pages 123–142. Elsevier, Oxford, 2018.
- [5] Hong Lu, Debra L. Rateri, Dennis Bruemmer, Lisa A. Cassis, and Alan Daugherty. Involvement of the renin–angiotensin system in abdominal and thoracic aortic aneurysms. *Clinical Science*, 123(9):531–543, 2012.
- [6] Raymundo Alain Quintana and W. Robert Taylor. Cellular mechanisms of aortic aneurysm formation. *Circulation Research*, 124(4):607–618, 2019.
- [7] Fang Luo, Xian-Liang Zhou, Jian-Jun Li, and Ru-Tai Hui. Inflammatory response is associated with aortic dissection. *Ageing Research Reviews*, 8(1):31–35, 2009.
- [8] Alan Daugherty, Michael W. Manning, and Lisa A Cassis. Angiotensin ii promotes atherosclerotic lesions and aneurysms in apolipoprotein e–deficient mice. *The Journal of Clinical Investigation*, 105(11):1605–1612, 2000.
- [9] Alan Daugherty, Debra L. Rateri, Israel F. Charo, A. Phillip Owens, Deborah A. Howatt, and Lisa A. Cassis. Angiotensin ii infusion promotes ascending aortic aneurysms: attenuation by ccr2 deficiency in apoe^{-/-} mice. *Clinical Science*, 118(11):681–689, 2010.
- [10] Debra L. Rateri, Jessica J. Moorleghe, Anju Balakrishnan, A. Phillip Owens, Deborah A. Howatt, Venkateswaran Subramanian, Aruna Poduri, Richard Charnigo, Lisa A. Cassis, and Alan Daugherty. Endothelial cell-specific deficiency of ang ii type 1a receptors attenuates ang ii-induced ascending aortic aneurysms in ldl receptor^{sup>0} mice. *Circulation Research*, 108(5):574–581, 2011.
- [11] Bram Trachet, Alessandra Piersigilli, Rodrigo A. Fraga-Silva, Lydia Aslanidou, Jessica Sordet-Dessimoz, Alberto Astolfo, Marco F.M. Stampanoni, Patrick Segers, and Nikolaos Stergiopoulos. Ascending aortic aneurysm in angiotensin ii-infused mice. formation, progression, and the role of focal dissections. *Arteriosclerosis, Thrombosis, and Vascular Biology*, 36(4):673–681, 2016.

Bibliography

- [12] Kiran Saraff, Fjoralba Babamusta, Lisa A. Cassis, and Alan Daugherty. Aortic dissection precedes formation of aneurysms and atherosclerosis in angiotensin ii-infused, apolipoprotein e-deficient mice. *Arteriosclerosis, Thrombosis, and Vascular Biology*, 23(9):1621–1626, 2003.
- [13] Bram Trachet, Lydia Aslanidou, Alessandra Piersigilli, Rodrigo A. Fraga-Silva, Jessica Sordet-Dessimoz, Pablo Villanueva-Perez, Marco F.M. Stampanoni, Nikolaos Stergiopoulos, and Patrick Segers. Angiotensin II infusion into ApoE^{-/-} mice: a model for aortic dissection rather than abdominal aortic aneurysm? *Cardiovascular Research*, 113(10):1230–1242, 06 2017.
- [14] E. H. Phillips, P. Di Achille, M. R. Bersi, J. D. Humphrey, and C. J. Goergen. Multi-modality imaging enables detailed hemodynamic simulations in dissecting aneurysms in mice. *IEEE Transactions on Medical Imaging*, 36(6):1297–1305, 2017.
- [15] Albert N. Swafford, Lisa M. Harrison-Bernard, and Gregory M. Dick. Knockout mice reveal that the angiotensin ii type 1b receptor links to smooth muscle contraction*. *American Journal of Hypertension*, 20(3):335–337, 2007.
- [16] Yingbi Zhou, Yanfang Chen, Wessel P. Dirksen, Mariana Morris, and Muthu Periasamy. At1b receptor predominantly mediates contractions in major mouse blood vessels. *Circulation Research*, 93(11):1089–1094, 2003.
- [17] Yingbi Zhou, Wessel P. Dirksen, Gopal J. Babu, and Muthu Periasamy. Differential vasoconstrictions induced by angiotensin ii: role of at1 and at2 receptors in isolated c57bl/6j mouse blood vessels. *American Journal of Physiology-Heart and Circulatory Physiology*, 285(6):H2797–H2803, 2003.
- [18] Stefano Masi, Monica Uliana, and Agostino Virdis. Angiotensin ii and vascular damage in hypertension: Role of oxidative stress and sympathetic activation. *Vascular Pharmacology*, 115:13–17, 2019.
- [19] Steven J. Forrester, George W. Booz, Curt D. Sigmund, Thomas M. Coffman, Tatsuo Kawai, Victor Rizzo, Rosario Scalia, and Satoru Eguchi. Angiotensin ii signal transduction: An update on mechanisms of physiology and pathophysiology. *Physiological Reviews*, 98(3):1627–1738, 2018.
- [20] Xiaoxi Ju, Ronald G. Tilton, and Allan R. Brasier. *Multifaceted Role of Angiotensin II in Vascular Inflammation and Aortic Aneurysmal Disease*. 2011.
- [21] M. R. Bersi, R. Khosravi, A. J. Wujciak, D. G. Harrison, and J. D. Humphrey. Differential cell-matrix mechanoadaptations and inflammation drive regional propensities to aortic fibrosis, aneurysm or dissection in hypertension. *Journal of The Royal Society Interface*, 14(136):20170327, 2017.
- [22] Jacopo Ferruzzi, Sae-Il Murtada, Guangxin Li, Yang Jiao, Selen Uman, Magdalene Y.L. Ting, George Tellides, and Jay D. Humphrey. Pharmacologically improved contractility protects

- against aortic dissection in mice with disrupted transforming growth factor- β signaling despite compromised extracellular matrix properties. *Arteriosclerosis, Thrombosis, and Vascular Biology*, 36(5):919–927, 2016.
- [23] Arina Korneva and Jay D. Humphrey. Maladaptive aortic remodeling in hypertension associates with dysfunctional smooth muscle contractility. *American Journal of Physiology-Heart and Circulatory Physiology*, 316(2):H265–H278, 2019. PMID: 30412437.
- [24] Paul Fransen, Cor E. Van Hove, Arthur J. A. Leloup, Dorien M. Schrijvers, Guido R. Y. De Meyer, and Gilles W. De Keulenaer. Effect of angiotensin ii-induced arterial hypertension on the voltage-dependent contractions of mouse arteries. *Pflügers Archiv - European Journal of Physiology*, 468(2):257–267, 2016.
- [25] Arthur J. A. Leloup, Sofie De Moudt, Cor E. Van Hove, Lindsey Dugaucquier, Zarha Vermeulen, Vincent F. M. Segers, Gilles W. De Keulenaer, and Paul Fransen. Short-term angiotensin ii treatment affects large artery biomechanics and function in the absence of small artery alterations in mice. *Frontiers in Physiology*, 9:582, 2018.
- [26] Aruna Poduri, III Owens, A. Phillip, Deborah A. Howatt, Jessica J. Moorlegghen, Anju Balakrishnan, Lisa A. Cassis, and Alan Daugherty. Regional variation in aortic at1b receptor mrna abundance is associated with contractility but unrelated to atherosclerosis and aortic aneurysms. *PLOS ONE*, 7(10):e48462, 2012.
- [27] M. J. Collins, M. Bersi, E. Wilson, and J. D. Humphrey. Mechanical properties of suprarenal and infrarenal abdominal aorta: implications for mouse models of aneurysms. *Medical engineering & physics*, 33(10):1262–1269, 2011. 21742539[pmid] PMC3235688[pmcid] S1350-4533(11)00131-7[PII].
- [28] Amber Russell and Stephanie Watts. Vascular reactivity of isolated thoracic aorta of the c57bl/6j mouse. *Journal of Pharmacology and Experimental Therapeutics*, 294(2):598–604, 2000.
- [29] Debra L. Rateri, Frank M. Davis, Anju Balakrishnan, Deborah A. Howatt, Jessica J. Moorlegghen, William N. O'Connor, Richard Charnigo, Lisa A. Cassis, and Alan Daugherty. Angiotensin ii induces region-specific medial disruption during evolution of ascending aortic aneurysms. *The American Journal of Pathology*, 184(9):2586–2595, 2014.
- [30] Evan H. Phillips, Adam H. Lorch, Abigail C. Durkes, and Craig J. Goergen. Early pathological characterization of murine dissecting abdominal aortic aneurysms. *APL Bioengineering*, 2(4):046106, 2018.
- [31] Chiara Barisione, Richard Charnigo, Deborah A. Howatt, Jessica J. Moorlegghen, Debra L. Rateri, and Alan Daugherty. Rapid dilation of the abdominal aorta during infusion of angiotensin ii detected by noninvasive high-frequency ultrasonography. *Journal of Vascular Surgery*, 44(2):372–376, 2006.

Bibliography

- [32] Christopher M. Haggerty, Andrea C. Mattingly, Ming C. Gong, Wen Su, Alan Daugherty, and Brandon K. Fornwalt. Telemetric blood pressure assessment in angiotensin ii-infused apoe^{-/-} mice: 28 day natural history and comparison to tail-cuff measurements. *PLOS ONE*, 10(6):e0130723, 2015.
- [33] Sai Wang Seto, Smriti M. Krishna, Hongyou Yu, David Liu, Surabhi Khosla, and Jonathan Golledge. Impaired acetylcholine-induced endothelium-dependent aortic relaxation by caveolin-1 in angiotensin ii-infused apolipoprotein-e (apoe^{-/-}) knockout mice. *PLOS ONE*, 8(3):e58481, 2013.
- [34] Jessica R. Gomolak and Sean P. Didion. Angiotensin ii-induced endothelial dysfunction is temporally linked with increases in interleukin-6 and vascular macrophage accumulation. *Frontiers in Physiology*, 5(396), 2014.
- [35] John T. Favreau, Binh T. Nguyen, Ian Gao, Peng Yu, Ming Tao, Jacob Schneiderman, Glenn R. Gaudette, and C. Keith Ozaki. Murine ultrasound imaging for circumferential strain analyses in the angiotensin ii abdominal aortic aneurysm model. *Journal of Vascular Surgery*, 56(2):462–469, 2012.
- [36] Hong-Tai Li, Carlin S. Long, Mary O. Gray, D. Gregg Rokosh, Norman Y. Honbo, and Joel S. Karliner. Cross talk between angiotensin at1 and α 1-adrenergic receptors. *Circulation Research*, 81(3):396–403, 1997.
- [37] Susana Jerez and A Peral de Bruno, M Coviello. Cross talk between angiotensin ii and alpha 1 adrenergic receptors in rabbit aorta: role of endothelium. *Journal of Cardiovascular Pharmacology*, 43(3):402–9, 2004.
- [38] Susana Jerez, Liliana Sierra, Fabricio Scacchi, and María Peral de Bruno. Hypercholesterolemia modifies angiotensin ii desensitisation and cross talk between α 1-adrenoceptor and angiotensin at1 receptor in rabbit aorta. *European Journal of Pharmacology*, 635(1):149–155, 2010.
- [39] Phillip G. Kopf, Laura E. Phelps, Chad D. Schupbach, Alan K. Johnson, and Jacob D. Peuler. Differential effects of long-term slow-pressor and subpressor angiotensin ii on contractile and relaxant reactivity of resistance versus conductance arteries. *Physiological reports*, 6(5):e13623, 2018. 29504268[pmid] PMC5835495[pmcid] Physiol Rep.
- [40] Zhichao Zhou, Vishal R. Yadav, Changyan Sun, Bunyen Teng, and Jamal S. Mustafa. Impaired aortic contractility to uridine adenosine tetraphosphate in angiotensin ii-induced hypertensive mice: Receptor desensitization? *American journal of hypertension*, 30(3):304–312, 2017. 28034895[pmid] PMC5861566[pmcid] hpw163[PII] Am J Hypertens.
- [41] S. S. M. Rensen, P. A. F. M. Doevendans, and G. J. J. M. van Eys. Regulation and characteristics of vascular smooth muscle cell phenotypic diversity. *Netherlands heart journal : monthly journal of the Netherlands Society of Cardiology and the Netherlands Heart Foundation*, 15(3):100–108, 2007. 17612668[pmid] PMC1847757[pmcid].

- [42] Gorav Ailawadi, Christopher W. Moehle, Hong Pei, Sandra P. Walton, Zequan Yang, Irving L. Kron, Christine L. Lau, and Gary K. Owens. Smooth muscle phenotypic modulation is an early event in aortic aneurysms. *The Journal of Thoracic and Cardiovascular Surgery*, 138(6):1392–1399, 2009.
- [43] Zhao An, Yang Liu, Zhi-Gang Song, Hao Tang, Yang Yuan, and Zhi-Yun Xu. Mechanisms of aortic dissection smooth muscle cell phenotype switch. *The Journal of Thoracic and Cardiovascular Surgery*, 154(5):1511–1521.e6, 2017.
- [44] Paul H. Ratz, Krystina M. Berg, Nicole H. Urban, and Amy S. Miner. Regulation of smooth muscle calcium sensitivity: Kcl as a calcium-sensitizing stimulus. *American Journal of Physiology-Cell Physiology*, 288(4):C769–C783, 2005.
- [45] Anand M. Prasad, Donald A. Morgan, Daniel W. Nuno, Pimonrat Ketsawatsomkron, Thomas B. Bair, Ashlee N. Venema, Megan E. Dibbern, William J. Kutschke, Robert M. Weiss, Kathryn G. Lamping, Mark W. Chapleau, Curt D. Sigmund, Kamal Rahmouni, and Isabella M. Grumbach. Calcium/calmodulin-dependent kinase ii inhibition in smooth muscle reduces angiotensin ii-induced hypertension by controlling aortic remodeling and baroreceptor function. *Journal of the American Heart Association*, 4(6):e001949, 2015.
- [46] I. A. Gallardo-Ortíz, S. N. Rodríguez-Hernández, J. J. López-Guerrero, L. Del Valle-Mondragón, P. López-Sánchez, R. M. Touyz, and R. Villalobos-Molina. Role of $\alpha 1$ -adrenoceptors in vascular wall hypertrophy during angiotensin ii-induced hypertension. *Autonomic and Autacoid Pharmacology*, 35(3):17–31, 2015.
- [47] W Bao, D Behm, S Nerurkar, A Zhaohui, and Bs Bentley. Effects of p38 mapk inhibitor on angiotensin ii-dependent hypertension, organ damage, and superoxide anion production. *Journal of Cardiovascular Pharmacology*, 49(6), 2007.
- [48] Lisa A. Cassis, Jing Huang, Ming C. Gong, and Alan Daugherty. Role of metabolism and receptor responsiveness in the attenuated responses to angiotensin ii in mice compared to rats. *Regulatory Peptides*, 117(2):107–116, 2004.
- [49] E. H. Phillips, M. S. Chang, S. Gorman, H. J. Qureshi, K. F. K. Ejendal, T. L. Kinzer-Ursem, A. N. Blaize, and C. J. Goergen. Angiotensin ii infusion does not cause abdominal aortic aneurysms in apolipoprotein e-deficient rats. *Journal of Vascular Research*, 55(1):1–12, 2018.
- [50] Nobuhiko Ayabe, Vladimir R. Babaev, YiWei Tang, Takakuni Tanizawa, Agnes B. Fogo, MacRae F. Linton, Iekuni Ichikawa, Sergio Fazio, and Valentina Kon. Transiently heightened angiotensin ii has distinct effects on atherosclerosis and aneurysm formation in hyperlipidemic mice. *Atherosclerosis*, 184(2):312 – 321, 2006.
- [51] Lisa A. Cassis, Manisha Gupte, Sarah Thayer, Xuan Zhang, Richard Charnigo, Deborah A. Howatt, Debra L. Rateri, and Alan Daugherty. Ang ii infusion promotes abdominal aortic aneurysms independent of increased blood pressure in hypercholesterolemic

Bibliography

- mice. *American Journal of Physiology-Heart and Circulatory Physiology*, 296(5):H1660–H1665, 2009.
- [52] Manesh Thomas, Dan Gavrilu, Michael L. McCormick, Jr. Miller, Francis J., Alan Daugherty, Lisa A. Cassis, Kevin C. Dellsperger, and Neal L. Weintraub. Deletion of p47phox attenuates angiotensin ii-induced abdominal aortic aneurysm formation in apolipoprotein e-deficient mice. *Circulation*, 114(5):404–413, 2006. 16864727[pmid] PMC3974117[pmcid] *Circulation*.
- [53] Sofie De Moudt, Arthur Leloup, Cor Van Hove, Guido De Meyer, and Paul Fransen. Iso-metric stretch alters vascular reactivity of mouse aortic segments. *Frontiers in Physiology*, 8(157), 2017.
- [54] Alexander W. Caulk, Jay D. Humphrey, and Sae-Il Murtada. Fundamental roles of axial stretch in isometric and isobaric evaluations of vascular contractility. *Journal of Biomechanical Engineering*, 141(3):031008–031008–10, 2019. 10.1115/1.4042171.
- [55] Il Murtada, Sae, Jay D. Humphrey, and Gerhard A. Holzapfel. Multiscale and multiaxial mechanics of vascular smooth muscle. *Biophysical Journal*, 113(3):714–727, 2017.
- [56] Luis Villacorta and Lin Chang. The role of perivascular adipose tissue in vasoconstriction, arterial stiffness, and aneurysm. *Hormone molecular biology and clinical investigation*, 21(2):137–147, 2015. 25719334[pmid] PMC4431551[pmcid] *Horm Mol Biol Clin Investig*.

Conclusions

1 Modelling the arterial circulation of the mouse

In cardiovascular research, mouse models have become a standard surrogate to emulate the human pathology and investigate etiologic mechanisms where human data are not readily available. Notwithstanding their frequent use, a thorough description of the reference murine arterial anatomy and hemodynamics therein has been lacking. Thanks to recent improvements in computer technology, modelling based on physical principles has become a powerful tool to simulate the hemodynamic properties of the human cardiovascular system and has been playing an increasingly important role in the diagnosis of cardiovascular diseases and the development of medical devices. Low dimensional physics-based models of the vascular network can describe the entire arterial tree at small computational costs, readily reproduce wave propagation phenomena and enable patient-specific modelling. In the first study of this dissertation (Chapter 1), we adjusted a one-dimensional model of the arterial network from humans to mice. We averaged the micro-CT-acquired aortic geometry of two commonly used mouse strains to obtain reference data of the mouse systemic arterial tree. We informed the model with available literature data and validated the predicted blood flow and pressure waveforms against in vivo ultrasound measurements of diameter and blood flow velocity as well as invasive pressure measurements. The result was a numerical model of the murine systemic circulation, representative of a healthy anesthetized mouse.

At first glance, translating an existing 1D model of the human systemic arterial tree into a murine setting can seem counterintuitive. When the natural workflow of biomedical research starts with animal experiments to ultimately reach a clinical application, what is the added value of following the reverse path to scale human data down to mice? While the main research interest lies with human physiology and disease, elucidating the anatomical and hemodynamic parameters of the most commonly used laboratory animal is instrumental. The cardiovascular system of mice is more than merely a downscaled, faster version of the human circulation; not all hemodynamic parameters downscale uniformly across the two species. While murine arterial dimensions are 10-times smaller and heart rate is 10-times faster, the

blood viscosity, blood flow velocity and pulse wave velocity have similar values in mice and humans. Both the Reynolds number, reflective of the turbulence of blood flow, and the Womersley number, reflective of the pulsatility of blood flow, are lower in mice denoting that murine flow is more laminar and organized than human flow. Whereas wave propagation was expected to be similar between the two species, as we moved from the heart to the periphery in the mouse model the pulse pressure did not amplify as in humans but was instead dampened. Setting the viscosity of blood equal to zero restored the effect of pulse pressure amplification, thus indicating that in the mouse high frictional losses override pulse pressure amplification.

The principle of the Three R's, to Replace, Reduce and Refine the use of animals in scientific research, is firmly anchored in recent legislative acts. This versatile generic 1D model of the mouse circulation can serve as an alternative for in vivo proof-of-concept studies. Altered experimental conditions, such as ligation of an artery, amputation, arterial stenosis or increased aortic stiffness can easily be simulated without sacrificing animals. This can lead to the reduction and ultimate replacement of animals during experimental design and harm-benefit analysis. It is important, however, to keep in mind that this in silico 1D model is fit for use depending on the research question it is meant to answer. It cannot and should not be used to substitute experiments which aim to describe the pathogenesis of cardiovascular pathologies arising from complex biological processes, such as aortic aneurysms and dissections.

2 Disease pathogenesis in a mouse model of aortic aneurysm and dissection

Understanding the triggering determinants of aortic pathologies such as dissections and aneurysms in which longitudinal human data are scarce, especially in early stages of disease, is a task next to impossible. Aortic aneurysms can progress over decades before rupture and acute aortic dissections can occur within hours - in both cases, human data temporally set at the onset of disease are difficult to obtain. Research using mice allows us to investigate questions impossible to address in human studies. In mouse models the temporal evolution of disease is well-defined, a large number of experimental parameters such as age or genetic background can be varied at will and the pre-diseased, longitudinal follow-up and postmortem data are readily available.

The most common mouse model used in aneurysm research for the last 20 years is that of systemic infusion of Angiotensin-II in mice. Following infusion, the animals present two clearly distinct and location-specific aortic pathologies: ascending aneurysms and abdominal dissections. Even though the model (like any other available model to date) is not a complete set of replica for either aneurysm or dissection, it can nonetheless provide useful insight in the underlying mechanisms driving the disease. In order to study the early stage of disease, one ideally wants to follow-up the same animal from baseline to sacrifice; such in vivo longitudinal monitoring is nowadays possible with contrast-enhanced micro-CT (to image the contrast-filled aortic anatomy) and ultrasound (to measure blood flow velocity, among others). Imaging

2. Disease pathogenesis in a mouse model of aortic aneurysm and dissection

the compromised structure of the mouse aortic wall is the most important aspect of study design, since it ultimately dictates the level of insight deduced from the study. Synchrotron-based imaging of aortas postmortem at the Swiss Light Source yields high-resolution 3D information on the mouse aortic wall. An added layer of insight stems from a fortuitous discovery during the first implementation of synchrotron-based imaging from our group: the micro-CT contrast agent injected in mice (originally meant to enhance the soft tissue contrast during the micro-CT scan) infiltrates the aortic wall *intra vitam* at spots of vascular damage, and is visible *ex vivo* on the synchrotron images. The micro-CT contrast agent can hence, apart from enabling the *in vivo* distinction of the aorta during a micro-CT scan, additionally serve as a proxy to localize early vascular damage of the vascular wall *ex vivo*. With a unique set of imaging tools at hand, we set out to tackle the main questions surrounding the Angiotensin-II mouse model of aortic aneurysm and dissection.

The most intriguing open question in this mouse model is:

Why do abdominal aortic dissections consistently occur in the suprarenal abdominal aorta rather than the infrarenal location that is observed in humans?

Prior to any targeted study to address this issue, one has to properly formulate the research question at hand and understand its context. Since the majority of previously published studies on this mouse model concentrated around abdominal dissections of the most advanced stage (often treatment studies meant to prevent or aggravate the pathological outcome), the first requisite step was to characterize the early-stage morphology of abdominal dissections in the mouse model. In chapter 2 using synchrotron imaging combined with the proxy of contrast agent at the inceptive stage of disease (prior to overt morphological changes of the vascular wall) we detected damage around the ostia of two major side branches: the **celiac and superior mesenteric** arteries. These findings are consistent with the location of medial tears in fully developed (late-stage) dissections. While a role for the major side branches in disease pathogenesis had been hypothesized in the past, we obtained for the first time early-phase data to support their direct involvement in disease formation.

In addition, early damage was found around the orifice of small suprarenal side branches of the abdominal aorta. This observation was also reflected in fully-fledged dissections that affected minor suprarenal branches in previous synchrotron-based studies from our group, highlighting a crucial role not only for major but also for **minor suprarenal side branches** at the disease onset. A serendipitously imaged *in-vivo* rupture during micro-CT follow-up further revealed that dissections in this model occur and propagate within only a few hours.

Following this early morphological characterization of abdominal dissections, we could reformulate the main research question posed above to:

What is the role of aortic side branches in disease initiation?

The scope of the subsequent studies of this dissertation was to address this question using a two-pronged approach, divided in a *biomechanical* and a *mechanobiological* arm. Motivated by the site-specificity of abdominal dissections, we hypothesized that local biomechanical forces acting in the vicinity of the coeliac and superior mesenteric arteries trigger the onset of dissection. Given the complex feedback loops between local mechanics and mechanobiology, effects of or potential changes in smooth muscle contractility could play a key role at the onset of disease. We therefore used the same mouse model to investigate whether the most dissection-prone regions within the suprarenal aorta spatially associate with a locally compromised vasoconstrictive capacity.

2.1 The initiation of aortic dissection: a biomechanical perspective

Given the focal damage around the orifices of side branches, in Chapter 3 we conjectured that local mechanical stimuli might trigger disease onset: it is, after all, intuitive that side branches stemming out of a tubular structure (in this case, the aorta) are a source of mechanical stress and strain concentration. The added value of our unique setting of synchrotron-based biomechanics is twofold: (i) mouse-specific geometries can be used to set up computational structural mechanics of the abdominal aortic wall, and (ii) mouse-specific validation can indicate whether locations of strain concentration coincide with early microstructural wall damage. The work of this study built on a strong foundation set up in our group via the development of a novel finite-element computational framework of synchrotron-based biomechanics, where the mechanical strains are computed by comparing unloaded (*ex vivo*) and temporally-averaged loaded (*in vivo*) configurations of the abdominal aortic wall.

Synchrotron image-guided histology showed that instances of micro-CT contrast agent intramural infiltration corresponded to precursor vascular damage of the aortic wall and occurred mainly at orifices of the celiac and superior mesenteric branches. The computed mechanical strain was higher in branching relative to non-branching regions of the aorta, with a predilection for high strain in the celiac, superior mesenteric and right renal branching sites. This resulted in a positive correlation between high mechanical strain and high vascular damage in the branching, but non in the non-branching, regions. These findings suggested a mechanically-driven initiating mechanism for the disease, with suprarenal branches acting as *loci minoris resistentiae* along the aorta. Further supporting evidence came from complementary synchrotron imaging of load-induced *ex vivo* delaminations in suprarenal aortas: the major delamination plane occurred near side branches and around the coeliac artery in particular. This study thus points towards an early mechanically mediated formation of microstructural defects at branching sites of the suprarenal aorta, which subsequently propagate into a macroscopic medial tear, eventually giving rise to abdominal aortic dissection.

2.2 The initiation of aortic dissection: a mechanobiological perspective

In order to complement the biomechanical approach of Chapter 3, in Chapter 4 we investigated why dissections arise in the region around celiac and mesenteric branches from a mechanobiological standpoint by assessing the local vascular function. As a first step, we identified, over the first 3 days of AngII infusion, the most appropriate time mark to characterize the suprarenal aorta's vasoreactivity. After quantifying in vivo dilatation and ex vivo vascular damage in both the ascending and the abdominal aorta, we found significant changes to have occurred only after 3 days of AngII infusion, which coincided with the duration of infusion in the previous study of Chapter 3 but preceded overt morphological changes of the aortic wall and any major aortic remodelling. The 3 aortic segments whose vascular function we characterized were physically demarcated by the major branches of the suprarenal aorta (namely the celiac, superior mesenteric and renal arteries). We additionally assessed the vasoreactivity of the side branches themselves (celiac, superior mesenteric and left renal artery). While the contractile capacity of the side branches was largely preserved, in the suprarenal aorta there was a tapering trend of endothelial and contractile dysfunction: starting from the most proximal supraceliac segment, the impairment became less severe towards the distal end.

2.3 A unified approach to explain a branch-related disease onset

The spatially varying response of compromised vascular function (impaired in the supraceliac segment, compromised in the paravisceral and preserved in the juxtarenal segment) fits well with the profile of dissection propensity along the suprarenal aorta, with the supraceliac segment considered the most dissection-prone¹. Bearing in mind the preserved vascular function of the arterial side branches, around the orifice of a side branch seems to arise a regional discontinuity in the profile of smooth muscle cell contractility and endothelial function (affected in the aorta, but healthy in the side branch). This further adds to the burden that the orifice of a branch has to sustain, as shown by our biomechanical data: in Chapter 3, we found that strain concentrations in the aorta occur mainly around the ostia of the celiac, superior mesenteric and right renal branching sites. It is thus at the focally, both biomechanically and functionally compromised area of the aortic wall around the orifice of these major branches that the initial parietal damage occurs.

Coming back to our research question, we showed that the initiation of dissections in this mouse model is branch-related (Chapter 2), and the combined findings of the biomechanical and mechanobiological studies of Chapters 3 and 4 have elucidated the role of major abdominal side branches in disease initiation. Summing up, it appears that the location specificity of dissecting AAAs around the celiac and superior mesenteric side branches arises from a conglomeration of factors that include focal concentrations of mechanical strain as well as local discontinuities in the function of endothelium and smooth muscle cell contractility.

Our results are consistent with the recent hypothesis proposed by Bersi et al.², which has been described in section 5.2 of the Introduction. At the earliest time point of their study at

4 days of infusion, they reported a local increase in stiffness in the suprarenal aorta (which was considered homogeneous). In their proposed mechanism, Bersi et al. submitted that elevated blood pressure increases the wall stress, and conversely increased contractility may act protectively to decrease the wall stress, in a dynamic but delicate balance. However, they noted that regional differences exist in the aortic response to these stimuli. Our findings show that the contractile capacity within the suprarenal aorta is compromised in a spatially varying way, and does not act protectively to stress-shield the wall. Further, we found that an important determinant of wall stress (or strain) distribution is the branching topology of the aorta. The regions of elevated mechanical strain, from where subsequent signalling through chemokine and MMP expression initiates the inflammatory recruitment, are therefore preferentially found around the orifices of aortic side branches.

Going hand in hand with the decaying profile of early endothelial and smooth muscle cell contractility dysfunction along the suprarenal aorta, from severe in the supraceliac to normal between the renal arteries, is the early aortic stiffening profile of the aorta. At the same time point of AngII infusion (3 days), the supraceliac segment has been the one found to stiffen significantly¹, followed by a milder trend distally. Recalling the mechanism of segmental aortic stiffening proposed in the elastase-induced mouse model of AAA³ described in section 5.2 of the Introduction, rapid local stiffening of a segment surrounded by adjacent compliant segments may lead to nonuniform wall deformations during systole and hence generate increased axial wall stress. The early stiffening of the supraceliac segment by ~ 40-50% may similarly create areas of increased axial wall stress at the boundaries of the segment where stiffness gradients occur. The boundaries of this stiffened segment are, however, hard to place *in vivo*. We can assume that in the distal direction, a physical boundary is imposed by the celiac artery. Stiffening at two more the distal points of the suprarenal aorta may be less pronounced but still occurs¹, implying that the stiffness gradients distally should be less abrupt than in the proximal aorta (thoracic aorta vs stiffened suprarenal segment). An *in vivo* aortic 3D strain mapping⁴ at this time point could elucidate the early regional variation in stiffening.

We note here that our findings do not preclude other synergistic mechanisms. For example, local perivascular support⁵, the loss of dorsal tethering to the spine at the level of the suprarenal aorta, the local natural vessel curvature and the anterior direction of wall expansion⁶ may also play key roles in the localization of AngII induced abdominal lesions.

3 Limitations and future perspectives

The caveats of this dissertation's studies have been presented in detail in their respective chapters. Here we will recapitulate the main limitations which could affect the essential conclusions of each study, and propose future research directions.

3.1 1D modelling of the arterial tree

Naturally, modelling the circulation as a 1D arterial tree entails some inherent limitations. First of all, the model does not take coronary, venous and pulmonary circulation into account. A number of modelling assumptions give rise to further limitations; we reiterate the main ones here. Arteries are described as straight tapering segments with a circular cross-section; the sigmoidal curve of the ascending aorta, aortic arch and descending aorta (as well as the coronary tree, if included in the future) makes these arterial segments far from straight *in vivo*. The flow is considered axisymmetric, however skewed velocity profiles are expected *in vivo* in areas of curvature. The arterial wall is considered thin, incompressible, distensible, with material properties that are homogeneous and isotropic over each short segment. Experimental research has shown that for most practical purposes, the arterial wall can be considered incompressible; however, the heterogeneity and anisotropy of material properties of the murine aortic wall *in vivo* have been well documented.

The 1D model of the murine arterial circulation is representative of a healthy mouse in an anesthetized state. Anesthesia relaxes vascular tone and baroreflex sensitivity, slows down heart rate, reduces cardiac output and pulse pressure, induces peripheral vasodilation and results in systemic hypotension. The next research step is hence to adapt the model to represent a mouse in the conscious state. The model can also be used to derive central aortic pressures from tail-cuff measurements of blood pressure in mice through a transfer function. Decreased distensibility values have been reported along the aorta following AngII infusion²; their implementation in the model will allow us to study alterations in flow and pressure wave propagation arising from this vessel property change.

3.2 Mouse models: what is their translational value?

A primary concern not limited only to the mouse model used in this dissertation but expanding to most animal models used in preclinical research is their translational value. How accurately these models mimic human pathophysiology is difficult to ascertain given our lack of detailed knowledge of the human disease (which leads to animal experimentation in the first place). The mouse model of Angiotensin-II infusion presents demonstrable differences from the human pathology. The exogenous administration of Angiotensin-II elevates the circulating Angiotensin II levels well beyond their physiological range, creating a non-physiological setting not directly translatable to humans. Moreover, Angiotensin-II receptors and signaling as well as numerous other molecular pathways differ between humans and mice. Any extrapolation from the mouse to the human setting should hence be made with great caution. Despite marked differences between the two species, mice offer the unique advantage of hypothesis-driven research. When seeking to address a specific measurable question, mouse models allow us to obtain the necessary and appropriate data to answer it. Investigating the specific role of side branches (Chapter 3) or contractility (Chapter 4) in disease initiation would not have been possible in a human setting. Imaging, particularly at the early stage, of aneurysm

or dissection in humans is incidental and resulting datasets are scattered and insufficient; hence investigations of specific hypotheses are hampered. Preclinical research will continue to elucidate the genetic, biomechanical and mechanobiological aspects of aortopathies and other cardiovascular diseases, revealing their driving pathogenetic mechanisms as well as potential therapeutic targets.

3.3 Blood pressure measurements

Infusion with Angiotensin II has been traditionally used as an animal model of hypertension; higher doses were only incidentally found to cause aneurysmal and dissecting dilatations in the ascending and abdominal mouse aorta. In a tentative mechanism proposed by Bersi et al.², blood pressure elevation is a key mediator in aortic lesion formation: the hypertensive loading increases the wall stress, and it in turn initiates the inflammatory response through chemokine and MMP expression. However, their conjecture is seemingly at odds with previous reports; the question of whether increased SBP plays a significant role in lesion formation has long engendered controversy. Since similar Ang II doses in normocholesterolemic and hypercholesterolemic mice lead to much higher incidence rates of dissecting AAAs in the latter, researchers were led to believe that blood pressure elevation alone is not sufficient to cause lesion development. In an effort to decouple the contribution of blood pressure elevation to lesion pathogenesis in the Ang II infusion model, several studies have administered vasoconstrictive drugs (other than Ang II) in doses adjusted to cause blood pressure increases equivalent to Ang II-mediated hypertension, and subsequently assess the development of dissecting aortic aneurysms. The absence of lesions following infusion of norepinephrine in ApoE-deficient mice^{7,8}, or co-infusion of Ang II and phenylephrine in a genetically modified strain protected from pressor response to Ang II alone⁹ has led several groups to the assumption that dissecting abdominal aneurysm development is not contingent on blood pressure elevation and its associated mechanical effects, but rather on the humoral effects of Angiotensin II. Our findings in Chapter 3 suggest there is a strong biomechanical determinant in lesion formation - but is not the only factor at play. Although trying to isolate effects of elevated blood pressure (and pressure-induced increase in stress) or AngII-induced injurious effects (e.g. proteolytic damage reducing strength) to the aortic wall can contribute to our understanding of the initiating steps, both are clearly operative *in vivo* and likely synergistic.

With such debate surrounding the effect of blood pressure rise on lesion development, undoubtedly one of the limitations of our studies was the lack of blood pressure monitoring in the initial phase of AngII administration. However, this was a conscious choice in our study design. Our extensive protocols of contrast enhanced micro-CT and ultrasound follow-up required significant amounts of anesthesia that put a heavy burden on the animals. In addition, our studies focused on short time periods (1-3 days), and a large number of *in vivo* measurements would not only be ethically difficult but would also compromise the reliability of our results. Particularly for blood pressure, which is stress-dependent and influenced by the precise thermoregulatory state of the animal, since mice are known to vasoconstrict their

tail under hypothermia (which is likely to occur after excessive anesthesia). The hypertensive response to AngII infusion has, moreover, been extensively characterized by others: blood pressure measurements using predominantly tail cuff on anesthetized and conscious mice, but also using telemetry over 28 days of infusion, are reported in literature¹⁰. Since abundant pressure measurements were available, taken under more reliable circumstances (long-term studies focusing exclusively on blood pressure monitoring without measuring other *in vivo* quantities), we decided to rely on those values to evaluate the hypertensive state of the animals over the first 3 days of AngII infusion.

3.4 Computational structural mechanics

An important limitation of the computational framework used in Chapter 3 concerns the difficulty of modelling small side branches or a collapsed aortic geometry. The resulting poor mesh element quality meant we were unable to model four out of six control geometries from saline-infused animals. The limited number of control animals prevented us from drawing a more solid and statistically relevant conclusion. If the presence of strain concentrations had been demonstrated to occur in the same locations in healthy and diseased animals, it would have potentiated the possible causative link between high strain and initial microstructural damage. The implementation of the framework to include small side branches in different aortic geometries showed that their presence can alter the localization of predicted strain hotspots, however their inclusion required extensive manual intervention by the operator. Hence depending on the application, the benefit from including the minor side branches in accurate spatial predictions of strain may or may not outweigh the effort required to implement them in the model - in all cases, it is important to be aware that they play an important role in the computed strain field. More flexibility in meshing of branching topologies can be achieved by modifying the Treemesh method, used to generate the unstructured hexahedral meshes. Allowing the user to manually orient the hexahedral blocks placed at the branching points can facilitate the inclusion of minor branches in the final mesh in the future.

A crucial limitation of our computational work is the assumed material model: the Arruda-Boyce hyperelastic constitutive model is a simplified model assuming homogeneity of the arterial wall. It is well known that the arterial wall is heterogeneous - especially near side branches, which represent regions of particular interest in our study, altered collagen fiber orientations may lead to local material heterogeneities which in turn impact intramural stress. Our results, especially at branching points, should therefore be interpreted with caution. Ideally, a mouse-specific heterogeneous constitutive model should be used. The incorporation of local fiber orientation in the area of bifurcations is of particular importance if the role of side branches is to be evaluated further.

The unloaded configuration we consider still has residual stresses not accounted for: the circumferential prestretch has not been calculated. An important step forward is the incorporation of residual stresses in the model, quantified by the opening angle when cutting and

unloading the aortic wall.

Given that synchrotron imaging of the aorta can (for now) only be performed *ex vivo*, we cannot unequivocally establish a causal link between high mechanical strain and vascular damage. Were synchrotron imaging possible *in vivo*, we would estimate the strain using synchrotron biomechanics on a healthy mouse and follow up the animal after 3 days of AngII infusion to compare sites of wall injury to locations of elevated mechanical strain. It is also impossible in our current setting to know which animals would have gone on to develop a dissection and which would have been protected, so as to investigate the differences underlying their dissimilar fates. An interesting extension to our study at present would be the additional implementation of models made to predict disease status based on a combination of baseline ultrasound metrics¹¹. Knowing which animals would be more likely to form a dissection and which not, we could identify strain distributions or geometric patterns that differ between the two cohorts.

3.5 Vascular reactivity assessment

In chapter 4 we used wire myography (uniaxial isometric testing) to assess the vascular reactivity of aortic rings within the suprarenal abdominal aorta, as well as arterial rings of the celiac, superior mesenteric and left renal branches. An important concern here is an inherent limitation of the technique itself, which obscures (physiologically relevant) aspects of *in vivo* loading such as axial stretch and luminal pressurization. A direct comparison of uniaxial isometric, biaxial isometric and biaxial isobaric-isometric testing has shown that biaxial testing holds particular advantages towards accurately evaluating smooth muscle function⁵. Nonetheless, isometric testing is high-throughput and easier to perform - therefore ideal for an exploratory initial characterization of vascular function, which was the scope of our work here.

An important limitation is incurred by the fact that the preload was the same for the infused and noninfused samples. Taking note of the documented decrease in circumferential strain after 3 days of infusion, we can expect that the local stiffening of the suprarenal aorta may alter the optimal initial tension that should be applied on the infused samples to achieve maximal smooth muscle responses. Further experiments will refine the temporal resolution of changes in contractility, to elucidate the state of smooth muscle function after 1 and 2 days of infusion. A still unidentified aspect is the possible switch of the smooth muscle cells from the contractile to the proliferative phenotype after 3 days of AngII infusion, which needs to be explored further - in first instance, with histological staining for contractile and synthetic proteins, reflective of the two states. The most exciting field of study is the exploration of the molecular pathways that mediate the localized loss of contractility we observed here, with particular focus on $\alpha 1$ adrenergic receptor-mediated contractions. Genetic knockout mice can be used to reveal in a direct manner the contribution of $\alpha 1$ receptor modulation to lesion development.

4 What's next?

In this dissertation, synchrotron imaging provided exquisite insight into the pathophysiology of the murine cardiovascular system *ex vivo*, reaching isotropic resolutions of 1.6 μm . Steps towards the *in vivo* application of synchrotron imaging are being made: an *in vivo* synchrotron-based microtomographic technique has recently been developed for the imaging of lung alveolae¹². Advances in computational methods stretch the potential of existing techniques even further. For example, *in vivo* 3D strain maps of the diseased mouse aorta have been acquired using 4D ultrasound and direct deformation estimation⁴.

In recent years, technological breakthroughs in preclinical imaging have offered increasing insight in previously unresolved questions of disease evolution, along with advancements in computer science which have begun to revolutionize medical image processing. The greatest leap forward in our understanding of disease etiology will be made with the advent of future clinical imaging methods, which may allow us to observe in humans the microstructural aspects of the disease initiation that we have in this dissertation started to grasp for the first time in mice.

Bibliography

- [1] John T. Favreau, Binh T. Nguyen, Ian Gao, Peng Yu, Ming Tao, Jacob Schneiderman, Glenn R. Gaudette, and C. Keith Ozaki. Murine ultrasound imaging for circumferential strain analyses in the angiotensin ii abdominal aortic aneurysm model. *Journal of Vascular Surgery*, 56(2):462–469, 2012.
- [2] M. R. Bersi, R. Khosravi, A. J. Wujciak, D. G. Harrison, and J. D. Humphrey. Differential cell-matrix mechanoadaptations and inflammation drive regional propensities to aortic fibrosis, aneurysm or dissection in hypertension. *Journal of The Royal Society Interface*, 14(136):20170327, 2017.
- [3] Uwe Raaz, Alexander M. Zöllner, Isabel N. Schellinger, Ryuji Toh, Futoshi Nakagami, Moritz Brandt, Fabian C. Emrich, Yosuke Kayama, Suzanne Eken, Matti Adam, Lars Maegdefessel, Thomas Hertel, Alicia Deng, Ann Jagger, Michael Buerke, Ronald L. Dalman, Joshua M. Spin, Ellen Kuhl, and Philip S. Tsao. Segmental aortic stiffening contributes to experimental abdominal aortic aneurysm development. *Circulation*, 131(20):1783–1795, 2015.
- [4] Hannah L. Cebull, Arvin H. Soepriatna, John J. Boyle, Sean M. Rothenberger, and Craig J. Goergen. Strain mapping from four-dimensional ultrasound reveals complex remodeling in dissecting murine abdominal aortic aneurysms. *Journal of Biomechanical Engineering*, 141(6):060907–060907–8, 2019. 10.1115/1.4043075.
- [5] Alexander W. Caulk, Jay D. Humphrey, and Sae-Il Murtada. Fundamental roles of axial stretch in isometric and isobaric evaluations of vascular contractility. *Journal of Biomechanical Engineering*, 141(3):031008–031008–10, 2019. 10.1115/1.4042171.
- [6] Craig J. Goergen, Kyla N. Barr, Diem T. Huynh, Jeffrey R. Eastham-Anderson, Gilwoo Choi, Maj Hedehus, Ronald L. Dalman, Andrew J. Connolly, Charles A. Taylor, Philip S. Tsao, and Joan M. Greve. In vivo quantification of murine aortic cyclic strain, motion, and curvature: Implications for abdominal aortic aneurysm growth. *Journal of Magnetic Resonance Imaging*, 32(4):847–858, 2010.
- [7] Nobuhiko Ayabe, Vladimir R. Babaev, YiWei Tang, Takakuni Tanizawa, Agnes B. Fogo, MacRae F. Linton, Iekuni Ichikawa, Sergio Fazio, and Valentina Kon. Transiently heightened angiotensin ii has distinct effects on atherosclerosis and aneurysm formation in hyperlipidemic mice. *Atherosclerosis*, 184(2):312 – 321, 2006.
- [8] Lisa A. Cassis, Manisha Gupte, Sarah Thayer, Xuan Zhang, Richard Charnigo, Deborah A. Howatt, Debra L. Rateri, and Alan Daugherty. Ang ii infusion promotes abdominal aortic aneurysms independent of increased blood pressure in hypercholesterolemic mice. *American Journal of Physiology-Heart and Circulatory Physiology*, 296(5):H1660–H1665, 2009.

- [9] Manesh Thomas, Dan Gavrilu, Michael L. McCormick, Jr. Miller, Francis J., Alan Daugherty, Lisa A. Cassis, Kevin C. Dellsperger, and Neal L. Weintraub. Deletion of p47phox attenuates angiotensin ii-induced abdominal aortic aneurysm formation in apolipoprotein e-deficient mice. *Circulation*, 114(5):404–413, 2006. 16864727[pmid] PMC3974117[pmcid] *Circulation*.
- [10] Christopher M. Haggerty, Andrea C. Mattingly, Ming C. Gong, Wen Su, Alan Daugherty, and Brandon K. Fornwalt. Telemetric blood pressure assessment in angiotensin ii-infused apoe-/- mice: 28 day natural history and comparison to tail-cuff measurements. *PLOS ONE*, 10(6):e0130723, 2015.
- [11] Amelia R. Adelsperger, Evan H. Phillips, Hilda S. Ibriga, Bruce A. Craig, Linden A. Green, Michael P. Murphy, and Craig J. Goergen. Development and growth trends in angiotensin ii-induced murine dissecting abdominal aortic aneurysms. *Physiological Reports*, 6(8):e13668, 2018. 29696811[pmid]PHY213668[PII]Physiol Rep.
- [12] Goran Lovric, Rajmund Mokso, Filippo Arcadu, Ioannis Vogiatzis Oikonomidis, Johannes C. Schittny, Matthias Roth-Kleiner, and Marco Stampanoni. Tomographic in vivo microscopy for the study of lung physiology at the alveolar level. *Scientific Reports*, 7(1):12545, 2017.

Lydia ASLANIDOU

1. Personal information

PhD assistant under Prof. Stergiopoulos

Research IDs :

Address: LHTC, STI-IBI, EPFL, Bâtiment MED
MED 3 2923, Lausanne 1015, CH

[Google Scholar ID](#)
[Google ORCID](#)

E-mail: lydia.aslanidou@gmail.com

+41 079 953 078 3

2. Education

August 2014 – present

PhD candidate in biomedical engineering
LHTC, EPFL, Switzerland
Under the supervision of Prof. Stergiopoulos
& Dr. Bram Trachet



February 2018 – July 2018

SNF-funded PhD mobility exchange
Center for Vascular Biology, New York, USA
Medical College of Cornell University
Under the supervision of Prof. Annarita di Lorenzo



August 2013 – March 2014

Diploma Thesis project between AUTH & EPFL
Exchange program of Joint Supervision
LHTC, EPFL, Switzerland
Under the supervision of Prof. Stergiopoulos
& Dr. Bram Trachet



September 2008 – April 2014

Joint degree (bachelor and master)
Chemical Engineering Department
Aristotle University of Thessaloniki (AUTH), GR
Grade 8.93/10 (top 1% of class), graduation
with highest honors. Academic awards from
Greek State Scholarship Foundation for
outstanding academic achievement for all years,
additional 2011-2012 scholarship award (1760€)



September 2002 – June 2008

High School Diploma
Anatolia College of Thessaloniki
Graduation with highest honors.
Top 1% of class for all consecutive years.



3. Employment history

August 2014 – present	PhD candidate in biomedical engineering LHTC, EPFL, Switzerland Under the supervision of Prof. Stergiopoulos & Dr. Bram Trachet
July 2011 – September 2011	Trainee in Proteinas Naturales SA Monterrey, Mexico IAESTE program, Employer Eng.Sergio Casares Maintenance work on heat exchangers



4. Teaching activities

Co-supervision of semester and master projects

Teaching assistant in the following courses of the EPFL Curriculum:

September 2013 – June 2017	<u>Fluid Mechanics for Life Sciences</u> Bachelor, 4 th semester
September 2016 – June 2017	<u>Biomechanics of the cardiovascular system</u> Master, 2 nd semester

Teaching duties within EPFL doctoral program

September 2014- June 2017	320 hours of teaching certified (Doctoral program's required amount: 300 hrs) <i>Hours include preparation, exercise solving, organization of simulation labs and seminars, answering students' questions, holding revision sessions</i>
---------------------------	--

5. Awards

Academic awards from Greek State Scholarship Foundation for outstanding academic achievement of 5 university years

Greek State Scholarship award of 1760€ for outstanding achievements of 2011-2012

Travel grant of 500€ for ESC Congress 2015, London, UK

SNF mobility supplementary grant for academic exchange in 2018-2019

Travel grant for WCCM 2018, New York, USA

List of Publications

- [1] Lydia Aslanidou, Mauro Ferraro, Goran Lovric, Matthew R. Bersi, Jay D. Humphrey, Patrick Segers, Bram Trachet, and Nikos Stergiopulos. Co-localization of microstructural damage and excessive mechanical strain at aortic branches in angiotensin ii-infused mice. *Biomechanics and Modeling in Mechanobiology*, Jul 2019.
- [2] Bram Trachet, Mauro Ferraro, Goran Lovric, Lydia Aslanidou, Gerlinde Logghe, Patrick Segers, and Nikolaos Stergiopulos. Synchrotron-based visualization and segmentation of elastic lamellae in the mouse carotid artery during quasi-static pressure inflation. *Journal of The Royal Society Interface*, 16(155):20190179, 2019.
- [3] Bram Trachet, Goran Lovric, Pablo Villanueva-Perez, Lydia Aslanidou, Mauro Ferraro, Gerlinde Logghe, Nikolaos Stergiopulos, and Patrick Segers. Synchrotron-based phase contrast imaging of cardiovascular tissue in mice—grating interferometry or phase propagation? *Biomedical Physics & Engineering Express*, 5(1):015010, nov 2018.
- [4] Gerlinde Logghe, Bram Trachet, Lydia Aslanidou, Pablo Villanueva-Perez, Julie De Backer, Nikolaos Stergiopulos, Marco Stampanoni, Hiroki Aoki, and Patrick Segers. Propagation-based phase-contrast synchrotron imaging of aortic dissection in mice: from individual elastic lamella to 3d analysis. *Scientific Reports*, 8(1):2223, 2018.
- [5] Mauro Ferraro, Bram Trachet, Lydia Aslanidou, Heleen Fehervary, Patrick Segers, and Nikolaos Stergiopulos. Should we ignore what we cannot measure? how non-uniform stretch, non-uniform wall thickness and minor side branches affect computational aortic biomechanics in mice. *Annals of Biomedical Engineering*, 46(1):159–170, Jan 2018.
- [6] Bram Trachet, Lydia Aslanidou, Alessandra Piersigilli, Rodrigo A. Fraga-Silva, Jessica Sordet-Dessimoz, Pablo Villanueva-Perez, Marco F.M. Stampanoni, Nikolaos Stergiopulos, and Patrick Segers. Angiotensin II infusion into ApoE-/- mice: a model for aortic dissection rather than abdominal aortic aneurysm? *Cardiovascular Research*, 113(10):1230–1242, 06 2017.
- [7] Lydia Aslanidou, Bram Trachet, Philippe Reymond, Rodrigo Fraga-Silva, Patrick Segers, and Nikolaos Stergiopulos. A 1d model of the arterial circulation in mice. *ALTEX - Alternatives to animal experimentation*, 33(1):13–28, Feb. 2016.
- [8] Bram Trachet, Alessandra Piersigilli, Rodrigo A. Fraga-Silva, Lydia Aslanidou, Jessica Sordet-Dessimoz, Alberto Astolfo, Marco F.M. Stampanoni, Patrick Segers, and Nikolaos Stergiopulos. Ascending aortic aneurysm in angiotensin ii-infused mice. formation, progression, and the role of focal dissections. *Arteriosclerosis, Thrombosis, and Vascular Biology*, 36(4):673–681, 2016.

